Electric and optical defect characterisation of Cu_2ZnSnS_4 and $CuIn_{1-x}Ga_xSe_2$ based thin-film solar cells

Van Puyvelde Lisanne

Supervisors:

Prof. dr. H. Vrielinck
Prof. dr. J. Lauwaert

Ghent University
Faculty of Sciences
Department of Solid State Sciences

UNIVERSITEIT GENT

Electric and optical defect characterisation of Cu_2ZnSnS_4 and $CuIn_{1-x}Ga_xSe_2$ based thin-film solar cells

Van Puyvelde Lisanne

Supervisors: Prof. dr. H. Vrielinck, Prof. dr. J. Lauwaert
Thesis submitted for the degree of Doctor of Science: Physics
March 2015

Examination committee:
Prof. dr. S. Siebentritt, University of Luxembourg(*)
Prof dr. D. Lamoen, University of Antwerp(*)
dr. S. Khelifi, Ghent University(*)
Prof. dr. P. Smet, Ghent University
Prof. dr. Z. Hens, Ghent University
Prof. dr. C. Detavernier, Ghent University
Prof. dr. J. Lauwaert , Ghent University
Prof. dr. H. Vrielinck, Ghent University
Prof. dr. D. Poelman, Ghent University
(*) Reading Committee

Ghent University
Faculty of Sciences
Department of Solid State Sciences
Chairman: Prof. dr. F. Callens
Krijgslaan 291-S1, 9000 Ghent, Belgium

UNIVERSITEIT GENT

'Like human defects,
those of crystals come in a seemingly endless variety,
many dreary and depressing,
and a few fascinating'

Ashcroft and Mermin

Contents

Abstract

Part I Background
One of the key challenges of the 21st century is the search for an economic and sustainable access to energy. The increasing energy needs in the world, the limited availability and the high pollution of fossil fuels give rise to increasing investments in renewable energy. As solar energy is the most abundant and reliable source of energy, the contribution of photovoltaic solar energy conversion continuously increases. However high conversion efficiency is necessary for cost effectiveness. The first generation crystalline Si solar cells feature high conversion efficiency, but they are very expensive in terms of material cost. Therefore, the terrestrial use of solar cells and modules is limited. One approach to reduce the costs is the development of thin-film solar cells where the light absorber of only a few μm thick is made from a cheap, direct band gap material deposited on a cheap glass substrate. The advantages of these devices are their low material usage, small weight, low energy consumption for fabrication and the application of large scale integrated fabrication processes. In addition such solar cells may also be synthesized on flexible substrates like metal or polyimide foil (PI) which opens a broader range of applications. A general introduction concerning the energy challenge and photovoltaics is found in **chapter 1**.

Research and development have originally concentrated on CdTe cells. Thereafter absorbers of the CIGS-family (with $Cu(In_{1-x}Ga_x)(S_{1-y}Se_y)_2$ absorbers), which avoid the toxic Cd element in the absorber layer, are developed. Recently it was shown [29] that beside Na incorporation in the CIGS layer, also the alkaline element K has a beneficial effect on the device performance. The use of K was a key element in recent considerable progress in the record efficiency of CIGS solar cells. At present $Cu(In_{1-x}Ga_x)Se_2$ offers the most efficient thin-film solar cells with cell record efficiency of 21.7% on glass substrate [30]. CIGS is a promising absorber material due to, amongst others, its high tolerance to off-stoichiometry and intrinsic defects. One of the main problems regarding CIGS absorbers is the scarcity of In, which is also an essential element for display technology. If In (and Ga) in CIGS is replaced by the abundant, inexpensive and non-toxic elements Zn and Sn, a promising alternative class of materials with high absorption coefficient and suitable band gap is obtained: $Cu_2ZnSn(S_{1-y}Se_y)_4$ (CZTSSe). The current record efficiency on lab scale for CZTSSe is 12.6 % [31]. The formation of secondary phases such as ZnS, SnS, CuS, Cu_2S, Cu_2SnS_3 is very likely as the region of stability in the phase diagram of CZTS is limited. A detailed description of the thin-film solar cell working principle and structure as well as the CIGS and CZTS absorber material properties can be found in **chapter 2**. Investigated CIGS thin-film solar cells were prepared by three stage co-evaporation process at the Laboratory of Thin Films and Photovoltaics (Empa, Zürich). Investigated CZTS thin-film solar cells were produced, using reactive co-sputtering, at the Ångström Solar Center (University Uppsala, Sweden).

Aim of this work
In both absorber materials a large number of possible intrinsic defects can be formed. The role of intrinsic point defects in CIGS and CZTS is of special importance as they control the recombination losses and hence the performance of the solar cell device. Recombination via

(deep-level) defects will limit the conversion efficiency by reduction of open-circuit voltage. Furthermore, intrinsic defects determine the conductivity type of the absorber. Understanding the defect structure in these absorber materials is crucial for further improvement of the cell efficiency [6]. Despite the amount of research already performed on CZTS and CIGS alloys, their optoelectronic properties, defect chemistry and recombination mechanisms are still rather poorly understood. Theoretical calculations did, so far, not come to an agreement. On the other hand, numerous experiments have been performed with different techniques (photoluminescence (PL), Hall measurements, deep level transient spectroscopy (DLTS), admittance spectroscopy (AS)) on different absorbers (Cu rich/poor, varying stoichiometry) made by a variety of growing techniques (single crystal, epitaxial film, polycrystalline film). As it is therefore difficult to make comparisons, contradictory assignments and long debates concerning interpretations still exist. A definitive picture of the defect structure is not yet achieved. The aim of this dissertation is the characterization of the defect physics in these absorber materials by means of electric and optical spectroscopy complemented with morphology information obtained by scanning electron microscopy (SEM) and composition information obtained by different analytical methods such as energy-dispersive X-ray spectroscopy (EDX), secondary ion mass spectroscopy (SIMS) and time-of-flight mass spectroscopy (TOFMS).

Part II Electric characterization

The capacitance based electric spectroscopic techniques used in this thesis are DLTS and AS. These techniques allow obtaining information about deep levels. The working principles can be found in **chapter 3**.

Results are reported in **chapter 4**. In DLTS measurements the detection of defect related signals might be hindered by signals originating from barriers caused by the multi-layer structure and by a possible type inversion layer at the interface. To investigate to which extent the DLTS signals actually arise from the CIGS absorber and to study the intrinsic properties of the absorber layer, the solar cells were simplified to a metal/semiconductor/metal structure by etching away the buffer and window layer and subsequent metal evaporation. The simplified structures are closer to the Schottky diodes normally measured in DLTS. Additional etch processes targeted at thinning the absorber layer and/or removing oxidation layers are also performed. AS is used to explore the possible effects on the defect structure, more in particular on the dominant shallow acceptor, of doping with Sb via an additional Sb layer underneath the CIGS absorber layer. Admittance spectra exhibit a dielectric freeze-out to the geometric capacitance plateau at low temperature (5-60 K). The signature of the intrinsic defects that provide the p-type conductivity of the CIGS absorber is determined from this freeze-out step.

Part III Optical characterization

In optical spectroscopy a variety of thin-film solar cells (CIGS or CZTS type) is investigated, each of them aiming for an improvement of the efficiency and/or lower the cost by adapting the deposition process or cell structure. The optical characterization contains external quantum efficiency (EQE) measurements and photoluminescence spectroscopy. A description of the optical characterization measurements and their related challenges can be found in **chapter 5**. EQE measurements give an indication of the origins for the efficiency losses (such as reflection, recombination losses). Photoluminescence emission and excitation measurements (PL-PLE) provide information about radiative transitions related to shallow defects and the onset of absorption.

A discussion of the results can be found in **chapter 6**. Generally the PL peaks of CZTS and CIGS thin-film solar cells are quite broad, and show a (small or large) influence of compensation in the material as a result of the Cu-poor composition of the absorber layer. The presence of compensation is shown by performing excitation power dependent measurements. A Gaussian fitting procedure for the PL spectra of CIGS and CZTS was applied.

• For CZTS: three reactively sputtered CZTS thin-film solar cells are analysed which differ in annealing step or buffer layer thickness. An optimisation of the annealing step is important

as it determines the crystallisation of the sputtered precursor film. Despite the differences in production, three similar broad PL signals appear in each cell. To link the PL results with the band gap of the investigated material, PLE measurements were performed on one of the cells. The separations between the band edge of the PLE signal and the PL peaks are large, which indicates that PL involves trapping of carriers by rather deep-level defects.

• For CIGS: four series of cells are investigated which all aimed for high efficiency in combination with low manufacturing cost. A reduction of the latter can be obtained by lowering the substrate temperature such that cheaper, temperature sensitive substrates (like flexible polymer substrates) instead of glass can be used. At reduced growth temperature, the production of a highly efficient solar cell is more challenging as grain growth of the absorber layer can be hindered, which could result in a lower cell performance. Furthermore, a different interdiffusion between the elements during low temperature deposition, and hence a different defect structure, can occur.

In the first and second series an attempt was made to promote grain growth. A partial compensation of the efficiency loss due to low growth temperature might be accomplished by growing the absorber in the presence of Sb, which can promote grain growth. In the **first series** of CIGS solar cells an additional Sb layer with varying thickness (7, 12 nm) was deposited on top of the Mo contact prior to CIGS deposition. The beneficial effect of Sb on efficiency and grain size is demonstrated with EQE and with SEM measurements, respectively. Three broad luminescence contributions are distinguished in all PL spectra by temperature dependent measurements and fitting procedure. In the **second series** the thickness of the Sb layer was fixed at 10 nm while the effect of substrate temperature was further tested via a comparison of cells made at three different reduced substrate temperatures. The comparison of cells with and without Sb layer, showed that Sb incorporation does not lead to improvement of the efficiency of these cells. This is in contrast with the results for series1, the beneficial effect is thus related with the specific growth process. EQE and SEM measurements showed a clear effect of substrate temperature, but no obvious effect of the Sb layer. The PL results on samples of series2 show again three broad luminescence contributions in samples with and without Sb layer.

The **third series** of CIGS thin-film solar cells was grown to investigate the effect of the Se evaporation rate during deposition at reduced substrate temperature. This rate has an influence on process speed (important for large scale production), on the texture and Se vacancy defect formation (important for device performance). PL studies show up to four broad emission peaks and an enhanced PL emission peak at higher energy for cells prepared at lower Se evaporation rate. It is suggested that the PL emission peak is related to the Se vacancy. The assignment of this peak is supported by different post annealing treatments of the cells. A study on the defect structure throughout the absorber layer is performed by thinning the absorber layers. A shift of the PL emission energy was found conform with the band gap grading in the absorber layer.

If PI is used as a substrate in the thin-film solar cells, besides the need of low growth temperatures, a distinct incorporation of the alkaline metals is necessary as there is no diffusion from the soda-lime glass. Cells from **series four** allow studying the effect of alkaline elements (Na and K) and incorporation methods in the CIGS absorber deposited on a PI foil. Thin-film solar cells in which Na and/or K was added during third stage of low temperature CIGS deposition and/or by post deposition treatment after CIGS deposition are investigated. It appears that the different Na and K incorporation methods have an effect on the interdiffusion of the elements and on the device performance. PL measurements show up to five peaks for which it is remarkable that they are considerably narrower than all other PL peaks of samples studied in this work. In the sample with highest efficiency a change in the dominant PL peak is noticed which might be related with the suggested improvement of the junction properties [29].

Nederlandstalig abstract

Part I Algemeen

Eén van de grootste uitdagingen van de 21ste eeuw is de zoektocht naar een economische en duurzame toegang tot energie. De toenemende vraag naar energie in de wereld, de gelimiteerde beschikbaarheid en de grote vervuiling van fossiele brandstoffen geven aanleiding tot een groei van investeringen in hernieuwbare energie. Vermits zonne-energie overvloedig aanwezig is en betrouwbaar is, stijgt de bijdrage van fotovoltaïsche energieomzetting. Hiervoor is een hoog rendement noodzakelijk voor een gunstige prijs-efficiëntie verhouding. De eerste generatie kristallijne Si zonnecellen hebben een hoge efficiëntie, de materiaal kost is echter vrij hoog. Hierdoor is het gebruik van zonnecellen en modules op aarde nog steeds beperkt. Een manier om de kosten te verlagen, is het ontwikkelen van dunne-film zonnecellen waarin de laag die licht absorbeert (absorber laag) slechts enkele µm dik is, bestaat uit een goedkoop materiaal met directe verboden zone en wordt afgezet op een goedkoop glassubstraat. De cellen hebben als voordeel het beperkt gebruik van absorber materiaal, laag gewicht en gereduceerd energie verbruik voor de fabricage waarin integratie van de cellen kan gebeuren op grote schaal. Deze cellen kunnen bovendien ook worden gesynthetiseerd op flexibele substraten zoals metaal of polyimide folie (PI) waardoor meerdere nieuwe toepassingsgebieden mogelijk worden. Een algemene inleiding omtrent de energie uitdaging en fotovoltaïsche energie kan worden teruggevonden in **hoofdstuk 1**.

In het begin was het onderzoek en de ontwikkeling voornamelijk geconcentreerd op CdTe dunne-film zonnecellen. Hierna werden absorberlagen van de CIGS-familie (met $Cu(In_{1-x}Ga_x)(S_{1-y}Se_y)_2$ absorbers), die het giftige element Cd in de absorberlaag vermijden ontwikkeld. Recent is aangetoond [29] dat naast Na toevoeging in de CIGS laag, ook het alkalische element K een gunstig effect heeft op de efficiëntie. Het gebruik van K was een belangrijke stap in de recente toename van de record efficiëntie van de CIGS zonnecellen. Momenteel geeft de $Cu(In_{1-x}Ga_x)Se_2$ absorber aanleiding tot de meest efficiënte CIGS zonnecel met een record efficiëntie van 21.7% op glassubstraat [30]. CIGS is een veelbelovend materiaal door onder andere zijn grote tolerantie voor afwijkingen van stoichiometrie en intrinsieke defecten. Eén van de grootste problemen voor CIGS absorbers is de schaarste aan In, dat ook een essentieel element is voor beeldschermtechnologie. Als In (en Ga) in CIGS worden vervangen door de overvloedig aanwezig, goedkope en niet giftige elementen Zn en Sn, ontstaat een nieuw veelbelovend alternatief type absorber materiaal met hoge absorptie coëfficiënt en geschikte verboden zone: $Cu_2ZnSn(S_{1-y}Se_y)_4$ (CZTSSe). De huidige record efficiëntie in laboratorium bedraagt 12.6% voor CZTSSe [31]. De vorming van secundaire fasen zoals ZnS, SnS, CuS, Cu_2S, Cu_2SnS_3 is zeer waarschijnlijk vermits de regio in het fase diagram waarin stabiliteit bereikt wordt, beperkt is. Een gedetailleerde beschrijving van het werkingsprincipe en structuur van de dunne-film zonnecel alsook van de CIGS en CZTS materiaal eigenschappen kan worden terug gevonden in **hoofdstuk 2**. De onderzochte CIGS dunne-film zonnecellen werden gemaakt in Laboratory of Thin Films and Photovoltaics (Empa, Zürich) via verdamping van de elementen in drie verschillende fasen. De onderzochte

CZTS dunne-film zonnecellen werden gemaakt via reactief sputteren in Ångström Solar Center (Universiteit Uppsala, Zweden).

Doel van dit werk
In beide absorber materialen kan een groot aantal intrinsieke defecten worden gevormd. De rol van deze intrinsieke puntdefecten in CIGS en CZTS is van speciaal belang vermits zij de recombinatieverliezen en hierbij dus de efficiëntie van de zonnecel controleren. Recombinatie via (diepe) defecten zal het redement beperken door reductie van de open-klemspanning. Verder zullen intrinsieke defecten bepalend zijn voor het geleidingstype van de absorber. Het begrijpen van de defectstructuur in deze absorber materialen is dus cruciaal voor verdere ontwikkeling en verbetering van het rendement [6]. Ondanks vele voorgaande studies uitgevoerd op CZTS en CIGS materialen, zijn de optisch-elektronische eigenschappen, de defectstructuur en recombinatie mechanismen nog steeds niet helemaal begrepen. Theoretische berekeningen hebben, tot nu toe, geen overeenkomst bereikt. Aan de experimentele kant zijn reeds vele experimenten uitgevoerd met verschillende technieken (fotoluminescentie (PL), Hall metingen, deep level transient spectroscopy (DLTS), admittantie spectroscopie (AS)) op verschillende absorbers (Cu-rijk/arm, verschillende stoichiometrie) gemaakt met verschillende groei/depositie technieken (éénkristal, epitaxiale film, polykristallijne film). Vermits deze verscheidenheid het moeilijk maakt om vergelijkingen te maken, bestaan tegenstrijdige verklaringen en lange discussies omtrent interpretaties nog steeds. Een finaal beeld omtrent de defectstructuur is nog steeds niet bereikt. Het doel van dit werk is de karakterisering van de defectstructuur in deze absorber materialen via elektrische en optische spectroscopie aangevuld met morfologie informatie bekomen via scanning elektronen microscopie (SEM) en informatie omtrent de samenstelling van de absorberlaag bekomen via verschillende analytische methoden zoals energie-dispersieve X-stralen spectroscopie (EDX) en secundaire ionen massaspectrometrie (SIMS).

Part II Elektrische karakterisering
De elektrische spectroscopische technieken, gebaseerd op capaciteit, die in dit werk werden gebruikt zijn DLTS en AS. Deze technieken laten toe om informatie te bekomen omtrent diepe defecten. De werkingsprincipes worden beschreven in **hoofdstuk 3**.
De resultaten verkregen door elektrische karakterisering worden beschreven in **hoofdstuk 4**. In DLTS metingen wordt de detectie van defect gerelateerde signalen gehinderd door signalen die afkomstig zijn van barrières veroorzaakt door de meerlagen structuur en door een mogelijke laag aan het interface met tegengesteld geleidsbaarheidstype. Om uit te maken in welke mate de DLTS signalen werkelijk afkomstig zijn van de CIGS absorber laag en om intrinsieke eigenschappen van deze laag te onderzoeken, werd de zonnecel vereenvoudigd tot een metaal/halfgeleider/metaal structuur door de lagen boven de absorber laag weg te etsen en hierna een metaal te verdampen. Deze vereenvoudigde structuren zijn meer gelijkend op de Schottky diode structuren die normaal in DLTS worden gemeten. Bijkomende ets processen, met als doel het verdunnen van de absorber laag en/of het verwijderen van mogelijke oxidelagen werden uitgevoerd. AS wordt gebruikt om mogelijke effecten, en dan meer in het bijzonder op de dominante ondiepe acceptor, van Sb dopering via een bijkomende Sb laag onder de CIGS absorber laag te onderzoeken. Admittantie spectra vertonen een diëlektrische uitvriezing naar het geometrisch capaciteitsplateau op lage temperatuur (5-60 K). Het kenmerk van de intrinsieke defecten die verantwoordelijk zijn voor p-type geleidbaarheid van CIGS wordt bepaald door deze uitvriezingsstap.

Part III Optische karakterisering
In optische spectroscopie is een variatie aan dunne-film zonnecellen (CIGS en CZTS) onderzocht, die elk een verbetering van de efficiëntie en/of verlaging van de kost nastreven door een wijziging in het depositieproces of de celstructuur. De optische karakterisering bevat externe quantum efficiëntie (EQE) metingen en fotoluminescentie spectroscopie. Een beschrijving van de

optische karakteriseringstechnieken en hun gerelateerde uitdagingen kan worden teruggevonden in **hoofdstuk 5**. EQE metingen geven een indicatie omtrent oorzaken van rendementsverlies (zoals reflectie, recombinatie verliezen). Fotoluminescentie emissie en excitatie metingen (PL-PLE) geven informatie omtrent de radiatieve recombinaties gerelateerd aan ondiepe defecten en omtrent de aanzet van absorptie.
Een discussie omtrent de resultaten kan teruggevonden worden in **hoofdstuk 6**. In het algemeen zijn de PL emissiepieken van CZTS en CIGS dunne-film zonnecellen vrij breed, en vertonen de pieken een (kleine of grote) invloed van compensatie in het materiaal door de Cu-arme samenstelling van de absorber laag. De aanwezigheid van compensatie is aangetoond door het uitvoeren van PL metingen als functie van excitatievermogen. Een Gaussische fitprocedure is toegepast op de PL spectra van CIGS en CZTS.
• Voor CZTS: zijn drie reactief gesputterde CZTS dunne-film zonnecellen, die verschillen in hun warmtebehandeling of in de dikte van de bufferlaag geanalyseerd. De optimalisatie van de warmtebehandeling is belangrijk vermits het de uiteindelijke kristallisatie van de absorberlaag bepaald. Ondanks de verschillen in de productie tussen de cellen, worden steeds drie brede PL pieken waargenomen. Om de PL resultaten te linken met de verboden zone van het materiaal, werden PLE metingen uitgevoerd op één van de cellen. De grote scheiding tussen het PL en PLE signaal wijst erop dat diepe defecten betrokken zijn in de radiatieve recombinatie.
• Voor CIGS: zijn vier verschillende series onderzocht die alle hoge efficiëntie in combinatie met lage productiekost nastreven. Een reductie van de laatstgenoemde kan verkregen worden door het verlagen van de substraattemperatuur zodat goedkopere, temperatuur gevoelige substraten (zoals flexibele polymeer substraten) i. p. v. glas kunnen worden gebruikt. Op een lagere depositietemperatuur is de productie van cellen met hoge efficiëntie een grotere uitdaging vermits korrelgroei kan worden gehinderd met lagere efficiëntie tot gevolg. Door de lagere temperatuur kan de diffusie van de verschillende elementen worden gewijzigd met een andere defectstructuur tot gevolg.
In de eerste en tweede serie van cellen werd geprobeerd om de korrelgroei te promoten. Een gedeeltelijke compensatie van het efficiëntie verlies door lage groeitemperatuur kan bekomen worden door het groeien van de absorber laag in de aanwezigheid van Sb dat korrelgroei kan promoten. In de **eerste serie** van CIGS zonnecellen is een bijkomende Sb laag met variërende dikte (7, 12 nm) afgezet op de Mo laag voor de CIGS depositie. Het gunstige effect van Sb of de efficiëntie en op de korrelgrootte werd aangetoond met EQE en SEM metingen respectievelijk. Drie brede luminescentie pieken kunnen worden onderscheiden in de PL spectra via temperatuurafhankelijke PL metingen en via een fitprocedure. In de **tweede serie** cellen werd de dikte van de Sb laag constant gehouden op 10 nm terwijl het effect van substraattemperatuur werd onderzocht via een vergelijking van cellen gemaakt op drie verschillende gereduceerde substraattemperaturen. De vergelijking van de cellen met en zonder Sb laag, wijst er op dat de toevoeging van Sb voor deze cellen niet tot een verhoging van de efficiëntie leidt. Dit is in tegenstelling met de resultaten voor serie1, waaruit volgt dat het gunstige effect van Sb gerelateerd is met het specifieke groeiproces. EQE en SEM meten geven een duidelijk effect van de substraattemperatuur weer maar geen duidelijk effect van de Sb laag. De PL spectra van serie2 tonen ook hier drie brede luminescentie pieken voor samples met en zonder Sb laag.
De **derde serie** van CIGS dunne-film zonnecellen is gegroeid om het effect van de Se verdampingssnelheid gedurende depositie op gereduceerde temperatuur na te gaan. Deze snelheid heeft een invloed op de productiesnelheid (belangrijk voor productie op grote schaal), de kristallografische structuur en vacature Se defect vorming (parameters belangrijk voor de efficiëntie). PL metingen vertonen vier brede pieken en een hogere PL piek op hogere emissie-energie voor de cellen vervaardigd bij lagere Se verdampingssnelheid. Een suggestie werd gemaakt om de oorzaak van deze PL piek toe te wijzen aan een transitie waarin vacature Se betrokken is. Deze toewijzing werd ondersteund door PL metingen op cellen met verschillende warmte nabehandelingen. Een studie omtrent de defectstructuur doorheen de absorberlaag werd mogelijk door de absorberlaag te verdunnen. Een opschuiving van de PL emissie-energie in overeenstemming

met de gradatie van de verboden zone doorheen de absorber laag werd waargenomen.
Indien PI wordt gebruikt als substraat in dunne-film zonnecellen is er, buiten de noodzaak aan lage groeitemperatuur, ook noodzaak aan een aparte methode om alkalische elementen in te brengen vermits er geen diffusie plaatsvindt vanuit het glassubstraat. Cellen van de **vierde serie** laten een studie toe omtrent het effect van alkalische elementen (Na en K) en de afhankelijkheid van toevoegingsmethode in een CIGS absorber afgezet op een PI substraat. Dunne-film zonnecellen waarin Na en/of K zijn toegevoegd in het laatste deel van het lage temperatuur depositieproces en/of toegevoegd gedurende een behandeling na afzetting werden onderzocht. Het blijkt dat de verschillende toevoegingsmethoden een effect hebben op de diffusie van de elementen en op de efficiëntie van de cel. PL metingen vertonen vijf pieken die opmerkelijk smaller zijn dan deze in de eerder gemeten spectra. Voor het sample met de hoogste efficiëntie werd een verandering in de dominante PL piek vastgesteld die mogelijk gerelateerd kan worden aan de verbeterde junctie eigenschappen voorgesteld in referentie [29].

Part I

Background

1 Motivation for photovoltaics

Contents

1.1 The energy challenge

We live in an exceptional time: the fossil-fuel (coal, oil, natural gas) era. The exploitation of fossil fuel energy distinguishes modern industrial society from all previous eras. Currently over 80% of the energy used by mankind comes from fossil fuels [32] as shown in figure 1.1 which represents the contributions of different energy sources to the world's total energy consumption in 2013.

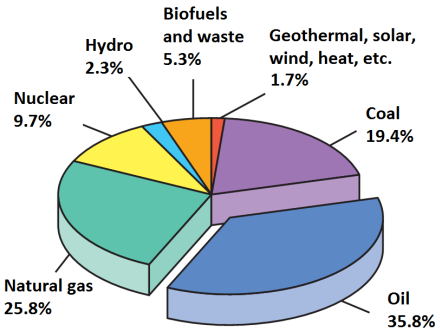

Figure 1.1: World total primary energy supply (2013). Data from the international energy agency (www.iea.org).

The fossil fuel era is an era of easy and cheap energy. Easy because oil, natural gas and coal are much easier to extract and transport than wood, the dominant fuel in the pre-industrial revolution era. Oil provides a unique fuel for transportation and natural gas is ideal for domestic

heating and cooking. Furthermore fossil fuel can easily be stored and has a big role in flexible, quick-start electricity generation. Therefore it can meet the fluctuation in energy demand.

Harnessing coal, oil and gas has led on the other hand to a dramatic expansion in energy use which entails severe consequences. The drawbacks and problems are listed underneath.

- *Non-renewable* Fossil fuels are a non-renewable resource that is going to exhaust. In the last 140 years we have consumed 120 trillion litres of oil. Currently the world's growing thirst for energy amounts to almost 120 000 litres of oil, 93 000 cubic meters of natural gas, and 221 tons of coal per second [33]. The finite resources of fossil fuels combined with the increasing energy demand will lead to a serious problem.
  Due to medical advances and massive increase in agricultural productivity, there has been a rapid population growth. In 1950 the world population was 2.6 billion people, hundred years later in 2050 it is expected that the population will be 9.2 billion people. This overpopulation will result in a huge increase in energy demand [32]. The second reason why energy consumption increases is development. The majority of people living on the earth, lives in countries that are still developing and the increase of the standard of living will ask for more energy to develop the agricultural, industrial, and trading activities. The increase in the world population and the increase of the standard of living in developing countries will lead to an increase of global energy consumption by about 2% per year [34]. The energy consumption will have multiplied by 7 by the year 2100. As fossil fuels are a finite resource this is clearly unsustainable. Alternative energy sources should be used.

- *Global warming and health problems* The use of fossil fuels causes severe damage to human health and the environment [32]. An increase in carbon dioxide concentration leads to an increase in the greenhouse effect that, in turn, increases the average global temperatures and can lead to a climate change. This will impact food security, water availability, fish production, global forests and permafrost melting. Figure 1.2 shows measurements of the CO_2 concentration in the air from the year 1000 up to the present. The year 1769 in which James Watt invented the steam engine, which started the industrial revolution, is indicated.

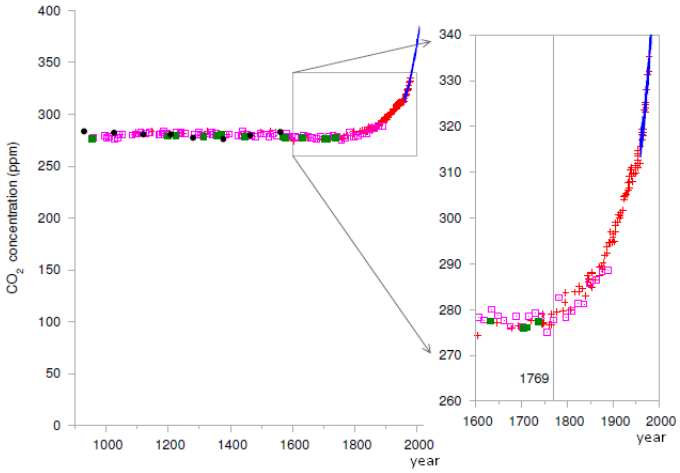

Figure 1.2: Carbon dioxide (CO_2) emission over the last 1100 years [33]

- *Uneven consumption/waste* Another critical aspect concerning fossil fuels is that their uneven allocation, coupled with the uneven waste generation and unfair distribution of wealth, leads to strong disparities in the quality of life among Earth's habitants. As an average, an American consumes about 300 GJ of energy per year, a quantity approximately

equal to that consumed by 2 Europeans, 4 Chinese, 17 Indians and 240 Ethiopians [32]. This situation is not preservable.

- *Security and safety* An important point is the security and safety of energy supply. Even if fossil fuels (e.g. oil and natural gas) are still available somewhere in the world, it would be better to rely on an independent energy production [33]. Figure 1.3 shows the energy production and energy consumption for different regions of the world. Some regions do not produce enough for their own needs and must import their energy. In the figure Russia is included in Europe. Russia has large energy resources, including a lot of natural gas. This brings Europe's production and consumption close to each other but does not reflect the real political situation. Indeed, the remaining part of Europe imports a lot of energy from Russia and elsewhere. Europe's dependence on external sources for its oil and gas is already large and is expected to increase the next decade [34].

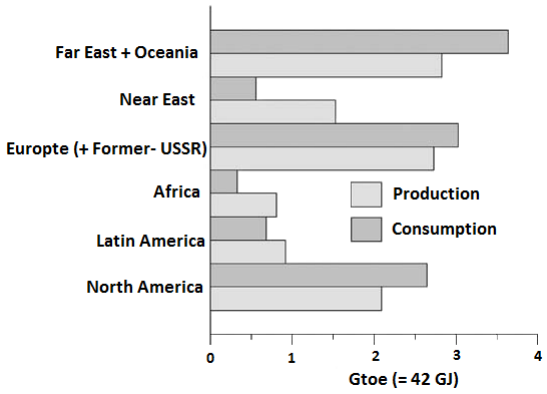

Figure 1.3: Production and consumption of primary energy (energy which has not been subjected to any conversion or transformation process) in different regions of the world, 2006

Concerning safety on the other hand, nuclear fission has serious issues. The energy obtained by nuclear fission does not emit greenhouse gases but it produces radioactive waste, whose safe disposal is an essentially unsolved issue. Other fears are exposure of radioactive materials in nuclear accident or terrorist attacks [32].

1.2 The huge potential of solar energy

The radiation reaching the surface of the earth is on average (including diffuse and direct light, average over winter/ summer, day/night) 197 W/m^2 [32, 34]. This received energy amount annually is more than 10 000 times larger than consumed annually by mankind. Solar energy is not only inexhaustible on any conceivable time-scale for human civilization, but is also widely abundant even in a scenario of doubling or tripling current energy demand. Presently, the solar energy incident on only about 5% of the desert area of the earth would be sufficient to satisfy the entire need for electric power in the world [34]. Storage and transport of electricity is of course another issue [32, 34]. Many technologies are used to exploit solar radiation. With properly designed technologies the solar electromagnetic flux can be converted into heat, electricity and biofuels which are the three essential forms of energy used in everyday life.

1.3 Photovoltaics

Photovoltaics (PV) includes the direct conversion of sunlight into electric energy. The transformation relies on the photovoltaic effect: an electron-hole pair, which is created after a semi-

conductor is exposed to light, is separated whereafter the free carriers are collected. A direct current is produced, which can be converted to an alternating current with electronic devices.

1.3.1 Advantages-disadvantages

PV has many benefits: highly reliable, renewable, pollution-free, noise free, low in operation costs (no moving parts) and construction costs, operating over a quite long period of time (in the case of grid applications photovoltaic modules can last more than 30 years). Electricity can be produced on demand at the place of consumption, avoiding transport losses over large distances. It needs no exploration for new sunshine reservoirs and no wars to get access over its fuel. It can be constructed to any size based on energy requirements.
Besides these advantages there are also some drawbacks. Although no greenhouse gas is emitted during operation of a photovoltaic cell, this is currently not the case for its fabrication. Solar cell technology requires a lot of energy, the initial cost (labour, materials, energy, ...) is quite high. The energy payback time (how long a PV system must operate to recover the energy consumed to produce it) is critical to technology viability. Thin-film technologies, which are studied in this work, perform on the module level better by at least a factor of two, less than one year, than the current dominant technology with multicrystalline Si modules (2-3 years) in southern regions [35]. Systems deployed in the next generation are expected to have shorter payback times. Another concern is that a PV system does not generate power when the sun does not shine. Supplemental means of energy storage are required. This also holds when the consumer is not connected to the electric grid. In 'stand-alone' applications batteries may be required to store electricity for use in periods without sunlight.

1.3.2 History

The photovoltaic effect was first reported by Edmund Bequerel in 1839 when he observed that the action of light on a silver coated platinum electrode, immersed in electrolyte, produced an electric current. Willoughby Smith (1873) reported about the photoconductivity of selenium. In 1876 William Adams and Richard Day discovered the photovoltaic effect in selenium which was contacted by two heated platinum contacts and exposed to light. The first functional solid state photovoltaic cell was made by Charles Fritts in 1883. He coated the semiconductor material selenium with an extremely thin layer of gold as a top contact. He noted, 'the current, if not wanted immediately, can be either stored where produced, in storage batteries, ... or transmitted over a distance and there used.' The first intentionally made PV device was a fact.
The early thin-film solar cells were Schottky barrier devices. A semitransparent layer of metal was deposited on top of the semiconductor. As the current produced was proportional to the intensity of the incident light, the photoconductive materials were used as photographic light meters. The photovoltaic effect in barrier structures was an added benefit, because the light meter could operate without a power supply. During the 1930s Walter Schottky, Neville Mott and others developed the theory of metal-semiconductor barrier layers.
In 1954 researchers at Bell Labs in the USA discovered accidentally that pn-junction diodes generated a voltage when the room lights were on. pn-junctions in silicon were developed by exposing n-type silicon to the boron tricholoride gas so that a p-type upper layer was formed. Within a year, a 6% efficient Si pn-junction solar cell was produced. Because the production cost was estimated very high, the cells were not considered for power generation for several decades. During the 1950s and 60s, silicon solar cells were widely developed for applications in space. Also in 1954 results of a thin-film heterojunction solar cell based on Cu_2S/CdS having 6% efficiency were published. In the following years studies on GaAs, InP and CdTe were performed. These studies were stimulated by theoretical work of Shockley and Queisser which developed the fundamental theory of a pn-junction solar cell. In 1973 most governments began programs to encourage renewable energy after the first World Oil Embargo. The energy crisis experienced by the oil-dependent western world gave an urgency to research (with increasing funding) and

application of alternative sources.
In the 1980s companies attempted to scale up the thin-film PV technologies like a-Si and $CuInSe_2$. These cells achieved efficiencies larger than 10% for small area (1 cm^2) devices which were made with carefully controlled laboratory scale equipment. The scale up was far more complicated than just scaling the size of the equipment. The first consumer-sized, small-scale power applications were developed. The solar-powered calculator, pioneered by Japanese electronics companies is the best-known example. During the 1990s the economics of photovoltaics improved primarily through economies of scale. The costs for PV modules had fallen but once again there was a lack of financial and technical resources for development of inverters and sun trackers, which had only limited application outside of a PV power system. Further during this period an attempt to help developing countries by rural electrification of remote villages was made. Late in the 1990s PV cells were integrated into standard building products, such as windows or roofs, lowering the incremental cost of PV installation [36, 37].

1.3.3 Global PV capacity

By the end of 2013, the installed photovoltaic capacity reached 139 gigawatts (GW) on the planet. Photovoltaics grew fastest in China, followed by Japan and the United States, while Germany remains the world's largest overall producer of photovoltaic power with a total capacity of 35.5 GW, contributing almost 6% to its national electricity demands.

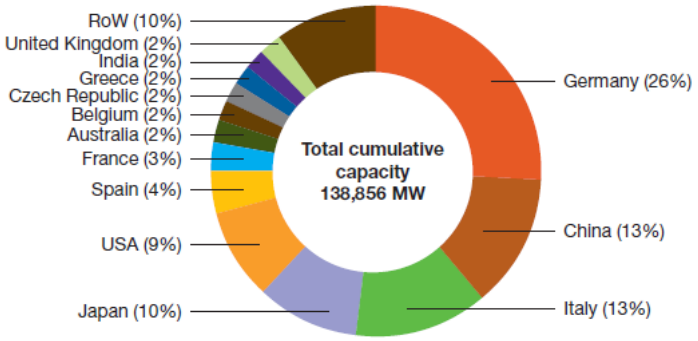

Figure 1.4: Global PV cumulative installed capacity share (2013) [38].

By 2018 the worldwide photovoltaic capacity is projected to have doubled (low scenario of 320 GW) or even tripled (high scenario of 430 GW). The European Photovoltaic Industry Association (EPIA) expects the fastest PV growth to continue in China, South-East Asia, Latin America, the Middle-East, North Africa, and India.

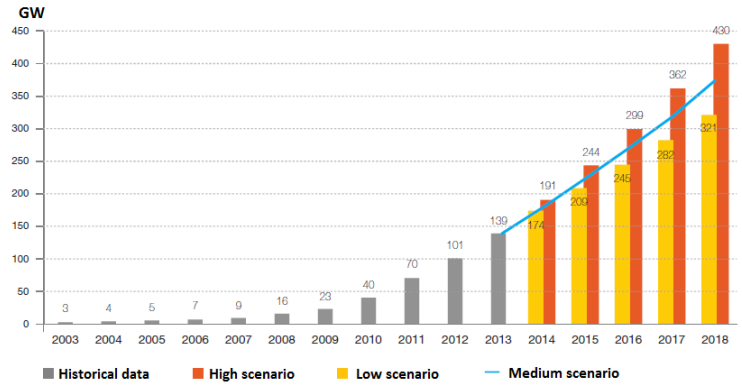

Figure 1.5: Global PV cumulative scenario until 2018 [38].

1.3.4 From thick to thin solar cell absorbers

The photovoltaic market today is mostly dependent on single crystalline and polycrystalline silicon solar cells. In 2013 Si technologies still made up almost 90% of the world PV market as shown in figure 1.6. This dominance decreases with the growth of the thin-film industry [34].

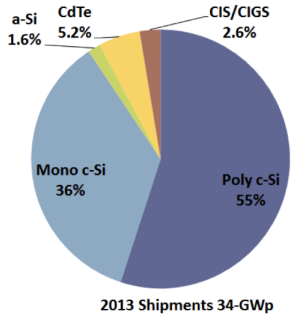

Figure 1.6: Market share by technology in 2013 (www.renewableenergyworld.com).

As Si is an important material for the electronics industry, a lot more information is available about the physical, chemical and optical properties of this semiconductor than for any other material. For monocrystalline silicon, the maximum recorded cell efficiency reaches 25.6% (Panasonic) in the laboratory and 20.4% (test centre: FhG-ISE) for polycrystalline cells [31]. In a commercial application, the typical efficiency of a module is 18.5% for multicrystalline Si (Q-Cells) [31] and thus well below that obtained in laboratory conditions.
Si has relatively small absorption coefficient related with its indirect band gap ($\alpha \approx 10^3$ cm^{-1} [39, 40] around 1.5 eV). Therefore a thick Si wafer of around 250 µm is used to have sufficient absorption of light [35]. The fabrication of the Si wafers (50% of the cost on module level [35]), encapsulation and wiring requires a lot of energy which results in a high cost. The latter is also related to the high temperature (above 1400°C) which is needed to obtain pure Si from sand after several melting steps [41].

A goal for the future is to produce solar cells with lower payback time. This can be done by making thin-film photovoltaic cells which needs less material and less energy for processing (temperature for processing < 550°C). The technology makes efficient use of raw materials: while 0.5-1 kg/m^2 of semiconductor grade silicon is required for a conventional module, the material consumption per square meter for the active films of a $CuInSe_2$ module is: 7-20 g molybdenum, 1.5-4 g copper, 3-9 g indium, 7-20 g selenium, and 1-3 g zinc (depending on the exact module structure and yield). This implies that the total material input is comparable to the material used for just the grid metallization of silicon modules. Another advantage of the thin-film solar cells is that they are light weight (due to the thin absorber layer and the possibility to use polymer substrates) which is attractive to space industry. The cost can be further reduced by roll-to-roll processing and the use of low cost substrates such as glass sheet, metal or polymer foil. The use of flexible substrates can moreover broaden the range of applications.
The main characteristics of the semiconductor absorber materials for thin-film solar cells are direct band gaps and high absorption coefficients. Different semiconductors meet these criteria: amorphous silicon, cadmium telluride (CdTe), copper indium galium diselenide ($Cu(In_{1-x}Ga_x)Se_2$, CIGS) and copper zinc tin sulfide (Cu_2ZnSnS_4, CZTS). The main characteristics for each of these thin-film semiconductor absorber type are listed underneath. The research in this thesis focusses on CIGS and CZTS thin-film solar cells.

⋆ Hydrogenated **amorphous silicon** (a-Si:H), which has assigned a direct band gap (E_g = 1.6-1.8 eV) [36], has a high absorption coefficient (α = 10^4-10^5/cm) [36] in the visible range of the solar spectrum. A 1 µm thick a-Si:H layer is sufficient to absorb 90% of the solar energy with energy larger than the band gap. The efficiency of amorphous silicon thin-films (13% [1]) is much smaller than those of crystalline Si cells. The light induced degradation of the modules is a great issue [35].

⋆ **CdTe** has a nearly optimally match to the solar spectrum for photovoltaic energy conversion (E_g = 1.5 eV, $\alpha > 10^4$/cm for E > 1.5 eV [36]). A record efficiency in lab conditions of 21.0% has been reached (First Solar) [1]. The most serious concern about CdTe technology is that Cd and Te are toxic. Cd waste and recycling the modules after their end of life could be hazardous to the environment. This technology is also hindered by the instability of the cells due to contact oxidation, contact degradation and humidity [41].

⋆ $\mathbf{Cu(In_{1-x}Ga_x)Se_2}$ (CIGS) is a very promising material for a thin-film solar cell (for $E_g \approx 1.15$ eV, $\alpha > 10^4$/cm for E > 1.2 eV) [40]). Some concerns about CIGS thin-film technology are the complexity of the material (problem for manufacturing) and the use of toxic CdS as buffer layer. Many CIGS related issues (Cu-poor surface layer, role of Na, role of Ga gradient, ...) are still unresolved. At the moment the lab record efficiency of CIGS on glass is 21.7% (ZSW) [30], 20.4% (Empa) [29] on flexible substrates and 16.6% (Avancis) for a 30 cm·30 cm module [42].

⋆ As there are some restriction on the usage of heavy metals such as cadmium, the limitation in supplies and fluctuation of prices for indium and tellurium, a low-cost, earth abundant alternative with high absorption coefficient and decent band gap was sought and found namely $\mathbf{Cu_2ZnSn(S,Se)_4}$ (CZTS) ($E_g \approx 1.5$ eV, $\alpha = 10^4$/cm for E >1.5 eV [43]). The cost of raw material for CZTS PV technology is around 5 and 20 times lower than for CIGS and CdTe respectively [44]. In 1996 a conversion efficiency of 0.66 % was reported a CZTS [39]. Due to research and further development a conversion efficiency of 9.2% (Solar Frontier) [45] for pure sulfide CZTS and 12.6% (IBM) [31] for CZTSSe solar cells has been reached so far.

1.3.5 Efficiency evolution

In figure 1.7 the evolution of the cell efficiencies are provided within different families of semiconductor. Next to the crystalline (e.g. Si, GaAs) and polycrystalline (e.g. CdTe, CIGS) solar cells, new PV technologies such as organic, dye-sensitized or perovskite solar cells arise and are further developed. The most recent world record efficiency for each technology is highlighted on the right edge of the figure [1].

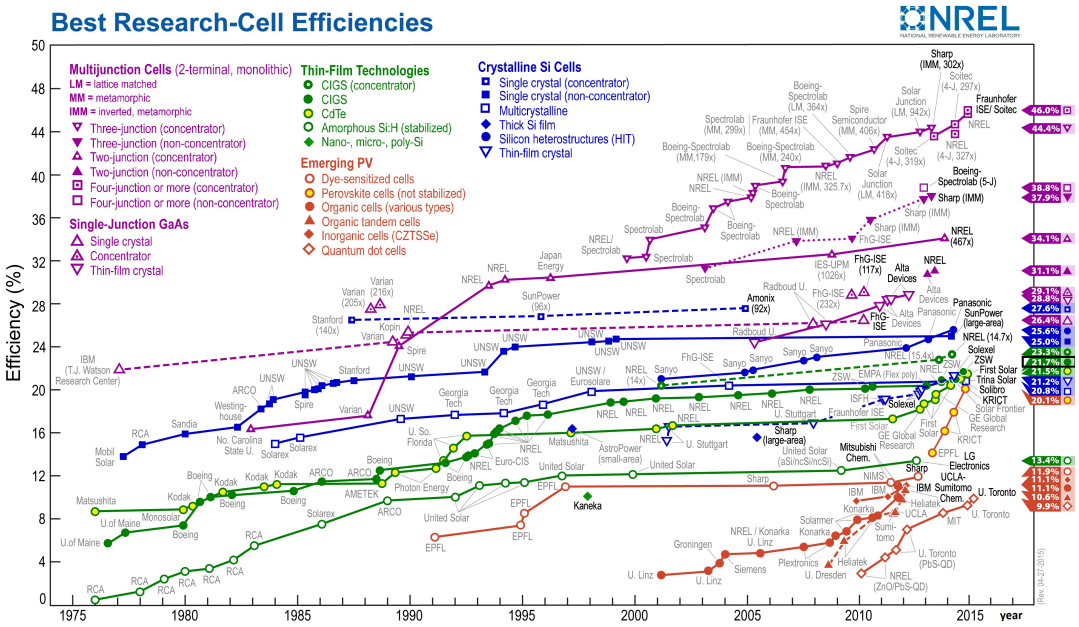

Figure 1.7: Evolution of the best small area solar cell efficiencies PV technologies (27/4/2015) [1].

1.3.6 Manufacturing

CIGS Table 1.1 is published in reference [46] and presents the status of CIGS modules manufacturing companies at the end of May 2012. A more detailed description of some companies can be found in reference [39]. All of these companies (besides Solibro) were founded at the end of the last century. However the first CIGS modules commercially available in modest volume arrived on the market only over the past few years. Large commercialization of CIGS modules on flexible substrates is in a rather early phase as tools for roll-to-roll deposition and appropriate equipment are nowadays lacking. In addition for the flexible modules, low-cost flexible encapsulation materials with sufficient moisture blocking properties need to be developed to guarantee long-term stability. A potential future challenge to move CIGS manufacturing to the multi-gigawatt level, needed to develop solar photovoltaic electricity generation into a major electricity source, is related to the abundance of In and Ga. At present there exists an ongoing discussion about whether indium and gallium are abundant enough at affordable prices [39].

Table 1.1: Overview of most important CIGS solar industry companies (published in reference [46]).

	Best cell η [%]	Best (mini) module η [%]	Area [cm^2]	Company	Founded [year]	Cap. [MWp/y]	Method	Notes
Rigid								
SLG		17.4*	16	Q-Cells (Solibro)	2006	135	Coevaporation, monolithic	Light soaking effect
SLG		17.8	900	Solar Frontier	1993 (Showa Shell)	1000	Sputtering, selenization	Cd-free, EVA and glass encapsulation
SLG		15.8*	900	AVANCIS	1981 (ARCO solar)	120	Sputtering of Cu-In-Ga:Na, Se evap., RTP sulphurisation	
SLG		12.6*	7500	Soltecture	2001 (Sulfurcell)	35	CIGS coevap.	EVA encapsulation, glass laminated
SLG		15.1	6500	Manz Automation	1999 (Würth Solar)	6	CIGS coevap.	Innovation production line
Flexible								
PI	14.1	11.7		Ascent Solar (ITN)	2005	30	CIGS coevap.	Monolithic
PI	13.4*			Solarion	2000	20	R2R coevap., ion-beam assisted	Shingling
SS	17.3	15.7*	10000	Miasolé	2003	100	All sputtering	Shingling, glass laminated
SS	15.4	13.2 (string)	3883	Global Solar	1996	75	Coevap.	ETFE front sheet, flexible strings and modules
SS	13.8*	13.4* (ap)		Solopower	2005	20	R2R electrodep.	Serial connection
Al foil	17.1*	11.6*		Nanosolar	2002	100	Non-vacuum printing	Serial connection, glass laminated
Cu tape	<10			Odersun	1994 (IST)	-	Galvanic deposition	n-type CIS, p-type buffer, shingling

Data based on companies' own website. *Externally certified values.

CZTS No solar cell company is using kesterites in their manufacturing process so far [39]. A collaboration between IBM, DelSolar, and Solar Frontier is set in 2010 to develop the CZTS technology further. As kesterite solar cells are (relative to other solar cell technologies) still in their early development stage, more research and development is necessary before manufacturing to compete with technologies already in commercial production. Price has to be low, efficiency has to be high and deposition processes should be made applicable for large scale production [39].

2 Thin-film photovoltaics

Contents

2.1 Working principle

2.1.1 Pn-junction

2.1.1.1 Homojunction

The current voltage characteristic of a pn-junction is deduced for an anisotype homojunction. This junction is formed when a n-type semiconductor with donor density N_d is in contact with a p-type semiconductor with acceptor density N_a of the same semiconductor crystal (band gaps of the n- and p-type semiconductor are thus equal). The concentration gradient between those two regions causes diffusion currents; electrons move from the n-type to the p-type and leave their positively charged donor atoms behind, analogously holes move from the p-type to the n-type and leave their negatively charged acceptor ions behind. This diffusion current of majority carriers is also labelled as *recombination currents* [47]. A fixed space charge at the interface (depletion region) is introduced and gives rise to an electric field. This electric field causes a drift current that counteracts the diffusion current. This drift current, also labelled as (thermal) *generation current*, is due to the minority carriers generated throughout the device (at small rate) by thermal excitation. The minority carriers that reach the junction without recombining are swept across the junction in opposite directions by the strong electric field. At equilibrium, the net current across the junction becomes zero. The generation and recombination currents balance each other and no net current flows through any part of the cell. The sum of hole and electron thermal generation currents density is called the saturation current density J_0 ($J_0 = J_{h,gen}+J_{e,gen} = J_{h,rec}+J_{e,rec}$).

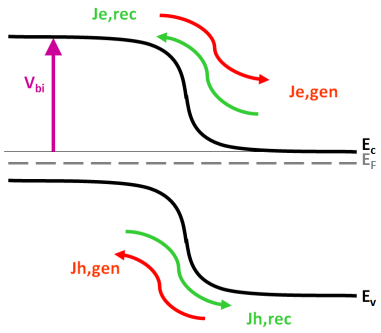

Figure 2.1: Dark pn-junction in the dark at equilibrium. Majority and minority carrier currents are indicated in green and red respectively [47].

The thermal equilibrium of drift and diffusion currents finds its expression in a coincident Fermi level E_F on both sides of the junction as seen in figures 2.1 and 2.2. Conduction and valence band energies with respect to the Fermi level become similar to the bulk far away from the interface (quasi-neutral region). To construct the energy band diagram of a pn-junction the vacuum level (which represents the energy of an electron at rest outside the material) is defined

as reference level. The energy required to remove an electron from the conduction band edge of the semiconductor (n- or p-type) to the vacuum level is labelled as the electron affinity ($\chi_{n,p}$).

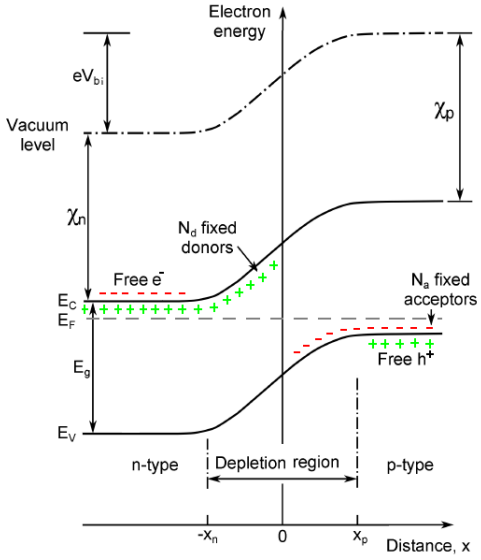

Figure 2.2: Band diagram for a pn-homojunction [9].

The electric field in the depletion region (also labelled as space charge region (SCR)) induces an built-in potential V_{bi} which can be written as

$$qV_{bi} = E_g - (E_F - E_v)_p - (E_c - E_F)_n + (\chi_p - \chi_n)$$

The width of the depletion region $W = x_n + x_p$ depends on the total voltage drop across the junction and the net ionized charge density.

$$W = \sqrt{\frac{2\epsilon_0\epsilon_r}{q}\left(\frac{1}{N_a} + \frac{1}{N_d}\right)(V_{bi} - V)} \tag{2.1}$$

2.1.1.2 Heterojunction

A heterojunction device is a combination of a n- and p-type semiconductor each with different band gaps. As a result the valence and conduction band are not continuous at the interface between different materials. Band offsets are formed. If the electron affinity of the n-type layer is smaller than that of the p-type layer (figure 2.3(a)), a positive conduction band offset ($\Delta E_c = E_{c,n} - E_{c,p} > 0$) is formed, which is labelled as 'spike'. In the opposite case (figure 2.3(b)) a 'cliff' is formed.

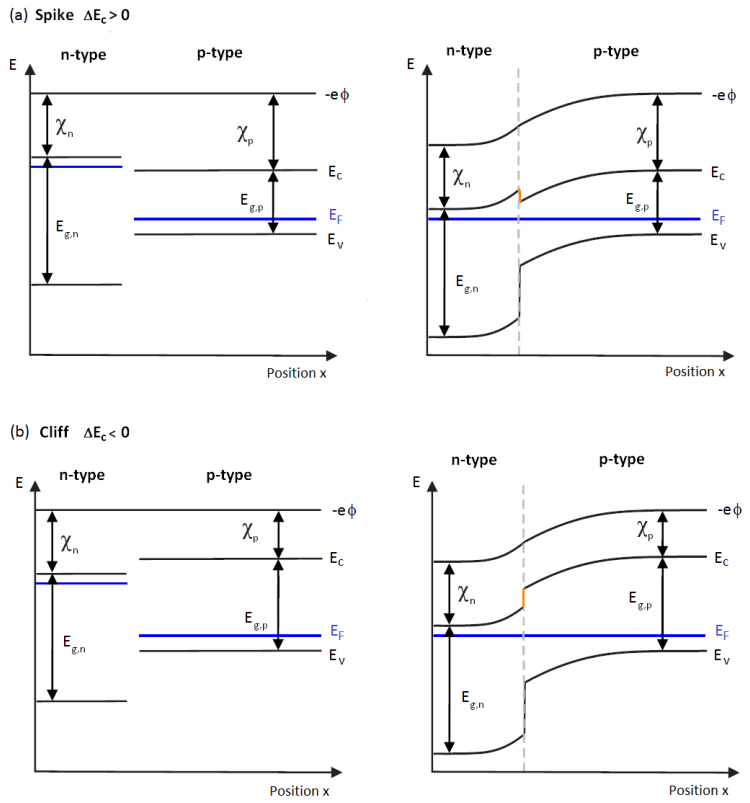

Figure 2.3: (a) spike, (b) cliff (adapted from [48]).

A spike obstructs the flow of photogenerated carriers from the absorber to the buffer layer, it forms a potential barrier for electrons. This influence is, according to simulation work, negligible when the offset is below 0.4 eV for $CuInSe_2$ [4].The higher the Fermi level lies to the conduction band, the higher is the recombination barrier for holes at the interface [49]. For a good buffer material it is important that the band offset ΔE_c is small.
A cliff leads to a reduced hole barrier which might increase interface recombination [4]. As interface recombination is not desired, a positive band offset (preferably close to zero) is important for high device performance.

2.1.2 Current transport in ideal diode

2.1.2.1 I-V characteristics

In the dark
Based on the continuity equation (see section A.1.2), the equation for the dark current density-voltage characteristic of an ideal diode can be written as

$$\begin{aligned} J(V) &= J_0 \left[exp\left(\frac{qV}{nkT}\right) - 1 \right] \\ \text{with } J_0 &= q\, n_i^2 \left(\frac{D_n}{N_a L_n} + \frac{D_p}{N_d L_p} \right) \end{aligned} \tag{2.2}$$

$L_{p,n}$ and $D_{p,n}$ indicate respectively the hole and electron diffusion length and diffusion constant. n_i^2 is the intrinsic concentration. The diode ideality factor 'n' is 1 for an ideal pn-junction. The assumptions necessary for the derivation of this equation are abrupt depletion layers, Boltzmann approximation for charge carrier densities, low injection conditions and no generation or recombination currents within the depletion layer [48]. This diode equations could thus be labelled

as 'ideal' diode equation or Shockley equation. The current density-voltage characteristic is presented in figure 2.4.

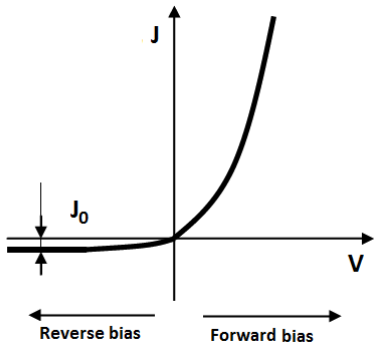

Figure 2.4: Current density-voltage characteristic of a pn-junction.

Under illumination

When a pn-junction is illuminated additional electron-hole pairs are generated in the semiconductor which leads to a non-equilibrium situation (quasi-Fermi levels for electrons and holes are distinct). The strong increase of the concentration of minority carriers on both sides leads to the flow of the minority carriers across the depletion region, due to the electric field, into the quasi-neutral regions. The direction of the photo-generated current density, J_{ph} is thus opposite to the direction of the diode current [47]. The net current density of the illuminated pn-junction can be described as

$$J(V) = J_0 \left[exp\left(\frac{qV}{nkT}\right) - 1 \right] - J_{ph} \tag{2.3}$$

The illuminated J-V characteristic of the pn-junction is thus the same as the dark J-V characteristic, but it is shifted down by the photo-generated current density J_{ph}. The superposition principle and characteristic performance parameters are illustrated in figure 2.5.

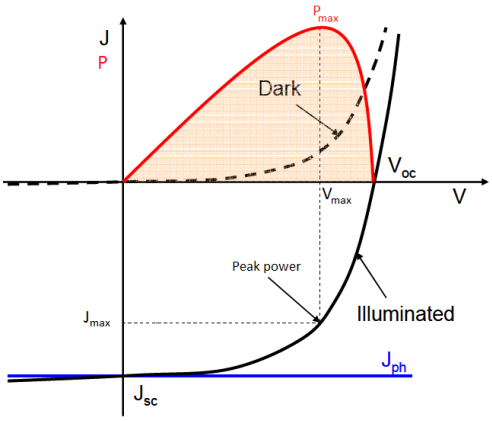

Figure 2.5: J-V characteristics of dark and illuminated pn-junction.

2.1.2.2 Performance characteristics

Short-circuit current

The short-circuit current J_{sc} is the current that flows through the external circuit when the electrodes of the solar cell are short-circuited (V = 0). In the ideal case (internal resistances are

negligible) J_{sc} equals J_{ph}. The band bending is not changed compared to the band bending in the dark but the quasi Fermi levels vary strongly in the depletion region [2] (figure 2.6(a)).

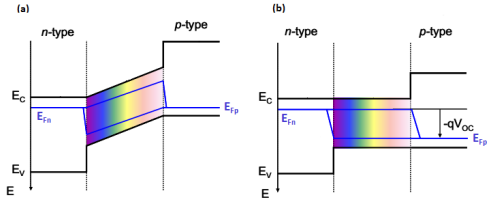

Figure 2.6: Band diagrams of a pn-junction under illumination (a) at short-circuit (b) at open-circuit (E_{Fn}, E_{Fp} are the quasi Fermi levels) [2].

Open-circuit voltage

If no external circuit is connected (J = 0) to an illuminated solar cell, charge accumulates at the front and back. This separation of charges gives rise to a potential difference between the two contacts which is known as the open-circuit voltage V_{oc}. As shown in figure 2.6(b), qV_{oc} is the difference between the quasi- Fermi levels [47]. V_{oc} corresponds to the forward bias voltage, at which the recombination current (majority diffusion current) compensates the photocurrent. It is not possible to extract any power from the device when operating at either open-circuit or short-circuit conditions. Assuming that the net current is zero, V_{oc} can be calculated as

$$V_{oc} = \frac{kT}{q}\, ln\Big(\frac{J_{ph}}{J_0} + 1\Big)$$

Inserting the saturation current (equation A.4) for a single sided p^+n-junction the open-circuit voltage for a p^+n solar cell can be written as [3]

$$\begin{aligned} V_{oc} &\approx \frac{kT}{q}\, ln\Big(\frac{J_{ph}}{q\,\frac{N_c N_v exp(-E_g/kT)}{N_d}\,\frac{D_p}{\tau_p}}\Big) \\ &\approx \frac{E_g}{kT} + \frac{kT}{q} ln\Big(\frac{J_{ph} N_d \sqrt{\tau_p}}{q N_c N_v \sqrt{D_p}}\Big) \end{aligned}$$

With N_c and N_v the conduction band and valence band effective densities of state respectively and τ_p the hole lifetime. The open circuit voltage is dependent on the lifetime as well as on the band gap E_g. A larger lifetime increases V_{oc}. Up to a certain point (as an increase of the band gap will result in a decrease of J_{ph}), V_{oc} increases linearly with increasing band gap [4].

Fill factor

The fill factor is the ratio between the maximum power (J_{max}·V_{max}) generated by a solar cell (indicated in figure 2.5) and the product of V_{oc} and J_{sc}.

$$FF = \frac{J_{max} V_{max}}{J_{sc} V_{oc}}$$

Conversion efficiency

The solar conversion efficiency of a solar cell is the power density at the maximum power point divided by the power density of the incident light (P_{inc}).

$$\eta = \frac{J_{max} V_{max}}{P_{inc}} = \frac{J_{sc}\, V_{oc}\, FF}{P_{inc}}$$

2.1.3 Current transport in non-ideal diode

In equation 2.3 J_{ph} is assumed to be voltage independent. In reality this does not have to be the case [11,48]: a crossing of the dark and illuminated J-V curves ('cross over effect'), a saturation of the current for $V>V_{oc}$ ('roll over') (in dark and light) and a reduction of the measured photocurrent under forward bias ($V<V_{oc}$) are frequently observed [6,48]. The 'roll-over' effect can be assigned to an additional barrier e.g. back contact barrier [6,10,11].

2.1.3.1 Current losses

Several power loss mechanisms can reduce the performance of a solar cell. Higher conversion efficiency could be achieved if losses are minimized. Two main groups of losses can be found: optical and electric losses.

Optical losses
Optical losses reduce the short-circuit current. These losses will be further discussed in relation with external quantum efficiency measurements in section 5.1.1. Three main optical losses can be found:

- surface reflection which is depended on the refractive index difference between the upper layer of the solar cell and the air.
- front contact shading due to the front contact grid.
- absorption losses due to absorption of light in regions that do not contribute to the photocurrent (e.g. window layer).

Electric losses
Electric losses are a result of parasitic Ohmic losses and recombination losses.

Parasitic Ohmic losses
In real cells, the J-V curve is distorted by parasitic effects [50,51]. A series resistance (R_s) and a shunt resistance (R_p) in parallel lower the efficiency of the solar cell. The diode equation when parasitic resistances are included can be written as

$$J = J_0 \left[exp\left(\frac{q(V - JR_s)}{nkT}\right) - 1 \right] + \frac{V - JR_s}{R_p} - J_{ph} \tag{2.4}$$

The effect of shunt and series resistances on the J-V curve is shown in figure 2.7. At low forward (and negative) voltage, the effect of shunt resistance becomes clear while at higher positive voltage series resistance dominates.

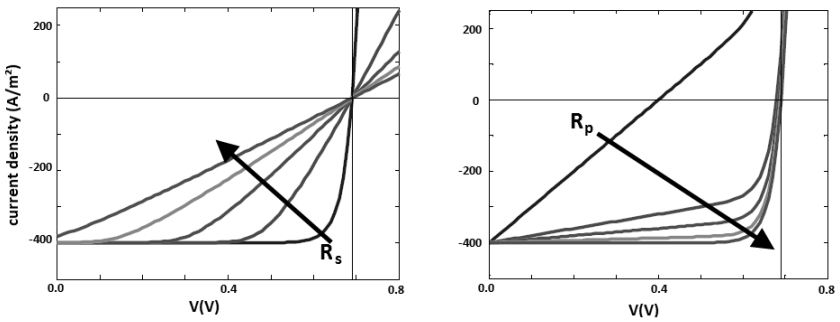

Figure 2.7: Influence of (a) series resistance, (b) shunt resistance on J-V characteristic.

- The ***series resistance*** has no influence on V_{oc} but lowers the fill factor [50]. Very large series resistance can reduce the short-circuit current. Sources of series resistance are illustrated in figure 2.8 and include
  - the metal contacts
    - grid fingers resistive losses ($R_{fingers}$)
    - lateral resistance of back contact (R1)
  - the transverse flow of current in the solar cell to the front grid
    - contact resistance between back contact and diode (R2)
    - bulk-semiconductor resistance (R3)
    - resistance of transparent conductive oxide (R4)
    - resistance between front electrode and semiconductor (R5)

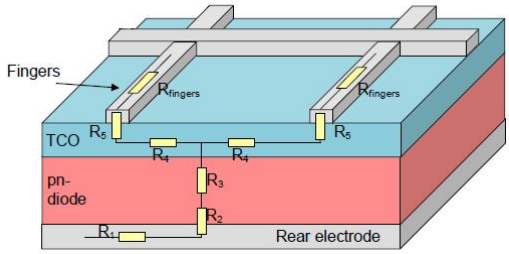

Figure 2.8: Illustration of possible series resistance losses [50].

- The ***shunt resistance*** can be due to a leakage current across the diode and along the edge of a solar cell [50]. Impurities and crystal defects in the depletion region contribute to a low parallel resistance. The shunt resistance has no influence on the short-circuit current. For small shunt resistance, V_{oc} is lowered, which result in a decrease of fill factor. If the diode is (almost) completely shunted, it is an ohmic resistance.

Recombination losses

Recombination losses (surface and bulk recombination) occur as photo-generated charges recombine before reaching the electrodes. This recombination reduces the open-circuit voltage and is the origin of a deviation in forward bias of a real solar cell compared to an ideal pn-junction.

2.1.3.2 Recombination

Recombination processes

When a semiconductor absorbs a photon with energy larger than the band gap, an electron is excited from the valence band into the conduction band leaving behind a hole. The thermal equilibrium is distorted. The equilibrium can also be distorted by applying a voltage. When the electron returns to its original state, it may do so through radiative (release of a photon) or non-radiative (no photon production) recombination. Not all charge carries that are generated in a solar cell are thus collected at the electrodes. This lowers the efficiency below the theoretical detailed balance limit. Figure 2.9 presents the mechanisms in which an electron in the conduction band can return to the valence band [48].

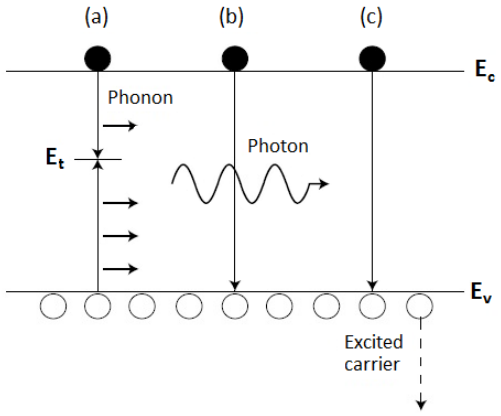

Figure 2.9: Recombination mechanisms: (a) non-radiative, (b) radiative (c) Auger.

- (a) Non-radiative Shockley-Read-Hall (SRH) recombination: during this recombination electron-hole pairs recombine through deep level impurities (at energy level E_t in the band gap). The energy liberated during the recombination is dissipated by lattice vibrations or phonons [52].
- (b) Radiative recombination: recombination with emission of a photon which carries away most of the excess energy. This process depends on the available electrons (holes) in the conduction band (valence band) and on temperature. The process can be mediated by defects in the band gap (section 5.2). In figure 2.9 band-band recombination is shown.
- (c) Auger recombination: recombination whereby the excess energy serves to accelerate a third charge carrier, which thermalizes rapidly by emitting phonons. Only in the case of high doping concentrations Auger recombination is the limiting process ($> 10^{18}$ cm^{-3}) [6].

Typical thin-film solar cells are made from amorphous or polycrystalline semiconductors that are far from defect free. The dominant recombination mechanism occurs via states in the band gap [5]. The lifetime τ of the charge carrier depends on the density of defect states N_T, the capture cross section σ of the defects and the thermal velocity v_{th} via $\tau = (N_T \cdot \sigma \cdot v_{th})^{-1}$. In reference [5] the influence of recombination via defects in the middle of the band gap on the current-voltage characteristic, calculated via numerical simulations, is reported. It seemed that as the lifetime decreases (by N_T increase), V_{oc} decreases as well. A high life time, by minimising recombination, is thus very important for high efficiency thin-film solar cells.

Non-radiative recombination paths

Non-radiative recombination through deep defect states is non negligible in thin-film solar cells. The effect on the current density-voltage characteristic is discussed below. In the calculation of the J-V characteristic of an ideal pn-junction, the recombination in the device was assumed to be dominated by recombination in the quasi neutral region. No recombination was assumed in the depletion layer. In reality different recombination mechanisms (indicated in figure 2.10) are possible. Tunneling enhancement can occur for recombination paths (1) and (2) due to the presence of high electrical fields in the junction region [53].

1. Interface recombination over the absorber band gap, between the buffer layer conduction band and absorber valence band
2. Recombination in the space charge region (SCR) of the absorber
3. Recombination in the quasi neutral region (QNR) of the absorber
4. Back contact recombination

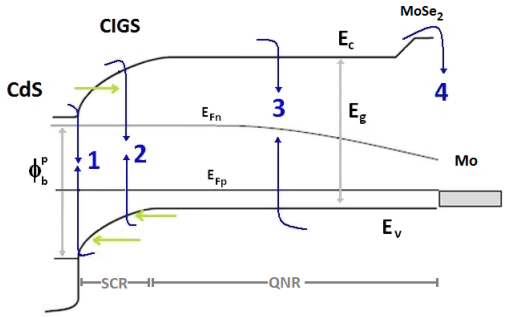

Figure 2.10: Possible recombination paths: 1. interface, 2. SCR, 3. QNR, 4. back contact recombination. ϕ_b^p shows the potential barrier for interface recombination. The green arrows indicate the tunneling enhancement of the recombination paths 1 and 2 [5].

J-V characteristics of dominant paths

The total recombination current density, which includes QNR, SCR and interface recombination (J_{rec}= J_{SCR}+J_{QNR}+$J_{Interface}$), can be obtained through an integration over the region, where the dominant recombination, with recombination rate R, takes place

$$J_r = q \int_0^{W+L} R(x)dx$$

In the integration boundaries, L is the width of the QNR, W is the width of the SCR. The general mathematical form of the voltage dependence of the diode current density for a real diode is given by [6, 54]:

$$J(V) = J_0 \left(exp\left(\frac{qV}{nkT}\right) - 1 \right) \tag{2.5}$$

$$\text{with } J_0 = J_{00}\, exp\left(\frac{-E_a}{nkT}\right) \tag{2.6}$$

J_0 is the saturation current density which is activated by the activation energy E_a which depends on the recombination mechanism [54]. The pre-factor J_{00} can be weakly temperature dependent. The ideallity factor 'n' expresses the deviation from an ideal pn-junction characteristic to a real solar cell [12,55]. A temperature dependent ideality factor denotes an important assistance from tunneling in the recombination process. As the ideality factor can be temperature dependent, it is proposed that the activation energy E_a can be determined using the following expression which is generally used [56–60]

$$nln(J_0) = \frac{-E_a}{kT} + nln(J_{00}) \tag{2.7}$$

A plot of $nln(J_0)$ versus inverse thermal energy 1/kT should yield a straight line and the slope provides the activation energy of recombination E_a from which the dominant recombination path can be deduced. In case of illuminated J-V curves the activation energy E_a of the saturation current is determined by a linear extrapolation of V_{oc} to T = 0 K [11] in the equation

$$V_{oc} \approx \frac{E_a}{q} - \frac{nkT}{q} ln\left(\frac{J_{00}}{J_{ph}}\right) \tag{2.8}$$

The characteristics of the saturation current density for each recombination path are discussed below.

1. Recombination in SCR [54]
Assuming a defect level in the middle of the band gap, the recombination rate R, described by the Shockley-Read-Hall equation, can be written as [5, 61]

$$R = \frac{n\,p - n_i^2}{\tau(n+p)} \tag{2.9}$$

with n (p) the electron (hole) concentration, n_i the intrinsic carrier concentration and τ the lifetime of electrons and holes which is assumed to be equal. As the recombination process requires both electrons and holes, to be present at the same position within the device, The maximum of the recombination is found when the Fermi level is approximately at midgap and n = p [48]. Most effective recombination centres are thus located near the middle of the band gap. The maximum recombination rate can be written as

$$\begin{aligned} R_{SRH}(n=p) &\approx \frac{n}{2\tau} \\ &\approx \frac{\sqrt{n\,p}}{2\tau} \end{aligned}$$

Assuming flat quasi-Fermi levels throughout the space charge region, n·p is proportional to n_i^2 exp(qV/kT). The recombination rate scales with V as [5]

$$\begin{aligned} R_{SCR}(n=p) &\propto \sqrt{n_i^2}\sqrt{exp\left(\frac{qV}{kT}\right)} \\ &\approx \sqrt{n_i^2}exp\left(\frac{qV}{2kT}\right) \\ &\approx exp\left(\frac{-E_g}{2kT}\right)exp\left(\frac{qV}{2kT}\right) \text{ with } n_i^2 = N_cN_vexp\left(\frac{-E_g}{kT}\right) \end{aligned}$$

The expression for the saturation current in case of recombination in the space charge region via a single defect becomes [3]

$$\begin{aligned} J_0 &= J_{00}\,exp\left(\frac{-E_g}{2kT}\right) \\ n &= 2 \\ E_a &= E_g \end{aligned}$$

If the recombination is dominated in the quasi-neutral regions, the ideallity factor in equation 2.4 is 1. If the recombination in the depletion region dominates, the ideallity factor is 2. The factor is in between 1 and 2 when the recombination in each region is comparable [36, 55, 62]. For a real device, the theoretical diode ideality factor is typically between 1 and 2. In practice ideality factors can be larger than 2 (due to e. g. tunneling enhanced recombination [5].) In literature [5, 12, 36, 62] a two-diode model is also proposed. In this model the standard Shockley equation for a pn-junction (J $\propto$ exp(qV/kT)) is extended by the recombination current in the depletion region (J $\propto$ exp(qV/2kT)).

$$J = J_1 \cdot exp\left(\frac{q(V-JR_s)}{kT}\right) + J_2 \cdot exp\left(\frac{q(V-JR_s)}{2kT}\right) - \frac{(V-JR_s)}{R_p} - J_{ph}$$

2. Interface recombination (IR)
The recombination probability of photo-generated electrons at the interface is dependent on the availability of holes and hence is determined by the energetic difference between the valence band maximum and the hole Fermi level (hole barrier energy ϕ_b^p) [48]. As the position of the

Fermi level ultimately determines the interface recombination, Fermi level pinning may be decisive for the recombination. The Fermi level can be pinned at a certain energetic position when the donor concentration at the interface is high enough to compensate the negative charged acceptors in the p-type layer [48, 63]. If a voltage is applied, the energy difference between the electron Fermi level and the conduction band minimum does not change. The occupation of the defect states is adapted to the external bias. For a higher defect density or shallower defects, the Fermi level is pinned closer to the conduction band minimum. Pinning mechanism and models are further discussed in section 2.3.1.3. In case of interface recombination the activation energy, calculated following equation 2.7, is lower than the band gap energy. In the case of Fermi level pinning the activation energy corresponds to the barrier for holes, in case of a cliff in the conduction band diagram the activation energy corresponds to the minimum distance between valence band edge and conduction band edge on either side of the junction [39].

3. Recombination in QNR

The diode ideality factor of 1 is expected and J_0 has an activation energy equal to the band gap.

$$\begin{aligned} J_0 &= J_{00}\, exp\left(\frac{-E_g}{kT}\right) \\ n &= 1 \\ E_a &= E_g \end{aligned}$$

4. Recombination at the back contact (BCR)

Recombination at the back contact might contribute as well to the total recombination loss [64]. Back contact recombination for CIGS is reduced by a thin $MoSe_2$ layer formed at the back contact (section 2.2.5) and by grading the Ga profile throughout the CIGS absorber layer (section 2.3.1.3). Back contact recombination can be neglected if the absorber layer thickness is larger than the carrier diffusion length [53].

2.2 Structure

Figure 2.11 shows the structure of a thin-film CIGS or CZTS solar cell. Solar irradiation passes through the transparent and highly conducting ZnO window layer and the n-type CdS buffer. The light is finally absorbed in the p-type CIGS/CZTS absorber layer. Photogenerated holes are transported to the Mo back contact, electrons are extracted from the ZnO layer via the Ni/Al front contacts (see appendix A.1.3). Properties and preparation of each layer are briefly discussed below.

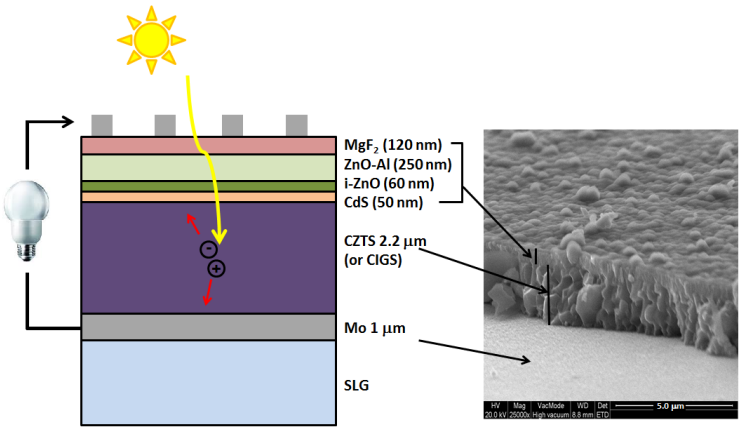

Figure 2.11: Schematic and SEM image of the stacking sequence of a thin-film solar-cell.

2.2.1 Anti-reflection coating

Record cells usually include an anti-reflection coating of MgF_2. The optimum thickness is related to the wavelength dependent reflectivity. Typically the layer thickness is around 120 nm. The relative gain in efficiency that can be achieved is in the range of 4-8% [65].

2.2.2 Window

The front contact should transmit the light to the absorber layer and extract photogenerated electrons. The preferred window or transparent conductive oxide (TCO) film consists of ZnO (n-type) which is transparent and conductive and thus satisfies the requirements. The absorption edge is around 375 nm (3.3 eV). Typically a thick layer (300-500 nm) of Al-doped ZnO is used [65]. This ZnO:Al layer is highly conductive, which avoids ohmic losses. Thickness and material properties of the heavily doped ZnO:Al layer are determined by a trade-off between transparency and conductivity. The deposition of a ZnO:Al film with high lateral conductivity (low resistance) directly onto the buffer increases the negative influence of local defects and local fluctuation of absorber properties (e.g. the band gap). Therefore a thin (50 nm) undoped (intrinsic) i-ZnO layer is deposited first. This layer is intrinsically n-type and has higher resistivity compared with the ZnO:Al layer. The i-ZnO decouples poorly performing locations (prevents shunting), the highly doped ZnO:Al layer is responsible for lateral current transport [35, 40]. Both ZnO layers are sputtered. On top of the ZnO window layer, a metallic contact grid out of Al and Ni is evaporated. Ni is applied to reduce the formation of a resistive Al_2O_3 barrier [40].

2.2.3 Buffer

A heterojunction solar cell has a large risk for interface recombination as defects and imperfections at the interface occur. The role of the buffer layer (and of the window layers) is to minimize interface recombination and provide a large total band bending across the junction [53]. The band gap of the buffer material should be chosen carefully because it determines the conduction and valence band offsets in the pn-junction as discussed in section 2.1.1.2. CdS, deposited by chemical bath deposition (CBD), is to date the preferred buffer layer for high efficiency thin-film solar cells (except for pure sulfide CZTS due to a cliff like band alignment [66]). The layer as well as the CBD process itself have beneficial effects on the performance [53, 65, 67]. The CdS buffer increases carrier lifetime as it permit a pinhole-free coating of the absorber [40], optimizes conduction band alignment, has decent lattice matching at the heterojunction interface and protects the absorber layer for sputter damage during the ZnO window layer deposition. During the CBD process the absorber surface and oxides can be etched in the bath prior to the CdS film growth. Furthermore the process may help to incorporate Cd into the CIGS lattice which could lead to type inversion at/near the junction (n-type absorber or buried junction, see section 2.3.1.3).
The band gap of CdS is 2.4 eV at room temperature. The device performance is controlled by the CdS thickness [67]; a thin buffer layer allows more light to reach the junction and increases the EQE at the short wavelength region but does not necessarily leads to higher total short circuit current. For a thin layer, losses in V_{oc}, FF and in the spectral response are noticed and explained by an increase in SCR recombination. As the CdS layer thickness increases, recombination is decreased. Via modelling a higher collection depth is noticed for thicker CdS layer. Typically the CdS thickness is around 50 nm. The use of CdS has a few disadvantages, stimulating the search for alternative buffer materials (Zn-OH, ZnS, In_2S_3, $In(OH)_xS_y$, ...). A first disadvantage is the relatively small band gap of CdS. A part of the light is absorbed before it can even reach the absorber layer (even for thin CdS layers). A second disadvantage is the toxicity of Cd (especially in a 'renewable environmentally' energy source). Last, the deposition

of the buffer layer via a CBD is a non-vacuum process. As the absorber and window depositions are both vacuum depositions, breaking the vacuum costs time and energy.

2.2.4 Absorber

The basic component of a thin-film solar cell is the absorber layer, where the conversion of photons into electron-hole pairs takes place. Ideally, the absorber semiconductor should have a band gap of 1.0-1.5 eV with a high solar optical absorption ($\alpha = 10^4$-10^5 cm^{-1}) in the wavelength region of 350-1000 nm (1.2-3.5 eV), a long carrier diffusion length and low recombination velocity [35]. Furthermore, the material must be stable for long-term outdoor accommodations and must be cheap (in raw material and for production).
In this work a study of defects was performed on two promising candidates for the absorber layer in a thin-film solar cell: Cu(InGa)Se_2 and Cu_2SnZnS_4. The specific material properties and advantages of these absorber materials will be discussed in section 2.3. First, more general properties of the absorber layer will be discussed: relation with the solar spectrum, optimal band gap by theoretical limit and defect types present in the absorber.

2.2.4.1 Solar spectrum

The wavelength region in which the absorber layer must have a high optical absorption coefficient is of course determined by the solar spectrum. The sun has a surface temperature of 5762 K and its spectrum can be approximated by that of a black-body radiator at that temperature (figure 2.12). Emission of radiation from the sun is isotropic. Because of the great distance from the earth to the sun only those photons emitted directly in the direction of the earth contribute to the solar spectrum as observed from earth. The radiation intensity just above the earth's atmosphere is about 1.353 kW/m^2. The spectral distribution is referred to as an air mass zero (AM0) radiation spectrum. The air mass defines the direct optical path length through the earth's atmosphere [36]. A widely used standard to measure a solar cell performance under standard test conditions is the AM1.5 which has an intensity of 1000 W/m^2 [11]. The absorber layer of a solar cell should have high optical absorption in the wavelength region where the solar spectrum is highest (between 350-1000 nm) as visible in figure 2.12.

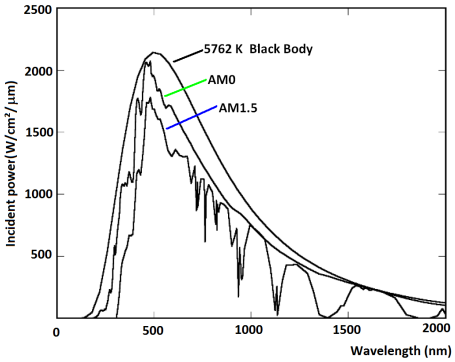

Figure 2.12: The radiation spectrum for a black body at 5762 K, AM0 and AM1.5 global spectrum [36].

2.2.4.2 Band gap constraints

The ideal region of the semiconductor band gap is determined by the thermodynamic efficiency limit for PV solar energy conversion, known as the Shockley-Queisser limit after its originators. The limit is calculated as a function of the band gap of the semiconductor used as absorber in the solar cell (figure 2.13).

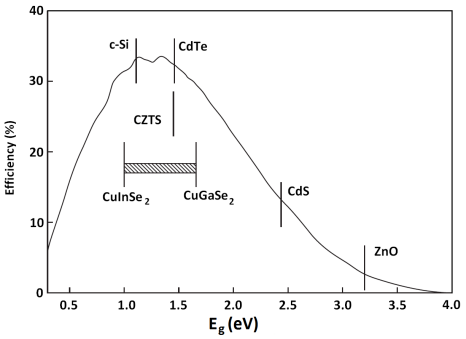

Figure 2.13: Maximum theoretical efficiency (Shockley-Queisser limit) for solar cells under AM1.5 global spectrum. The band gap of CIGS can be tuned by controlling the In/Ga ratio [68].

The Shockley-Queisser limit relies on four basic assumptions [5]:

- (1) The probability for the absorption of solar light through generation of a single electron-hole pair in the photovoltaic absorber material is unity for all photon energies $E > E_g$ and zero for $E < E_g$. There are losses because of non absorbed photons. As the band gap increases, less photons are absorbed. This step like function does not take into account fluctuations in the band gap.
- (2) All photogenerated charge carriers thermalize (excess energy of the electron-hole pairs is released as heat to the semiconductor lattice) to the band edges which leads to thermalization losses. A higher band gap includes less thermalization, whereby the useful energy of the electron-hole pair remains higher. Due to a higher band gap, a higher maximum voltage can be obtained when the circuit is open (V_{oc}).
- (3) The collection probability for all photogenerated electron-hole pairs at $V = 0$ is unity. High mobilities are necessary to achieve this.
- (4) The only loss mechanism (other than non-absorbed photons and thermalization losses) is the spontaneous emission of photons by radiative recombination. This is due to the interconnection, by the principle of detailed balance, of light absorption by generation of free carriers and light emission by recombination of electron-hole pairs. Radiative recombination is an unavoidable loss mechanism.

Assuming a single pn-junction solar cell with a band gap of 1.4 eV, the maximum conversion efficiency is around 33.7% under standard AM1.5 illumination. Figure 2.13 presents the maximum theoretical efficiency for monocrystalline silicon and for thin-film common absorber materials. The band gaps op the CdS and ZnO are shown for comparison. As the derivation of the maximum limit is based on assumptions for an ideal case, the achievable conversion efficiency for real cells is lower. For example the achieved open-circuit voltages are far below the radiative limit as recombination in a thin-film solar cells is dominated by non-radiative processes. Because recombination losses are enhanced by defects, defect identification is essential for the improvement of the efficiency.

2.2.4.3 Defects types

In real semiconductors impurities are incorporated during synthesis and processing. Even if these can be avoided, thermodynamics predict that (small) concentrations of intrinsic defects will inevitably occur. In semiconductors, these defects affect the physical, chemical, mechanical and electronic properties [69]. Point defects create a disturbance in the crystal structure of

semiconductors. Based on the effect on the periodicity of the potential energy of the crystal, shallow or deep levels can be distinguished:

Shallow: the disturbance creates a long range potential disturbance which may extend over ten or more unit cells, a shallow defect level is formed [70]. Shallow defects determine the conductivity type of the material.

Deep: the disturbance creates a crystal potential profile which is deep and localized. Due to the larger distance to the band edges, deep levels are not efficient at generating free electrons or holes. They rather capture free carriers and thus lead to a reduction of conductivity [71]. In the strong potential, the charge carrier of the deep defect is tightly bound to the defect. The high localization in position space corresponds to a delocalization in the momentum space. As a result recombination via deep levels is thus likely to be non-radiative [9].

Point defects can be classified by intrinsic and extrinsic defects. Intrinsic or native defects are defects which do not involve foreign atoms. Different types of intrinsic defects are

- *Vacancy*: a host atom A is missing (V_A) (figure 2.14(a))
- *Self-interstitial*: host atom A is located at site that is not occupied in the perfect lattice (non-lattice site) (A_i) (figure 2.14(a))
- *Anti-site*: occurs when the lattice contains at least two kinds of atoms. An antisite B_A is formed if in an AB compound a host atom B occupies the site of different host atom A (figure 2.14(b))

Defects involving foreign atoms (impurities) are referred to as extrinsic defects (figure 2.14(c)). These defects are caused by an outside source, such as growth conditions or processing factors. Depending on the location of the impurity atom, two defects types can be distinguished:

- *Substitutional impurity*: the impurity atom C is located on a lattice site, replacing native atom A (C_A)
- *Interstitial impurity*: the impurity atom C is located at an interstitial site (C_i)

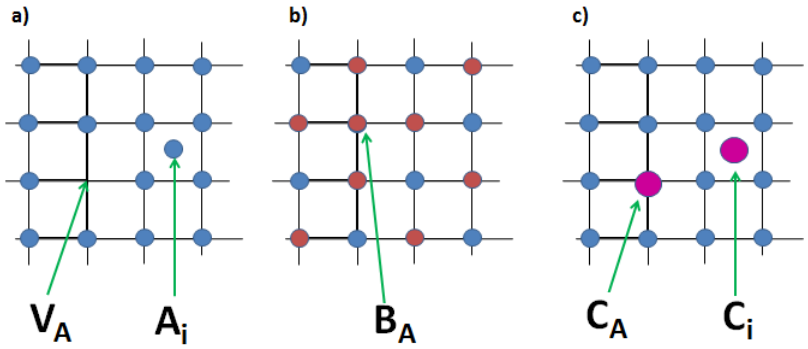

Figure 2.14: Point defects types in a crystal [55].

Defects which are composed of a small number of point defects are referred to as defect complexes. Many important defects are electrically active. Donors are defects which can contribute free electrons to the conduction band of the host crystal. Defects which can contribute holes to the valence band (remove electrons) are known as acceptors. For a donor, the charge state changes between 0 and + for being occupied by an electron or not. When ionized, the donor is positive. For an acceptor the charge state changes between 0 and 1 for being occupied by a hole or not.

2.2.5 Back contact

The back contact is a conductive layer used to make the electrical contact at the backside of the solar cell. For CIGS thin-film solar cells a Mo layer is standard because of its high melting point, low cost and low expected diffusivity in the semiconductor [6]. A drawback of the Mo layer is the low reflectivity which is disadvantageous when absorber layers are smaller than 2 µm [11, 65]. The Mo back contact is sputtered and has a thickness of 0.5-1.0 µm.
During absorber deposition a $MoSe_2$ film forms at the Mo surface. This layer is a p-type semiconductor with a band gap of 1.3 eV. Whether an Ohmic or a Schottky contact is formed is still disputed and is dependent on the characteristics of the $MoSe_2$ layer [6, 65]. Anyhow, a low-resistive contact to CIGS is formed [47, 65, 72]. Due to the small conduction-band offset of $MoSe_2$ with respect to the absorber bulk material, $MoSe_2$ acts as an electronic mirror ('back surface field' shown in figure 2.15) for the photo-generated electrons and diminishes back-surface recombination [47].

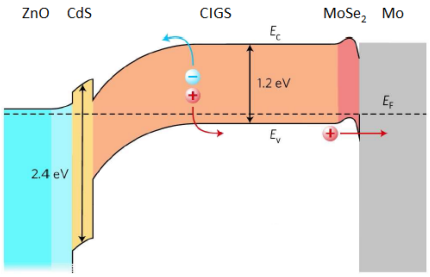

Figure 2.15: Band diagram of CIGS in which the back surface field created by $MoSe_2$ is indicated [73].

For CIGS the diffusion of Na from the sodalime glass is important for the device performance as described in section 2.3.1. The Mo back contact has the advantage that Na diffusion through this layer is very efficient, except when very dense Mo layers are used [65].

For CZTS absorber layers, it is demonstrated in reference [74] that the CZTS/Mo interface may not be as chemically stable as the CIGS/Mo interface. During thermal processing MoS_2 is formed together with a phase separation into Cu_2S, ZnS, and SnS at the back contact. SEM cross sections reveal large grains in the bulk phase, and smaller particles, due to the secondary phases at the back contact. In reference [74] it is concluded that the CZTS/Mo interface is unstable during annealing.

2.2.6 Substrate

There are a number of substrate materials that are suitable for thin-film solar cells. Today, the standard substrate is **soda-lime glass** (SLG). SLG is a suitable substrate mainly because high processing temperatures up to 600°C (melting point of glass) can be used [72]. SLG has a well matched thermal expansion coefficient, exhibits a smooth surface and is cheap. Moreover it releases Na and K into the CIGS absorber. A drawback is the possible variation in Na and K out-diffusion during CIGS deposition.
As a flexible substrate **polyimide foils** (PI) can be used. For these substrates, lower processing temperatures (< 500°C) must be applied [73]. As the polyimide foils do not contain any alkaline elements, these elements have to be included in the absorber layer after the absorber growth process e.g. by post deposition. The use of flexible substrates offers new possibilities, for example for building integration by application on uneven surfaces such as tiles. Another advantage is that flexible cells are very thin and lightweight. Therefore, they are attractive for space applications; more weight is saved and this reduces launch costs significantly. Flexible substrates

have a great potential to be used for roll-to-roll deposition. In this process, a roll of flexible substrate is unrolled and transported through a production system which deposits the individual layers on the moving substrate. After the deposition the thin-film solar cell is rolled up again [5]. The roll-to-roll process is considered to be favourable for large scale production with low cost. As polyimide foils are anyhow cheaper than the expensive SLG substrate, cost is already reduced. Another low cost substrate is **metal foil** (e.g. stainless steel). A drawback of this substrate is that impurities (such as Fe and Ni) can diffuse in the absorber layer where they can form deep defect levels which lower the efficiency of the device. The CIGS growth temperature on metal foils reaches around 520-600°C, which is very close to the temperatures used for the growth of CIGS films on glass [75].

2.2.7 Module interconnection

The electric current delivered by a solar cell depends on the illuminated area. Because of severe current loss due to the limited conductivity of the transparent conducting front contact, the cell should not be too large. Small-area cells are connected in series, which results in a large-area device (the solar module) that delivers comparatively high voltages and low currents. Series interconnection can be achieved in thin-film modules with monolithic cell integration during production which is considered as an advantage in terms of manufacturing costs. Silicon-wafer based modules cannot be fabricated directly as the cells have to be made first before the series interconnection can be constructed. For the monolithic cell integration of thin-film solar cells, three patterning steps have to be performed [65, 76]. They are visualised in figure 2.16.

- P1 scribe: Mo patterning often carried out by laser ablation. The back contact for the different cells is separated.
- P2 scribe: after deposition of the absorber, buffer and highly resistive i-ZnO layer, a trench is made by mechanically scribing that does not penetrate the Mo layer.
- P3 scribe: after deposition of the Al:ZnO layer, a trench is made next to the P2 trench which goes through all layers except the back contact. The cells are now in series and separated from each other.

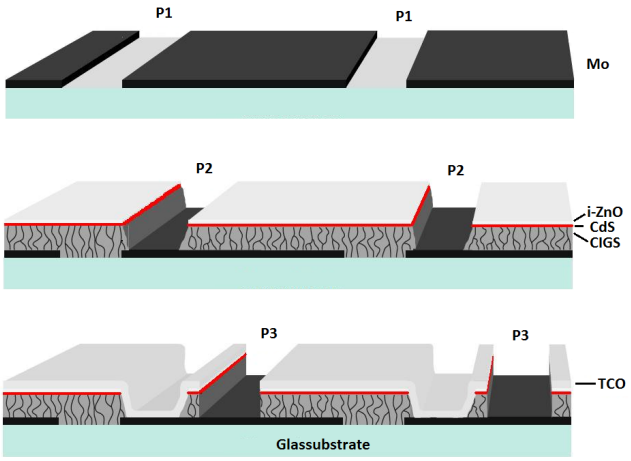

Figure 2.16: Diagram of the manufacturing steps to make monolithic series interconnection for CIGS thin-film modules [36].

2.3 Properties absorber material

2.3.1 CIGS layer

2.3.1.1 Structure and composition

$CuInSe_2$ and $CuGaSe_2$ (I-III-VI_2) compounds crystallize in the chalcopyrite structure. The tetragonal unit cell is presented in figure 2.17. Every metal atom has four Se atoms as nearest neighbours and every Se atom is tetrahedrally bonded to two Cu and two In (or Ga) atoms. In CIGS the III metal site is statistically occupied by In and Ga atoms.

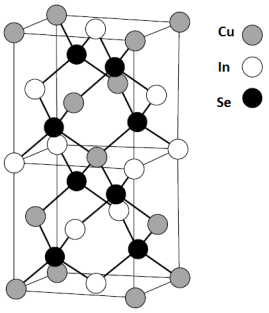

Figure 2.17: Chalcopyrite unit cell [36].

CIGS is relatively tolerant against variations in the stoichiometry without appreciable differences in opto-electronic properties. This characteristic is most important for the potential of CIGS as a material for low cost thin-film solar cells. The [Ga]/([In]+[Ga]) (GGI, also denoted as 'x') ratio as well as the [Cu]/([Ga]+[In]) (CGI, also denoted as 'y') ratio can be varied. Solar cells with high performance are fabricated with CGI ratio ranging from 0.7 to 1.0 and a GGI ratio about 0.3-0.4 [11, 73]. The high performance cells have thus a Cu-poor composition. An off-stoichiometry of 1% would lead to a defect concentration of the order of $10^{20}cm^{-3}$. This high concentration is five orders of magnitude higher than the acceptable density of recombination centres and four orders of magnitude higher than the maximum useful net carrier concentration. This high defect concentration is therefore not very likely to be electrically active (no contribution to recombination nor to free charge carriers) [77]. The presence of the electrically inactive, self compensating defect complex $2V_{Cu}+In_{Cu}$ explains the tolerance to non stoichiometric composition. This is further discussed in section 2.3.1.5.

2.3.1.2 Absorption

Figure 2.18 presents a comparison of the absorption coefficients for different solar cell materials. The absorption edge for $Cu(In_{1-x}Ga_x)Se_2$ is shifted towards higher energy compared to $CuInSe_2$. As opposed to the indirect band gap for silicium, CIGS has a direct band gap. CIGS is well suited for solar cells because of its high absorption coefficient ($\alpha = 10^5$ cm^{-1} in the energy region 1.2-2.5 eV) compared to crystalline silicon ($\alpha = 10^3$-10^4 cm^{-1} in the energy region 1.2-2.5 eV) [65]. Due to this high absorption coefficient, an absorber layer of only 2 μm thickness is required for a CIGS solar cell.

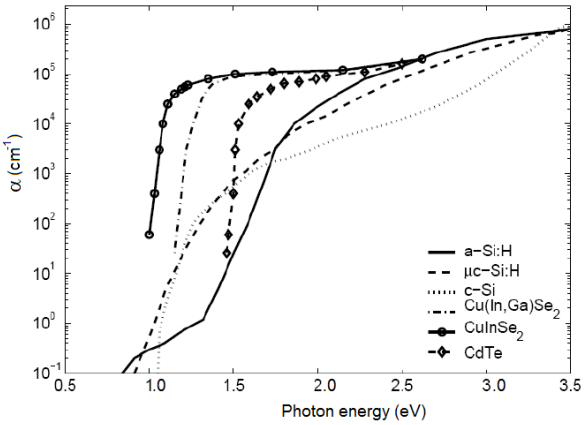

Figure 2.18: Optical absorption coefficients as a function of photon energy for commonly used materials in solar cells [49].

As indicated in reference [78], different optical studies have been performed on CIGS in order to determine the optical constants. The reported optical absorption coefficients for $CuInSe_2$ vary in the range $7{\cdot}10^4$ to around $2{\cdot}10^5$ cm^{-1}. In reference [78] spectroscopic ellipsometry on thin CIGS layers (60 nm), with different compositions, have been performed. Relatively low absorption coefficients, below 10^5 cm^{-1}, were found. For y = 1, x = 0.38 and y = 0.91, x = 0.4 α is between $3{\cdot}10^4$-$2{\cdot}10^5$ cm^{-1} for wavelengths between 700-300 nm. In reference [79] spectroscopic ellipsometry measurements revealed lager absorption coefficients ranging from $5{\cdot}10^4$ to $4{\cdot}10^5$ cm^{-1} in the wavelength region 700-300 nm, for composition ratios of y = 1 and x = 0.18-0.20.

2.3.1.3 Band gap

Effect of Ga

As stated above, the absorption edge is primarily influenced by the GGI ratio (also denoted as 'x' ratio). The band gap of $CuInSe_2$ is around 1.01 eV, the band gap of $CuGaSe_2$ is around 1.70 eV. The band gap of $Cu(In_{1-x}Ga_x)Se_2$ can be varied between the values for these two compounds depending on the value of x (Vegard's law). The change of the band gap with 'x' [11] is slightly non-linear and depicted in figure 2.19

$$E_g = (1-x)\cdot 1.01\,eV + x\cdot 1.7\,eV - b\cdot x\cdot(1-x) \quad \text{with} \quad 0 \le b \le 0.3 \tag{2.10}$$

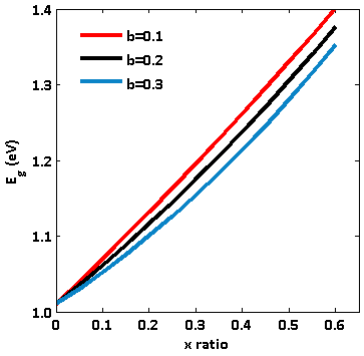

Figure 2.19: Band gap dependence of x ratio following equation 2.10.

Reference [78] indicates, based on spectroscopic ellipsometry measurements, a more linear dependence of the band gap with x for a y ratio between 0.81 and 0.95.

• *High voltage limit of Ga increase*
One could reason that $CuGaSe_2$, due to its larger band gap, would result in a higher V_{oc} (less thermalization loss) [16]. However in practice, the delivered V_{oc} increases at a lower rate than the band gap energy of the absorber [80] and record CIGS cells have a quite low GGI ratio (0.2-0.3) [40]. The low increase in V_{oc} as the Ga content increases, is due to a change in the dominant recombination mechanism. The increase of the band gap energy (due to increase of Ga content), is accommodated almost exclusively by an increase of the energy of the conduction band minimum [16,48,81]. A cliff is thereby formed in wide band gap chalcopyrites. The barrier for interface recombination (ϕ_b^p) remains thus essentially unchanged with respect to the value for low Ga absorbers. Hence, with increasing Ga content, the relative contribution of interface recombination could be increased. The change from space charge dominated to interface dominated recombination happens about a GGI ratio of 0.22-0.23. It can be assumed that a cliff in the conduction band forms for GGI $\geq$ 0.23 [49].

• *Band gap grading*
As the GGI ratio determines the band gap, a band gap grading (towards the front and back contact) can be induced by a variation of this ratio throughout the absorber layer. This 'band gap engineering' has led to high-efficiency solar cells [65]. The position of the dip (minimum) in the profile and the total grading profile have been found to be crucial for the device performance [73]. More recently it has been shown in reference [82] that there is some degree of freedom in the shape of the band gap grading for high efficiency devices. GGI profiles of cells with efficiency above 20% can deviate strongly from each other. The required double band gap grading can be achieved in a three stage co-evaporation process (section 2.3.1.9).

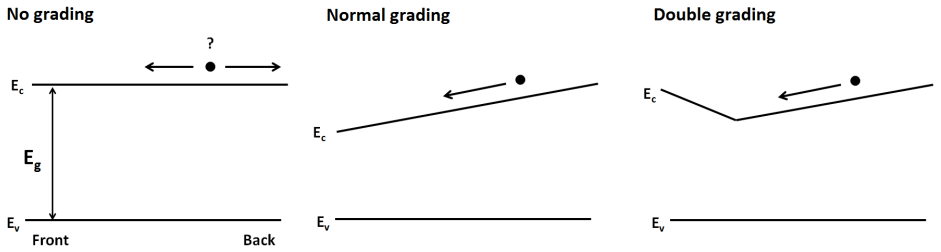

Figure 2.20: Possible band gap grading profiles induced by changing the GGI ratio. The effect on an electron excited to the conduction band is illustrated [65].

By increasing the GGI ratio towards the back of the absorber layer (figure 2.20 normal grading), a back-surface field (BSF) is created. This gives rise to an increase of the conduction band minimum, while the valence band maximum is nearly unaffected. As a result recombination of electrons at the defect rich absorber/back contact interface is therewith suppressed. Further because of the grading towards the back contact the driving force on excited electrons towards the depletion region is enhanced. This increases the collection efficiency of minority carriers. An optimum of the band gap increase should be found because the electron-hole pair generation decreases as the band gap increases.
An increase of Ga in the space charge region (figure 2.20 double grading) is expected to enhance V_{oc} whereby the device performance can be enhanced. The increase should not overcompensate the band bending induced by the built-in electric field, because then the electron transport will be hindered. A steeper band gap gradient towards the front contact can act under forward bias as a barrier for electrons generated in the absorber. This leads to enhanced recombination and a decrease in cell efficiency [73]. An optimum grading towards the front contact should be thus found.

In reference [83] the calculation of the different band gap values throughout the CIGS absorber with different Ga grading profile (figure 2.21) is reported. For the 25% Cu excess curve a decrease

of 0.22 in the GGI ratio, leads to a decrease of 72 meV in the band gap from surface to Ga dip. The largest difference can be seen for the 50% curve and is around 100 meV.

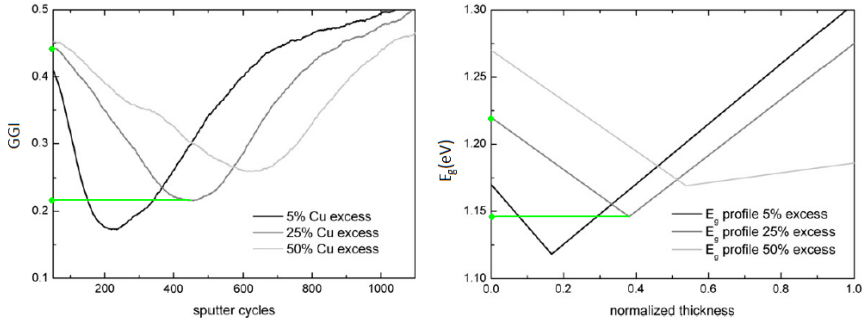

Figure 2.21: Left: GGI ratios. The difference between the curves is a different CGI ratio at the end of the second stage. Right: Calculated band gap grading of the samples with different GGI profiles shown in the left figure [83].

Temperature dependence

The band gap of chalcopyrites has been reported to be essentially constant below 60-100 K [84]. The maximum reported shift in band gap between 5 K and room temperature is 33 meV for $CuInSe_2$ according to reference [85]. This comes down to an average shift of 0.11 meV/K in the whole temperature range. Similar results are reported in reference [86] for $CuInSe_2$ and $CuGase_2$.

Inversion layer

An increase of the hole barrier (ϕ_b^p), to reduce interface recombination, can be achieved by lowering the conduction band of the p-type absorber as close as possible to the Fermi energy at the interface or by surface band gap widening [16]. This 'type inversion' at the interface is one of the key-points regarding the design of high efficiency hetero-junction solar cells. It is shown that the surface type inversion reduces with an increase in Ga content, as the latter results in an increase of the distance of E_F to the conduction band. The type inversion disappears with GGI ratio larger than 0.8 [87].

Several junction models are proposed to explain the observed inversion layers for the CIGS solar cells (figure 2.22). The type inverted layer can be the result of (a) a secondary phase, (b) Fermi level pinning by donor like defects at the interface (pinning model) or (c) n-type doping at the surface (doping model) [87, 88]. The exact nature of the electronic junction of the CIGS cells still remains an unsettled issue.

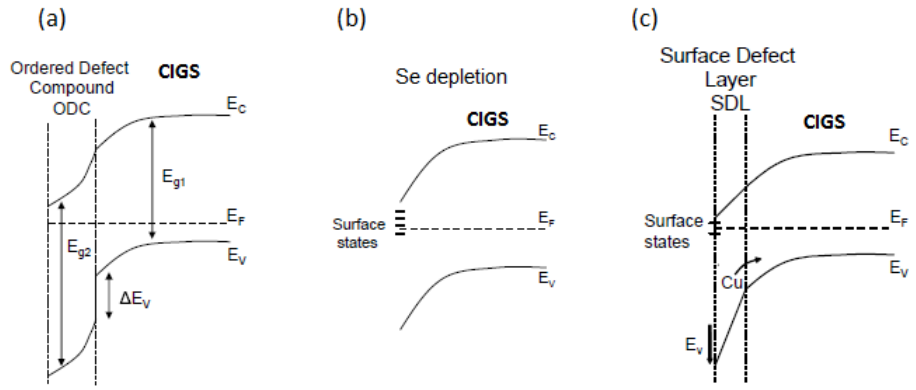

Figure 2.22: Band diagrams of secondary phase and pinning models (a) Ordered defect compound (ODC) layer at the surface with a larger band gap than the bulk, (b) Cahen-Noufi pinning model: large concentration of surface states V_{Se} causes a large band bending or Herberholz pinning model: a surface defect layer is created due to the migration of Cu from the surface into the bulk, (c) doping model [87].

(a) The first explanation for the origin of type inversion is a $CuIn_3Se_5$ or $CuIn_5Se_8$ phase that precipitates as a ***secondary phase*** on the thin-film surface [87, 89]. The deviation of the CIGS surface composition from the bulk composition is experimentally proven [90]. The inversion layer is called ordered vacancy compound (OVC), because vacancies are expected to orderly occupy particular crystallographic sites in the crystal structure. A reason for the existence of this layer is that the CIGS surface is self-reconstructed to be energetically more stable as shown by a theoretical calculation [91]. The theoretical calculation has explained the existence and stability of the secondary phase by the presence of $(In_{Cu}{}^{2+} + 2V_{Cu}{}^{-1})$ donor-acceptor defect pairs which have very low formation energies. Therefore the layer is also referred to as ordered defect compound (ODC) layer. The inversion layer is n-type, has a larger band gap and shifts the pn-junction away form the CdS/CIGS interface (burried pn-junction).

(b) For the ***pinning model*** two explanation exists.

- 1. In the first model a *Se depleted surface* (Cahen-Noufi model [92]) is proposed. This model assigns the origin to shallow surface donors rather than to a distinct n-type surface phase. It is proposed that due to a deficiency of Se surface states (V_{Se}), indium on the surface gives electrons to the conduction band. Positively charged surface donor states of indium are formed and pin the Fermi level. The conduction band bends down and the surface becomes inverted. Air-annealing of bare absorbers passivates the surface states and reduces the type inversion. Oxygen gets electrons from the conduction band and forms O^{2-} which binds to V_{Se}. The surface of CIGS films is found, in some cases, to be nearly in flat band conditions after a long exposure to air. It is believed that the CBD treatment of the CdS buffer layer removes the passivating oxygen and restores the positive surface charges of the absorber and hence also the beneficial type inversion of the film surface.

- 2. A second model to explain the pinning is by a *surface defect layer* (Herberholz [93]). In this model the net positive surface charge is due to the absence of Se at the surface. These positively charged donor states on the surface cause an electric field (band bending) which drives Cu^+ ions away from the surface sites towards the neutral part of the film. The remaining acceptor Cu vacancies ($V_{Cu}{}^-$) result in a high density of acceptor states close to the surface. This diffusion leads to a decrease of effective doping density [88] in the bulk and a higher acceptor concentration at the surface (p^+ layer [48]). The band gap of this surface defect layer is larger than that of the bulk. The Cu-poor surface composition is

thus a consequence of the type inversion (rather than its origin) as the Cu is driven away from the surface by the built-in electrical field.

(c) The ***doping model*** is based on a diffusion of Cd into the CIGS absorber as seen in different experiments [94–96]. Reference [97] reports on Cd diffusion along the grain boundaries. There is no agreement on the depth of the Cd diffusion caused by the CBD, different depths from 1-3 atomic layers to 200 nm in the absorber layer are reported [87, 96]. Together with the Cd diffusion, a decrease of Cu content at the surface is observed. In reference [98], it is was suggested that a higher Cu deficiency near the buffer/absorber surface enhances the Cd_{Cu} donor concentration. It is very likely that the diffused Cd atoms substitute Cu vacancies because the ionic radii of Cd^{2+} (0.097 nm) and Cu^{+} (0.096 nm) ions are very similar. In this doping model Cd replaces Cu atoms or fills Cu vacancies during CBD [94].

2.3.1.4 Electrical properties

$CuInSe_2$ with an excess of Cu is always p-type, In-rich films can be made p-type or n-type [49]. $CuGaSe_2$ remains p-type under all stoichiometry deviations [16, 81]. For CIGS polycrystalline absorbers, slightly Cu-deficient, p-type material is used. The carrier concentration is around 10^{15}-10^{17} cm^{-3}. This carrier concentration can be increased through the presence of alkaline elements such as Na and K.

Literature reports do not agree on the dominant current transport. Bulk, space charge region and interface recombination with or without a tunneling contribution are indicated as dominant recombination mechanisms. The dominant recombination mechanism seems to be dependent on the composition of the CIGS solar cell [49, 80, 99, 100], on the net carrier concentration (which can be altered by Na concentration) [100, 101] and the buffer type [56]. According to references [80, 99, 102] Cu-poor absorbers have dominant recombination in the bulk, while Cu-rich absorbers have dominant recombination at the interface. The difference is explained by the existence on an inversion layer which enlarges the band gap energy of the Cu-poor absorbers. The enhanced interface recombination (or tunneling assisted interface recombination due to high doping level) is, according to reference [102], regarded as the reason for avoiding a Cu-rich absorber despite its better transport and life time properties.
For the comparison of literature reports, one has to be attentive if the calculations are performed on dark or illuminated I-V characteristics. In references [49, 103] the calculated activation energies were larger in the cases were the calculation is performed on dark I-V currents compared to illuminated I-V currents. References [104–107] report on a difference in ideality factor determined from illuminated and dark I-V measurements.

2.3.1.5 Defects

The defect structure of CIGS is very complicated as a large number of intrinsic defects are possible. Already twelve intrinsic point defects exist for the ternary compound $CuInSe_2$: three vacancies V_{Cu}, V_{In}, V_{Se}, three interstitials Cu_i, In_i, Se_i, and six anti-site defects In_{Cu}, Cu_{In}, Se_{Cu}, Cu_{Se}, Se_{In} and In_{Se}. Moreover additional defects can be formed due the in-diffusion of additional elements such as Cd, Na, K and O [49]. Theoretical studies show that it is difficult to introduce shallow donors or acceptors in the CIGS absorber by doping [36].
In CIGS it is remarkable that better cell performance is obtained with polycrystalline material than with single crystalline material. This can be explained by the segregation of defects onto the grain boundaries, which makes the defect density inside the grains lower than in the single crystal. The defects at the grain boundaries are left electrically inactive. Na could play a role in the passivation of the grain boundaries [69, 108]. Besides defects in the bulk absorber, defect at interfaces (back contact/absorber and buffer/absorber), as a consequence of lattice mismatch,

can also contribute to the recombination. If the defect density at the interface is high enough, the Fermi level can be pinned at the interface at a certain position. Depending on this position this can be detrimental or beneficial.
Because of a large number of possible defects, it is on experimental basis (Deep Level Transient Spectroscopy, admittance, photoluminescence, ...) difficult to assign transitions to specific defects. Theoretical calculations (via for example density functional theory) could provide a basis for the identification of the defects by the information of the transition and formation energies. In the following discussion it is shown that the strategy of comparing experimental and theoretical calculations is not straightforward because little agreement is found in experimental as well as in theoretical results.

Theoretical calculations
Over the years different calculation methods have been used which led to different results. An overview of the results within the local-density approximation (1) and calculations based on hybrid exchange correlation functionals (2) is given below.
1) First theoretical calculations of intrinsic defects in $CuInSe_2$ and $CuGaSe_2$ [91,109] have been conducted within the *local-density approximation (LDA)* implementation of density functional calculations. It was found that the most important intrinsic acceptor is V_{Cu} which makes the material p-type. In Cu-poor and stoichiometric material a negative formation energy is even calculated. This would imply the spontaneous formation of large numbers of this defect. In Cu-rich material, the Cu_{In} acceptor (responsible for the p-type) has found to have a low (but positive) formation energy [47]. The most important donors which can compensate the acceptors were found to be In_{Cu} and V_{Se}. From calculations about the effect of Ga on the defects, it seemed that acceptor formation energies are larger and acceptor transition levels are shallower in $CuGaSe_2$ compared to $CuInSe_2$. The Ga_{Cu} donor level resulted in a much deeper level than In_{Cu} level [109]. Table 2.1 shows the calculated metal-related defect activation energies in references [91,109].

Table 2.1: Defect activation energies in $CuInSe_2$ and $CuGaSe_2$ calculated by [91,109]. Defects with lowest formation energy for Cu-poor material are indicated in bold [91].

Defects	Charge state	$CuGaSe_2$ (M=Ga)	$CuInSe_2$ (M=In)
$\mathbf{V_{Cu}}$	(-/0)	E_v + 0.01	E_v + 0.03
V_M	(-/0)	E_v + 0.19	E_v + 0.17
V_M	(2-/-)	E_v + 0.38	E_v + 0.41
V_M	(3-/2-)	E_v + 0.66	E_v + 0.67
Cu_M	(-/0)	E_v + 0.29	E_v + 0.29
Cu_M	(2-/-)	E_v + 0.61	E_v + 0.58
$\mathbf{M_{Cu}}$	(0/+)	E_c - 0.49	E_c - 0.25
$\mathbf{M_{Cu}}$	(+/2+)	E_c - 0.69	E_c - 0.34
Cu_i	(0/+)	E_c - 0.21	E_c - 0.20

It seemed furthermore, that formation energies of defect complexes such as ($2V_{Cu}$, In_{Cu}), (Cu_{In}, In_{Cu}) or ($2Cu_i$, Cu_{In}) are low [91]. The defect complex ($2V_{Cu}$, In_{Cu}) is most likely to occur in Cu-poor material as it can accommodate a large amount of In excess and according to the calculations it does not exhibit an electronic transition (very shallow level close to conduction band). Due to the formation of the ($2V_{Cu}$, In_{Cu}) complex, Cu-poor CIGS is heavily compensated [47,48]. The complex explains why highly efficient CIGS solar cells can exhibit off-stoichiometric compositions with CGI ratios of 0.7-0.9. Ordered arrays of defect complexes can be considered as the building blocks of $CuIn_3Se_5$ and $CuIn_5Se_8$ secondary phases.
Defect complexes of $(In,Ga)_{Cu}$-V_{Cu} and V_{Se}-V_{Cu} may also exist and are regarded as responsible for the metastabilities in CIGS [110–112]. Theoretical calculations [111] have indicated that the unoccupied positively charged $(V_{Cu}\text{-}V_{Se})^+$ defect acts as a shallow compensating donor. A con-

figurational change occurs when the defect becomes negatively charged, which leads to a shallow acceptor. The two configurational positions are separated by an energy barrier. The behaviour of $(In,Ga)_{Cu}$ defect complexes is similar [112]. Metastable effects have been observed after illumination and/or voltage bias and are persistent below 200-250 K [113]. The metastablity of the CIGS absorber can be noticed by the open-circuit voltage which relaxes over a long time during illumination towards a higher value at room temperature [47]. The presence metastability complicates different characterization techniques (current or capacitance voltage, admittance and DLTS measurements) [12, 113]. A relaxed, thermal equilibrium state of the sample is reached by storing the sample under dark conditions, without applied bias at room temperature for at least 1 hour [12].

The results of the first theoretical density functional theory (DFT) calculations within the local density approximation [91, 109] for explaining the type and carrier concentrations of CIGS are thus that the copper vacancy and cationic antisites are the most important point defects and that off-stoichiometry is explained by complexes of such defects. More recently, the local density approximation has been questioned, as the calculation method suffers from an underestimation of semiconductor band gap due to an inadequate description of electron-electron interactions. In materials with strongly localized Cu d-orbitals, such as in $CuInSe_2$, this can even lead to a vanishing band gap [81, 114]. A way to overcome the uncertainties related to the band gap underestimation, is by applying a posteriori corrections which could stretch out the gap up to its experimental value [81, 114]. Other uncertainties in the calculation can be related to computational restrictions on the supercell size (supercells of 32 or 62 atoms) [115].

2) A more recent development in the implementation of DFT calculations is *hybrid exchange-correlation functionals*. The need for a posteriori band gap correction is eliminated when using such functionals since the since the band gap is correctly described. However, the finite size problem has remained, or even got worse as these calculations are much more computationally demanding [115]. An overview of some recent results is described below.

• References [116, 117] describe calculations of intrinsic point defects in $CuInSe_2$ and $CuGaSe_2$ based on screened-exchange hybrid density functional theory. Low formation energies are found in $CuInSe_2$ and $CuGaSe_2$ for the defects $(In,Ga)_{Cu}$, V_{Cu}, $Cu_{(In,Ga)}$ and Cu_i. V_{Cu} is characterized as a very shallow acceptor (< 50 meV), in accordance with reference [91], and is regarded as the main acceptor. In_{Cu} is found to be a very shallow donor defect or is even found to be located within the conduction band. Therefore, following reference [116], the defect does not play a role in the device performance. This result does not agree with the result in reference [91] in which the In_{Cu} defect was calculated to be a deep donor ($E_a < 250$ meV). Dominant intrinsic recombination centres following reference [116] are the deep electron trap Ga_{Cu} and hole traps Cu_{In} and Cu_{Ga} (see table 2.2). As the binding energies for complexes with V_{Cu} are found to be rather small, defect complexes with V_{Cu} will not exist in large quantities which is in (large) disagreement with reference [91].

Table 2.2: Charge transition levels (eV) above the valance band maximum ('shallow' $\approx <$ 50 meV i.e. smaller than accuracy). Defects with low formation energy are indicated in bold.

$CuInSe_2$	Transition energy (eV)	$CuGaSe_2$	Transition energy (eV)
$\mathbf{V_{Cu}}$	shallow	$\mathbf{V_{Cu}}$	shallow
$\mathbf{In_{Cu}}$	shallow	$\mathbf{In_{Cu}}$	shallow
$\mathbf{Ga_{Cu}}$	shallow	$\mathbf{Ga_{Cu}}$	1.26 (+2/+1), 1.33 (+1/0)
$\mathbf{Cu_{In}}$	0.14 (0/-1), 0.62 (-1/-2)	$\mathbf{Cu_{Ga}}$	0.20 (0/-1), 0.75 (-1/-2)
$\mathbf{Cu_i}$	shallow	$\mathbf{Cu_i}$	shallow
V_{Se}	0.08 (+2/0), 0.98 (0/-1)	V_{Se}	0.34 (+2/0), 1.26 (0/-1), 1.66 (-1/-2)
V_{In}	0.03 (0/-1), 0.42 (-1/-2)	V_{Ga}	0.01 (0/-1), 0.34 (-1/-2)
V_{In}	0.69 (-2/-3)	V_{Ga}	0.82 (-2/-3)
In_i	0.34 (+3/+2), 0.48 (+2/+1)	Ga_i	0.05 (+3/+2), 0.39 (+2/+1)
Se_i	0.19 (+2/+1), 0.20 (+1/0)	Se_i	0.15 (+2/+1), 0.48, (+1/0),
Se_i	0.64 (0/-1)	Se_i	1.08 (0/-1), 1.32 (-1/-2)

• References [114, 115, 118] present different results using hybrid-functional calculations for $CuInSe_2$. It is found that, among the intrinsic defects, copper-related defects such as V_{Cu}, Cu_{In}, In_{Cu} and Cu_i stand out as the most prominent, in agreement with reference [116]. The very low V_{Cu} formation energy is in line with the easily grown Cu-poor form of $CuInSe_2$ [118]. The formation of indium defects, V_{In} and In_i, is suppressed [118]. Unlike the results in references [91,116], Cu_{In}, In_{Cu}, V_{Cu}, V_{In}, Cu_i and In_i do not yield single particle levels in or near the band gap [114, 118]. Selenium-related defects are regarded as responsible of the experimentally observed ionization levels. The selenium vacancy is found to form a (very) deep double acceptor level (0/-2) with a transition energy of 0.85 $\pm$ 0.20 eV. Further it is found that the selenium interstitial can also exist in a dumbbell configuration $(Se\text{-}Se)_{Se}$, which is characterized by two selenium atoms sharing the same Se site, creating a shallow acceptor level [114].
• Reference [81] has determined, using hybrid functional method, that In_{Cu} and Ga_{Cu} are shallow donors. Shallow acceptors are V_{Cu} (most shallow), $V_{In,Ga}$ and $Cu_{In,Ga}$. In-rich growth conditions causes n-type conductivity in $CuInSe_2$ due to the native In_{Cu} donor. As for In-poor growth conditions the formation energy of In_{Cu} donor increases, the conductivity type alters to p-type. In $CuGaSe_2$ n-type conductivity is inhibited due to pinning of the Fermi level far away from the conduction band minimum.

The previous description concerning theoretical findings about defect activation (energy difference between defect level and closest band (valence or conduction band)) and formation energies demonstrates that the results are quite contradictory. This is also the case for experimental results. They do not yet reach a consensus concerning defect activation energies as described below.

Experimental results
Experimentally determined defect activation energies for $CuInSe_2$ obtained from various experimental methods are shown in table 2.3. The table on the left gives information about shallow defects. On the right information about deep defects as measured from DLTS can be found. This table shows that the defect activation energies can vary over 30 meV for one defect. Furthermore no clear agreement with theoretical calculations can be found.

Table 2.3: Observed donor (D) and acceptor (A) ionization energies (respectively with respect to conduction band minimum and valence band maximum) in meV for $CuInSe_2$. Measurements methods are: electrical measurements (Electr.), photoconductivity (PC), photovoltage (PV), optical absorption (Opt. abs.) and photoluminescence (PL) [91].

Method	E_{D1}	E_{D2}	E_{D3}	E_{A1}	E_{A2}	E_{A3}	E_{A5}
				n-type samples:			
Elect.	10		220				
Elect.	12		180				
Elect.	7						
Elect.	5	80					
Elect.	6						
Elect.+PL	35	75	145		105		
Opt. abs.	6			41			
Opt. abs.	26	90		54			
Opt. abs.			232			154	
PL		70		40			
PL	35	72			100	150	
PL	10			33			
PL	35			45		130	
PL		60–80		40			
PC	7		225				400
PV	11						
				p-type samples:			
Elect.				20–28			
Elect.				35	100		400
Opt. abs.			232	38		154	
PL				40			
PL					85		
PL	35	72			100	150	
PL		55		30	85	130	
PL		70		40	80		
PL		60		40	80		
PL	43			17		162	
DLTS				16–39	87–92	166–191	

Type	E_{D3}	E_{D4}	E_{D5}	E_{A3}	E_{A4}	E_{A6}	Ref
n		370					41
n	182	335					43
n		350	570				44
p				200		540	41
p					280,320		41
?					250	520	42
?				120–190	260–280		45
p				186	250	520	43
p					220–280		44
p				166–191	276		46

$E_{D1} = V_{Se}^{(0/+)}$
$E_{D2} = V_{Se}^{(+/2+)}$ or $(In_{Cu} + V_{Cu})^{(0/+)}$
$E_{D3} = In_{Cu}^{(0/+)}$ or $Cu_i^{(0/+)}$
$E_{D4} = In_{Cu}^{(+/2+)}$

$E_{A1} = V_{Cu}$
$E_{A2} = Cu_{In}\text{-}Cu_i^{(-/0)}$
$E_{A3} = V_{In}^{(-/0)}$
$E_{A4} = Cu_{In}^{(-/0)}$
$E_{A5} = V_{In}^{(2-/-)}$
$E_{A6} = Cu_{In}^{(2-/-)}$

Another overview of experimentally determined defect activation energies on $CuInSe_2$ can be found in reference [4] (table 2.4). The activation energies differ from the defect activation energies presented in figure 2.3. The In_{Cu} anti-site and V_{In} are more shallow. The activation energy for V_{Cu} can be quite large.

Table 2.4: Experimentally determined activation defect energies from reference [4].

Donor defect	E_a (meV)	Acceptor defect	E_a (meV)
In_{Cu}	35-45, 10-20	Cu_{In}	30, 40-60
V_{Se}	10	V_{Se}	60-80
Cu_i	21, 55	V_{Cu}	40, 85
In_i	53, 80	V_{In}	33, 80, 90, 230, 300-330
		Cu_{Se}	230
		Se_i	89-130, 153

Temperature dependent conductivity measurements on $CuInSe_2$ are published in reference [119] (table 2.5). No good agreement between these results and these above can be found. The In_{Cu} anti-site is determined as very shallow (8 meV).

Table 2.5: Overview of different donor and acceptor levels found from temperature dependent conductivity measurements [119].

Donor defect	E_a (meV)	Acceptor defect	E_a (meV)
In_{Cu}	8	V_{Cu}	12-30
V_{Se}	80	V_{In}, Cu_{In}	65, 82, 98
In_i	180	Fe^{2+}_{In}	400

Figure 2.6 presents the defect transition energy values for $CuGaSe_2$ (single crystals) found by PL experiments in different reports. The energy of the V_{Se} defect ranges over 30 meV. The Ga_{Cu} defect is found to be shallow while theoretical calculations [109] have shown this defect is rather deep.

Table 2.6: Ionization energies from PL measurements on single crystal $CuGaSe_2$ [120].

Donor defect	E_a (meV)	Acceptor defect	E_a (meV)
Ga_i	120	V_{Cu}	40, 50
V_{Se}	80, 110	Se_i	40, 80
V_{Ga}	15	Ga_{Cu}	15

From the above it is clear that there is no (good) agreement between different theoretical calculations, between theoretical and experimental determined activation energies and between the experimental reports. This makes the identification of the photoluminescence (PL) emission peaks and DLTS signals far from straightforward. Besides the reported different activation energies, a range of possible interpretations of the PL/DLTS spectra can be found. An overview of various PL experiments with very distinct peak assignments can be found in chapter 5 of reference [4]. As will be discussed in section 5.2.1.2, the assignment of the PL peaks is even more complicated by the dependence on the composition. Potential fluctuations in a highly compensated material smear out the information about the discrete defect states and as a results it is difficult to track the origin of the defect. The ambiguous interpretation of DLTS spectra is further discussed in section 3.4.

2.3.1.6 Effect of Sodium

In order to achieve high efficiency devices a small (0.1 %) concentration of Na is necessary [121]. Several models of the direct an indirect influences of Na have been proposed, but still there is no agreement [47]. Na is commonly introduced by diffusion from the soda lime glass during the absorber deposition. Soda lime glass contains up to 14% NaO_2. Other possibilities for the Na introduction are co-evaporation from a NaF source, a NaF precursor layer on Mo before CIGS deposition, diffusion from a Na containing Mo layer, post deposition treatment with NaF, ... In a post deposition treatment a thin NaF layer (around 30 nm) is deposited on the CIGS absorber and then annealed in Se atmosphere which facilitates the decomposition of NaF at the CIGS surface [122]. A reaction of F with Se (from the chamber and/or from the CIGS surface) occurs forming the volatile selenium hexafluoride (SeF_6), which then desorbs the surface [122].
In reference [123] it is shown that Na reduces the diffusivity of Ga and can thus alter the composition in the absorber layer. This is confirmed by reference [124], where the Na concentration in CIGS films was controlled using alkali-silicate glass thin layers of various thickness deposited on substrates prior to CIGS growth. It was noticed that an enhanced presence of Na in the absorber layer leads to a reduction of interdiffusion during growth, which led to an increased depth of the GGI dip. References [108,125,126] report that the presence of Na in the CIGS film and/or surface can have an influence on Se as it suppresses Se diffusion via grain boundaries and in this way impedes Se loss.

One of the models explaining the beneficial influence of Na on the device performance is that Na modifies the ***film growth***. Because of smaller grain sizes, more grain boundaries may act as recombination centres for photogenerated charge carriers, degrading the device performance. Therefore grain size is often used as a quality marker for the CIGS absorber. More recently it has been shown that the presence of different grain sizes are not as detrimental for high efficiency devices [82, 127]. Reports on the influence of Na on the grain size are contradictory and seem to be dependent on the absorber formation [6].
In reference [108] the ***passivation of grain boundaries*** by Na is considered to improve the device performance, rather than modification of the CIGS growth kinetics, as the in-diffused Na from PDT is expected to reside predominantly at grain boundaries. The latter is confirmed in reference [128] in which atom-probe tomography (ATP) results show that irrespective of the Na source (SLG or PDT), Na segregates at the grain boundaries. ATP results in reference [122] show that due to NaF PDT an average Na concentration of around 0.015 at. % is estimated in the grain interiors while an average Na concentration of around 0.2-2 at. % was estimated at the grain boundaries. It is suggested in reference [128] that Na_{Cu} defects are most likely reducing the number of compensating In_{Cu} defects.
The most obvious electronic effect of supplying Na to CIGS, is an increase in carrier concentration which improves the cell performance. As the increase in conductivity is also seen in films where Na is incorporated after the deposition process, it can be concluded that the effect of Na doping is not (only) related to structural changes but also related to an ***electronic effect*** [6]. In reference [11] a hole concentration before Na treatment is reported of around 10^{14} cm^{-3}. With NaF post deposition a hole concentration of $8{\cdot}10^{15}$ cm^{-3} was reached. The increase of the hole density is explained in several models [6, 123, 129]:

- *Oxygen model*: donor-like V_{Se} defects are neutralized through an enhanced chemisorption of oxygen atoms in the presence of Na. Na catalyses O_2 dissociation whereby oxygen is supplied for the oxygen incorporation on V_{Se}. There is no agreement in literature reports whether or not O_{Se} is electrically active nor about its defect energy level. The activation energy of the O_{Se} defect is around 120-140 meV according to [124] and 75 meV according to reference [130]. The latter reference states further that O_{Se} is an isoelectronic defect and is electrically active because the electronegativity difference between O and Se produces a weak acceptor character. In references [131, 132] it is stated otherwise: the O_{Se} defect is an electrically inactive deep acceptor due to the same valency of oxygen and selenium. Theoretical calculations in reference [129] show that the O_{Se} acceptor defect is very deep: 550 meV for the (-/0) and 670 meV for the (2-/-) transition. Hence no free holes are expected to be created by the O_{Se} defect.

- *Na phase model*: Na replaces the V_{Cu} forming the $NaInSe_2$ compound that has a larger band gap at the surface

- *In_{Cu} model*: via Na there is an elimination of the compensating anti-site donor defect In_{Cu}. The formation of Na_{Cu} replacing In_{Cu} is exothermic, and therefore removal of In_{Cu} donor states could be the main influence of Na doping.

2.3.1.7 Effect of Potassium

As K also diffuses from the soda lime glass substrate (0.2-0.3% K_2O), K has been frequently observed in CIGS absorber layers. However its influence on the properties of the final device has mostly been neglected or considered as similar to the effects stemming from Na. The unique beneficial role of additional K (by KF PDT) in the absorber layer was only recently been discovered and demonstrated [29]. To date only few reports on the effect of K are available. More investigations still have to be performed to completely understand the role of K.

In CIGS layers grown on soda lime glass, K and Na were found by atom-probe tomography to segregate at grain boundaries [133]. In references [108, 121] it was suggested that the alkaline elements from PDT reside at grain boundaries as well. By means of secondary ion mass spectroscopy (SIMS) measurements it is shown that KF PDT leads to a significant incorporation of K and removal of Na in the CIGS layer [29,134]. Reference [29] suggests that by an ion exchange mechanism, the presence of K over Na is favoured. K is chemically very similar to Na, only the ionic radius of K^+ is larger than that of Na^+ which could result in a lower diffusivity of K. KF PDT and to a smaller extent also NaF PDT, induce a depletion of Cu and Ga at the surface according to reference [29]. Cu depletion due to KF PDT was confirmed by references [134,135]. References [65,121,136,137] concluded that K acts in a similar way as Na: it passivates donor like defects, like In_{Cu}, which results in an increase of the net charge carrier density. In reference [121] elemental depth profiles show that the composition of the CIGS layer and the concentration profiles of the constituent elements did not change by KF PDT. The observed increase in V_{oc} between K doped and undoped samples is larger than what would be expected only from enhanced carrier concentration. A record efficiency of 21.7% (with AR coating) has been reached by applying a alkaline PDT [30]. The KF PDT process can overcome the saturation of the V_{oc} for higher gallium content that is normally observed. Higher Ga contents can be thus used.

In reference [138] it was found by hybrid functional calculation that Na and K improve the conduction band offset. The band gap is changed and the valence band offset is enlarged (especially for K). K introduction leads to a stronger reduction of the conduction band offset (0.05 eV) than for Na (0.45 eV). As K tends to destabilize the ordered defect phase near the CIGS surface, optimisation of Na and K ratios is necessary. Reference [135] finds evidence for a lowered valence band edge (0.3 eV-0.4 eV) at the KF treated CIGS surface which is found to be Cu depleted in the first few nanometers.

2.3.1.8 Effect of Antimony

Generally it was believed that high growth temperatures of 600°C were a prerequisite for reaching high efficiency CIGS devices. The maximum applicable temperature for polyimide foils, which can lower the costs, is constrained to 500°C. Due to this lower temperature different interdiffusion of the elements and hampering of the crystal grain growth may appear. Partial compensation of the efficiency loss, due to smaller grains, might be accomplished by Sb doping of the absorber, which has been reported to have a positive effect on the morphology of the absorber layer [139–143]. References [144, 145] report no enhancement on the grain size. Reference [141] suggests that the benefit by the Sb incorporation is related to a synergistic effect of Sb atoms with the Na atoms diffused from SLG substrates. In literature there is no consensus about the Sb diffusion throughout the CIGS absorber layer [139, 141–143] nor about the effect of Sb on the band gap [139, 146].
Besides the effect on grain size, it is reported in reference [146] that the incorporation of Sb can alter the conductivity of CIGS. Because Sb doped $CuInS_2$ crystals are p-type, references [144,147] suggest that the dominant shallow acceptor type defect can be assigned to an Sb atom on the S site (Sb_S).

2.3.1.9 Deposition

The CIGS absorber layer is deposited by a three stage co-evaporation process (figure 2.23) from elemental sources (Cu, In, Ga, Se). The first stage consists of deposition of In, Ga and Se. Thereafter, in the second stage, Cu and Se are deposited until the composition is Cu-rich. In the last stage, In, Ga and Se are added again. The temperatures for each stage can differ. The final layer is Cu-poor (CGI < 1) [11].

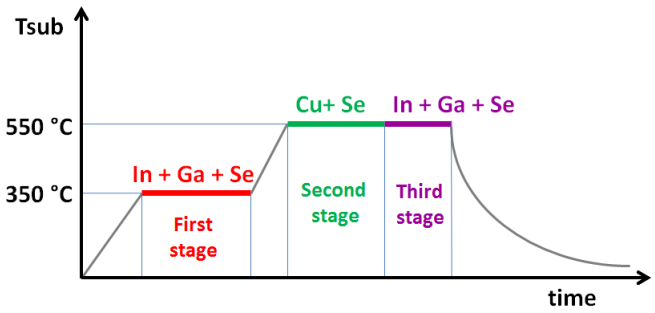

Figure 2.23: Temperature profile of the growth of CIGS during the three stage co-evaporation process [4].

Due to a preferred reaction of In with Cu over Ga with Cu during film growth, this deposition sequence results in a double-graded composition profile with a higher Ga content towards the back and the front of the CIGS film [148]. In the first stage there is a good interdiffusion in the $(In,Ga)_2Se_3$ film and no Ga gradient. However when Cu is added during the second stage, the mobility of In and Ga differs. An accumulation of Ga towards the back contact and an increased In content towards the front arises because In has a higher mobility than Ga. To maintain a stable composition, the in-diffusion of three Cu ions must be compensated by out-diffusion of one group III element. The out diffusion of In dominates. In the third stage, In moves towards the back contact and Ga moves towards the front contact. An opposite gradient to the first is formed and gives a notch profile.
The location and depth of this notch are determined by the relative proportions of the three stages, deposition rates, sodium content during the growth and growth temperature [73]. Cu diffusion in the films during growth is sufficiently fast so that a homogeneous Cu distribution through the finished absorbers is established in most cases. Se is supplied in excess in order to avoid Se deficiency. Excess Se is not incorporated into the growing film and instead re-evaporates from the surface [65].

2.3.2 CZTS

2.3.2.1 Structure and composition

CZTS (I_2-II-IV-VI_4) structure is derived from the chalcopyrite structure $CuInS_2$ by replacing of the In atoms with Sn and Zn. Unlike CIGS wherein the [In]/[Ga] ratio can be varied continuously, the [Zn]/[Sn] ratio in CZTS is far less flexible [149]. The variable for CZTS, which can alter the band gap, is the [S]/[Se] ratio.

The two principal structures of low symmetry are the tetragonal stannite and the kesterite structures (figure 2.24). The difference between these structures lies in the arrangement of the Cu and Zn atoms. The kesterite structure has the lowest energy, but as the bindings energy difference (1.3-3.4 meV/atom [150,151]) is very small, it is very likely that stannite coexists with kesterite [150]. Furthermore if the Cu and Zn atoms are arranged randomly on their lattice plane, the structure is labelled as partially disordered (PD-kesterite) [151]. The disorder among the Cu and Zn cations could be a possible cause of the limited open circuit voltage (and low efficiencies as a consequence) [152]. Even 70% ordering in kesterite corresponds to large numbers of Cu/Zn antisite defects. These defects are calculated to cause band gap fluctuations (around 100 meV) which could explain the voltage deficit [152].

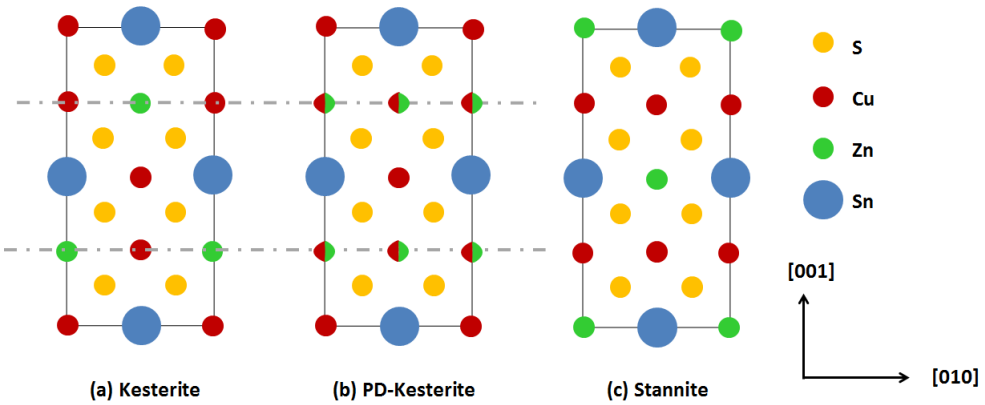

Figure 2.24: Crystal structures of CZTS. Dashed lines indicate the planes of Cu-Zn disorder for kesterite (after [151]).

The difference between the stannite and kesterite structure is difficult to detect. Because Cu^{+} and Zn^{2+} are isoelectronic, X-ray diffraction cannot distinguish between kesterite and stannite. Neutron powder diffraction measurements showed experimentally that the partially disordered kesterite structure can exist [153]. Neutron diffraction is however unsuitable for thin-films as large sample volume is necessary for the analysis [39, 152]. Another method to detect different phases in the material is by Raman spectroscopy. This technique is an optical, non-destructive, surface-sensitive technique which gains information about the phonon behaviour of the crystal lattice by detecting frequency shifts of the in-elastically scattered light from the near surface of the sample. As the shifts are specific for each phase, the Raman shifts provide information about the different phases in the material [39]. Reference [152] showed that Raman spectroscopy is convenient tool to track Cu/Zn disorder in CZTS thin-films. A comparison between CZTS powders which differed in the cooling rate after synthesis and thin-films with different post annealing was performed. The determination of the critical temperature for the transition from ordered to disordered kesterite was determined to be relatively low (around 260°C). This low critical temperature has important consequences. As CZTS is normally grown at 450-550°C, which is far above the critical temperature, it implies that ordered kesterite cannot exist. Disordered kesterite is formed at these high deposition temperatures. The ordering among Cu and Zn begins only when the temperature drops below 260°C, i.e. during post-synthesis cooling. The low temperature final step of the cooling seems to determine the level of disorder and hence the Cu_{Zn} and Zn_{Cu} defect concentrations which are decisive for the device characteristics. Details on the low temperature part of the cooling wherein the ordering apparently occurs, are rarely reported in literature [152].

2.3.2.2 Secondary phases

The comparatively low efficiencies of CZTS thin-film solar cells are ascribed to inhomogeneities due to secondary phases. Therefore secondary phases should be a avoided during crystal growth [154]. It is however very challenging to grow pure CZTS as the single phase region of CZTS in the phase diagram is very narrow (figure 2.25) [149, 150]. The formation of secondary phases such as ZnS, SnS, CuS, Cu_2S, Cu_xSnS_y (CTS) is very likely. Both CuS and CTS phases have small band gaps that can cause shunting and can act as detrimental recombination centres. ZnS, on the other hand, is a highly resistive, wide band gap semiconductor with less negative impact on efficiency [149].

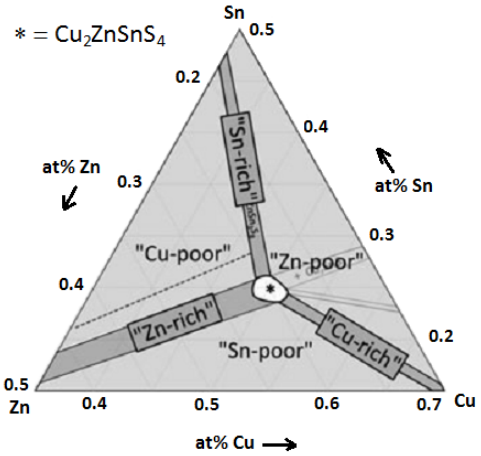

Figure 2.25: The pseudo-ternary phase diagram of the Cu_2S-ZnS-SnS_2 system at 400°C in which a stoichiometric amount of S is assumed [151].

So far CZTS solar cells with high performance are slightly Zn-rich and Cu-poor. Under these growth conditions ZnS is the main competing phase [155]. The content control of Zn should be taken very carefully. To avoid the ZnS secondary phase formation, the Zn concentration should not be too high. On the other hand, the Zn concentration should not be too low as large amount of Cu_{Zn} antisite defects can than be formed.

For increasing solar cell efficiency, the detection and characterization of these secondary phases is important. Nevertheless, it is commonly recognized that detecting secondary phases using only XRD (X-ray diffraction) in CZTS is not as easy as in CIGS. XRD can usually assign a phase with confidence, unless there are several coexisting phases with similar symmetry and lattice parameters. Unfortunately, this is the case here: kesterite CZTS shares multiple peaks with cubic ZnS and CTS. Furthermore the small volume of the material renders the measurements difficult. Raman spectroscopy is therefore often combined with XRD results to characterize the phases in a CZTS thin-films [43]. Unfortunately, overlapping peaks also hinder the interpretation of the Raman spectroscopy results.

2.3.2.3 Absorption

It is commonly recognized that CZTS has an absorption coefficient of 10^4 cm^{-1} for photon energies exceeding 1.5 eV [39, 151]. Theoretical studies of the absorption coefficient of CZTS [156] confirm the value of 10^4 cm^{-1} at low energy. However at high energies (E > 2.5 eV) the theoretically determined absorption coefficient is higher (about 10^5 cm^{-1}) compared to experimental studies [23, 157, 158].

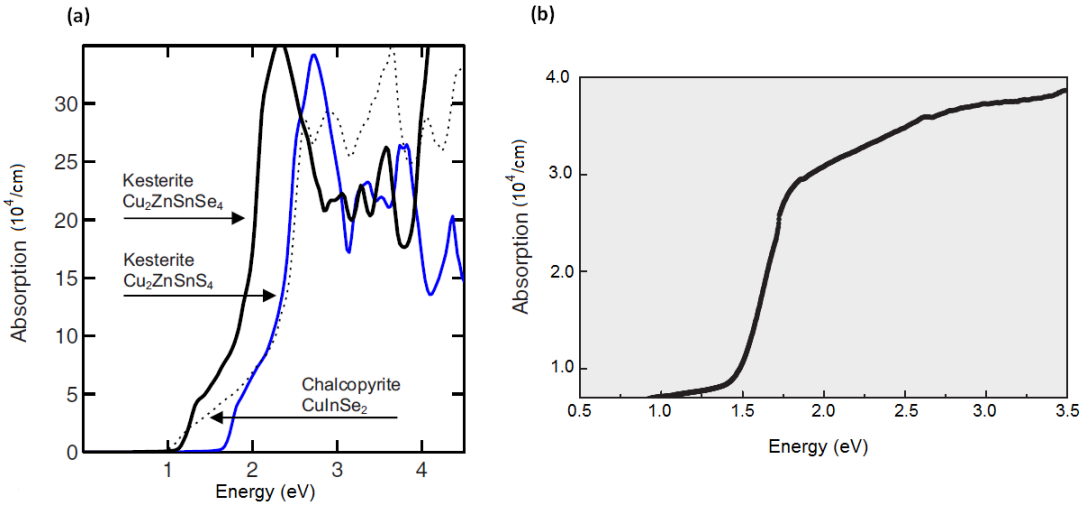

Figure 2.26: Absorption of CZTS (a) theoretical calculation [156], (b) experimental [23].

2.3.2.4 Band gap

The band gap can be varied by changing the [S]/[Se] ratio. In most experiments a band gap of 0.96 eV for $Cu_2ZnSnSe_4$ is found [149], while a band gap close to 1.50 ± 0.01 eV [150] is found for Cu_2ZnSnS_4. There are discrepancies on the reported experimentally determined band gap values which can be due to different deposition methods (compositional changes or variations in heat treatments) [149] or to the existence of secondary phases [159] with quite divergent band gap values. In reference [160] the estimated band gap for tetragonal Cu_2SnS_3 is 1.35 eV (in accordance with [161]), for cubic Cu_2SnS_3 $E_g \approx 0.96$ eV and for orthorhombic Cu_3SnS_4 $E_g \approx 1.60$ eV. $Cu_{2-x}S$ has a band gap varying from 1.3 to 2.3 eV. The band gap of ZnS is 3.7 eV [162]. For SnS the direct band gap was determined at about 1.3 eV [163–165]. Bulk MoS_2 has an indirect band gap of 1.15-1.30 eV while a monolayer has a direct band gap (1.8-1.9 eV) [166].

Theoretical calculations show that the band gap of the kesterite structure [167] agrees quite well with the experimentally determined band gap (see table 2.7). The band gap value for the disordered kesterite is calculated to be 40 meV [167] lower than for the ordered kesterite structure. For stannite the calculated band gap value is around 150 meV [150, 151] (see table 2.7) lower than for the ordered kesterite structure.

Table 2.7: Overview of calculated band gap values for kesterite and stannite reported in reference [151].

E_g (eV) Stannite	E_g (eV) Kesterite	Difference (eV)
1.38	1.50	0.12
1.42	1.56	0.14
1.30	1.49	0.19

Reports on the temperature dependence of the band gap of CZTS are very scarce, especially at low temperatures. The few reports that exist do not reach a consensus. In reference [24] a band gap energy shift smaller than 10 meV was noticed from 22 to 300 K ($3.6 \cdot 10^{-5}$ eV/K). In reference [20] the average band gap narrowing coefficient was $8.6 \cdot 10^{-4}$ eV/K in the range 77-410 K, estimated from transmittance data. At 10 K the band gap was about 1.64 eV. In reference [19] the band gap at 10 K in a Cu-rich CZTS crystal was determined via the exciton emission peak leading to a band gap of 1.52 eV.

2.3.2.5 Electrical properties

The commonly observed conductivity of CZTS thin-films is p-type. Contrary to CIGS, the dominant accepting defect the most easily formed is not V_{Cu} but the deeper Cu_{Zn} anti-site defect according to references [154, 168]. Because this accepting defect is not as shallow as V_{Cu}, a carrier freeze-out could be an issue for CZTS concerning high-efficiency devices [168]. References [22, 169] suggest that the copper vacancy is the dominant acceptor in Cu-poor and Zn-rich CZTS. The hole concentration was reported to vary from 10^{16} to 10^{18} cm^{-3} [43].

2.3.2.6 Defects

Information about defect activation energies is very scarce and the values determined in different reports are not similar. In general, experimental values indicate low activation energies while theoretical calculations rather point towards high activation energies.

First principles calculations
By first principles calculations it was found that the formation of point defects involving Sn is unlikely due to the covalent character of the Sn-S bonds. Cu and Zn are the most likely source of defects as their bonds are to a large extent ionic [170]. First principles calculations in reference [154] show that the acceptor defects which have low formation energy and lead to the p-type conductivity are Cu_{Zn}, Cu_{Sn}, Zn_{Sn}, V_{Cu} and V_{Zn}. The deeper acceptor Cu_{Zn} has lower formation energy than the shallower V_{Cu}. First principles calculations in reference [155] confirm that Cu_{Zn} is the dominant acceptor. n-type doping is very difficult for CZTS due to the easy formation of compensating acceptor defects. The formation energy of charged acceptors decreases as the Fermi energy shifts upward and can become negative. The negative formation energy means these defects will form spontaneously, reducing the free electrons and pinning the Fermi level [154]. This may be the reason why there are no reports on n-type CZTS material [150] and donors have higher formation energy. The most likely donors are the Zn_{Cu} anti-site and Cu_i interstitial with higher formation energy [154].
The role of electrically neutral defect complexes is predicted to be important. The defect complexes have remarkably low formation energies and electronically passivate deep levels in the band gap. The formation energy of the neutral defect complex $[Cu^{-}_{Zn}\text{-}Zn^{+}_{Cu}]^0$ is the lowest [154, 170]. This defect can also be regarded as the occupational exchange between Cu and Zn crystallographic sites which correspond to the structural disorder found in the kesterite phase [150, 154].

Reference [171] expresses some points of criticism on the previous theoretical studies. In this reference it was pointed out that the very low or negative formation energy calculated for Cu_{Zn} in reference [154] would imply that the material would always be metastable. Calculations performed in reference [171] showed that none of the defects had negative formation energy and CZTS is considered as a thermodynamically stable material. Another point of criticism found in reference [171], is the assignment of Cu_{Zn} as the dominant defect as this is in contrast with the Cu-poor and Zn-rich optimal growth conditions which would suppress the formation of this defect. Most important defects in CZTS are, recording to reference [171], Cu_{Zn}, Zn_{Cu}, Zn_{Sn}, Sn_{Zn}, $(Cu_m)_{Sn}$ (m = 1-3), V_{Cu}, V_S, and Cu_i. The Sn_{Zn} anti-site and the defect complex $(Cu_3)_{Sn}$ are identified as the dominant acceptor traps. The Cu-poor and Zn-rich conditions suppress the formation of the dominant defects. In figure 2.27 the differences between the transition energies of intrinsic defects in CZTS calculated by references [154] and [171] are shown.

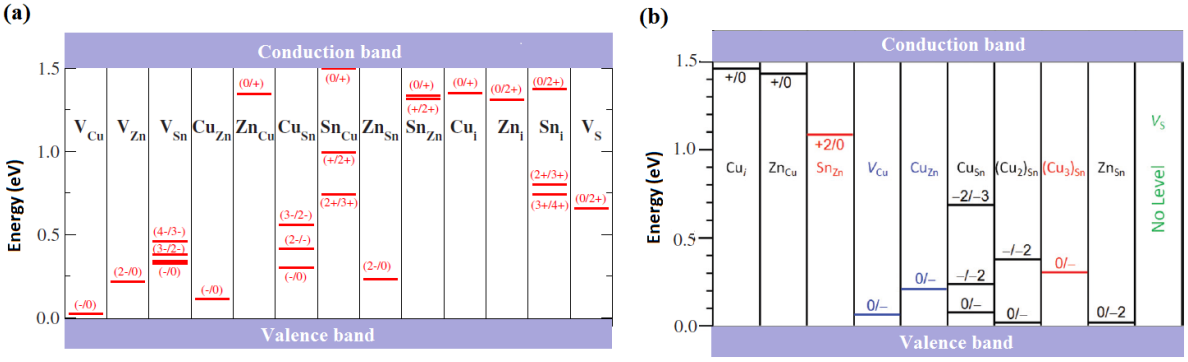

Figure 2.27: Ionization levels of intrinsic defect of CZTS following (a) reference [154], (b) reference [171].

Unfortunately, in references [154] and [171] accurate defect activation energy values are only published for the most important defects (table 2.8).

Table 2.8: Reported defect activation energies values for CZTS.

Defect	E_a (eV) [154]	E_a (eV) [171]
Cu_{Zn} acceptor	0.12	0.22
V_{Cu} acceptor	0.02	0.07
Cu_i donor	0.15	0.07
Zn_{Cu} donor	0.15	0.05

Experimental results

Electric and optical spectroscopy measurements have been performed to find which are the dominant defects present in CZTS absorber layers. No agreement is reached.
In reference [169] the origin of the p-type conductivity was ascribed to V_{Cu} based, on the composition of the single crystals which were made with a Cu-poor, Zn-rich and S-rich composition. In the work of reference [168] it was found that the CZTSSe capacitance spectra exhibit a dielectric freeze-out to the geometric capacitance plateau. This step is attributed to a deep acceptor (E_a = 130-200 meV depending on E_g) which leads to a carrier freeze out resulting in a high series resistance at low temperature. It is stated that the large activation energy is consistent with theoretical studies which indicate that the dominant acceptor impurities are rather deep defects such as the Cu_{Zn} anti-site. Other reports assign the capacitance step(s) directly to defects which are more shallow: in reference [172] a single defect with activation energy of 63 meV (attributed to V_{Cu}) is found for CZTSSe, in reference [173] two defect levels are found (E_a = 120 and 167 meV) for CZTSSe and in reference [174] two defect levels (E_a = 44 and 112 meV) are revealed for CZTS by modelling an equivalent circuit to the admittance measurement.
Besides the assignments of a capacitance step to defects, a step in the capacitance spectra can also be explained by a parasitic effect [175]. One step in the CZTS admittance spectra was seen and it was, by applying a simple circuit model, proven that an increasing series resistance with decreasing temperature can result in this capacitance step. In other words parasitic effects distort the admittance spectrum. The secondary phase ZnSe has been attributed to be the cause of the series resistance. The findings of reference [175] suggest that the interpretation of the admittance spectra should be handled with caution as an admittance step is thus not always related to defects.

Most PL studies on Cu-poor CZTS material show a broad peak around 1.3 eV [21, 24, 176–178]. Two broad PL bands were detected in reference [179]. PL measurements indicate that the material is strongly compensated [5, 16, 84, 180, 181] which makes it very difficult to extract

defect information from the PL measurements [19,150]. Up to now there is no clear defect model which explains the origin of the broad PL band. Transition energies calculated from thermal quenching are rather small from 30-60 meV [21, 24, 176]. Like for CIGS, only Cu-rich material provides narrow peaks in the PL spectra. Reports on Cu-rich CZTS are very scarce [19,182]. The activation energies found in reference [19] are ranging from 5-30 meV. Besides the assignment of the PL peak to defect transitions, a few reports mention the influence of other phases on the PL spectra [177, 179].

2.3.2.7 Deposition

The CZTS solar cells investigated in this work are made by sputtering deposition of a precursor (Cu, Zn, Sn) and annealing of this precursor at an elevated temperature in an atmosphere of sulfur [39, 51]. The deposition step gives a homogeneous precursor film with full chalcogen content. The short anneal allows the film to crystallize into CZTS. This two step method is a more successful fabrication process compared to a single-step vacuum deposition process. A single-step vacuum deposition (typical for CIGS) at high temperature is not well-suited as CZTS material has shown a tendency to decompose when high temperatures (needed for annealing) are combined with low pressures (during deposition) [39].
During the sputtering, atoms of a target (source material) are knocked out by bombarding ions of a working gas introduced in the evacuated chamber. The atoms are transferred to a substrate where they adhere. The substrate is thus coated by a thin-film. The target is the cathode, the substrate is the anode. The working gas is argon because it is a noble gas with low ionization energy and it is not expensive. Sputtering with direct current voltage works only for conducting materials. In the case of insulating materials, the surface charges because of the charge transferred by the argon ions. To avoid this problem, alternating current voltage is used (e.g. for ZnO sputtering). A magnetic field is applied (magnetron sputtering) in order to confine the electrons in the target's vicinity whereby the electrons then suffer more collisions with argon atoms which can lead to higher deposition rates and can reduce the substrate heating. If several targets are sputtered at the same time (Cu, Zn, Sn) this is labelled as co-sputtering. An homogeneous mixture of several compounds can be achieved in this way. The investigated samples are sputtered in a H_2S atmosphere. After the precursor deposition an annealing is applied (with or without additional sulphur). More detailed information can be found in chapter 9 of reference [39].

Part II

Electric characterization

3 Concepts of electric defect characterization

Contents

3.1 Electrically active defects

A donor-like trap can be neutral or positively charged when unoccupied by electrons, an acceptor-like trap can be neutral or negatively charged when occupied by electrons. The free carrier concentration is enlarged by shallow doping levels, as the levels are practically ionized for all temperatures. Their impact on the semiconductor can be regarded as positive. Next to the shallow doping, electrically active centers located closer to mid gap (traps or deep levels) exist. The impact of deep traps on the semiconductor is in general more negative. The closer the defect

level is to the middle of the gap, the more it tends to act as a recombination center [13, 183]. As pointed out in section 2.2.4.3, recombination via deep states occurs mainly by non-radiative transitions making the observation of photoluminescence signals from transitions via deep defect states rather improbable. As deep traps can enhance or compensate (e.g. unoccupied donor trap in p-type semiconductor) the space charge in the depletion region, they can alter the depletion width and therewith the capacitance. Properties of deep states can thus be investigated by capacitance spectroscopy [9].

3.2 Rate equations

3.2.1 Carrier capture and emission

Recombination of charge carriers via defects is often described by the Shockley-Read-Hall theory. Four different processes, presented in figure 3.1, can occur between the deep levels and the conduction and valence band whereby the state of a trap level changes. The processes and their respective generation (emission) and recombination (capture) rates are given as [7]

A) capture of an electron from the conduction band to the trap ($c_n p_t$);

B) electron emission from the trap to the conduction band ($e_n n_t$);

C) capture of a hole from the valence band to the trap (i.e. emission of an electron from the trap to the valence band) ($c_p n_t$)

D) hole emission from the trap to the valence band (i.e. capture of an electron from the valence band to the trap) ($e_p p_t$)

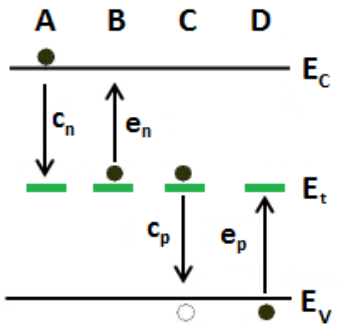

Figure 3.1: Basic processes involved in Schockley-Read-Hall recombination theory. Full circles represent electrons and open circles represent holes. The arrows represent the transition of an electron between different energy levels [184].

The number of traps occupied by electrons (holes) is given by n_t ($p_t = N_t$-n_t) respectively, with N_t the total number of trap states. c_n and c_p represent the capture rates for electrons and holes of unoccupied state. The emission rates per trapped charge carrier for electrons and holes are respectively e_n and e_p. e_n represents thus the probability per unit time that a particular electron is emitted [7]. The capture rates are calculated as the product of capture cross section $\sigma_{n/p}$, the average thermal velocity of free charge carriers $\langle v_{th} \rangle = \sqrt{\frac{3kT}{m^*}}$ (m^* the effective mass) and the free carrier concentration in the conduction and valence band (n, p).

$$c_n = \sigma_n \langle v_{th,n} \rangle n \qquad \text{electrons} \tag{3.1}$$

$$c_p = \sigma_p \langle v_{th,p} \rangle p \qquad \text{holes} \tag{3.2}$$

The change in electron densities is calculated as

$$\frac{dn}{dt} = e_n\, n_t - c_n\, p_t \tag{3.3}$$

The change in hole densities is calculated as

$$\frac{dp}{dt} = e_p\, p_t - c_p\, n_t \tag{3.4}$$

The time dependence of the number of occupied traps (n_t and p_t) can be calculated from the time dependence of electron (3.3) and hole densities (3.4). The Shockley-Read-Hall recombination process will be deduced underneath for a deep donor level in a n-type material with energy E_t from the conduction band with a the total concentration of trap states N_t.

3.2.2 Transient trap response

The change in the occupation of the deep defect by electrons ($n_t = N_t$-p_t) is given by following differential equation [7]:

$$\begin{aligned}
\frac{dn_t}{dt} &= \frac{dp}{dt} - \frac{dn}{dt} \\
&= (e_p\, p_t - c_p\, n_t) - (e_n\, n_t - c_n\, p_t) \\
&= (e_p + c_n)\, p_t - (c_p + e_n)\, n_t \\
&= (e_p + c_n)(N_t - n_t) - (c_p + e_n)\, n_t
\end{aligned}$$

If n_t in the above equation is replaced by N_t-p_t, the expression for the traps occupied by holes is obtained. The rates c_n, c_p, e_n and e_p are assumed time independent. The general solution, having $n_t = n_t(0)$ at $t = 0$, is

$$n_t(t) = n_t(\infty) - (n_t(\infty) - n_t(0))\, exp\left(-\frac{t}{\tau}\right) \tag{3.5}$$

where $n_t(\infty)$ is the steady state occupancy and given by

$$n_t(\infty) = \frac{c_n + e_p}{c_n + e_p + c_p + e_n}\, N_t$$

$1/\tau$ is the rate constant which describes the relaxation of the concentration of occupied traps occupied (in this case by electrons) back to the equilibrium occupancy. The rate constant is given by

$$\frac{1}{\tau} = c_n + e_p + c_p + e_n \tag{3.6}$$

Whether the state is occupied or not, depends on the position of the quasi-Fermi level as it determines the free carrier concentration. The sense of the relaxation depends on whether $n_t(0)$ is greater or less than $n_t(\infty)$ (equation 3.5). When the state is initially fully occupied ($n_t(0) = N_t$) there is a decrease of $n_t(t)$. When the state is initially empty ($n_t(0) = 0$) there is an increase of $n_t(t)$ with time. The transients are given in figure 3.2.

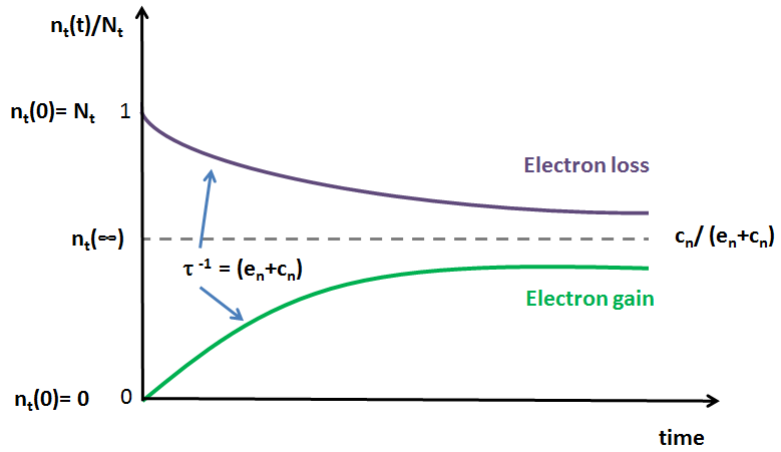

Figure 3.2: Relaxation of the occupancy $n_t(t)/N_t$ of an electron trap in n-type material, from full and empty initial conditions, to the steady state occupancy. The time constant is the same in both cases [7].

3.2.3 Detailed balance condition in thermal equilibrium

In thermal equilibrium the capture and emission processes must satisfy the principle of detailed balance and not simply the steady state requirement $dn_t/dt = 0$. The principle of detailed balance states that in thermodynamic equilibrium two processes, one of which is the inverse one of the other, should have the same probability to happen. Thus, in a semiconductor in thermodynamic equilibrium, the capture and emission rates of electrons (holes) must be the same. If this were not so, a net transfer of electrons from one band to the other could occur while the trap occupancy remained in a steady state [7].

$$e_n\, n_t = c_n\, p_t = c_n\,(N_t - n_t) \qquad \text{electrons} \tag{3.7}$$

$$e_p\, p_t = c_p\, n_t = c_p\,(N_t - p_t) \qquad \text{holes} \tag{3.8}$$

These equations allow to derive the thermal equilibrium occupancy of the trap:

$$\frac{n_t}{N_t} = \frac{c_n}{c_n + e_n} = \frac{e_p}{e_p + c_p} \qquad \text{electrons} \tag{3.9}$$

$$\frac{p_t}{N_t} = \frac{c_p}{c_p + e_p} = \frac{e_n}{e_n + c_n} \qquad \text{holes}$$

3.2.4 Temperature dependence of emission rate

The occupancy of a trap in thermal equilibrium (n_t) is defined by the product of the total number of trap states (N_t) and the occupation probability which is given by the Fermi-Dirac distribution function. For a deep state with energy E_t and degeneracy factor g_0, when empty of electrons, and g_1, when occupied with electrons (g_1 different ways to occupy the state), the occupancy is given by [7, 183]

$$\frac{n_t}{N_t} = \frac{1}{1 + \frac{g_0}{g_1}\, exp\left(\frac{E_t - E_F}{kT}\right)} \tag{3.10}$$

Combining equation 3.9 and 3.10 gives for electron and hole emission respectively

$$e_n = c_n\, \frac{g_0}{g_1}\, exp\left(\frac{E_t - E_F}{kT}\right) \qquad \text{electrons} \tag{3.11}$$

$$e_p = c_p\, \frac{g_1}{g_0}\, exp\left(\frac{E_F - E_t}{kT}\right) \qquad \text{holes}$$

The fraction of degeneracy factors g_0/g_1 is often assumed to be about 1. From equation 3.11 it is clear that the position of the Fermi level (E_F) relative to the trap state determines the occupation of the trap state.
If $E_t < E_F$, $c_n > e_n$ and $c_p < e_p$, the trap state is (mostly) occupied by electrons.
If $E_t > E_F$, $c_n < e_n$ and $c_p > e_p$, the deep level is (mostly) unoccupied by electrons.
If $E_t = E_F$, $c_n = e_n$ and $c_p = e_p$, 50% of the states are occupied by electrons (for g_0/g_1 =1).

The above statements can also be related to the dependence of the capture rate on the free carrier concentrations ($c_n = \sigma_n v_{th} n$). For a non-degenerate ($n < N_c$ and $p < N_v$) semiconductor, the free charge carriers can be calculated by:

$$n = N_c \, exp\left(-\frac{E_c - E_F}{kT}\right) \qquad \text{electrons} \tag{3.12}$$

$$p = N_v \, exp\left(-\frac{E_F - E_v}{kT}\right) \qquad \text{holes} \tag{3.13}$$

N_c and N_v are the effective densities of states in the conduction and valence band, respectively:

$$N_{c/v} = 2\Big(\frac{2\pi m^*_{e/h} kT}{h^2}\Big)^{\frac{3}{2}} \tag{3.14}$$

where $m_{e/h}{}^*$ represents the effective mass of the carrier. The temperature dependence of the electron (hole) emission can be calculated by formulas 3.1, 3.11, 3.12 and 3.14:

$$e_n(T) = \sigma_n \, v_{th} \, N_c \, exp\left(-\frac{E_c - E_t}{kT}\right) \qquad \text{electrons} \tag{3.15}$$

$$e_p(T) = \sigma_p \, v_{th} \, N_v \, exp\left(-\frac{E_t - E_v}{kT}\right) \qquad \text{holes} \tag{3.16}$$

From the above equations it can be stated that capture cross section and the energy level of the defect may be considered as primary properties of the trap from which the emission rate of carriers to a band can be deduced. States in the upper half of the band gap (E_c-E_t < E_t-E_v) have $e_n > e_p$ and states in the lower half of the band gap have $e_p > e_n$. Because the dominant emission rate depends on the relative position of the trap state within the band gap, a discrimination between majority carrier traps an minority carrier traps can be made. For example for a p-type semiconductor where electrons are considered as minority carriers, 'the minority trap' ($e_n > e_p$) is positioned in the upper half of the band gap.

Taking into account the temperature dependencies $v_{th} \sim T^{1/2}$ and $N_v \sim T^{3/2}$ a temperature-independent prefactor K_T can be introduced. Equation 3.15 is then transformed to (same principle for holes) [7]

$$e_n(T) = K_T \, T^2 exp\left(-\frac{\Delta E_a}{kT}\right) \tag{3.17}$$

$$\text{with } K_T = \frac{2\sqrt{3}\,(2\pi)^{3/2}\, m^* \, k^2 \, \sigma_n}{h^3} \tag{3.18}$$

$$\text{and } \Delta E_a = E_c - E_t \tag{3.19}$$

In the above equation K_T is called the pre-exponential factor which is related to the capture cross section. ΔE_a is the activation energy which is the distance between the energetic position of the trap level within the band gap and the band edge it corresponds with. For an electron trap it is the energy necessary to excite one electron thermally to the conduction band. A plot of $\ln(\tau \, T^2)$ as a function of $\frac{1}{T}$, know as the 'Arrhenius plot', yields a straight line.

$$ln(\tau\, T^2) = ln\left(\frac{T^2}{e_n}\right) = \frac{\Delta E_a}{k}\frac{1}{T} - ln(K_T) \tag{3.20}$$

The slope is determined by ΔE_a, while the intercept with the ordinate gives the value of K_T. Values of the energy level and capture cross section, which are primarily used to characterize the trap, can be obtained via equations 3.20 and 3.18.
It must be noted that for the derivation of equation 3.17, a temperature independent σ_n is assumed. However, the capture of charge carriers for many deep states (e. g. in III-V compounds like GaAs [7]) is thermally activated. The activation energy and capture cross section determined experimentally via equation 3.20 can thus be distorted [5]. A capture process by multiphonon emission is described by [8]

$$\sigma_n(T) = \sigma_\infty exp\left(\frac{-\Delta E_\sigma}{kT}\right)$$

With σ_∞ the capture cross section for T at ∞ and ΔE_σ a barrier for carrier capture. Other temperature dependence for the capture cross section (like a cascade capture process) have been suggested [7].

3.3 Experimental techniques

In the preceding section, the interaction of charge carriers with defect states was discussed. Information on the characteristics of the defects in a semiconductor can be obtained from the capacitance of Schottky barriers or pn-junctions. The rate equations, derived in section 3.2, will be essential in the analysis of the capacitance spectroscopy measurements. After discussing capacitance-voltage measurements, the capacitance based spectroscopic techniques Deep Level Transient Spectroscopy (DLTS) and Admittance Spectroscopy (AS) are discussed.

3.3.1 Capacitance-voltage (C-V) profiling

3.3.1.1 Depletion capacitance

In a pn-junction the capacitance arises from the fixed space charge of the ionized donors or acceptors in the depletion region [55,183,185]. This region is depleted of free carriers (depletion approximation) and hence acts as a dielectric insulator. The effect of the depletion approximation and the neglected presence of deep levels will be discussed further (section 3.3.1.3). The charge configuration in a pn-junction in thermal equilibrium mimics that of a parallel plate capacitor. The capacitance of the diode with an area A and depletion width W can be written as

$$C = \frac{\epsilon_r\, \epsilon_0\, A}{W} \tag{3.21}$$

where ε_r is the relative permittivity of the material, ε_0 is the vacuum permittivity. Rather than being constant (like it is the case for a typical fixed capacitor), the capacitance of a pn-junction varies with the reverse bias by the voltage dependence of the depletion width (figure 3.3).

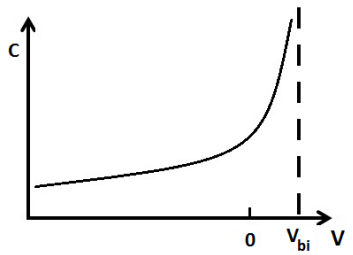

Figure 3.3: Depletion layer capacitance as a function of bias voltage [55].

To measure the capacitance, a dc bias V is applied to widen or shrink the depletion layer. A small ac signal voltage with certain frequency is superimposed to this bias V in order to probe the actual capacitance at this bias. A small increment ΔV increases the depletion width, leading to an increase in fixed charge per area ΔQ. The differential capacitance is defined as (with W for an asymmetrical n^+p-junction (equation A.2)):

$$\begin{aligned} C &= \lim_{\Delta V \to 0} \left| \frac{\Delta Q}{\Delta V} \right| \\ &= \left| \frac{dQ}{dV} \right| \\ &= \left| \frac{d(q\, N_a\, W\, A)}{dV} \right| \\ &= A \sqrt{\frac{q\, \epsilon_r \epsilon_0\, N_a}{2(V_{bi} - V)}} \end{aligned} \tag{3.22}$$

3.3.1.2 Doping concentration

Because the capacitance is dependent on the doping concentration (doping may also include here shallow level intrinsic defects), capacitance-voltage measurements are commonly used to determine the doping concentration or doping depth profiles ($N_a(x)$). To this end a plot $1/C^2$ versus V ('Mott-Schottky plot') is made. For a uniformly doped junction, equation 3.22 can be written as [183]

$$\frac{1}{C^2} = \frac{2(V_{bi} - V)}{q\, \epsilon_r\, \epsilon_0\, N_a\, A^2} \tag{3.23}$$

The apparent doping N_a can be determined via

$$N_a = \frac{-2}{q\, \epsilon_r\, \epsilon_0\, A^2} \left(\frac{d(1/C^2)}{dV} \right)^{-1} \tag{3.24}$$

The Mott-Schottky plot yields a straight line for uniform doping. The built-in voltage can be determined as the applied bias for which $1/C^2 = 0$. A non-uniform doping density ($N_a(x)$) gives rise to a deviation from a straight line in the Mott-Schottky plot. However, equation 3.23 remains valid since the charge fluctuations only occur at the depletion layer edge. In this case the concentration is determined as a function of the distance (varying W with applied bias) to the junction.

$$N_a(W) = -\frac{2}{q\, \epsilon_r\, \epsilon_0\, A^2} \left(\left. \frac{d(1/C^2)}{dV} \right|_V \right)^{-1} \tag{3.25}$$

An increased leakage current (non-ideal reverse saturation current), can influence the capacitance measurement at high reverse voltage. Solar cells are damaged if the applied reverse voltage is too high. Therefore the region wherein the doping density can be calculated is limited [10]. Temperature dependent C-V measurements reveal a decrease in capacitance. As a result of carrier freeze-out, the net fixed charge density decreases and enlarges the depletion region which lowers the capacitance. The freeze-out of shallow defects starts to appear at low temperatures. The freeze-out of deep defects already sets in at higher temperatures. When the whole absorber layer is in depletion (depletion region reaches the back contact of the cell) at very low temperatures, the geometrical capacitance is reached. The C-V curve becomes independent of the applied voltage and is thus horizontal. The thickness of the absorber layer can be estimated from such measurement (see section 3.3.3.2).

3.3.1.3 Effect of defects on C-V profiling

In section 3.3.1.2 the depletion approximation was assumed to derive the doping density profile ($N_a(W)$). When capture and emission processes from deep defects in the depletion region occur, the approximation does no longer hold. The deep defects can contribute to the measured capacitance and hence to the carrier concentration (contribution N_t) when the ac frequency is not high enough or the temperature is not low enough [5, 9, 11]. At a frequency of 1 MHz for C-V measurements, there would be no effect of deep defects on the doping density according to reference [11, 15].
Figure 3.4 shows the effect of deep levels and the measurement frequency on C-V profiling by a simulation [5]. At low frequency ω_L ($\omega_L < e_p$), the total doping density measured by C-V (N_{cv}) is equal to N_a+N_t as deep traps can respond to the low frequency. At high frequency ω_H ($\omega_H > e_p$), the deep defects cannot follow the frequency. However the trap states may adjust their charge state to the dc bias conditions which results in artefacts in the C-V profiles and non-uniform concentration profiles. The static charge accumulated at deep states follows the dc voltage sweep and influences the capacitance. N_{cv} is in this case a function of the dc bias [5, 6].

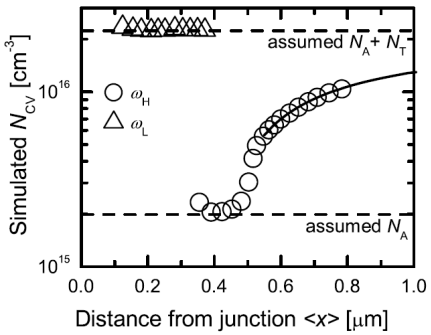

Figure 3.4: Simulated C-V profiles at two frequencies show the effect of deep states. N_{cv} denotes the doping density as measured from C-V [5].

3.3.2 Deep Level Transient Spectroscopy

3.3.2.1 Conventional majority pulse sequence

The basis of the depletion region technique used in DLTS will be deduced for a Schottky contact with an n-type semiconductor which has a single majority carrier defect level (electron trap) [5,7]. To observe the emission process of electrons (majority carriers) from a deep trap a sequence of bias pulses, as shown in figure 3.5, should be applied.

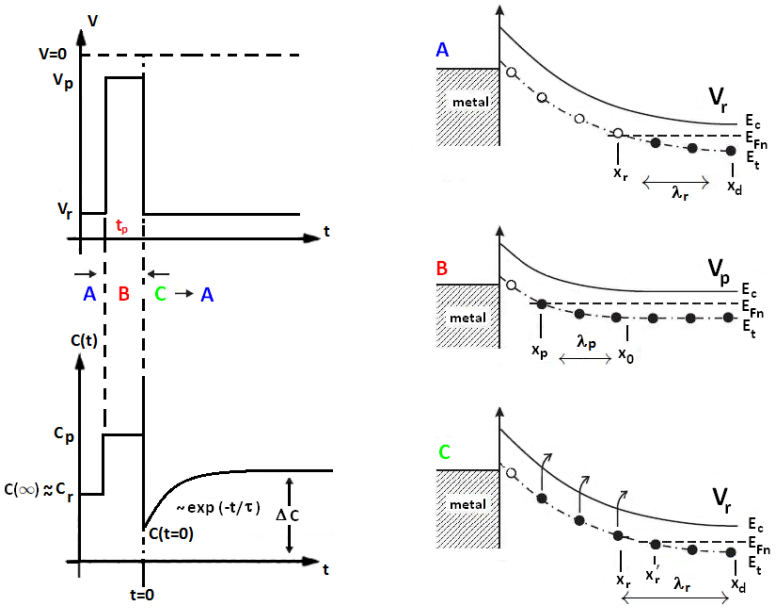

Figure 3.5: Left: Applied bias and capacitance and as a function of time. Right: Band diagram illustrations before, during and after the bias pulses. Full circle represents an occupied trap [183].

The bias is always negative and $V_r < V_p < 0$ should be valid, with V_r the reverse bias pulse and V_p the filling pulse bias. The conventional work cycle is as follows:

A: $V_r \rightarrow C_r$ First a reverse bias is applied which depletes the n-type semiconductor from electrons. The trap level is occupied by electrons up to the intersection point (x_r) between the trap level E_t and the quasi-Fermi level for electrons E_{Fn}. The capacitance at reverse bias voltages is labelled as C_r.

B: $V_p \rightarrow C_p$ The negative bias is reduced during a filling pulse time (t_p). The V_p bias is still negative to avoid minority carrier injection. Because of the reduced potential difference, the band bending is reduced. The position where E_t crosses E_{Fn} is now closer to the junction (x_p). Deep states upon x_p are now filled with electrons. The reduced potential difference during the filling bias pulse reduces the space charge region which implies an increase of the capacitance (equation 3.21). The capacitance during filling pulse is C_p.

C: $V_r \rightarrow < C_r$ When the first reverse bias is restored, the excess free carriers will be swept away and the depletion width is again larger. However, the trapped majority carriers can not instantaneously be emitted due to the thermal activation of this process (equation 3.15) and reduce the net positive space charge in the space charge region in comparison with the equilibrium situation A. This increases the depletion width compared to situation A and causes the capacitance to drop below C_r directly after the voltage pulse. The intersection of E_t and E_{Fn} (x_r') is larger than x_r. The trapped carriers are bit by bit thermally emitted from the deep states between x_p and x_r'. The net positive space charge increases, the depletion width decreases down to its equilibrium value (x_r) and the capacitance increases back to C_r. By measuring the capacitance transients, the emission of majority carriers can be deduced. An increasing capacitance shall result in a positive DLTS signal (by convention, see section 3.3.2.4). For a p-type material the emission of holes after the filling pulse, will make the depletion region more negatively charged. Hereby the depletion width will decrease which leads to an increase in capacitance. An increasing capacitance results in this thesis, in a positive DLTS signal.

3.3.2.2 Capacitance transient of conventional pulse

The time dependent net space charge density in the n-type semiconductor during the emission process after a majority carrier pulse sequence can be written as (for a donor like majority trap)

$$\rho(t) = q\,(N_d + N_t - n_t(t))$$

For a p-type semiconductor the density of traps occupied by electrons n_t can be replaced by N_t-p_t to obtain the number of traps occupied by holes. From the differential capacitance (equation 3.22) whereby $N_{a/d}$ is replaced by the time dependent space charge density $\rho(t)$, the time dependent capacitance at constant reverse bias ($|V_r| >> |V_{bi}|$) can be written as

$$\begin{aligned} C(t) &= A\sqrt{\frac{\epsilon_r\,\epsilon_0\,\rho(t)}{2V}} \\ C(t) &= C(\infty)\sqrt{\left(1 - \frac{n_t(t)}{N_d + N_t}\right)} \\ \text{with} \qquad C(\infty) &= A\sqrt{\frac{q\,\epsilon_r\,\epsilon_0\,(N_d + N_t)}{2V}} \end{aligned} \tag{3.26}$$

As the concentration of deep levels is smaller than the impurity concentration ($N_t << N_d$), $C(\infty)$ can be regarded as the capacitance of a device without deep level impurities at reverse bias V_r and equals C_r for large time. A Taylor expansion of equation 3.26 (N_t, $n_t <<< N_d$) and defining $\Delta C(t) = C(t)$-$C(\infty)$ gives further simplifications

$$\begin{aligned} \frac{\Delta C(t)}{C(\infty)} &= -\frac{n_t(t)}{2(N_d + N_t)} \\ &= -\frac{n_t(t)}{2N_d} \quad \text{with } N_t << N_d \end{aligned} \tag{3.27}$$

For emission from an electron trap ($e_n >> e_p$ and c_n, $c_p <<<<$), the steady state occupancy $n_t(\infty)$(equation 3.2.2) is zero and equation 3.6 becomes $1/\tau_n = e_n$. At $t = 0$, $n_t(0) = N_t$. Hence the transient response (equation 3.5) can be written as

$$\begin{aligned} \frac{\Delta C(t)}{C(\infty)} &= -\frac{N_t}{2N_d}\,exp(-e_n\,t) \\ \text{or } C(t) &= C(\infty)\,\left(1 - \frac{N_t}{2N_d}\,exp(\frac{-t}{\tau_n})\right) \end{aligned} \tag{3.28}$$

Equation 3.28 shows that the capacitance increases exponentially with time as carriers are emitted from the trap. As the relation of the time constant of the capacitance transient (τ) and the thermal emission rate equals $1/\tau = e_n$, equation 3.17 can be applied. From measurement of the capacitance transient during the emission as a function of temperature, the emission rate (e_n) can be derived through the Arrhenius diagram (see equation 3.20).

$$\frac{1}{\tau} = e_n(T) = \sigma_n\,v_{th}\,N_c\,exp\left(-\frac{E_c - E_t}{kT}\right) \tag{3.29}$$

$$= K_T\,T^2 exp\left(-\frac{\Delta E_a}{kT}\right) \tag{3.30}$$

The amplitude of the transient $\Delta C(0)/C(\infty)$ in equation 3.28 equals $N_t/2N_d$ and allows, in principle, to determine the trap concentration. However one should keep in mind that a few

assumptions (e. g. that all traps were filled prior to emission, emission occurs over the full depletion width, depletion approximation,...) were made and corrections to this basic formula are necessary. The depletion approximation assumes that no carriers are present for $x < x_d$ and $x < x_0$. In fact, the free charge carrier concentration decreases exponentially within the depletion region with the square of the distance from the depletion edge (x_d or x_0) [9]. The transition region where free charge carriers spill over from the bulk into the depletion region is given by the Debye length [9]. The distribution of free carriers near the depletion region is labelled as Debye tail. In reality the defects can be filled up to the intersection of the Fermi level and the defect level (see figure 3.5). This additional filling has its implications on the effective emission region. The regions, x_d-x_r and x_0-x_p, are labelled as transition regions and are indicated in figure 3.6. The region of the emission process goes from x_p to x_r (crossing points of E_{Fn} and E_t and not from x_0 to x_d (depletion widths at V_p and V_r)) (figure 3.6). As the probed emission region by DLTS is not the region between the depletion widths of reverse and filling pulse bias, a correction (by the pulse correction factor $(x_r^2\text{-}x_p^2)/x_d^2$) for concentration depth profiling should be made [7, 10].

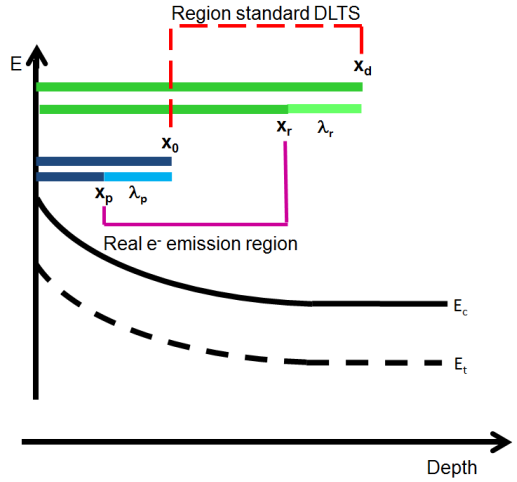

Figure 3.6: Part of a band diagram of a one side diode showing the conduction band edge (E_c and trap level (E_t). The effective region of electron emission is indicated.

During a filling pulse, carriers are captured by a capture rate c_n in the region x_r-x_0. Capture in the transition region x_0-x_p can occur due to the distribution of free carriers in the Debye tail. The capture process will be very slow as the concentration of free majority carriers is lower. For large filling pulse times the slow capture process can occur and can enlarge the amplitude of the capacitance transients [10].

3.3.2.3 Pulse sequences

Conventional minority carrier pulse sequence

To detect the emission of minority carriers (holes for the n-type semiconductor in the chosen example) the same sequence as for the majority carries can be applied, only V_p is larger than zero [5]. First a reverse bias applied. Then minority carriers are injected into the depletion region by a positive forward bias ($V_p > 0$) during a filling pulse time. Hole traps in the n-type material capture injected holes, whereby the positive space charge increases, which results in a decrease of the depletion width and an increase of the capacitance. When the reverse bias pulse is applied again, the captured holes are emitted and the capacitance transient is measured. A decreasing capacitance will result in a negative DLTS signal (by convention, see section 3.3.2.4).

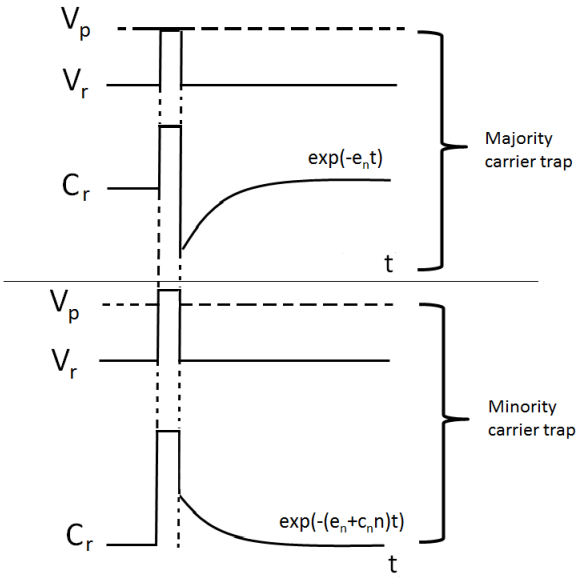

Figure 3.7: Capacitance transients for majority and minority carrier traps.

Complementary majority carrier pulse sequences

For a complementary pulse sequence ($V_p < V_r < 0$) the pulses of the conventional signal are inverted whereby the capture process is now monitored. During the filling pulse at higher negative bias voltage ($V_p < V_r$), the traps can emit their carriers. When the first pulse at lower negative bias is again applied, emptied traps capture the carriers again. For a n-type material the capture of a electron will make the depletion region less positive, whereby the depletion width increases. This results in a decrease of the capacitance. As the capture process does not go infinitely fast, the depletion width is smaller compared to the width at the first applied voltage V_r, the capacitance will thus be higher than C_r at the beginning of the transient.

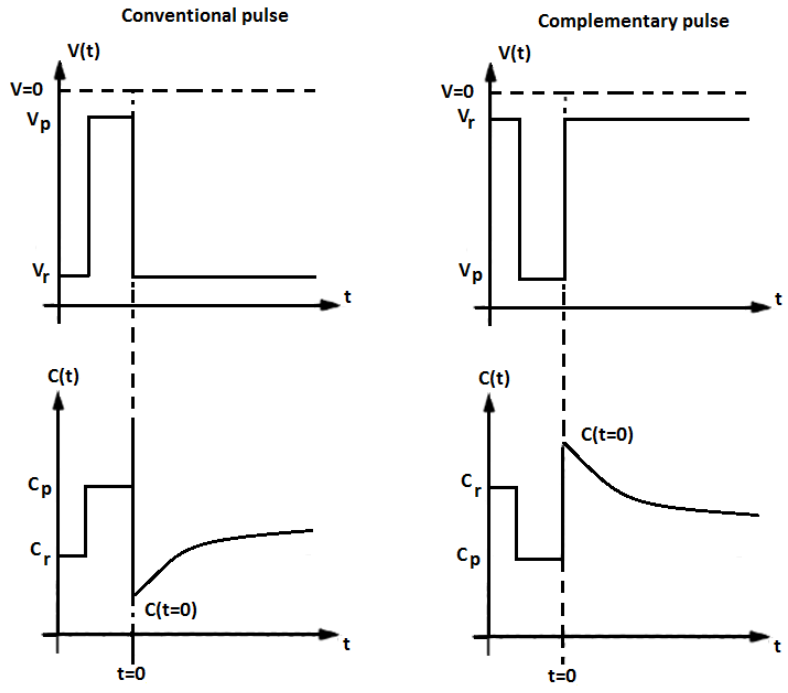

Figure 3.8: Time and capacitance evolution for conventional and complementary pulses.

3.3.2.4 Filter functions

Double boxcar method

Before DLTS was proposed, the usual process to study deep levels was by monitoring carefully some capacitance transient at a fixed temperature after a voltage pulse was applied. This was very time consuming, as a very detailed measurement of the capacitance transient was needed [184]. D. V. Lang proposed the DLTS method in 1974 and reasoned that monitoring the capacitance change yields the emission rates which are a function of temperature (equation 3.17). He proposed to monitor the change of the capacitance at two fixed times (t_2-t_1 = t_w, window time) as a function of temperature [52,184]. By varying the temperature, the decay time constant is changed. This includes that by measuring a repetitive capacitance versus window time at different temperatures, a peak will appear in the ΔC versus temperature plot. This time window concept is illustrated in figure 3.9. When the temperature is low, the transient is slow. As the capacitance does not change much, ΔC = C(t_2)-C(t_1) is very small. As the temperature is increased, the decay rate of the transient increases (equation 3.17) which causes an increase in ΔC. The signal increases with temperature until the transient decays so fast that most of the decay occurs before t_1 and ΔC is again zero. Upon increase of temperature, a peak in ΔC thus occurs.

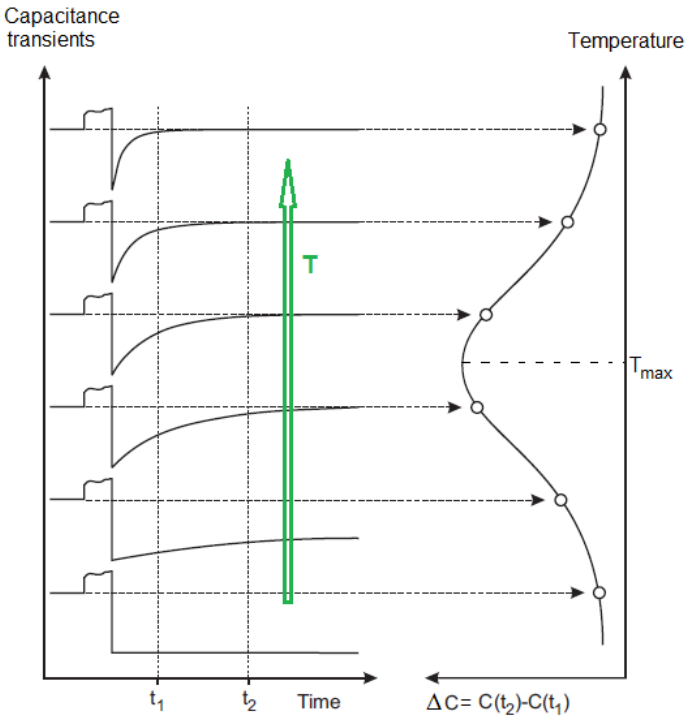

Figure 3.9: Left: several capacitance transients of a trap at different temperatures. Right: ΔC as function of temperature shows a maximum [52, 186].

To describe the capacitance signal in figure 3.9, Lang proposed to monitor the temperature dependent signal S [184]

$$S(T) = \frac{C(t_1) - C(t_2)}{\Delta C(0)}$$

whereby ΔC(0) = C(t_1)-C(∞) is the change in capacitance between the initial state (at time t_1 after the filling pulse) and final state, after a very long time such that the capacitance has reached a constant value. In exponential terms this equals

$$S(T) \sim exp\left(\frac{-t_1}{\tau}\right) - exp\left(\frac{-t_2}{\tau}\right)$$

The above equation exhibits a maximum at a certain temperature (T_{max}). Differentiating this equation with respect to τ and setting the result equal to zero gives τ_{max}:

$$\tau_{max} = \frac{t_2 - t_1}{\ln(t_2/t_1)} = \frac{1}{e_n} \tag{3.31}$$

For other values of t_1 and t_2, the maximum of the peak occurs at different temperatures because of the temperature dependence of the emission rate. To obtain several data points (T_{max}, τ_{max}) one needs to run the sample through several temperature sweeps, each sweep corresponding to a different value of the rate window. One temperature sweep results in one DLTS peak with maximum at that temperature where the emission constant is given by equation 3.31. This set of data (T_{max}, τ_{max}) can be used to obtain an Arrhenius diagram.
The choice whether one looks at the capacitance difference $\Delta C = C(t_1)$-$C(t_2)$ or the opposite $\Delta C = C(t_2)$-$C(t_1)$ is arbitrary. If $\Delta C = C(t_1)$-$C(t_2)$ then majority carrier emission, which gives increasing exponential transient, leads to a negative ΔC and hence negative DLTS spectrum. If $\Delta C = C(t_2)$-$C(t_1)$ then the spectrum is positive for majority carrier emission as ΔC is positive. In the DLTS studies performed for this thesis, the later definition is followed: a majority emission (increasing signal) results in a positive DLTS spectrum.

Fourier transform DLTS
The double boxcar method explained in the previous section is only one example of a correlation technique in which the weighing function w(t) is multiplied to the capacitance signal C(t) and the resulting signal is integrated over time [187]. The weighing function for a double boxcar is the sum of two opposite Dirac delta functions separated in time. A general expression for the filtering is written as

$$S(t) = \int_0^{t_w} C(t)w(t)dt$$

The original DLTS set-up as ascribed by Lang used a boxcar averager to detect the maximum change of the exponential decay for a given window time. Due to the advances in computer technology, most of the modern DLTS techniques include digitizing the whole capacitance waveform and storing it electronically for further data analysis [188]. Different kinds of filter functions can be used after the measurement [10]. An alternative to the boxcar integrator, can be the use of a lock-in amplifier, whereby the transient signal is convoluted with a sine wave (weighing function) of a fixed frequency. In this case essentially the same occurs as for the boxcar averager but the lock-in uses the complete signal and hence is less sensitive to noise, which leads to an improved signal-to-noise ratio [187]. The boxcar method of Lang and the lock-in amplifier weighting function are shown in figure 3.10.

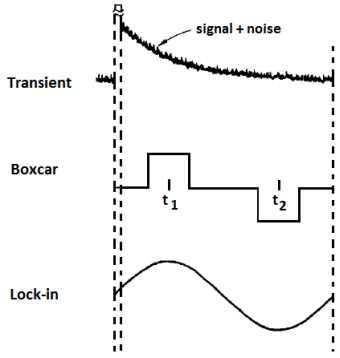

Figure 3.10: Comparison of capacitance signal and boxcar rate window operation [187].

The Fourier transform analysis, which maps a function of time into a function of frequency, is used in this thesis and will be discussed underneath. The method is developed by Weiss and

Kassing in 1988. The capacitance transient can be written as

$$C(t) = A\, exp\left(-\frac{t+t_0}{\tau}\right) + B \tag{3.32}$$

The time t_0 is the 'dead time', the time between the end of the filling pulse and the start of the measurement of the transient. The transient C(t) is determined in the time interval $t \in [0, t_w]$. The capacitance transient in equation 3.32 can be written as a Fourier series:

$$\begin{aligned} C(t) &= \frac{a_0}{2} + \sum_{n=1}^{\infty} [a_n cos(n\,\omega\,t) + b_n sin(n\,\omega\,t)] \\ \text{with} \quad \omega &= \frac{2\pi}{t_w} \end{aligned}$$

The continuous analytical Fourier coefficients a_n and b_n can be written as:

$$a_n = \frac{2}{t_w}\int_0^{t_w} C(t) cos(n\,\omega\,t) dt \quad n = 0, 1, 2, \ldots \tag{3.33}$$

$$b_n = \frac{2}{t_w}\int_0^{t_w} C(t) sin(n\,\omega\,t) dt \quad n = 1, 2, 3, \ldots \tag{3.34}$$

If one looks carefully at the above equations, it is clear that the coefficients can be regarded as a transient signal weighted with a sine or cosine function. The Fourier coefficients a_n and b_n can be calculated following equation 3.34 for the capacitance transient in equation 3.32 as

$$\begin{aligned} a_n &= \frac{2A}{t_w} exp\left(-\frac{t_0}{\tau}\right)\left[1 - exp\left(-\frac{t_w}{\tau}\right)\right]\frac{n\omega}{1/\tau^2 + n^2\omega^2} \\ b_n &= \frac{2A}{t_w} exp\left(-\frac{t_0}{\tau}\right)\left[1 - exp\left(-\frac{t_w}{\tau}\right)\right]\frac{1/\tau}{1/\tau^2 + n^2\omega^2} \end{aligned} \tag{3.35}$$

From coefficient A, which represents the total amplitude of the transient, the concentration of deep levels N_t can be determined following equation 3.28. The carrier emission or capture time constant can be evaluated from the ratios of two Fourier coefficients [10].
In practice the continuous transient C(t) is not known, only a discrete number of data points is known. The analog C(t) transient is discretized after the 'dead time' by the analog-to-digital-converter in the capacitance meter. N capacitance values ($C_0, \ldots, C_N$) are obtained by sampling the C(t) curve at N different values of time. The time between two capacitance points is the sample-interval (Δt). The total period can be written as $N\Delta t$. In the performed experiments N = 512. If the signal to be analysed is a discrete function of time, discrete Fourier transform is used. When the beginning of the transient (C_0) is not equal to the end of the measured transient (C_N), the discrete Fourier transform is defined as

$$F_n = \frac{C_0}{2} + \sum_{k=0}^{N-1} C_k \frac{exp(-2\,\pi\,i\,n\,k)}{N} + \frac{C_N}{2} \quad n = 0, 1, 2, \ldots, N-1$$

The relation with the continuous Fourier transform is: $F_n = N\ C_n$. Due to a digitization, the whole transient can be saved during the measurement and different filter functions can be applied during the maximum evaluation afterwards (e.g. double square lock-in, different boxcar filters, ...). The DLTS software used in this thesis includes 28 filter functions (listed in reference [10]). These filter functions have different characteristic decay times determined by shape of the function and time window which is applied [10]. Due to the different filter functions, the number of points on the Arrhenius diagram is enlarged. An overview of the functions is reported

in reference [10].

The coefficients in equation 3.34 are rarely calculated for a very large number of orders (1,...,n). It is usually and safely assumed that the transient is comprised of only low frequencies superimposed on the high frequency noise signal. Moreover, the amplitude of the coefficients decreases with increasing order. As greater amplitude most of the times also entails better signal to noise ratio, calculating of only the first few lower order coefficients suffices [188].

3.3.2.5 Practical considerations for isothermal and temperature scan

In a standard DLTS measurement the temperature is varied while the time window is kept constant. The temperature scan is illustrated in figure 3.11(a). As the time window decreases, the peak shifts towards higher temperature. In an isothermal scan (also called frequency scan) the time window is varied while the temperature is kept constant (figure 3.11(b)). The peak shifts towards smaller time window as the temperature at which the scan is performed, increases. When very deep defects are present, large window times or high temperatures should be chosen to detect the maximum on the DLTS spectrum when a temperature scan is applied. In practice window times larger tan 1 or 2 seconds are not feasible and temperature can be limited by the sample itself (e.g. like for solar cells) or by the cryostat. An isothermal scan can therefore more easily detect the maximum signal related to deep defects as large window times can be applied.

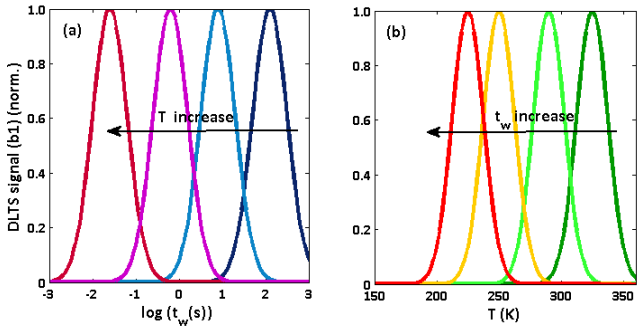

Figure 3.11: a) isothermal scan, b) temperature scan.

By applying during a temperature scan a sequence of complementary pulses (described in section 3.3.2.3) it would in principle be possible to observe the capture rate. This method is however not practically feasible as the capture rate is much larger than the emission rate as indicated in reference [7]. As the electron capture rate is written as $c_n = \sigma_n \cdot v \cdot_{th,n} \cdot n$ (equation 3.1) the capture rate could be estimated around 10^8-10^9 s^{-1}, assuming σ_n around 10^{-12} - 10^{-15} cm^{-2} [6, 11, 12], n around 10^{15} - 10^{16} cm^{-3} [12] and $v_{th,n}$ around 10^7 cm s^{-1} (around 300 K) [6, 12, 13]. The capture rate is thus much larger than the emission rate and cannot be adjusted easily by changing the doping density [7]. This large capture rate includes that at the temperature where emission is measured the capture process is much too fast to be measured using standard DLTS equipment [7, 14]. In order to measure a capture transient, temperature should be very low. Hence the time window for emission would be very long and be limited by the practically feasible maximum measurement time window [14]. As the capture rate is very large, isothermal complementary measurements cannot monitor the capture signal (time window restricted to minimum of around 1 ms). The most common method of studying carrier capture is to perform isothermal conventional (emission) DLTS measurements as a function of filling pulse duration. By analysing the amplitude of the signals as a function of filling pulse, information about capture cross section can be obtained [7, 14].

As described in the preceding, it is in practice impossible to measure capture rates by the DLTS method as these are too fast. However as shown in section 3.3.2.2 slow capture processes can occur for free carriers near the edge of the depletion region (Debye tail). Due to this process, the amplitude of the complementary signal increases as temperature decreases in a temperature scan. The maximum in the complementary signal arises because the emission process also plays a role. The time constant during the measurement of the complementary capacitance signal is dependent on the capture rate as well as on the emission rate ($1/\tau = e_n + c_n$) as carriers can also be thermally emitted from the defects. With decrease of temperature during the complementary measurement, less defects will emit their charge carrier, which lowers the possibility of the slow capture process on the defects as these remain filled. The peak in the complementary signal is hence invoked by a combination of emission and slow capture process.

3.3.2.6 Set-up

Temperature dependent DLTS measurements are performed using a Phystech Fourier Transform-DLTS setup (Phystech FT1030) in combination with a Boonton 72B capacitance bridge. The capacitance is measured at a fixed frequency of 1MHz. FT-DLTS analysis is performed on the digitized capacitance transients. The sample is mounted in a He contact gas cryostat and the temperature can be varied between 4 and 310 K. Two coaxial cylinders form the cryostat. The inner chamber contains the sample holder and is filled with He as contact gas (pressure 750 mbar). In the outer cylinder there is a spiral tube, which is in thermal contact with the inner chamber. Through this outer cylinder helium or nitrogen is pumped. The outer chamber is pumped vacuum (10^{-5} mbar) by a combination of rotation- and diffusion pump. The temperature is measured with a Si diode (Lakeshore DT-470) temperature sensor which is located next to the sample stage, and regulated with a temperature LakeShore 331 control unit.

3.3.3 Admittance spectroscopy

3.3.3.1 Measurement

Admittance measurements on solar cells are commonly interpreted as if the admittance $Y(\omega)$ consists of a parallel connection of a frequency dependent capacitance $C(\omega)$ (imaginary part) and conductance $G(\omega)$ (real part).

$$Y(\omega) = G(\omega) + i\,\omega\,C(\omega)$$

The real and imaginary components of the current response to a sine voltage signal are related to each other via the Kramers-Kronig relation [12, 185]. The analysis of the capacitance and conductance is equivalent, however the evaluation of the capacitance data has become customary [13]. The conductance term in a pn-junction is due to series and parallel resistances, the capacitance arises from the depletion layer in the device (equation 3.21) [185]. The solar cell can be simplified by the following circuit diagram: the sample has a bulk capacitance (C_p) parallel with the bulk resistance (R_p) and in series with a series resistance (R_s). The latter is generally very small and can be neglected.

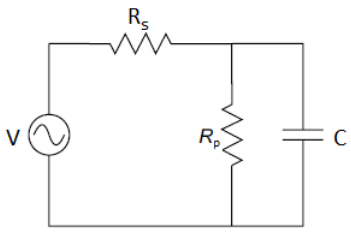

Figure 3.12: Equivalent circuit model for the solar cell device [5].

When a small ac voltage with amplitude V_{ac} and angular frequency (ω) is applied to the sample [5, 185]

$$V = V_{ac}\, exp(i\omega t) = V_{ac}(cos(\omega t) + i\, sin(\omega t))$$

the current response can be written as

$$I = \frac{V}{R_p} + C\,\frac{dV}{dt} = \frac{V_{ac}}{R_p}\, cos(\omega t) - V_{ac}\,\omega C\, sin(\omega t)$$

From the equation above it is clear that the linear current response can consist of both a component in phase with the applied voltage, and a component that is 90° out of phase. By the use of a lock-in amplifier, the capacitance component of the current response can be determined.

3.3.3.2 Analysis

Measurement of the sample admittance as a function of applied ac frequency and temperature is termed admittance spectroscopy (AS). The emission rates (equations 3.16 and 3.15), which define a characteristic time for a defect to emit charge to and capture charge from the valence or conduction band, impose a frequency limit on the ability of the defect to 'follow' an ac-voltage perturbation at a particular temperature. In AS the frequency (or temperature) is swept to cross this transition frequency.

Defect response

When the frequency is too high ($\omega > \omega_0$), the deep defect cannot adapt its ionization state and does not contribute to the measured capacitance. When the frequency is low enough, defect states with emission rates $\omega < e_{n,p}$ respond to the applied ac voltage and contribute to the measured capacitance. The limit for which a defect can be charged and discharged by the ac modulation is denoted as the characteristic frequency ω_0 (figure 3.13). The response comes from the region in the sample where the quasi-Fermi level at the bias voltage crosses the energy level of the defect. At the position where the quasi-Fermi level crosses the energy of the defect state, the defect charging and discharging will be most efficient. The occupation of a defect level at this position can thus be modulated by the frequency which results in a capacitance change. The contribution of a single defect level to the capacitance is given by [5, 6, 62]

$$C(\omega) = C_{hf} + \frac{1}{1+\omega^2\tau^2}(C_{lf} - C_{hf})$$

where C_{hf} is the depletion capacitance and C_{lf} is the depletion capacitance enhanced by the contribution of the deep defect. The difference (C_{lf} - C_{hf}) is the capacitance of the defect response [6]. A non step like C-f behaviour is an indication of the presence of more traps or a distribution of traps [62]. The characteristic frequency (ω_0) can be derived from the a maximum in the plot $-\omega \cdot dC(\omega)/d\omega$ versus ω (differential capacitance) as illustrated in figure 3.13 [5, 12].

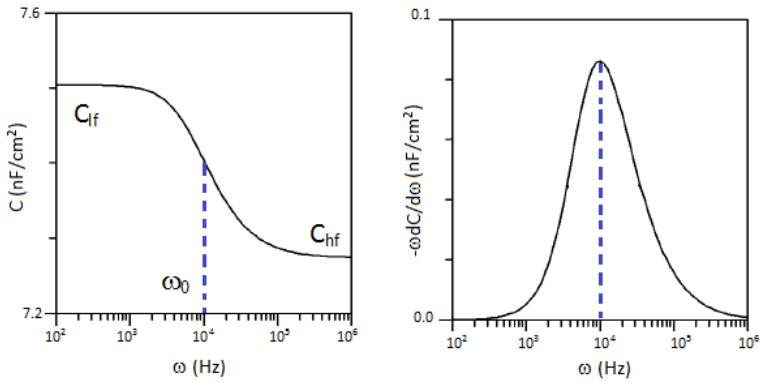

Figure 3.13: Capacitance frequency measurement. The characteristic frequency ω_0, indicated on the left, corresponds to the maximum of the derivative on the right [12].

ω_0 is related to the emission time constant τ by [6, 7, 105]

$$\omega_0 = 2e_{n,p} = 2c_{n,p}N_{c,v}\ exp\left(\frac{-E_a}{kT}\right) = 2\,\nu_0\ exp\left(\frac{-E_a}{kT}\right) \tag{3.36}$$

The factor 2 stems from the fact that in admittance spectroscopy the signal is measured at the depletion edge and capture as well as emission processes are probed. As the level E_t equals the Fermi level, e_p equals $c_p p$ for a p-type semiconductor. The time constant ($\tau = 1/(e_p + c_p p)$) can then be written as $\tau = 1/(2 \cdot e_p)$. In DLTS the capacitance is measured at a reverse bias voltage, a depletion region without free carriers is present. Capture processes can be neglected and $\tau = 1/e_p$ for a p-type semiconductor.
ν_0 in equation 3.36 is the attempt to escape frequency and equals $N_{c,v} v_{th} \sigma_{n,p}$. As $v_{th} \propto T^{1/2}$ and $N_{c,v} \propto T^{3/2}$ the pre-exponential factor is proportional to T^2 [6]. In literature one can also find the relation $\nu_0 = \xi_0 T^2$ whereby ξ_0 is labelled as the attempt to escape frequency [11].
The graph of $-\omega dC(\omega)/d\omega$ versus ω can be transformed into the defect density N_t as a function of energy. An analytical model which takes into account a distribution of defects in the semiconductor was developed by Walter et al. [189]. According to this model the defect density $N_t(E)$ at a certain energetic position E_a can for a pn^+ diode with parabolic band bending be calculated by (with C the capacitance per area)

$$N_t(E_a) = -\frac{2V_{bi}^{3/2}}{W\sqrt{(q(qV_{bi} - (E_{f\infty} - E_a)))}}\frac{\omega}{kT}\frac{dC}{d\omega} \tag{3.37}$$

whereby $E_{f\infty}$ indicates the position of the Fermi energy in the bulk, V_{bi} the built-in potential and W the depletion width. Because bulk defects are broadly distributed in space but show a narrow energy distribution, the characteristic frequency does not change as the applied bias changes. This is not the case for interface defects as these are discrete in space and most of the time have a broad energy distribution. A change of the applied bias results for defects at the interface in a change of the characteristic frequency [6]. The emission rate of electrons is expected to decrease at negative bias due to an increased energetic distance between the quasi-Fermi level and the band edge [190].

Dielectric freeze-out response

At low temperatures and/or high frequencies, it is possible to freeze-out the ac-response from all the defects as well as from the shallowest dopants in the device. In this regime there is no time for carriers in the bulk (undepleted absorber) to move to the modulated depletion edge in response to the applied voltage. Information about the dielectric carrier freeze-out of majority carriers (which include mobility changes) and series resistance changes can be measured. When the frequency exceeds the dielectric carrier response frequency ($\omega_D = \sigma/\varepsilon_r\varepsilon_0$, with σ the conductivity,

ε_r the relative permittivity and ε_0 the vacuum permittivity), the whole semiconductor behaves as a dielectric, and the capacitance converges to the geometric capacitance $C_{geo} = \varepsilon_r \varepsilon_0 A/t$, with t the thickness of the absorber and A the area of the cell [5, 191]. The capacitance measured under these conditions comes entirely from the geometry of the device. For frequencies below ω_D the semiconductor behaves as a conductor and the depletion capacitance is measured.
In reference [192] the semi-neutral portion of the absorber over a distance t-W, (with W the depletion region width) is modelled by the equivalent circuit of a parallel connection of bulk conductance G_g and a geometrical capacitance C_g. The total capacitance of the n^+p solar cell is modelled by a series connection of the depletion capacitance ($C_d = \varepsilon_r \varepsilon_0 A/W$) and the capacitance of the quasi-neutral region (parallel connection of C_g and G_g). The characteristic frequency (ω_0) at which the capacitance exhibits a step due to dielectric relaxation of the absorber, is given by [192, 193]

$$\omega_0 = \frac{W}{t}\frac{\sigma}{\epsilon}$$

The characteristic frequency is voltage dependent due to its dependence on the depletion width. As $W \propto (V_{bi}\text{-}V)^{1/2}$ the characteristic frequency shows a red-shift as V increases towards forward bias [192]. As the conductivity can be expressed in terms of the product $q\mu_h p$ (where q, p and μ_h are the elementary charge, the free hole density and hole mobility, respectively), the characteristic frequency, and hence freeze-out exhibits thermal activation due to combined contributions from mobility and carrier concentration. Following equation for the characteristic frequency is obtained [193]

$$\begin{aligned} \omega_0 &= \frac{W}{t}\frac{\sigma}{\epsilon} \\ \omega_0 &= \frac{W}{t}\frac{q\,\mu_h\,N_v\,exp((E_v - E_{Fp})/kT)}{\epsilon} \\ \omega_0 &= \xi_0 T^m exp(-E_a/kT) \text{ with } E_a = -(E_v - E_{Fp}) \end{aligned} \tag{3.38}$$

Here k is the Boltzmann constant, T is the absolute temperature, N_v the effective density of states in the valence band and E_a the energy distance between the shallow acceptor defect level (on which carrier freeze-out occurs) and the valence band. From equation 3.38 it follows that the activation energy E_a of the intrinsic shallow acceptor defects can be measured in the step at lowest temperatures. E_a can be extracted from the plot ω_0/T^m versus 1/kT (Arrhenius diagram). The exponent m results from the temperature dependence of the effective density of states ($N_v \propto T^{3/2}$) and the temperature dependence of the mobility. In case of impurity scattering ($\mu_h \propto T^{3/2}$ [4]) the exponent m equals 3.

When the absorber is entirely depleted ($\omega > \omega_D$), the capacitance becomes voltage independent and approaches the geometrical capacitance [12,191]. The dielectric carrier freeze-out of majority carriers can thus be distinguished from other capacitance steps by its independence of applied bias on the high-frequency side of the step [191–194] as shown in figure 3.14.

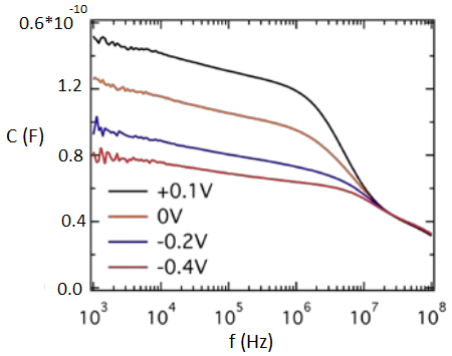

Figure 3.14: C-f measurement of a CIGS solar cell measured under various biases [194]. At high frequency a bias independence is visible.

3.3.3.3 Set-up

Temperature dependent capacitance-frequency (C-f) measurements were performed with an Agilent meter (in collaboration with CoCooN, research group of department of Solid State Sciences at Ghent University) and carried out in a contact gas cryostat cooled with liquid helium (see description in section 3.3.2.6). The superimposed small ac signal voltage used for probing the actual capacitance at the given bias had an amplitude of 30 meV.

3.4 Literature overview CIGS

Although capacitance profiling is a standard technique for determining carrier concentration and distribution of defects in the absorber layer, the interpretation of the results is not straightforward and is an object of discussion. CIGS solar cells have been found to exhibit two distinct responses [12, 15], originally attributed to defects. The first feature has an activation energy E_a around 100 meV, the second is a deeper defect state contribution, with an activation energy E_a around 250-300 meV. The first signal is labelled in accordance with references [15, 190] as N1, the second as N2.

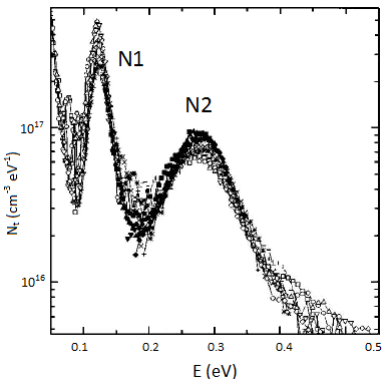

Figure 3.15: Density of states derived (assuming defect distributions in the bulk) from admittance spectra of a $CuInSe_2$ cell (f = 0.4-400 kHz, T = 80-320 K (ΔT = 10 K)). The defect distributions at different temperatures are superimposed [190].

N2

The N2 signal is a broad peak which is seen at high temperatures (250-300 K) as illustrated in figure 3.15. The signal has been assigned to a broad hole trap defect distribution in the bulk of the absorber layer [6, 190]. In reference [195] it was shown that the concentration of these hole

traps is inversely proportional to the solar cell efficiency. An inverse relation between the N2 density and V_{OC} was indicated. The defect levels can thus be considered as major recombination centres. In reference [196] it was demonstrated that an N2-like signal can, at least in part, also be produced by a non-Ohmic contact in the solar cell structure.

N1

In contrast to the N2 signal, the N1 peak is much narrower (figure 3.15). A corresponding relatively narrow peak is also found in DLTS measurements shown in figure 3.16. The identification of the N1 signal has been a subject of controversy because of its unusual features which lead to different interpretations. A short overview of the unusual features and models is given below.

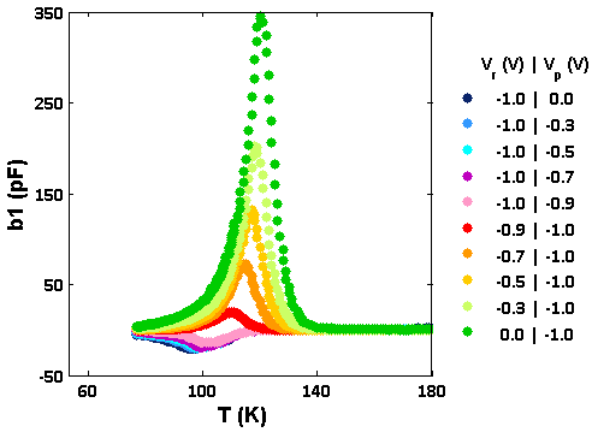

Figure 3.16: N1 signal measured in DLTS measurements with varying applied biases (t_w= 0.005 s, t_p = 0.500 s).

- **N1 unusual features**
  In air annealing experiments, the activation energy of N1 was observed to change in admittance measurements. The corresponding Arrhenius plots are very often non-linear which suggests that the calculated trap parameters are far from their true values. For conventional bias pulses, the DLTS signal is negative as visible in figure 3.16. Further the time constants of the signals are dependent on the bias pulses and the intensities of the signals for complementary and conventional pulses are not equal [12].

- **N1 models**
  A) Interface defect In a repetitive air annealing admittance experiment, the activation energy of the N1 signal increased as the annealing time increased [88]. It is difficult to explain the continuous shift deeper into the band gap by a bulk defect, this rather points to interface states. Oxygenation leads to passivation of Se vacancies at the CIGS surface and air annealing results in a decrease of Cu concentration at the absorber surface [88]. This theory of a minority carrier interface trap (electron trap) is also supported by the negative sign of the DLTS signals. One difficulty when explaining N1 as a (close to) interface defect, is that its properties remain the same independent of the buffer and buffer depositing technique. This implicates that N1 is neither related to the buffer material nor to a modification of the hetero-interface during the CBD process. As a consequence the electron trap should not be related to the CIGS interface [190].

  B) Bulk defect: acceptor or donor type In admittance measurements with applied reverse bias, no change in the energetic position for the N1 peak was seen. This is a characteristic

of a bulk defect [190]. In reference [197] drive level capacitance profiling (DLCP) and capacitance voltage profiling is used to study the N1 signal. DLCP is quite analogous to C-V profiling. In DLCP the amplitude of the ac voltage is varied whereby the trap density is provided more directly [5]. Since DLCP is quite insensitive to any interface response, the signal was interpreted as a hole trap (acceptor trap). The variation of the activation energy over different samples as well as the negative sign in DLTS can however not be explained in this model. Moreover to detect a bulk trap, the level should have an intersection with the quasi-Fermi level. To detect a level of 50 meV (sometimes low activation energy for N1), a very high doping density would be necessary [12]. In reference [198] the N1 signal is attributed to one of the two charge states of the In_{Cu} compensating donors in the bulk of the absorber.

C) Type inversion or Fermi level pinning The absence of a shift of the activation energy for AS measurements at reverse and zero bias can be explained by a continuous distribution of electron traps at the absorber surface whereby the Fermi level is pinned at the interface or by type inversion at the interface [12]. The activation energy represents the position of the pinned electron Fermi level. In annealing experiments, a shift in the pinning of the Fermi level can occur which alters the activation energy seen in the annealing experiments [12]. In experiments in which the buffer layer thickness was changed, it was proposed that the defects states are located within the n-type inverted region [190] and that the N1 signal is part of the ordered defect compound layer. Following reference [110] the signal corresponds to compensating In_{Cu} donor levels close to a n-type inverted CdS/CIGS interface region.

D) Hopping conduction In reference [199] it is suggested that hopping conduction in CIGS at low temperature leads to the observed response in the C-f measurements.

E) Back contact Arguments against defect response via admittance spectroscopy and DLCP measurements are given in reference [15] and discussed first. Thereafter the arguments of references [14, 200] based on DLTS results are described.

→ AS: In the general case of a pn-junction, the capacitance extends over the whole depletion width in n- and p-type semiconductor $C = \varepsilon_r \varepsilon_0 A/(x_n + x_p)$. The dependence on the step height in admittance measurements is thus expected to be partly dependent on the SCR width at the n-side of the pn-junction and hence on the thickness of the buffer layer. In the models of a defect contribution at or close to the absorber/buffer interface C_{Hf} equals $\varepsilon_r \varepsilon_0 A/(x_n + x_p)$ (for $\omega > \omega_0$) and reflects the contribution of the n- and p-side SCR widths whereas C_{Lf} equals $\varepsilon_r \varepsilon_0 A/x_p$ (for $\omega < \omega_0$) and is thus determined only by the SCR width of the absorber such that

$$\Delta x = (x_n + x_p) - x_p = \epsilon_r \epsilon_0 A \left(\frac{1}{C_{Hf}} - \frac{1}{C_{Lf}} \right)$$

Δx should directly yield the thickness of the (expected depleted) buffer layer. In the admittance experiments, thin-film solar cells with different CdS buffer layer thickness (0-160 nm), with an In_2S_3 buffer or with a Schottky barrier junction, all show the characteristic admittance N1 step at shallow energies (40-160 meV). The samples with In_2S_3 buffer or with a Schottky barrier junction have strongly altered interface properties compared to the CdS/CIGS interface which would lead to different response in case of interface defects. No correlation between the buffer layer thickness and the capacitance step was found (figure 3.17). Hence a model of involving interface defects can ruled out.

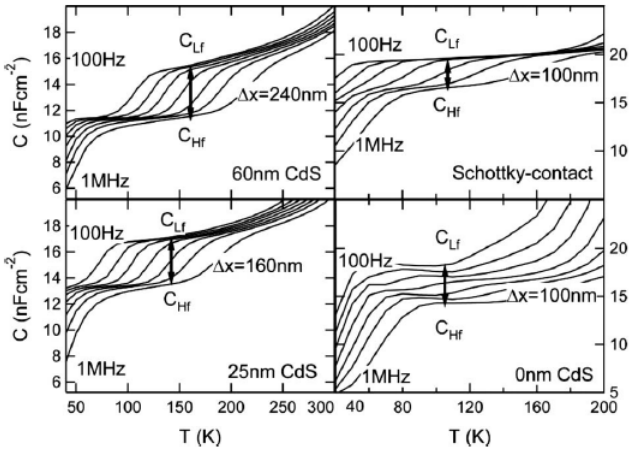

Figure 3.17: N1 step in the admittance spectra as function of temperature for cells with different CdS thickness and for a Schottky contact [15].

→ DLCP: measurements have been performed at frequencies just below (carrier and defect concentration are measured) and above (only free carrier concentration is measured) the N1 resonance frequency at a certain temperature. The profiling density did not change for the different frequencies indicating that the N1 admittance signal is not related with a bulk defect.

→ DLTS: The DLTS signals obtained by applying conventional and complementary pulses with varying height of the pulses exhibits certain characteristics which allow to rule out a defect response as the origin of the signals [14,200]. Figure 3.16 shows that for conventional pulses ($V_r < V_p < 0$) the DLTS signals are negative and converge to each other as ΔV (= V_r-V_p) decreases. A negative DLTS signal occurs a result of a decreasing capacitance due to an increase in depletion width. The later is in a p-type semiconductor the result of a smaller negative charge density in the depletion region which can occur in case of emission of electrons (a) or capture of holes (b).

(a) The emission of an electron is ruled out because

- the maximum of the conventional signal lies at lower temperature than the maximum of the complementary signal. This would imply that the emission process is faster than the capture process. This leads to a contradition as the emission time constant for a defect ($1/e_n$) is always larger than the capture time constant ($1/(e_n+c_nn)$) (with c_n capture coefficient [200]).

- the capture rate (e_n+c_nn) is always larger than the emission rate (e_n) (in fact always larger than $2e_n$) the complementary and conventional signals should not converge to each other as the pulse height ΔV decreases. For a defect level a clear difference between the time constants of these signals is visible independent of ΔV.

(b) The process of hole capture is not likely as it requires a higher hole concentration at V_r than at V_p which is not expected.

Other arguments against capture or emission by defect levels are:
- the intensities of capture and emission peaks are not equal.
- it is not straightforward to see capture and emission process just by changing the order of the pulses. At the temperature where emission occurs, the capture is usually too fast to be measured. Capture can only be seen in the slow capture regime (capture at edge of depletion region [10]). At low temperature the capture process could be seen, but the

emission process is then too slow to be measured as well.

From the results and discussions in references [14, 15, 200] it follows that the N1 signal cannot assigned to a deep level in the band gap of the material. The above features can be explained by a barrier (ϕ_{BC}) in the solar cell structure as proposed in reference [15]. The band diagram which includes a non-Ohmic back contact (according to [15]) is presented in figure 3.18(a). The Schottky contact at the back contact gives rise to a depletion region (W_{BC}). W_J is the depletion width of the main junction.

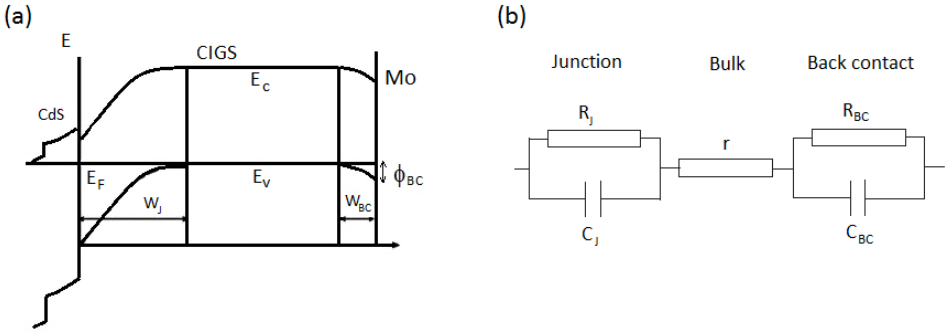

Figure 3.18: (a) Band diagram of a CdS/CIGS/Mo structure with back contact barrier. The barrier height at the back contact is ϕ_{BC} [15].
(b) Equivalent circuit of thin-film solar cell [200].

The assumption of a non-Ohmic back-contact at the Mo/CIGS interface is also followed and successfully modelled in references [14,200]. It is shown that depending on the back contact properties, positive or negative DLTS signals can occur [14]. The analytical calculation to describe the effect of a back contact is based on an equivalent circuit (figure 3.18(b)) which contains only resistors and capacitors. C_J and C_{BC} are the capacitance of the junction and back contact, R_J and R_{BC} the shunt resistance of the junction and back contact, and r the resistance of the bulk semiconductor. For back contact diodes with $R_J C_J > R_{BC} C_{BC}$ four distinctive properties, which can be related to features of N1, are found [14, 200].

- negative signal for ΔV (V_r -V_p) < 0
- the time constants converge to the same value for $|\Delta V| \to 0$
- the signal for $\Delta V > 0$ has the largest amplitude
- the amplitude scales with $\Delta V \cdot C_r^4$ (for a uniform doping profile).

The experimental result [14] on a model circuit in which the non-ideal back contact is a germanium diode inversely polarized with respect to the main junction is shown in figure 3.19. A negative signal for a conventional ($V_r < V_p < 0$) DLTS pulse is visible.

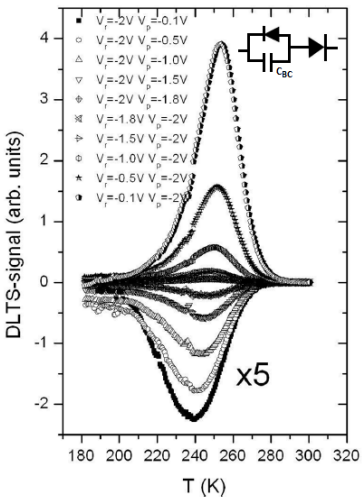

Figure 3.19: DLTS spectrum with reverse polarized diode back contact. The equivalent circuit is indicated op the top right [14].

The DLTS signal of a non-ideal Ohmic contact exhibits thus certain characteristics which allow to distinguish it from that of defects. Modelling in reference [200] has shown that the properties of the N1 signal for CIGS thin-film solar cells follow the properties of DLTS signals for an RC like contact listed above. A change in the time constant of the N1 signal could in this model be explained by the fact that main and back contact junction form a coupled system: the characteristics of the main junction can affect the properties of the observed capacitance transient of the back contact [14].

3.5 Metal-semiconductor contacts

In this thesis the thin-film solar cell was simplified to a metal-semiconductor-metal structure to compare DLTS measurements on these devices with results on complete solar cells. Studying Schottky diodes structures can provide a more elementary method to investigate the intrinsic properties of the absorber layer. In the following Fermi level pinning and current transport mechanisms of a metal-semiconductor (Schottky) contact are discussed. The band alignment in a Schottky devices is described in section A.2.

Barrier height
The band bending at the metal-semiconductor interface establishes a built-in potential or Schottky barrier height ϕ_{b}. According to the Schottky model [3] the electronic transport across the metal semiconductor interface is controlled by this Schottky barrier height. The Schottky barrier height for electrons $\phi_{\mathrm{b}}^{\mathrm{n}}$ is given by [201, 202]

$$\phi_b^n = \phi_M - \chi_S$$

The corresponding hole barrier height $\phi_{\mathrm{b}}^{\mathrm{p}}$ can be written as

$$\phi_b^p = \frac{1}{q}E_g - (\phi_M - \chi_S)$$

with ϕ_{M}, the metal work function which is the difference between vacuum level and Fermi energy. χ_{S} is the electron affinity ($\chi_{\mathrm{CIGS}} = 4.5$ eV [16]). Reported work function values in literature often cover a considerable range depending on the measurement method and surface cleanliness. This makes the calculation of the barrier height not unambiguous. Typical values for the work functions of Au, Al and In are: ϕ_{Au}: 5.10-5.47 eV, ϕ_{Al}: 4.06-4.26 and $\phi_{\mathrm{In}} \sim 4.1$ eV [3, 203, 204].

Fermi level pinning

In practice it appears difficult to alter the barrier height by using metals of varying work functions. The above equations are only valid when the influence of interface states is assumed to be negligible or non-existent. In practice, in most Schottky contacts a large number of interface states is present. These states can be due to dangling bonds, imperfections at the interface and the fact that the crystal lattices of metal and semiconductor do not match up perfectly. Electrical properties of the Schottky device can be altered by the interface states. The insensitivity of the experimental Schottky barrier height to the metal work function is labelled as 'Fermi level pinning' [52, 204, 205]. In the absence of interface states, the depletion charge Q_d in the semiconductor must be equal and opposite to the charge on the metal surface Q_m. Due to a sharp termination of the semiconductor, interface surface levels within the band gap (which can be either donor of acceptor states) are created. In figure 3.20 the continuous distribution of interface states characterised by a neutral level ϕ_0 is depicted. Due to the presence of the interface states, there is an additional charge at the interface, Q_{ss}. The charge neutrality condition becomes $Q_M = (Q_d + Q_{ss})$.

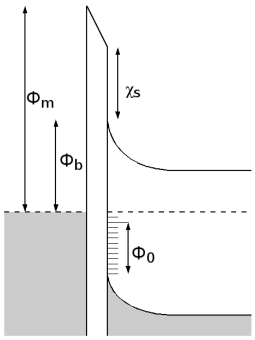

Figure 3.20: A continuous distribution of interface states (characterized by a neutral level ϕ_0) causes the Fermi level to be pinned [201].

During the metal deposition some vacant states have to be filled in order to maintain charge neutrality at the semiconductor surface. Depending on whether the neutral level is above or below the semiconductor Fermi level, the net result will be a reduction or increase in electron Schottky barrier height, respectively. In the limit, when the density of interface states is very high, the barrier is said to be pinned. The barrier height is given by

$$\phi_b = E_g - \phi_0$$

Different metal contacts on chemically etched $Cu(In,Ga)(Se,S)_2$ layers are investigated in reference [206]. The formation of barrier height is found to be independent of the metal work function (Ag, Cu/Au and Au) and the chemical etchant used. The Fermi level is pinned at four specific values above the valence band. Depending on the surface defect concentrations present at the chemically etched surfaces, the Fermi level pinning occurs at one of the dominant deep levels. Oxidizing chemicals enhance the Fermi level pinning at the interface. High barrier heights, in the order of 0.77-1.03 eV were found. Reference [101] confirms that $Cu/CuGaS_2/Au$ Schottky diode junctions were affected by the interface conditions rather than work function of the metals. Furthermore, the Fermi level pinning is dependent on the surface treatment.

Current transport

In metal-semiconductor devices majority carriers are responsible for the current. The majority carriers must surmount the abrupt barrier to contribute to the current (thermionic emission). Other contributions are thermionic field emission (high energy carriers tunnel through the upper part of the barrier) and field emission (carriers tunnel through the barrier at the Fermi level)

presented in figure 3.21. The bias conditions determine which of these components dominate the carrier transport [201, 202, 207].

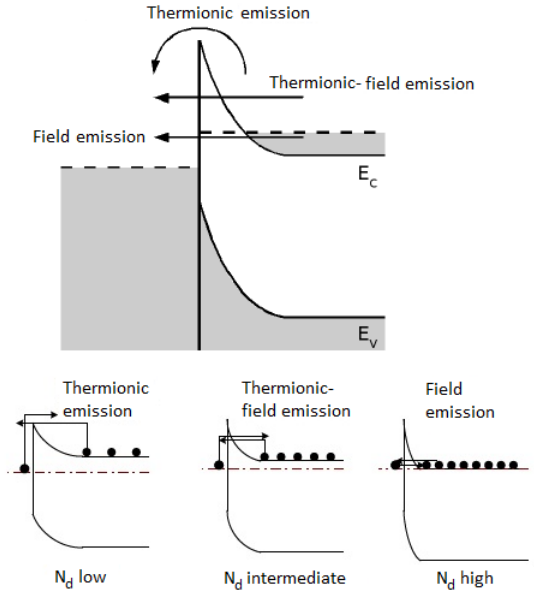

Figure 3.21: Three possible components contributing to carrier transport in a Schottky contact under applied bias [201].

The I-V relationship for a Schottky contact based (with diode area A) on the thermionic emission current theory by Bethe is given by [3] ($q\phi_b >> kT$)

$$I = I_0 \left[exp\left(\frac{qV}{nkT}\right) - 1 \right] \tag{3.39}$$

$$\text{with } I_0 = A^* T^2 A \, exp\left(\frac{-q\,\phi_b}{kT}\right) \tag{3.40}$$

The factor A^* is the effective Richardson constant and can be calculated as $A^* = 4\pi\, q\, m^* k^2/h^3$ (m^* the effective mass, k Boltzmann constant, h Planck constant, q the elemental charge). In reference [36] the effective mass for holes is denoted as 0.71 m_0 and 0.092 m_0 for electrons (m_0 electron mass). If the barrier height is not temperature dependent a so-called Richardson plot (equation 3.41) should yield a straight line [208].

$$ln\left(\frac{I_0}{T^2}\right) = ln(A\,A^*) - \frac{q\,\phi_b}{kT} \tag{3.41}$$

If the barrier ϕ_b is temperature dependent, the barrier is for each temperature calculated directly from the I_0 values by

$$\phi_b = \frac{kT}{q} ln\left(\frac{A\,A^*\,T^2}{I_0}\right) \tag{3.42}$$

Often there is a deviation from the ideal current, therefore a ideallity factor (n) is incorporated in equation 3.39. This factor n takes into account the image-force effect (lowering of the barrier by the electric field produced when an electron is transported across the barrier [209]), tunneling contributions and recombination or trapping at interface states. The barrier height can be extracted from a plot ln(I) versus the applied forward voltage (figure 3.22). If the forward current is extrapolated logarithmically to zero, the intercept at the saturation current I_0 can be revealed. From this the barrier height can be determined when the Richardson constant is known. The ideallity factor can be determined from the slope $\frac{\partial \ln(I)}{\partial V} = \frac{nkT}{q}$.

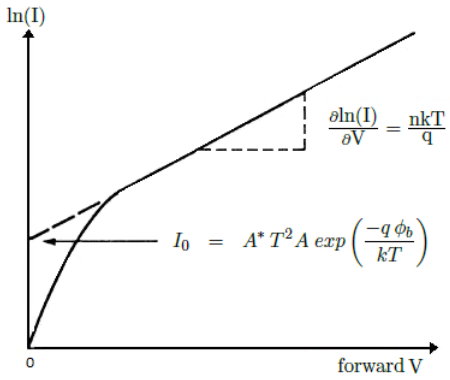

Figure 3.22: Logarithmic plot of the forward current as a function of applied forward bias. Extrapolation to zero bias determines the saturation current I_0 [210].

4 Experimental results of electric defect characterization

Contents

4.1 CIGS: DLTS study on simplified structures

4.1.1 Motivation

As shown in section 3.3.2 information on the characteristics (activation energy, capture cross section) of deep level defects in a semiconductor can be obtained by DLTS measurements via the extraction of the emission rates of deep levels from a transient capacitance signal. The interpretation of the DLTS signals on a thin-film hetero junction solar cell is, however, not straightforward because of three reasons.

- The CIGS absorber has a complex defect structure because a large number of intrinsic point defects and, complexes of these, are possible as demonstrated in section 2.3.1.5.
- There is a possibility of the altering the band diagram by a type inversion or thin oxide layer at the absorber surface. Different models concerning the type inversion are listed in section 2.3.1.3. As the specific band bending around the pn-junction is altered, this can have an influence on the DLTS spectra.
- The thin-film ZnO/CdS/CIGS/Mo hetero junction solar cells consist of a complex layered structure and different interfaces, which make the system far more complicated than the 'ordinary' metal-semiconductor contacts on which the DLTS spectroscopy technique is normally applied.

In this study we aim to eliminate the mentioned problems for the interpretation of the DLTS signals. The first problem cannot be overcome as the defect structure is intrinsic and cannot be changed. However the other problems can, at least in a part, be avoided or altered. In a first attempt to perform a more basic DLTS study, $CuInS_2$ single crystals using the vertical Bridgman growth method were grown. PL investigations did show similar spectra for the $CuInS_2$ crystal and a $CuInS_2$ on Cu-tape thin-film solar cell. After metal evaporation on both sides of the crystal, a structure which is normally measured in DLTS could be obtained. Unfortunately crystal quality was not sufficient to perform DLTS measurements. In a second attempt to avoid the multiple layer structure and to perform a more basic DLTS study, a simplification of the original thin-film solar cell to a metal/semiconductor/metal (M/S/M) structure was made by etching away window and buffer layer and subsequent metal evaporation. Different metals on cells with originally different buffer layers (CdS and In_2S_3) were tested. As an inversion layer can be present at the absorber surface, an additional Br-etch, to remove part of the CIGS absorber layer, was performed. It is assumed that by the Br etch, the surface and hence the barrier height could drastically changed. Further the possible effect of an oxidation layer near the absorber/buffer interface was tested by applying different surface treatments (HF etch, water treatment, glow discharge). The analysis of the Schottky diodes based on thermionic field emission theory (section 3.5) is discussed. The plausible existence of Fermi level pinning will be investigated. In all DLTS spectra shown in the results below, the low temperature signals meet the criteria for a non-ideal contact modelled in references [14, 200].

In reference [15] similar M/S/M structures have been used for admittance spectroscopy. It was found that the admittance responses of cells with different buffer layers and M/S/M structures were similar, despite the strongly modified interface properties. Based on these results the N1 response was attributed to a non-ideality of the back contact by these authors.

4.1.2 Sample preparation

Investigated solar cells The CIGS absorber layers were produced by a three stage co-evaporation process as described in section 2.3.1.9 (different evaporation profiles) on Mo coated soda lime glass substrates. The In_2S_3 buffer layer was deposited by ultrasonic spray pyrolysis [211], the CdS buffer by CBD [145]. On top of the buffer layer an i-ZnO/ZnO:Al window layer and Ni/Al grid were deposited. Complete cells with In_2S_3 and CdS buffer are labelled as $cell_{In_2S_3}$ and $cell_{CdS}$ respectively.
Figure 4.1 represents the composition of the investigated samples by EDX cross section measurement. For EDX analysis a FEI Quanta 200 instrument, equipped with EDAX Genesys 4000 setup was used in collaboration with Lumilab (research group of the department of Solid State Sciences at Ghent University). The characteristic X-rays of Cu_K, Se_L, In_L and Ga_L were monitored at an acceleration voltage of 15 kV. The Ga profile is higher and more pronounced for $cell_{CdS}$. As the composition is not exactly the same, only similar DLTS signals are expected for the two cells. Both cells have a Cu-poor composition.

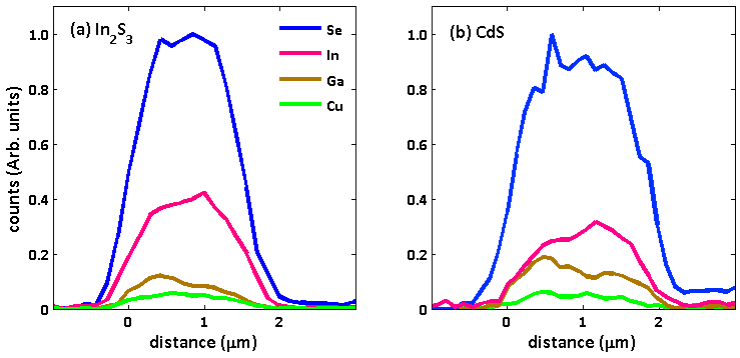

Figure 4.1: EDX cross section of the investigated cells (signal normalised to Se signal). (a) $\text{cell}_{\text{In}_2\text{S}_3}$, (b) cell_{CdS}.

For the HF test another sample ($\text{cell}_{\text{CdS2}}$) which originally had a CdS buffer is used. The composition details of this cell are discussed in section 6.3, where they are of greater importance.

M/S/M preparation Procedures for HCl, Br and HF etches as well as their effect according to literature are described below.

- HCl etch: To remove the grid, window and buffer layer a HCl etch (10% in H_2O) was performed. The samples were rinsed with methanol and deionized water. Direct after this etching the sample was dried by blowing N_2 over the surface. After HCl etch planar EDX measurements were taken to check if the etching of the buffer layer works decently. No traces of Cd or S could be detected as shown in figure 4.2. SEM images show that the surfaces are rather rough.
  Literature reports concerning the effect on composition of a HCl etch are very scarce. In reference [212] it was reported that an etching with HCl can remove surface oxides (Ga and In oxides). In reference [95] an HCl etched sample seemed, from X-ray photoelectron spectroscopy (XPS) measurements, to contain relatively little oxide even after a deionized water rinse and brief air exposure. However residual Cd was clearly detectable in the first one to three monolayers of the surface. The strongly bound Cd atoms occupy Cu sites which could result in a n-type surface inversion layer.

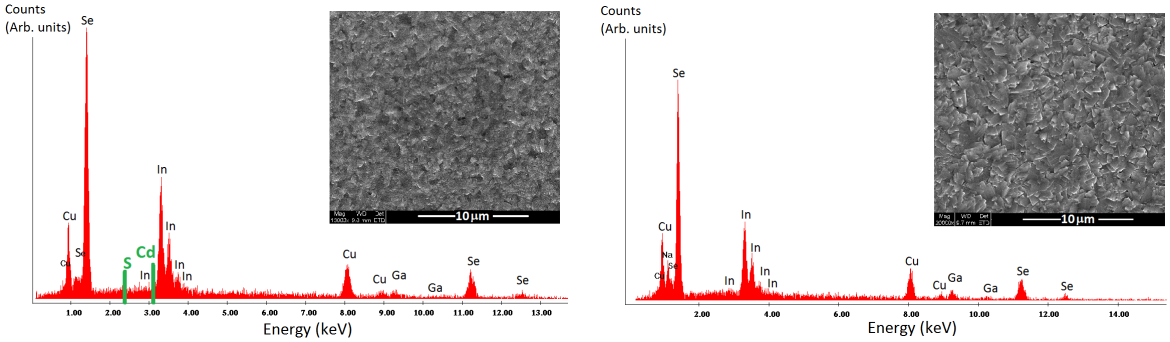

(a) $\text{cell}_{\text{In}_2\text{S}_3}$ (b) cell_{CdS}

Figure 4.2: EDX and SEM (planar) of samples etched in HCl. The positions of Cd_L and S_K are indicated in figure(a).

- Br etch: To asses unambiguously the effect of a type inversion layer, an additional etch was performed using a 0.1 vol% bromine in methanol solution to thin the absorber layer in the Mo/CIGS structure. The duration time of the etch was 35 minutes. In references [212–214] it was reported that due to the Br etch a thin Se^0 layer can be formed on top of the CIGS

surface. References [213,214] report a surface smoothing after Br etching. SEM images in figure 4.3 show the cross sections of sample cell_{CdS} after HCl etch and after Br etch. The initial absorber layer thickness after HCl etch was 2.02 µm, the thickness after Br etching is 1.58 µm which confirm the thinning of the absorber layer. The surface of the Br etched sample is less rough in agreement with references [213,214]. The composition at the surface is altered as can be seen in EDX measurements represented on figure 4.3(b). By thinning the absorber, the Ga profile near the surface is drastically changed: the double-graded Ga profile is no longer observed. An increase of the Se concentration at the surface, as demonstrated in references [212–214], cannot unambiguously be demonstrated by EDX measurements.

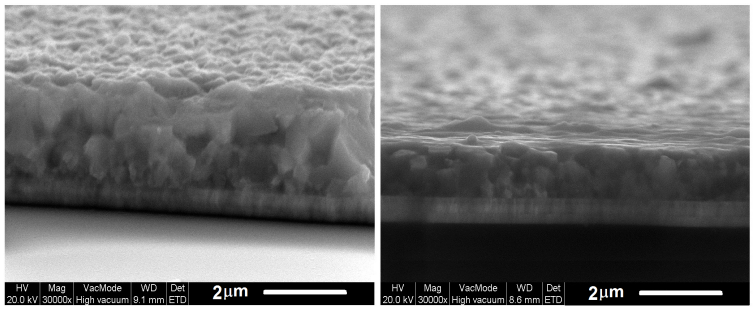

(a) SEM cross sections left: hetero-junction, right: Br etched.

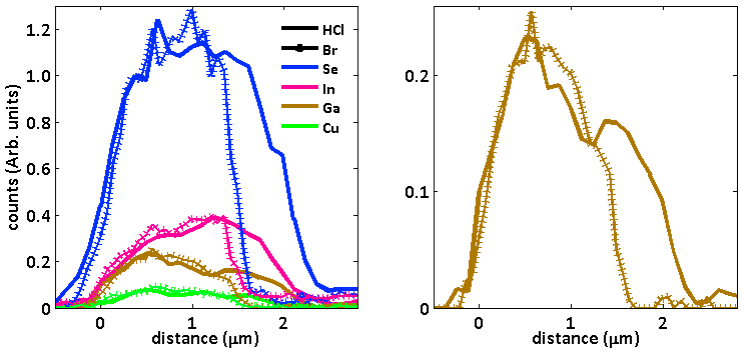

(b) EDX measurements of HCl (solid line) and Br etched (crossed line) samples. Left: Cu, In, Ga and Se profiles. Right: Ga profiles

Figure 4.3: Effect of Br etching on $\text{cell}_{\text{CdS-HCl}}$.

- HF etch: For the CBD of the CdS layer onto the CIGS absorber layer the vacuum in the thin-film solar cell processing is interrupted. A very thin oxide layer between absorber and buffer layer could be formed as indicated in reference [215]. Prior to CBD, the surface contains oxides, mainly indium oxide, gallium oxide, selenium oxide and sodium carbonate. These oxides are reduced after ca. 1 min of CBD as shown by XPS. However the CBD method yields a lot of oxygen- and carbon-related impurities in the CdS films ($CdCO_3$, $Cd(OH)_2$) and the absorber/buffer interface should not be considered as completely oxygen and carbon free.
  To remove the (possible) native oxide from the front surface of the absorber layer, an etch in dilute hydrofuoric acid ($HF/HNO_3/H_2O$ (1:1:4)) was performed during 20 s after the HCl etch. Reference [204] reported that the best Schottky contacts on $CuGaSe_2$ were made by a removal of surface oxides such as Cu-O and Ga-O using an HF solution. The same was done in reference [216] for Al/CIGS Schottky samples.

On the bare absorber layer a metal was evaporated to form a Schottky contact with the p-type absorber. The metal evaporation was performed, directly after the etching, through a stainless

steel mask with a diameter of 2 mm using electron beam evaporation. Under a pressure of 10^{-2} mbar a current of 30-40 A is sent through a tungsten boat. The metal on top of this boat melts and evaporates. Investigated evaporated metals give rise to a rectifying contact.
The HCl etched cells with different metal contact (metal = Au, Al, In) are labelled as metal$_{In_2S_3}$ or metal$_{CdS}$. Samples with original CdS buffer, which had an additional Br etch are labelled as metal$_{Br\text{-}CdS}$. The sample with additional HF etch is labelled as metal$_{HF\text{-}CdS2}$.

4.1.3 Static measurements on solar cells

I-V-T

Temperature dependent I-V curves (figure 4.4) for cell$_{CdS}$ are shown in the temperature region 80-300 K. A small surface area (around 1 mm^2) is measured. No 'roll-over' effect (section 2.1.3) is visible on the I-V characteristics. With decreasing temperature a shift of the I-V curves towards higher voltages is noticed. This can be explained by the temperature dependence of the saturation current $I_0 = I_{00}\exp(-E_a/nkT)$.

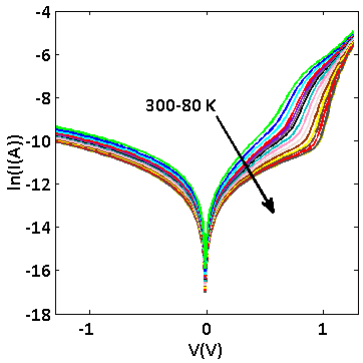

Figure 4.4: I-V as a function of temperature for cell$_{CdS}$.

R_s-T

The forward bias I-V characteristics deviates considerably from linearity on a semi-logarithmic scale due to the effect of series resistance. The series resistance can be deduced from dark I-V measurements following (for high forward bias and $R_s << R_p$ [49])

$$I = I_0\left[exp\left(\frac{q(V-IR_s)}{nkT}\right)-1\right] \tag{4.1}$$

$$V(I) = IR_s + nkT\,ln\left(\frac{I}{I_0}+1\right) \tag{4.2}$$

$$\text{and}\quad \frac{dV}{dI}|_{V\to+\infty} = R_s = \frac{1}{\frac{dI}{dV}}|_{V\to+\infty} \tag{4.3}$$

Figure 4.5 represents the series resistance as a function of temperature. The series resistance decreases strongly with increasing temperature which, can have following origins: lack of free carrier concentration at low temperatures [217], a change in the hole mobility or even to a back contact barrier [168]. The obtained values are in the same order of magnitude as in references [47, 56, 59, 62, 218]. Typical value for the series resistance is 1 Ω cm^2 according to reference [218].

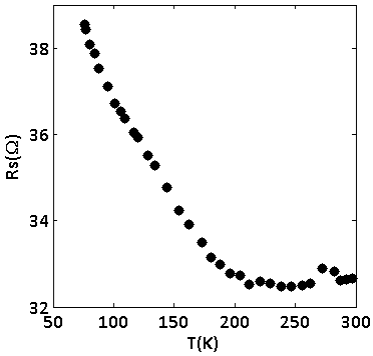

Figure 4.5: Series resistance as a function of temperature for cell_{CdS}.

It must be noted that determining the ideality factor and the saturation current density from the slope and the ordinate intercept on the semi-logarithmic plot of I versus V can be heavily influenced by series resistance [49, 54]. As the series resistance increases with temperature, this can result in an overestimate of the ideality factor at low temperatures [9]. In order to circumvent the influence of the series resistance an evaluation of short-circuit current densities and open-circuit voltages extracted from I-V curves under various illumination intensities can be performed [54].

C-V-T

An estimate of the carrier density can be calculated from capacitance-voltage curves as indicated in section 3.3.1.2. Following the Mott-Schottky analysis a carrier density of the order $2.0{\cdot}10^{17}$ cm^{-3} is found (figure 4.6(c)) which is quite large. The doping is non-uniform as the carrier density, for each temperature, increases towards the bulk of the absorber. It can be noticed that with decrease of temperature, the carrier density shifts slowly deeper into the absorber. This can be explained by a (rather small) carrier freeze-out as temperature decreases. As a result, the carrier density decreases whereby the depletion width enlarges. This freeze-out is also visible by the shifting of the capacitance curves towards lower capacitance values as temperature decreases. As this freeze-out already starts at high temperatures, the defect activation energy of the defect whereupon the carriers are freezing-out should be large [10].

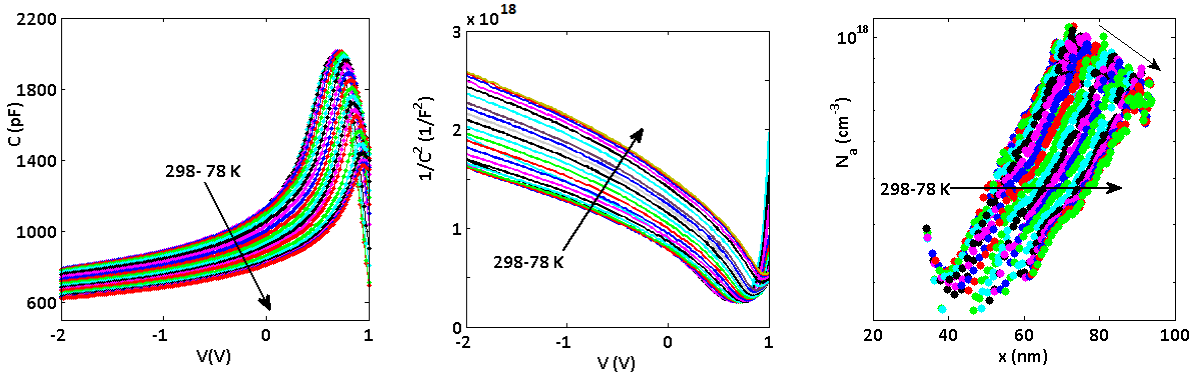

(a) C-V as a function of T (b) Mott-Schottky plot (c) Carrier density

Figure 4.6: C-V-T analysis of sampleA-heterojunction

4.1.4 Static measurements on simplified structures

To make sure that the quality of the Schottky contacts is decent, the shunt resistance was determined and compared to the shunt resistance of the cell. Further as the barrier height is a crucial parameter for the Schottky contacts, barrier heights were compared.

Shunt resistance

For low (negative) voltages and low series resistance, the shunt resistance can be deduced from the intercept on the ordinate in the log(I)-log(V) plot (figure 4.7, red solid line). The shunt resistance for cell_{CdS} and $\text{metal}_{\text{CdS}}$ are similar (cell_{CdS}: $0.2{\cdot}10^5$ Ω, Au_{CdS}: $0.2{\cdot}10^6$ Ω, $\text{Al}_{\text{Br-CdS}}$: $0.3{\cdot}10^6$ Ω), this shows that decent Shottky devices were obtained. The ideality factors of cell_{CdS}, Au_{CdS} and $\text{Al}_{\text{Br-CdS}}$ are 4.3, 2.4 and 6.6 respectively. The factors are quite high.

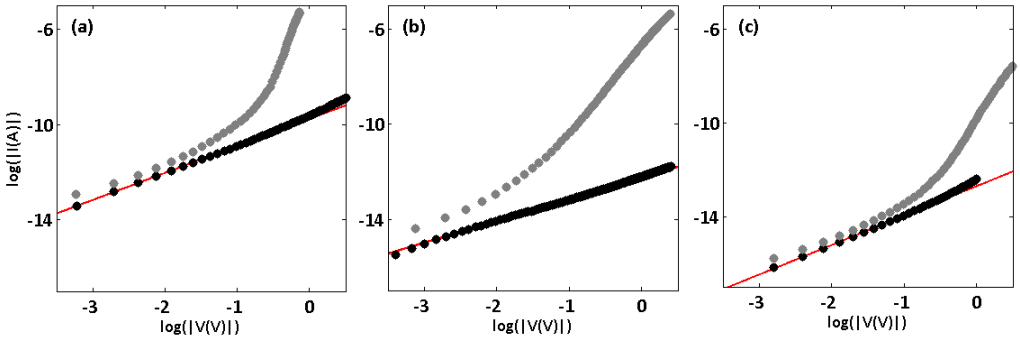

Figure 4.7: Shunt resistance determination of (a) cell_{CdS}, (b) Au_{CdS} and (c) $\text{Al}_{\text{Br-CdS}}$. Grey: forward bias, black: reverse bias, red: linear fit.

The shunt resistances for $\text{metal}_{\text{In}_2\text{S}_3}$ samples are in the order of 10^3-10^6 Ω ($\text{In}_{\text{In}_2\text{S}_3}$: $3.8{\cdot}10^3$ Ω, $\text{Al}_{\text{In}_2\text{S}_3}$: $1.4{\cdot}10^6$ Ω, $\text{Au}_{\text{In}_2\text{S}_3}$: $5.2{\cdot}10^4$ Ω).

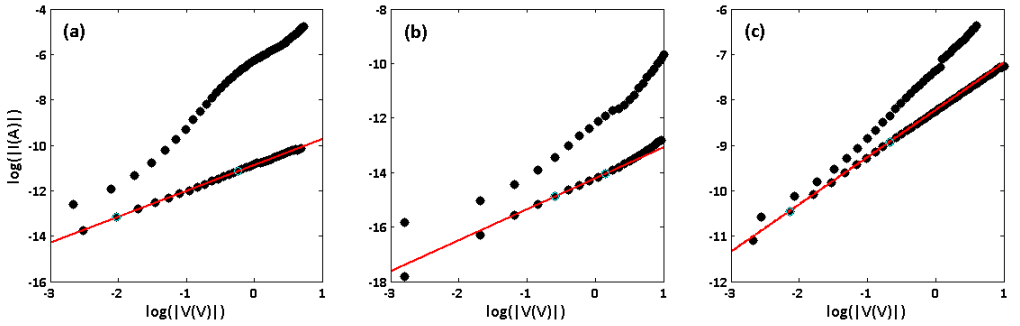

Figure 4.8: Shunt resistance determination of (a) $\text{Au}_{\text{In}_2\text{S}_3}$, (b) $\text{Al}_{\text{In}_2\text{S}_3}$ and (c) $\text{In}_{\text{In}_2\text{S}_3}$. Red curve is a fit at the reverse current voltage.

Barrier height

Several metals with different work functions were evaporated on the CIGS surface in order to alter the barrier height ϕ_{b} and hence change the electronic transport described by the Schottky model (equation 3.40). Typical values for the work functions of the metals used here are: ϕ_{Au}: 5.10-5.47 eV, ϕ_{Al}: 4.06-4.26 and $\phi_{\text{In}} \sim 4.1$ eV [3, 203, 204]. Because of Fermi level pinning, the barrier height can become independent of the metal as described in section 3.5.

According to equation 3.40, the barrier height is calculated from I_0 which is determined by an extrapolation of the log(I) versus V curve to zero bias. The fits of the barrier heights are shown for $\text{metal}_{\text{CdS}}$ samples in figure 4.9.

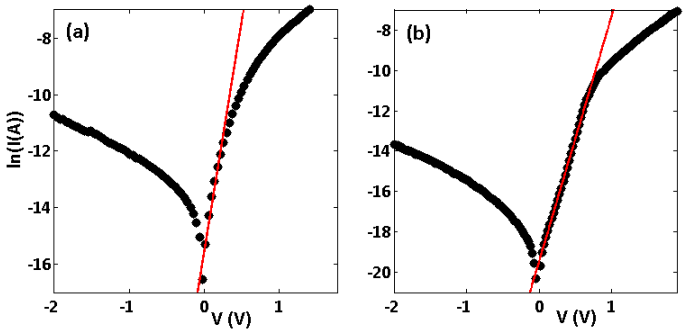

Figure 4.9: Barrier height determination of (a) Au_{CdS} (ϕ_b = 717 meV, n = 2.4) and (b) Al_{CdS} (ϕ_b = 804 meV, n = 3.3).

Although the metal work functions vary by $\sim$ 1 eV, a barrier height between 650 and 800 meV was found for all samples (table 4.1). No further correlation between the barrier heights could be deduced, they appear to be sample dependent. Fermi level pinning appears to be confirmed by these results.

Table 4.1: Calculated barrier heights ϕ_b (meV).

metal	$metal_{In_2S_3}$	$metal_{CdS}$	$metal_{Br\text{-}CdS}$
Au	658	717	752
Al	736	804	704
In	675		

4.1.5 DLTS

Temperature dependent DLTS measurements were performed between 10-300 K or 70-300 K. Before starting the DLTS measurements, the solar cells were kept in the dark during 1h in order to bring them into the relaxed state. In comparisons between cells only the relative peak positions will be compared and not the heights of the peaks, because different surface areas are measured.

4.1.5.1 Effect of different metals

Figure 4.10 shows the DLTS spectra at high temperature of $cell_{In_2S_3}$ and $metal_{In_2S_3}$ (metal = Au, Al, In). In all spectra the low temperature (N1) signal appears around 120 K. Figure 4.10(a) has been discussed in more detail in relation with a non-ohmic back contact signal in reference [200].

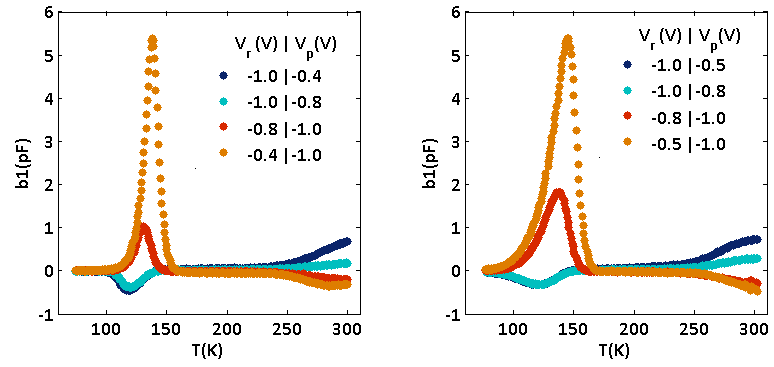

(a) $\text{cell}_{\text{In}_2\text{S}_3}$ (b) $\text{Au}_{\text{In}_2\text{S}_3}$

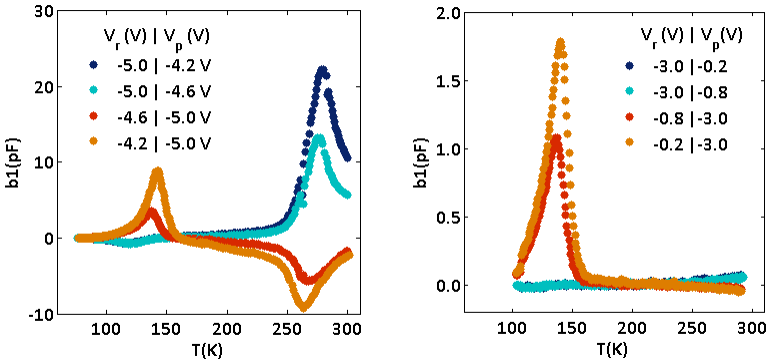

(c) $\text{Al}_{\text{In}_2\text{S}_3}$ (d) $\text{In}_{\text{In}_2\text{S}_3}$

Figure 4.10: DLTS spectra at $t_w = 0.005$ s, $t_p = 0.050$ s.

At higher temperature (above 250 K), the broad onset of a peak is visible in the spectra of $\text{In}_{\text{In}_2\text{S}_3}$, $\text{Au}_{\text{In}_2\text{S}_3}$ and $\text{cell}_{\text{In}_2\text{S}_3}$, exhibiting essentially the same characteristics for these three samples. A detailed analysis and interpretation of the high temperature signals for these cells and those with CdS buffer is difficult to make at this moment. Indeed, the maximum of the DLTS spectra does not appear in the measured temperature range. Moreover, in reference [196] it is demonstrated that correct interpretation of the transients with large time constants, observed for CIGS cells at high temperature, requires lengthy measurements since reproducibility can only be attained in a steady state regime. DLTS measurements which take a very long time are however not feasible. Therefore, only the qualitative features of the DLTS spectra of cells and Schottky diodes with different metals are discussed.

With this in mind, only the $\text{Al}_{\text{In}_2\text{S}_3}$ sample is found to yield deviant results (figure 4.10(c)): in the temperature range 250-300 K a component arises which exhibits a clear maximum. The maximum of the complementary signal lies at lower temperature than the conventional signal. This can be understood in terms of capture and emission on defects. Because the capture rate for a hole trap in a p-type semiconductor (e_p+c_p) is normally much faster than the emission rate of the hole trap (e_p), the peak position of the capture process (complementary signal) will appear at lower temperature than the peak position of the emission [14]. As the maximum of the high temperature signal is visible, one can, by looking at the peak shift which occurs when applying different voltages, distinguish between interface and bulk defects, assuming that this peak is indeed related to defects. As the absolute value of the filling bias ($|V_p|$) decreases, the peak shifts towards higher temperature (higher activation energy) for the conventional peak. This shift is opposite to what is expected for emission from defects at the interface. As the absolute value of the filling bias ($|V_p|$) decreases, more defects with smaller activation energy at the interface could be filled which gives rise to a shift towards lower temperatures. For a small $|V_p|$ more traps could be filled (transition region increases) and the peak becomes broader, which is visible in figure 4.10(c). In the case of pure bulk defects, no shift should be visible

when the applied filling bias is changed. The peak shift opposite to an interface peak shift could be explained by a very high density of defects [10]. For the standard DLTS theory $N_t << N_d$ is assumed (see equation 3.27). If this is not valid a distortion of the DLTS spectra can occur. In reference [10] simulations have proven that a large defect concentration can explain a peak shift towards larger defect activation energy (shift to larger window times/temperatures). It is tempting to relate the high temperature signal in sample $Al_{In_2S_3}$ with Al diffusion in the absorber. More DLTS and depth profile investigations about a possible Al in-diffusion will be necessary for the interpretation of the high temperature peak in $Al_{In_2S_3}$ samples.

4.1.5.2 Effect of buffer layer

To test the effect of the buffer layer type and deposition technique, DLTS experiments were also performed on a CIGS cell with CdS buffer layer (figure 4.11). The spectra of $cell_{CdS}$ and $metal_{CdS}$ (metal = Al, Au) look very similar: N1 and a signal at high temperature with substructure are present. Even if the window and buffer layer (different type) are removed, the same signals still arise. Hence, the intense high temperature DLTS signals cannot be directly related to the window and buffer layers (i.e. defects in these layers or at their interfaces).

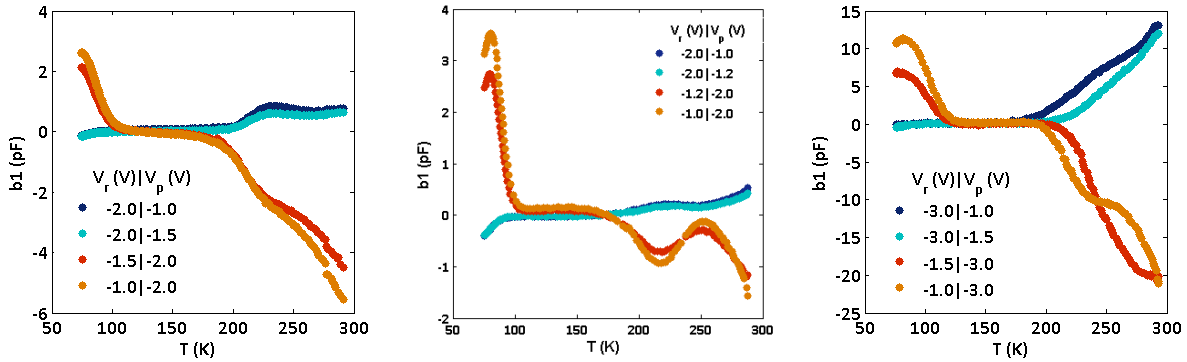

(a) $cell_{CdS}$ (b) Au_{CdS} (c) Al_{CdS}

Figure 4.11: DLTS spectra of samples with original CdS buffer (t_w = 0.005 s, t_p = 0.050 s).

It can be noticed that the exact position and amplitude of the N1 peak is slightly different for the different samples (e.g. comparison with In_2S_3 buffer samples). Following reference [14] the position of the N1 peak is determined by a coupled system of back contact junction and (to a small extent) main junction. Despite the small contribution of the latter to the time constant, a change of the electric characteristics of the main junction can still affect the properties of the observed capacitance transient of the back contact.

4.1.5.3 Effect of thinning absorber layer

SEM images in figure 4.3 showed a thinning of the CIGS absorber by the Br-methanol solution by about 440 nm for sample $cell_{CdS}$ which had first an HCl etch. The EDX measurements showed that the double-graded Ga profile is no longer present. In spite of the severe composition changes near the surface, the DLTS spectra are hardly affected. The spectra after an additional Br etch (figure 4.12) look very similar to those of the other samples (figures 4.11(b) and 4.11(c)). These experiments seem to rule out a possible influence of a type inverted layer created by Cd diffusion on the DLTS spectra, as Cd diffusion is expected to be limited to the surface (section 2.3.1.3).

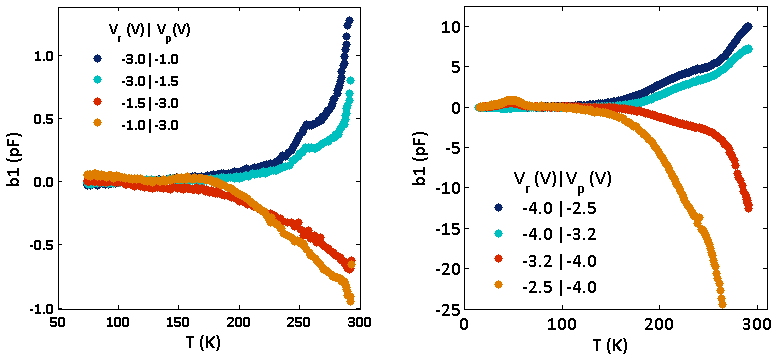

(a) $Au_{Br\text{-}CdS}$ (b) $Al_{Br\text{-}CdS}$

Figure 4.12: DLTS spectra of Br etched test (t_w = 0.005 s, t_p = 0.050 s).

4.1.5.4 Effect of oxidation

As a thin oxide layer at the absorber/buffer or absorber/metal interface could effect the DLTS signals, different tests were applied to test the possible effect of oxidation.

1) HF etch

In order to test whether an oxide layer on top of the absorber layer could influence DLTS signals, an HF etch after the HCl etch was performed. The test was performed on $cell_{CdS2}$. The results for an Al contact with or without additional HF etch are shown in figure 4.13.

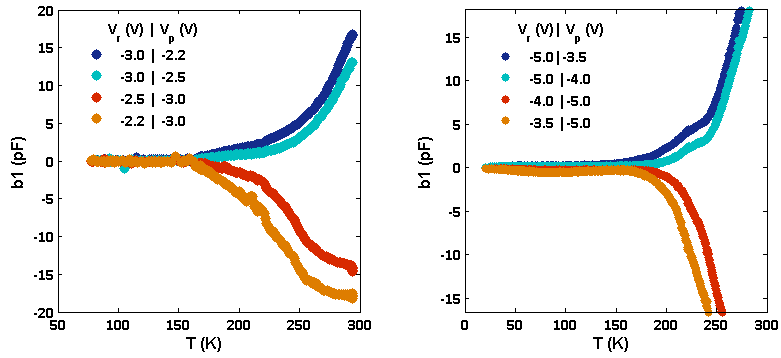

(a) Al_{CdS2} (b) $Al_{HF\text{-}CdS2}$

Figure 4.13: DLTS spectra of HF test (t_w = 0.005 s, t_p = 0.050 s).

The spectra do not show the N1 signal (signals appears below a temperature of 70 K) but only an onset of a peak at higher temperature. As the DLTS spectra of the sample with and without additional HF etch yield very similar spectra, oxidation does not seem to have a strong effect on the DLTS signals.

2) Water treatment

In order to investigate the possibility of an oxidation effect on the DLTS signals, an attempt was made to create an oxide layer by adding water on top of the HCl etched sample and wait for 15 minutes. Thereafter Al was evaporated on top of the water treated sample. In figure 4.14 the DLTS spectra of samples with and without water treatment are shown. The water treatment, which induces very probably an oxide layer, changes the DLTS spectrum in the temperature region 160-250 K but does not alter the basic features, the high and low temperature signal are still visible.

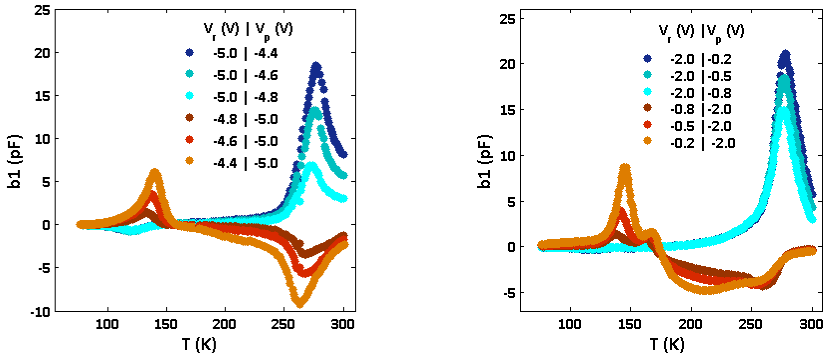

(a) $Al_{In_2S_3}$ t_w = 0.005 s, t_p = 0.500s (b) Water treated $Al_{In_2S_3}$ t_w = 0.010 s, t_p = 0.200 s

Figure 4.14: Effect of a water treatment before evaporation of Al.

It must noted that the applied voltages are different between the measurements. By applying different pulses, different regions in the absorber can be probed in principle. Experiments show that the main features of the DLTS signals are not affected by the bias region (see 4.1.5.5).

3) Glow Discharge

Because there is still some time between the etching (in HCl, Br or HF) and the evaporation of the metal, an oxide layer could still be formed between the absorber layer and metal layer. In collaboration with the research group DRAFT (research group of department of Solid State Sciences at Ghent University), prior to Al sputtering, a glow discharge was performed. The glow discharge is expected to clean the surface whereby the oxide layer should be removed. No significant changes in the high temperature region of the DLTS spectra are noticed in figure 4.15 compared to measurements on the same sample with Al contact (figure 4.13). The onset of the high temperature signals between 230-300 K is still visible. An additional substructure around 200 K is more pronounced in this measurement. As the peak appears at lower temperature than in the spectra of the sample $Al_{In_2S_3}$, the peak is probably not related to Al in-diffusion. More investigations should be done to explain the appearance of the substructure.

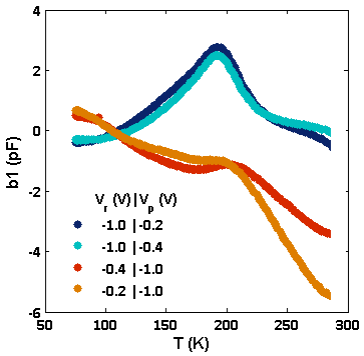

Figure 4.15: DLTS spectrum of 'glow discharge-Al_{CdS2}' (t_w = 0.005 s, t_p = 0.500 s).

4.1.5.5 Variation pulse region

In all previous DLTS measurements, the pulse regions were chosen in the voltage region wherein the CV profile showed the largest variation. Figure 4.16 shows the effect upon altering the pulse region. Different voltage pulses were applied to investigate different regions wherein carriers can be trapped. Apart from a difference in amplitude of the pulses, main characteristics remained unaltered. From this it was concluded that altering the bias pulse region has no large effect on

the main DLTS signals.

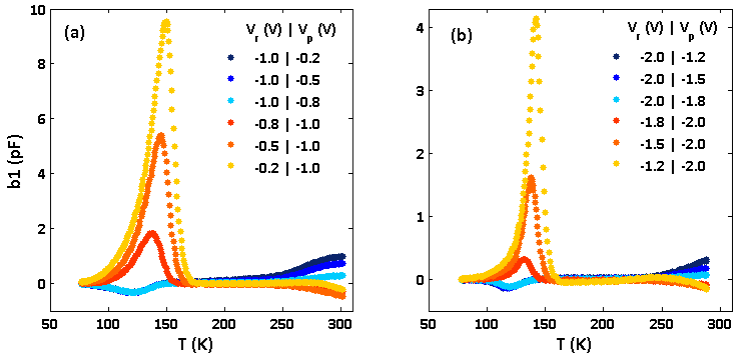

Figure 4.16: Variation of bias pulses on $\text{cell}_{\text{In}_2\text{S}_3}$ (t_w = 0.005 s, t_p = 0.050 s). The pulse region in (a) is nearest to the interface.

4.1.5.6 Discussion on high temperature signal

Long window time: A detailed analysis and interpretation of the high temperature signals is difficult because the maximum of these signals does not appear in the measured temperature range. Without this maximum no activation energy for carrier emission can be derived in the case the signal would arise from a defect. An increase of t_w would shift the signal for carrier emission towards lower temperatures. In figure 4.17 spectra for different window times and filling pulse times can be seen. The bias voltages in the pulses (V_r and V_p) are equal.

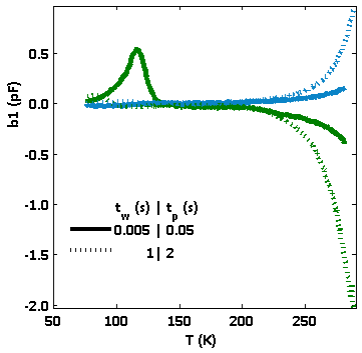

Figure 4.17: DLTS spectra of $\text{Au}_{\text{In}_2\text{S}_3}$ for different window times. Blue: conventional pulse (V_r = -1.5 V, V_p = -0.8 V), Green: complementary pulses (V_r = -0.8 V, V_p = -1.5 V)

Although long window and filling pulse times were used, still the maximum of the high temperature signal is not completely reached in the available temperature range. Another method to obtain the maximum of the high temperature signal is by increasing the temperature above 300 K. Attempts were made by using a high temperature cryostat. Unfortunately the thin-film solar cell is not resistant to high temperatures: DLTS measurements performed while heating the sample differ from measurements during cooling. No reliable information about the maximum could be deduced from such measurements.

Isothermal measurement: Another way to determine the maximum of the DLTS peaks at high temperature is by performing isothermal measurements as explained in section 3.3.2.5. Figure 4.18 displays isothermal measurements on $\text{cell}_{\text{In}_2\text{S}_3}$ performed at 300 K with filling pulses ranging from 0.001 s to 100 s.

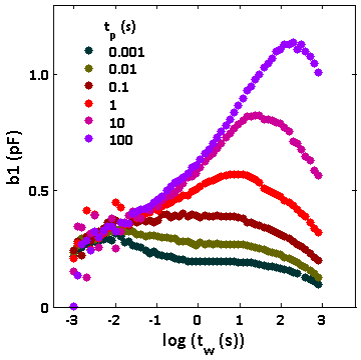

Figure 4.18: Isothermal DLTS spectra of cell$_{In_2S_3}$ at 300 K for different filling pulse times (V_r = -1.2 V, V_p = -0.2 V).

A maximum in the spectra can indeed be noticed. As for longer filling pulse time more defects can capture carriers, the intensity of the DLTS signal increases. For very long filling pulses the intensity of the signal saturates. From this increase in peak intensity with increasing filling pulse, the capture cross section could, in principle, be calculated. However an anomalous effect of filling pulse duration, namely a shift of the DLTS peak towards longer window times for increasing filling pulse times, disturbs this calculation as the peak maximum appears at different window times. Due to this anomalous filling pulse behaviour, the interpretation of the signal becomes again non-unambiguous. In reference [10] it is shown by modelling that the shift with increasing filling pulse could be induced by a high defect density (in the standard DLTS theory it is assumed that $N_t << N_d$). As shown in figure 4.18, the time constant of the N2 signal at room temperature is larger (about 10 s for filling pulse of 1 s) than the window times one typically uses in DLTS measurements. Regarding the slowly varying electrical properties observed in a CIGS solar cell (metastabilities [6]), one could wonder on which scale these slow processes (with unknown large time constant) could alter the DLTS measurements [196].

4.1.6 Summary

Thin-film solar cells were simplified to M/S/M structures by chemical etching of the buffer and window layers, and vacuum evaporation of different metals on the CIGS absorber. In almost all cases the DLTS spectra of complete cells and of M/S/M samples were strikingly similar, even if the surface modification is enhanced by thinning the absorber layer - eliminating type inverted layers near the surface (Cd doping or ordered vacancy compounds) - or when etching is performed targeted at removing surface oxide layers. All spectra exhibit one signal below 150 K and a signal at high temperature, possibly with substructure.
The current set of experiments are inconclusive regarding the origin of the high temperature signal. Further investigations will be necessary. Nonetheless, a good attempt was done by simplifying the structure as the present experiments already seem to exclude direct influences of the window and buffer layers, and of the special defect state of the absorber near its interface with the buffer. The results do not contradict an attribution to defects in the CIGS absorber bulk but are also not conclusively to confirm such identification. In none of spectra, obtained by different DLTS measurement types (frequency scan and isothermal scan) or on different samples types (cells or M/S/M structures) a basic defect related feature could be seen. Understanding the reasons for the Fermi level pinning in the metal-CIGS Schottky diodes might be an element in the interpretation of these high temperature features.

4.2 CIGS: Admittance study on the influence of an Sb layer

4.2.1 Motivation

In order to reduce large scale manufacturing costs and to enable affordable solar electricity, a roll-to-roll set-up which produces flexible solar cells has great potential. As the maximum applicable temperature for polyimide foils, one possible flexible substrate, is restricted to below 500°C, these lower growth temperatures can have drawbacks for the performance of the device. First, the substrate temperature is found to be an important parameter (besides deposition rate, sodium content, deposition ratios during three stage process) for the formation of the Ga grading profile, which can influence the device performance (section 2.3.1.3). Further if soda lime glass is used as a substrate the Na in-diffusion from the glass, which is beneficial for device performance, can be altered at lower substrate temperature. Last, due to the low temperatures smaller grains are formed. In order to minimize recombination effects, grain sizes have to be large because less grain boundaries are then present.
In this section we report on an attempt to obtain high efficiency devices, despite low-temperature deposition processes by adding an antimony layer on top of the Mo layer. As shown in section 2.3.1.8 Sb doping of the absorber can promote growth of the CIGS grains under relatively mild thermal treatment conditions. As not all studies [144, 145] report such unambiguously positive effect of Sb doping, it may imply that Sb has a more complex influence on the CIGS properties. The substrate used for the samples was still soda lime glass, such that Na is present in the absorber layer.

The possible effect on the defect structure was investigated in this section by means of admittance spectroscopy (AS). As it is reported that Sb can alter the conductivity of CIGS (Sb_S for Sb doped $CuInS_2$ is suggested as dominant shallow acceptor in references [144, 147]), low temperature AS measurements are performed to explore the possible introduction of a shallow acceptor (Sb_{Se}). In references [15, 26, 219], carrier freeze-out in CIGS layers was observed at low temperatures ($<$ 50 K) and a shallow acceptor with an activation energy slightly below 30 meV was identified. Based on density functional theory calculations Cu vacancies (V_{Cu}) were proposed to form this shallow acceptor [91]. The very efficient 'self-doping' ability of $CuInSe_2$ was attributed to the exceptionally low formation energy of Cu vacancies.

4.2.2 Preparation and performance

Cell preparation Sb was incorporated in the solar cell structure by evaporating an Sb layer on top of a Mo coated soda-lime glass substrate, as shown in figure 4.19. Cells with a Sb precursor layer of 0, 7, or 12 nm thickness were synthesized, referred to as Sb0, Sb7 and Sb12, respectively. The samples are labelled as series1. This Sb layer was coated with a thin Cu layer to prevent evaporation of Sb during early stages of the CIGS absorber deposition. The Na diffusion from the soda lime glass to the absorber might also be affected by the changed cell geometry. The experiments presented in this paper do not allow the effects of Na and Sb to be separated. These problems deserve further investigation. In the investigated cells of the next section Na was also incorporated by post deposition treatment. If experiments would be performed on PI foil, a distinct incorporation of Na (by NaF post deposition process) would be necessary. The CIGS absorber was grown by a low temperature multi-stage process. A substrate temperature of around 350°C was used during the first stage. The substrate temperature of the second and third stage was 450°C (normally around 600°C on glass). The CIGS absorber was covered with CdS by chemical bath deposition. The ZnO window layer and Ni/Al/Ni grid were deposited by RF sputtering and e-beam evaporation, respectively. No anti-reflection coating was applied.

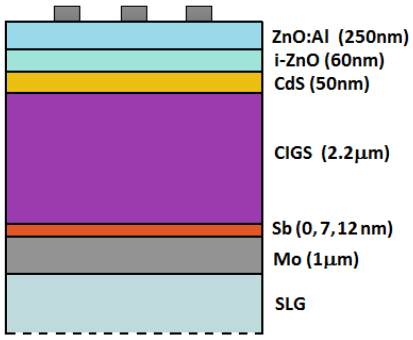

Figure 4.19: Structure of Sb-doped CIGS solar cell.

Solar cell device parameters Device performance parameters of the best cell of each sample are listed in the table 4.2. Series and and shunt resistance values are taken from measurements under illumination and hence only provide an estimate. An improvement in efficiency for cells with an additional Sb layer is obtained due to an increased J_{sc}, while V_{oc} is not altered much.

Table 4.2: Device performance of series1 (numbers provided by Empa).

Sample	V_{oc} (mV)	J_{sc} (mA/cm^2)	FF (%)	η (%)	R_s (Ωcm^2)	R_p (Ωcm^2)
Sb0	641	28.8	65.7	12.1	0.8	704
Sb7	637	31.2	68.4	13.6	0.9	900
Sb12	646	31.8	65.9	13.5	0.9	712

As indicated in section 3.3.1.3 the interpretation of carrier density profiles derived from CV measurements should be handled with care. Even at a measurement frequency of 1MHz (one expects that deep defects could not follow this frequency [11, 15]) the calculated carrier density can be distorted by the static charge accumulated at deep states which follows the voltage sweep [5, 11]. Therefore the carrier density , calculated from CV measurements, could not be very precise and is therefore not calculated. High-frequency DLCP could provide a more accurate estimation of free carrier density [5]. Another error could appear in the measurement of the area in the CV measurement.

4.2.3 Morphology

SEM images (figure 4.20) show that grain size in samples with Sb layer is clearly larger than in the sample without Sb layer. Despite low substrate temperature during deposition, a large grain size can thus still be obtained by including Sb. Increased CIGS grain size with increasing Sb precursor layer thickness is in agreement with different reports [139–143, 220]. The increased grain size and associated reduced grain boundary recombination might explain the improvement of the solar cell efficiency (due to larger J_{sc}) as shown in table 4.2. For all cells, the thickness of the absorber layers is around 2.1-2.2 µm.

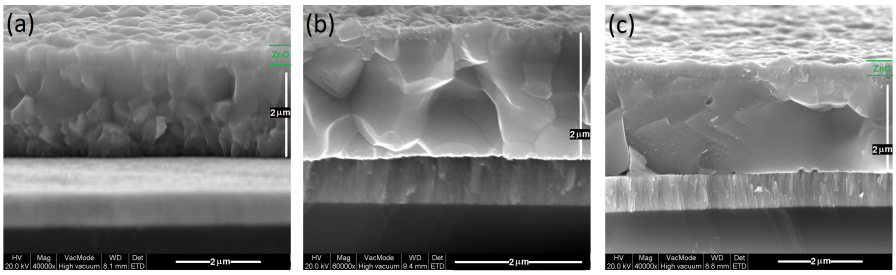

Figure 4.20: SEM micrographs of cross sections of the thin-films (a) Sb0, (b) Sb7 (after HCl etch) (c) Sb12. Length scales are indicated on the right of each figure. Region of ZnO is indicated in green.

4.2.4 Composition

XRF

The average composition ratios for all three cells are around 0.86 for CGI and 0.38 for GGI, as determined by X-ray fluorescence (XRF) measurements performed by Empa. The cells have thus a Cu-poor composition.

TOFMS

Depth profiling data were obtained with Plasma Profiling Time of Flight Mass Spectrometry (PP-TOFMS) in collaboration with Horiba Scientific (France). PP-TOFMS is, like SIMS (secondary ion mass spectrometry), a depth profiling technique based on material erosion and dynamic measurement of sputtered species. In PP-TOFMS a plasma source is coupled with a time of flight mass analyzer [221–223]. The intensity and energy of the commonly used Argon ions and fast neutrals causing material sputtering is much higher in PP-TOFMS compared to SIMS, leading to much faster analysis. Furthermore, in PP-TOFMS the sputtering and ionization processes in the discharge volume are two separated processes. As a result, PP-TOFMS is semi-quantitative for most inorganic materials. In SIMS only the ionized particles coming off from the material are collected and measured. As the distance between the Al/Ni grid and the Mo stripes is smaller than the size of the crater diameter (4 mm) in the PP-TOFMS measurement, samples were etched in 10% HCl prior to depth profiling in order to remove metal grid and front contact.
Element depth profiles of Cu, In, Ga and Se of samples without (Sb0) and with (Sb12) Sb layer do not reveal large qualitative differences between these two cells (figure 4.21(a)). Nevertheless, for sample Sb12 the measurement reveals a clear diffusion profile of Sb, whereas for Sb0 the antimony signal remained below the detection limit. In order to illustrate this, the Ga and Sb profiles for the two cells, applying the same scaling procedure, are shown in figure 4.21(b). From these measurements it becomes clear that in-diffusion of Sb into the absorber layer is rather limited and most of the Sb remains in the layer on the Mo back contact. Nonetheless, a slight increase of the Sb concentration near the CIGS surface is also observed. Such concentration profile indicates that Sb has diffused through the CIGS absorber layer and hence may be compatible with the possibility of Sb enhancing the CIGS grain growth.

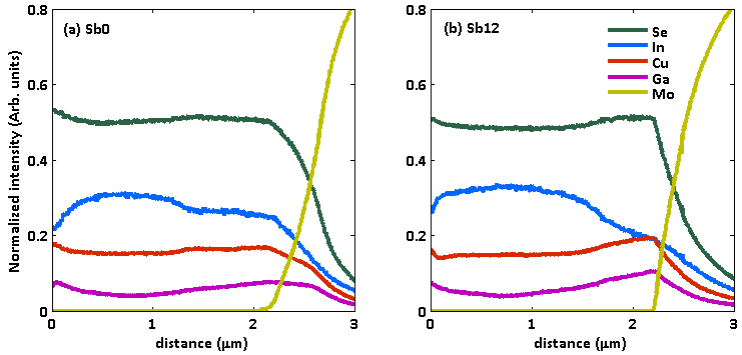

(a) Cu, In, Ga and Se profiles.

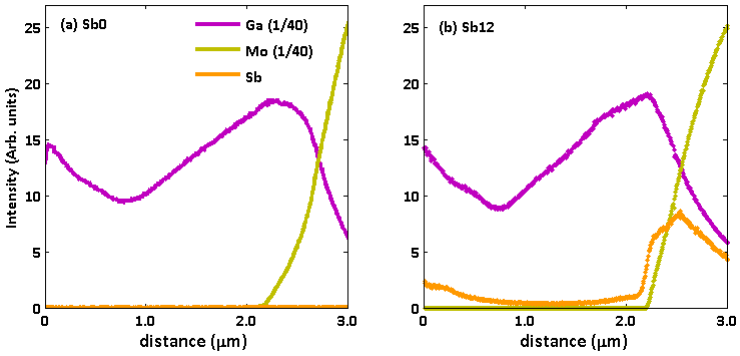

(b) Ga, Mo and Sb signals.

Figure 4.21: Depth profile signals of sample (a) Sb0, (b) Sb12.

4.2.5 Admittance spectroscopy

Cells were measured in the relaxed state (in darkness for 1 h at room temperature) in the frequency range 100 Hz-2 MHz. The capacitance was measured at dc biases of 0.6, 0.0, -0.3 and -0.6 V. Admittance measurements performed in the temperature range from 5-250 K at a reverse bias of -0.3 V on Sb0 and Sb7 are presented in figures 4.22(a) and 4.23(b), respectively.

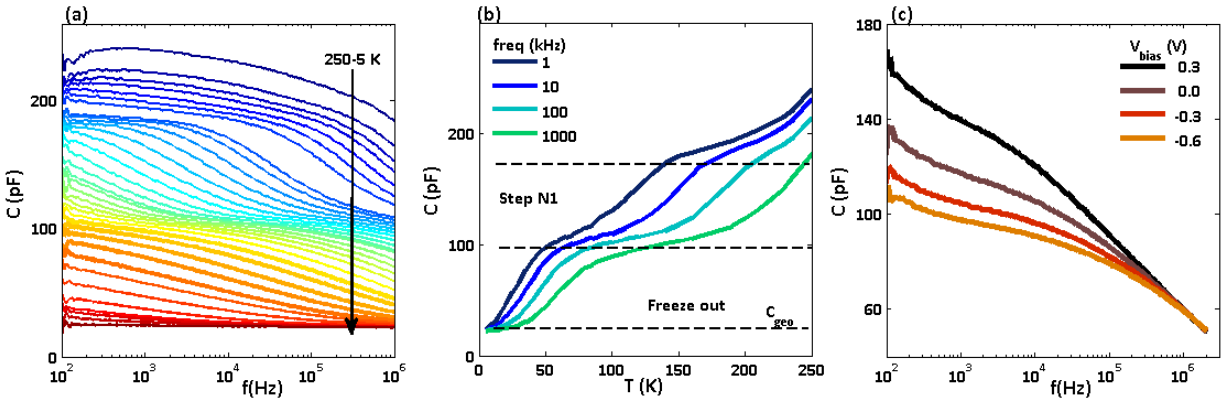

Figure 4.22: Admittance spectra and measured freeze-out for Sb0.
(a) C-f-T spectra for Vr = -0.3 V, (b) C-T for Vr = -0.3 V, (c) C-f at 60 K.

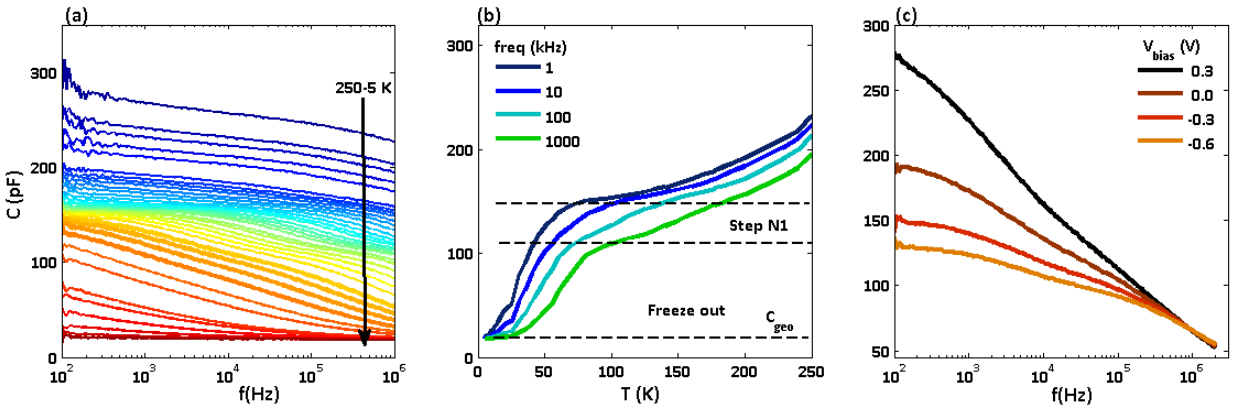

Figure 4.23: Admittance spectra and measured freeze-out for Sb7.
(a) C-f-T spectra for Vr = -0.3 V, (b) C-T for Vr = -0.3 V, (c) C-f at 60 K.

In the C-f-T spectra for both samples, three capacitance steps can be discerned. Figures 4.22(b) and 4.23(b), where capacitance is plotted as a function of temperature for different frequencies, show an onset of a third step at the highest temperatures (> 200 K), very probably related with very deep-level defects. At intermediate temperatures (120-165 K) a capacitance step occurs which is commonly observed in CIGS solar cells and labelled N1. Various interpretations have been suggested in literature for the assignment of this capacitance step as discussed in section 3.4. Deep level transient spectroscopy measurements on these cells are in accordance with the characteristics typical for a non-Ohmic contact as described in references [14, 200]. In these experiments, we will concentrate our attention on the step at lowest temperatures.
At the lowest temperatures (< 100 K) and frequencies exceeding the dielectric carrier response frequency ($\omega_D = \sigma/(\varepsilon_0\varepsilon_r)$), the whole semiconductor behaves as a dielectric. The capacitance measured at such frequencies is the geometric capacitance $C_{geo} = \varepsilon_0\varepsilon_r A/t$ (as indicated in section 3.3.3.2) [5,191]. The step due to dielectric freeze-out is visible in C-f (figures 4.22(a) and 4.23(a)) and C-T spectra (figures 4.22(b) and 4.23(b)) for high frequencies (≈ 0.1-1 MHz) around 50 K. The dielectric freeze-out step can be distinguished from the other capacitance steps by its independence of applied bias on the high-frequency side of the step [191]. This independence is shown in figures 4.22(c) and 4.23(c) which present C-f spectra at 60 K for different bias. For sample Sb0 and Sb7 a geometric capacitance C_{geo} of $2.25 \cdot 10^{-11}$ F and $1.85 \cdot 10^{-11}$ F, respectively, is reached (figures 4.22(a) and 4.23(a)) for a sample area of around 0.6 mm^2. If one calculates the thickness of the film (using $\varepsilon_r = 10$ for CIGS [11,16]) values of 2.3 µm (Sb0) and 2.8 µm (Sb7) are derived, which are in fair agreement with the film thickness observed in SEM measurements (figure 4.20).

As indicated in section 3.3.3.2, the activation energy E_a of the intrinsic and perhaps extra Sb-doping-related shallow acceptor defects can be measured in the step at lowest temperatures which exceed 20 K (in order to have a large enough capacitance step above the geometric capacitance). E_a can be extracted from the plot of ω_0/T^m versus 1/kT. The characteristic frequency is determined as the maximum of the differential capacitance curves ($-\omega/kT \cdot dC/d\omega$ versus ω). The differential capacitance curves corresponding to the C-f curves indicated in bold in figures 4.22(a) and 4.23(a), are shown in figure 4.24.

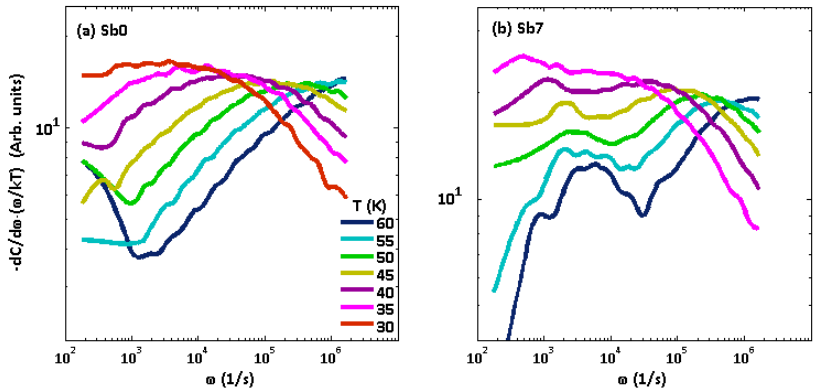

Figure 4.24: Differential capacitance calculated from C-f-T spectra for low temperatures (a) Sb0, (b) Sb7.

If one assumes a temperature independent mobility (m = 3/2), the activation energies are 25 meV for Sb0 and 22 meV for Sb7 (figure 4.25(a)). An estimate of the error is made by comparing the values obtained taking m values between 0 and 3 (mobility determined by impurity scattering, $\mu_h \propto T^{3/2}$ [4]), we then estimate the error at 5 meV. The calculated activation energy is similar for both samples and around 25 ± 5 meV. This value should yield a good approximation of the activation energy of the shallow defect, responsible for the p-type conductivity of the CIGS layer. As, within experimental resolution, the activation energies derived from the low temperature capacitance step for the two samples are very similar, we conclude that Sb treatment did not change the activation energy of dominant acceptor defect. C-T data at a frequency of 100 kHz, normalized at T = 85 K after reduction of geometric capacitance (figure 4.25(b)), indeed show that the carrier relaxation for both samples is very similar. Following the interpretation of previous very similar experimental [15, 26, 219] and density functional modelling [91] results, we tentatively assign this level to the copper vacancy.

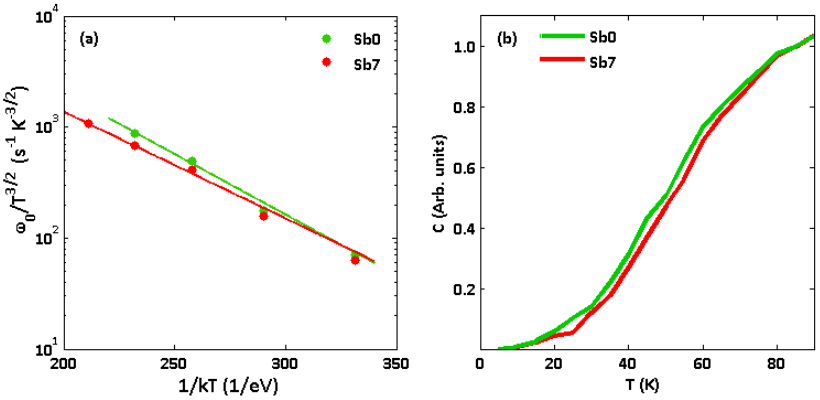

Figure 4.25: (a) Arrhenius diagram for m = 3/2.
(b) C-T spectra at frequency of 100 kHz and bias -0.3 V.

4.2.6 Summary

The thin-film CIGS solar cells investigated here were produced by a three stage co-evaporation process at reduced deposition temperature. An Sb layer with varying thickness (0, 7, 12 nm), which is expected to promote CIGS grain growth, was included prior to CIGS deposition. Enhanced efficiency values are probably related to the larger grain size in these cells, as demonstrated by SEM. PP-TOFMS depth profiling measurements revealed a very limited Sb diffusion in the CIGS absorber layer, however, a small Sb concentration was also observed in the surface region. Admittance measurements could not reveal a direct effect from Sb addition on the de-

fect structure. Both in cells with and without Sb layer, a shallow acceptor level with activation energy estimated around 25 ± 5 meV was found and assigned to the dominant acceptor in CIGS absorber, probably the V_{Cu} intrinsic defect.

Part III

Optical characterization

5 Concepts of optical defect characterization

Contents

5.1 Quantum efficiency

5.1.1 Current loss mechanisms

The spectral response of a solar cell can be quantified by quantum efficiency measurements. External quantum efficiency (EQE) is defined by the number of electrons collected per photon incident on the solar cell [5]. EQE includes all photons arriving at the surface of the device. A quantum efficiency of 1 means therefore that for each photon one electron-hole pair is contributing to the photogenerated current. For an ideal device this is the case for all photons with an energy above the band gap of the absorber. The quantum efficiency would be 0 for photons with a lower energy [5].

$$\begin{aligned} EQE(\lambda) &= \frac{\text{electrons collected}}{\text{incident photons}} \\ &= \frac{J_{ph}(\lambda)/q}{\phi(\lambda)} \end{aligned}$$

The photon flux ϕ is given in number of photons/(m^2s) [5], J_{ph} (λ) is photocurrent density as a function of the incident photon wavelength. Internal quantum efficiency (IQE) is defined as the number of collected electrons per number of photon absorbed in the solar cell [5], the influence

of reflection is eliminated.The EQE is thus measured, while the IQE can be calculated from the EQE measurement following the relation [5]

$$EQE(\lambda) = (1 - R_\lambda)IQE(\lambda)$$

R_λ represents the overall reflectance of the device [5]. EQE is the more commonly reported result. Typically the EQE is measured under zero bias voltage. The wavelength dependency of quantum efficiency QE(λ) can be related to the short circuit density by [11]

$$J_{sc} = q \int_\lambda \phi(\lambda) EQE(\lambda) d\lambda$$

As mentioned before in the ideal case the EQE value would be 1, but this value is -obviously- not reached in real devices because of several loss mechanisms. By means of quantum efficiency measurements loss mechanisms in the device can be found [6, 11, 224]. Optical losses visible on EQE measurement are depicted in figure 5.1.

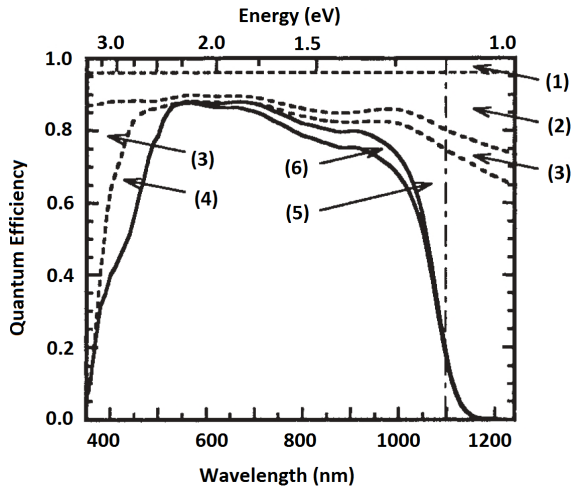

Figure 5.1: Loss mechanisms in quantum efficiency measurements on CIGS cells [224].

1. *Grid shading*: Often QE measurements are done with a small light spot not touching the grids, whereby the loss due to grid shading does not occur. The contact grid can give a 2-3% loss over the whole spectrum.

2. *Reflection*: All interfaces before the absorber reflect a fraction of the incident light. In record efficiency cells this reflection is strongly reduced by a anti-refection coating (MgF_2) or patterning of the surface.

3. *Window absorption*: For short wavelengths (in the UV) the band gap of the window layer is the limiting factor for the QE. Carriers created by absorption in this highly doped layer have a short lifetime and cannot diffuse into the space charge region. Across the visible part of the spectrum, the window layer has an absorptivity of 1-5%.

4. *Buffer absorption*: The buffer has a smaller band gap than the window, but larger than the absorber layer. Part of the light transmitted by the window, will be absorbed by the buffer (E_g for CdS is around 2.5 eV, E_g for In_2S_3 is around 2 eV [54]). The step in QE between 400 nm and 520 nm for CdS and 620 nm for In_2S_3 is created by this absorption. As the buffer layer is a part of the heterojunction, created charge carriers can diffuse and give a contribution to the current. Furthermore, as the buffer layer is very thin (50 nm), a fraction of the light can reach the absorber layer. For a CdS buffer thicker than 150 nm, all photons between 400 nm and 520 nm are absorbed. The height of this step depends

thus on the thickness and absorption coefficient of the buffer layer and on the efficiency of diffusion of charge carriers from the buffer towards the interface [12]. If there is an inverted layer or Fermi level pinning close to the conduction band, holes generated in the buffer have more chance to recombine at the interface which leads to a reduction of EQE for short wavelengths.

5. *Absorber band gap*: If the wavelength of incident photons is shorter than the maximum wavelength, which corresponds to the band gap, charge carriers can be created. The cut-off is not abrupt because of several reasons: the presence of an absorption tail (Urbach tail), band gap gradients and composition gradients in the absorber. The shape of the sub-band gap tail ($E < E_g$) may obey an exponential law of the Urbach type with α proportional to $\exp((h\nu\text{-}E_2)/E_u)$ with E_u the Urbach energy and E_2 an energy close to the band gap. The Urbach energy corresponds to the optical transitions between band tails below the band edges [71, 178]. Such tails can originate from deviations from the perfect crystal (e.g. due to defects or doping) or from fluctuation of electronic energy bands due to lattice vibrations [71].

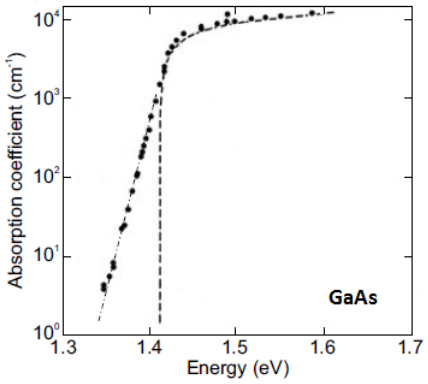

Figure 5.2: The dashed line is the theoretical dependence (equation 5.1), the circles are the experimental absorption spectrum of GaAs at room temperature on a semilogarithmic plot. The exponential tail below the band gap is called the Urbach tail [187].

6. *Incomplete Collection*: recombination before charge carriers are collected. This loss is stronger for longer wavelengths as these penetrate deeper into the absorber. As the distance to the space charge region is longer, recombination becomes more probable.

5.1.2 Band gap determination methods

As the emission energy in PL measurements is related to the band gap energy (see section 5.2.1.1), an estimate of donor and/ or acceptor energy could be given if the band gap energy is known. As the long wavelength side of EQE measurements is determined by the band gap, one could in principle determine the band gap. However although the EQE strongly depends on the absorber band gap, the determination of the band gap value is not unambiguous. As already mentioned, the absorption edges are not sharp due to band tails which hinder the determination of the band gap [224]. Furthermore several methods are used in literature to model the energy dependence of the absorption coefficient, which leads to differences in 'the' optical band gap. An overview of different methods is given here.

1. A first method found in literature consists of taking a linear extrapolation at the long wavelength side. Three different possibilities exists:

- performing a linear fit to the EQE edge and defining the band gap as the intercept of that line [225].

- If one assumes EQE $\propto \alpha$ and α for photon energies near the band gap is given by the parabolic equation 5.1 for a direct band gap, the intercept of a linear fit of EQE^2 on the abscis yields the value of E_g.

$$\alpha(h\nu) \propto (h\nu - E_g)^{1/2} \tag{5.1}$$

- Besides equation 5.1 for the absorption coefficient another equation (Tauc relation) for a direct band gap semiconductor is used (equation 5.2). This relation is used to determine the optical gap in amorphous thin-film materials. The intercept of the linear fit at EQE^2 yields again the band gap value.

$$\alpha(h\nu)h\nu \propto (h\nu - E_g)^{1/2} \tag{5.2}$$

2. A second method to calculate the band gap is differentiating the EQE curve. The band gap of the absorber is then determined as the extreme at low energy of the dEQE/dλ curve [224].

3. The band gap is determined as the energy where the EQE has dropped to or 20% or 50% [225] of its maximum value on the long wavelength side.

4. The relationship between the EQE and the absorption coefficient of an ideal junction can be approximated by [36, 151, 226].

$$EQE = 1 - \frac{exp(-\alpha W)}{1 + \alpha L_n}$$

For small minority diffusion lengths ($\alpha L_n < 1$) the above equation can be written as

$$EQE \propto 1 - exp(-\alpha W)$$

wherein the expression for the absorption coefficient (equation 5.1 or 5.2) can be inserted. A plot of $(\ln(1\text{-EQE}))^2$ or $(h\nu\ln(1\text{-EQE}))^2$ versus $h\nu$ yields a straight line which intersects the x-axis where $h\nu$ equals E_g.

An example of the different band gap values calculated following the different methods, is shown in the table below. As the variation between the calculated band gap values is large (1.44 -1.54 eV), estimating the donor/acceptor activation energy from the PL emission energy and the band gap determined via EQE measurements could yield large errors.

Table 5.1: Band gap energies calculated from EQE (figure right) following different methods found in literature. Error on the calculations is about 0.02 eV.

method	E_g (eV)
$\alpha(h\nu) \propto (h\nu\text{-}E_g)$	1.41
$\alpha(h\nu) \propto (h\nu\text{-}E_g)^{1/2}$	1.48
$\alpha(h\nu)h\nu \propto (h\nu\text{-}E_g)^{1/2}$	1.49
dEQE/dλ	1.53
50% of maximum	1.54
$(\ln(1\text{-EQE}))^2$	1.51
$(h\nu\ln(1\text{-EQE}))^2$	1.52

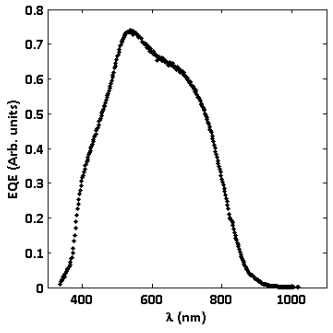

5.1.3 Set-up

All presented EQE measurements are performed at Empa unless stated otherwise. The solar cell is illuminated by a halogen lamp via a monochromator which selects the desired wavelength [12,62]. A chopper (frequency usually around 180-250 Hz) is placed between the halogen lamp and the monochromator in order to compare the signal under illumination with the dark current. A lock-in amplifier is used to determine the photocurrent produced by the monochromatic light.

For an EQE measurement the number of created charge carriers can be calculated as I_{sc}/q and the number of incident photons can be calculated as $\phi \cdot A$ with A the surface area and ϕ the photon flux. EQE can be written as [62]

$$\begin{aligned} EQE &= \frac{I_{sc}}{q\,\phi\,A} \\ &= \frac{I_{sc}}{P}\frac{hc}{q\lambda}\frac{1}{A} \\ &= S_{cell}\frac{hc}{q\lambda}\frac{1}{A} \end{aligned}$$

whereby P equals the incident light power ($P = \phi \cdot E = \phi \cdot \frac{hc}{\lambda}$) and S_{cell} corresponds to the spectral response of the cell ($S_{cell} = I_{sc}/P$). As the incident light power P is difficult to determine, a reference cell whose response is known ($S_{ref} = I_{sc,ref}/P$), is measured under the same conditions. As reference cells a calibrated Si and InGaAs cells are used. Following relations can be deduced [62]:

$$P = \frac{I_{sc,cell}}{S_{cell}} = \frac{I_{sc,ref}}{S_{ref}}$$

$$\frac{I_{sc,cell}}{I_{sc,ref}} = \frac{S_{cell}}{S_{ref}}$$

By substituting S_{cell} from the above equation, the EQE can be written as

$$EQE = S_{ref}\frac{I_{sc,cell}}{I_{sc,ref}}\frac{hc}{\lambda}\frac{1}{A} \tag{5.3}$$

5.2 Photoluminescence

The netto emission of light from a solid as a result of deviations from thermodynamic equilibrium electron occupation is described as luminescence. Various ways of disturbing the thermal equilibrium exists e.g.: application of external voltage (electroluminescence), incident electron beam (cathodeluminescence), absorption of light (photoluminescence)... As photoluminescence (PL) offers a non-destructive, sensitive tool for the spectroscopy of defects in semiconductors with low concentrations, it is used in this thesis for the identification of shallow-level defects in the CIGS/CZTS absorber.

5.2.1 Radiative recombination transitions

5.2.1.1 Non-compensated material

In a PL experiment, a photon is absorbed by the semiconductor and creates an electron-hole pair. The electron occupying the higher energy state can radiatively recombine with a hole in

a lower-energy state. A photon with the energy equal to the difference of the two energy states is emitted. Depending on the measurement conditions and the material properties, different transitions can occur in a PL measurement [5,10,16]: excitonic transitions (Free exciton (FX) or bound exciton (BX) transition), transitions between a free carrier in the band and a defect state (Free to Bound transitions (FB)), transitions between defects (Donor-Acceptor Pair transitions (DAP)) and transitions between the bands (Band to Band transitions (BB)). FB and DAP transitions are, naturally, most informative with respect to defects in semiconductors. Figure 5.3 gives an overview of the possible optical transitions as a function of increasing temperature. Each type of transition exhibits, depending on temperature (T) and excitation power (P_{exci}), certain peak shifts. Small overview of the characteristics of each transition type (in the order of their occurrence with increasing temperature) is given below.

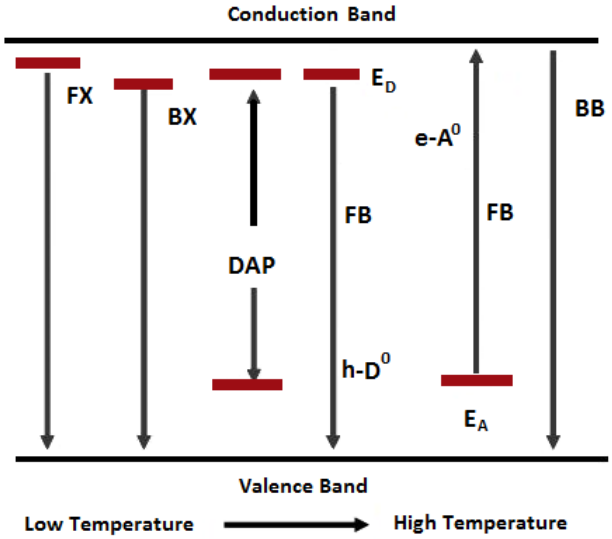

Figure 5.3: Possible transitions in PL measurement. Exciton transitions are observed at low temperature, band band transitions are observed at high temperature [5].

FX, BX: Exciton transitions

At low temperature, free excitons are formed due to the Coulomb attraction between electrons and holes. Free excitons recombine by emission of a narrow spectral line at energy E_g-E_X, with E_X the exciton binding energy [10]. The binding energy of the free exciton is calculated by the hydrogenic model [5, 16]: $E_X = \frac{m_r e^4}{2\hbar^2(4\pi\epsilon_0\epsilon_r)^2 n^2}$ with m_r the reduced mass ($1/m_r = 1/m_e + 1/m_h$) and m_e and m_h the electron and hole effective mass, respectively. The quantum number n specifies the possible excited states of the exciton. Levels different from the first levels are only visible in very good single crystals [16]. For $CuGaSe_2$ and $CuInSe_2$ a free exciton binding energy of 10 meV [5] and 18 meV [4] respectively, is expected.

Free excitons easily get bound to impurities. The binding energy of the bound exciton (E_{BX}) is increased, due to the attractive interaction between exciton and defect, by an amount proportional to the ionization energy of the defect. The transition energy for the bound exciton emission is given by E_g-E_{BX} [5, 10].

•*FX, BX: P_{exci} dependence*

Since the excitonic emission intensity depends on the concentrations of holes and electrons, each of which are proportional to the excitation power P_{exci}, the intensity of the PL emission (I_{PL}) follows a power law $I_{PL} \sim P_{exci}^k$, with k = 2 [10]. Because of possible alternative recombination paths, the exponent k can be smaller than 2 [16]. If the excitation intensity is increased, excitons do not exhibit a shift in their transition energy.

•*FX, BX: T dependence*
A decrease in PL intensity is expected with increasing temperature. With increasing thermal energy, carriers at states with low binding energies (shallow defects, excitons) will dissociate (thermalize into the bands) which leads to a decrease of transitions involving these states and hence a decrease in PL emission intensity. The thermal quenching of the free exciton luminescence can be described by [16]

$$I_{PL}(T) = \frac{1}{1 + a \cdot T^{3/2} exp\left(\frac{-E_a}{kT}\right)} \tag{5.4}$$

where the activation energy (E_a) corresponds to the exciton binding energy if the quenching process corresponds to the dissociation of the excitons into free carriers. The factor $T^{3/2}$ reflects the temperature dependence of the effective density of states at the band edge. If the density of states is temperature independent, the factor is omitted [16]. The energy position of the exciton follows the temperature dependence of the band gap, therefore a red-shift with increasing temperature is expected [10]. Only when the temperature is sufficiently low, optical transitions related to free excitons can be observed ($k_B T < E_X$). At higher temperature dissociation occurs. Since exciton transitions are not observed in the polycrystalline thin-films studied here, no further details will be given.

DAP: Donor-Acceptor Pair transition
If both donors and acceptors are present, donor-acceptor pair recombinations (DAP) can be observed. The electron from a neutral donor state recombines with a hole from a neutral acceptor state (donors and acceptors having previously captured a free carrier).

$$D^0 + A^0 \longrightarrow D^+ + A^- + h\nu$$

In the final ground state of the transition, the donors and acceptors become ionized. The Coulomb interaction between the donor and acceptor will make the energy of the emitted photon larger than the energy difference between the donor and acceptor states because the additional Coulomb energy (E_{Coul}) is transferred to the photon. The emission energy is given by [4,5,10,16]

$$E_{DAP} = E_g - (E_A + E_D) + E_{Coul} \text{ with } E_{Coul} = \frac{e^2}{4\pi\epsilon_0\epsilon_r r_{DA}} \tag{5.5}$$

where E_A and E_D are the ionization energies of the acceptor and donor, respectively and r_{DA} is the distance between the donor and acceptor. This distance depends on the impurity density and the excitation intensity. A large density of donors and acceptor implies that the average separation r_{DA} is small, which results in a higher peak energy. Further a large density gives rise to a large PL intensity as donor-acceptor pairs with small separations have higher transition rates because recombination occurs via tunneling [18]. A further evidence for a change in defect density can be provided by the half width of the peaks. It has been found empirically that the PL line width increases as the doping density is increased. Broadening can however also stem from grain boundaries [18].

•*DAP: P_{exci} dependence*
With increasing excitation density the number of photo-generated electrons and holes increases. As a result the average donor-acceptor separation decreases and the DAP emission line thus shifts to higher energy. The dependence of luminescence peak energy (E_{peak}) as a function of excitation power (P_{exci}) can be described as [180]

$$\begin{aligned} P_{exci} &= P_0\, exp\left(\frac{E_{peak}}{\beta}\right) \\ log(P_{exci}) &= C + \frac{E_{peak}}{\beta} \cdot log(e) \end{aligned}$$

which can be written as

$$E_{peak} = C + B \cdot log(P_{exci}) \quad \text{with } B = \frac{\beta}{log(e)} \tag{5.6}$$

A value of B of about 1-6 meV/decade is an indication for a DAP transition in weak -or non-compensated material [16]. In the case of compensated material the shift is much larger as will be explained in section 5.2.1.2. The maximum possible value for this shift in non-compensated material can be estimated by the ionization energy of the defect in the DAP with the largest spatial extension within the hydrogen like defect approximation [5, 84, 227]:
$E_{max} = \frac{e^2}{(4\pi\epsilon_0\epsilon_r)(2a_B)} = \frac{m_e^* e^4}{2\hbar^2(4\pi\epsilon_0\epsilon_r)^2}$ with a_B the Bohr radius of the spatially more extended defect and m_e^* the electron effective mass [84]. For $CuInSe_2$ with typical values of $\epsilon_r = 13.6$ and $m_e^* = 0.09m_0$, a maximum shift of E_{max} 6.6 meV is estimated [84].
For the luminescence yield as a function of excitation intensity, k = 1 is expected in the ideal case. In practice significantly smaller values are observed in the case of different competing transition types [16].

•*DAP: T dependence*
The temperature dependence of the luminescence intensity for DAP recombination is described by an expression similar to equation 5.4. Differences in the applied equation and variations in the interpretation can be found in literature. A small overview is given below.
- References [24, 146, 179, 228] apply, for DAP recombination, equation 5.4 which includes only one parameter for the activation energy. Different interpretations of the activation energy exist. In reference [228], the activation energy is assigned to the level with highest activation energy, while in reference [24] it is interpreted at the total donor-acceptor activation energy.

- In references [5, 10, 16] equation 5.4 is extended to equation 5.7 which contains two activation energies (for the shallower and deeper impurity state). The factors c_1 and c_2,which are proportional to the degeneracy factor ratio between the corresponding level and the ground state [21], can be proportional to $T^{3/2}$. References [5, 229] indicate that it is not always possible to get meaningful fits using equation 5.7.

$$I_{PL}(T) = \frac{1}{1 + c_1 \cdot exp\left(\frac{-E_{a1}}{kT}\right) + c_2 \cdot exp\left(\frac{-E_{a2}}{kT}\right)} \tag{5.7}$$

- The inapplicability of equation 5.7 for fitting the temperature dependences of PL intensity in CdTe, is discussed in detail in reference [229]. In CdTe the calculated small activation energy of a few meV for E_{a1} is not easy to explain. Equation 5.8, which takes into account a temperature dependent capture cross section of the carriers at the centres, is suggested. Reference [176] uses this fitting model in the PL analysis of a S-poor CZTS sample. E_a is interpreted as the acceptor activation energy in the DAP transition. References [179, 230] on the other hand use equation 5.8 for free to bound recombination in case of potential fluctuation.

$$I_{PL}(T) = \frac{1}{1 + a_1 \cdot T^{3/2} + a_2 \cdot T^{3/2} exp\left(\frac{-E_a}{kT}\right)} \tag{5.8}$$

- In reference [19] equation 5.9 is applied for fitting the PL intensities in Cu-rich CZTS. For E_{a1} a value of 28 meV is found, for E_{a2} a values 2 meV (smaller than the assumed exciton binding energy of 10 meV) is found.

$$I_{PL}(T) = \frac{B}{a_1 \cdot T^{3/2} exp\left(\frac{-E_{a1}}{kT}\right) + a_2 \cdot T^{3/2} exp\left(\frac{-E_{a2}}{kT}\right)} \tag{5.9}$$

As different models and interpretations exist for the temperature dependence of the PL intensity, it is not straightforward to compare different fitting results. In this work many attempts were however made to extract for CIGS series1-2 and also for CZTS series, activation energies from the PL intensity quenching behaviour using equation 5.7. No convincing agreement between the activation energies for the different samples could be found. Possible reasons for this are very divergent.
The temperature dependent intensity fitting can, in the first place, be influenced by the temperature range whereupon PL intensity can be measured. The fitting becomes more reliable if PL spectra can be measured at higher temperatures.
Second the PL spectrum consist of multiple contributions, a fitting of the underlying contributions at each temperature should be made prior to the fitting of the PL intensity as a function of temperature. The fitting of the temperature dependent spectra is in the cases where the individual peaks are not clearly indistinguishable, not straightforward and hence not free of errors. The temperature dependent fitting is further complicated due to the red-shift as a result of a decrease of band gap with increasing temperature and because of the effect of potential fluctuations on the spectra. It appears furthermore that only the temperature dependence of the peaks with highest intensity could be fitted very well.
Third the excitation power can have an influence on the electrostatic potential fluctuations (see section 5.2.1.2) and hence on the PL process as well. Therefore a good comparison of temperature dependent spectra of different samples might be complicated (explained for figure 6.31).
In sections 6.3.1.6 and 6.4.6 an unusual temperature dependence is noticed for CIGS samples. With increase of temperature an increase of the intensity was noticed for some peaks in certain samples. This is certainly not in agreement with the formulas used for fitting the PL intensity quenching behaviour.
Finally, reference [10] argues that the calculated activation energy might be influenced by non-radiative thermally activated processes.
Because of the different problems arising when fitting the quenching behaviour, it was not possible to extract reliable defect activation energy information from these fittings.

For DAP recombinations, the temperature dependence of the luminescence peak energy shows a blue-shift with increasing temperature [10, 16]. This can be explained by the fact that the recombination process involves a tunneling step which depends on the distance of the recombination pairs. With increasing temperature the thermal emptying of defects becomes more and more probable. More distant pairs get thermally re-emitted to the bands before they recombine hence the number of close pairs in the radiative recombination is increased as the recombination of the short-distance pairs is faster. The larger Coulomb term for the close pairs leads to a blue-shift of the order of kT of the emission spectrum with increasing temperature. When the shallower defect is thermally emptied, a free to bound transition between the deeper defect and the opposite band may remain.

FB: Free to Bound transition
The free to bound recombinations involve transitions of carriers from energy bands to the defect levels in the band gap. When there are donor or acceptor states in the band gap, two possible transitions can occur

- a free electron in the conduction band can recombine with a hole bound to an acceptor
  $A^0 + e \longrightarrow A^- + h\nu$
- an electron bound to a donor can recombine with a free hole in the valence band
  $D^0 + h \longrightarrow D^+ + h\nu$

Shallow transitions from the conduction band to donors or from the valence band to acceptors are unlikely, because the probability for phonon related transitions is much higher than the

probability of transitions involving the release of a photon. The shape of the luminescence intensity is given by [4, 10, 16]

$$I_{PL}(E) \propto (E - (E_g - E_{A/D}))^{1/2}\, exp\left(\frac{-(E - (E_g - E_{A/D}))}{kT}\right)$$

where $E_{A/D}$ represents the donor or acceptor ionization energy. The shape reflects the square root-like density of states in the band (for direct-gap semiconductors) and the quasi thermodynamic equilibrium occupation of carriers in the band [5]. Setting the derivative of the above equation to zero, the peak position of the transition can be found. The peak position is related to the optical band gap as [5, 10]

$$I_{PLmax}(E) \propto E_g - E_{A/D} + kT/2$$

•*FB: T dependence*
The above equation implies that as the temperature increases, the peak maximum shifts towards higher energy, if the temperature dependence of the band gap may be neglected (see section 5.2.3) [10]. The thermal quenching of the luminescence yield is again described by equation 5.4 [5]. The activation energy represents the ionization energy of the impurity state ($E_{A/D}$).

•*FB: P_{exci} dependence*
The PL intensity is proportional to the concentration of one free carrier type and on the density of defects. Since the former depends linearly on the excitation power and the latter is independent of the excitation intensity, k = 1 is expected [5, 10, 16]. Due to alternative recombination paths, the exponent can be reduced. The energetic position of a FB transition does not change with increasing excitation intensity.

BB: Band to Band transition
With increasing temperature, photo-excited electrons and holes more and more end up in the conduction and valence band, respectively [10]. As these free carriers can be regarded as moving independently (e.g. at room temperature) recombination takes place between these free carriers [16]. Band to band luminescence is, at low temperature, only observed in very pure materials [10, 186]. If there are impurity levels within the band gap, electrons and/or holes get trapped by these impurities.

•*BB: Temperature dependence*
The shape of the emission intensity as a function of energy reflects the square root-like density of states at the band edge of a semiconductor multiplied with the Boltzmann factor of the occupation [16]

$$I_{PL}(E) \propto \begin{cases} (E - E_g)^{1/2} exp\left(\frac{-(E-E_g)}{kT}\right) & \text{for E} > \text{E}_g \\ 0 & \text{for E} < \text{E}_g \end{cases}$$

For energies smaller than the band gap, there is a very sharp edge. The peak maximum can be found at energy E_g+kT/2 [16], which is larger than the band gap due to the kinetic energy of the free electron and hole [10].

•*BB: P_{exci} dependence*
Both free-carrier types are involved in band-band transitions, therefore a k value > 1 [5] is expected for the ideal case.

Phonon replicas
In a PL transition interaction between the electron and the crystal lattice (electron-phonon coupling) can occur. Phonons are the quantized quasi-particles of the lattice vibrations (normal

modes) [71]. Radiative transitions can occur with the emission of phonons, leading to so-called phonon replicas of the transitions [10]. This depends on the electron-phonon coupling strength and the measurement temperature. The energy spacing between different phonon replicas is the same as shown in figure 5.4. Different references [4, 5, 16, 64] state that the LO-phonon energy is around 30 meV for CI(G)S. For CZTS the LO-phonon energy is 41 meV following reference [39].

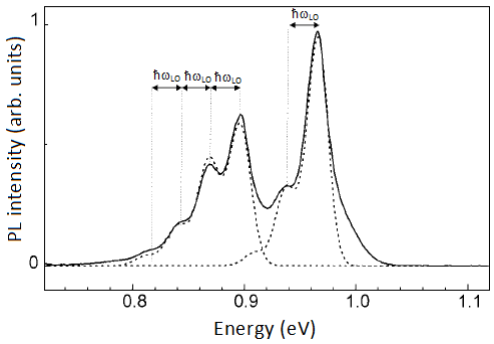

Figure 5.4: PL spectrum of Cu-rich CuIn(Ga)Se_2 at T = 4.2 K. The separation between the phonon peaks is 29 meV. The two bands are related to DAP recombination [227].

Overview transitions in non-compensated material

Table 5.2 summarizes the temperature and excitation power dependencies on the PL peak positions in non-compensated semiconductor material. The temperature dependence of the band gap is ignored.

Table 5.2: Peak shifts with increasing temperature and excitation power.

Transition	Increasing T	Increasing P_{exci}
FX, BX	red	no
DAP	blue	blue
FB	blue	no
BB	blue	no

5.2.1.2 Highly compensated material

Potential fluctuations of the bands

In a semiconductor, spatial fluctuations in the conduction and valence band edge energy positions can occur. Two fundamental types of fluctuations exists [231].

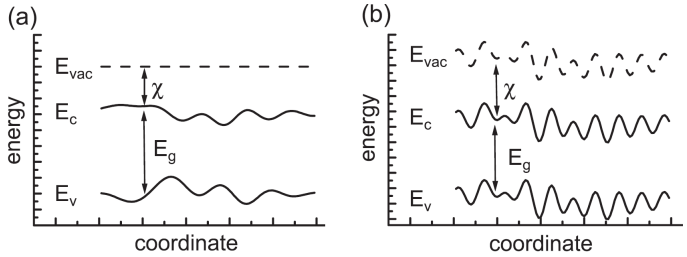

Figure 5.5: The two types of potential fluctuations for the conduction band and valence band edge. (a) band gap fluctuation, (b) electrostatic fluctuation [231].

- (a) Band gap fluctuations
  The fluctuations are independent for the conduction band and valence band (figure 5.5(a)). As a result the band gap is spatially inhomogeneous. The fluctuations can be due to

variations in the alloy composition (such as Cu_xSe phase), stress and non-stoichiometry (Ga or Cu content).

- (b) Electrostatic fluctuations
  The band gap width is constant, but the conduction and valence band edges fluctuate in parallel (figure 5.5(b)) [231]. The fluctuations are due to localized charges. Sources are a high degree of compensation (high density of charged donors and acceptors which is not screened by free carriers), grain boundaries of different orientations and charged dislocations [11, 232].

PL in compensated material with electrostatic fluctuations
For high concentration of donors and acceptors ($N_{a/d}$ a_B^3 >> 1) the impurity wave functions start to overlap and an impurity related band is formed which can perturb the conduction and valence bands [5]. When the high densities of acceptors and donors are comparable, the semiconductor becomes compensated. The net doping (N_a^++N_d^-) density is much lower than the dopant concentration (N_a+N_d). In the compensated material the minority defects lose their charge carrier to the majority defect. Both defects are charged (ionized) without generating free charge carriers that normally would screen the fixed space charges. For random spatial distributions of these defects, the situation leads to areas with a higher density of positively charged donors and areas with a higher density of negatively charged acceptors. This local variation of fixed space charge cannot be screened by the low free carrier density. This causes an irregular distortion of the band structure by spatial fluctuation of the electrostatic potential [5]. The band gap energy is everywhere the same (figure 5.5(b)). The average depth of the fluctuation γ is dependent on the total charged impurity concentration ($N_t = N_a^+$+N_d^-) and the screening by the free carrier concentration p [5].

$$\gamma = \frac{e^2}{4\pi\epsilon_r\epsilon_0}\frac{N_t^{2/3}}{p^{1/3}} \tag{5.10}$$

A typical γ value for polycrystalline $CuInSe_2$, with $N_a \approx N_d \approx 10^{18}$ cm^{-3}, p $\approx 10^{16}$ cm^{-3} and $\varepsilon_r = 13.6$, is 78 meV [5]. An example of the influence of potential fluctuations on the PL spectra is visible in figure 5.6 which shows PL spectra for samples in which the [Cu]/[Ga] or [Cu]/[In] ratio changed from Cu-rich to Cu-poor. The composition change implies a change from non-compensated to highly compensated absorber layers [84, 233]. Films grown under Cu-excess conditions show a completely different PL behaviour than those grown under Cu-poor conditions [16]. For Cu-rich films, excitonic luminescence and sharp transitions involving defects is visible. The narrow peaks change to a single broad emission band at lower energy for Cu-poor films.

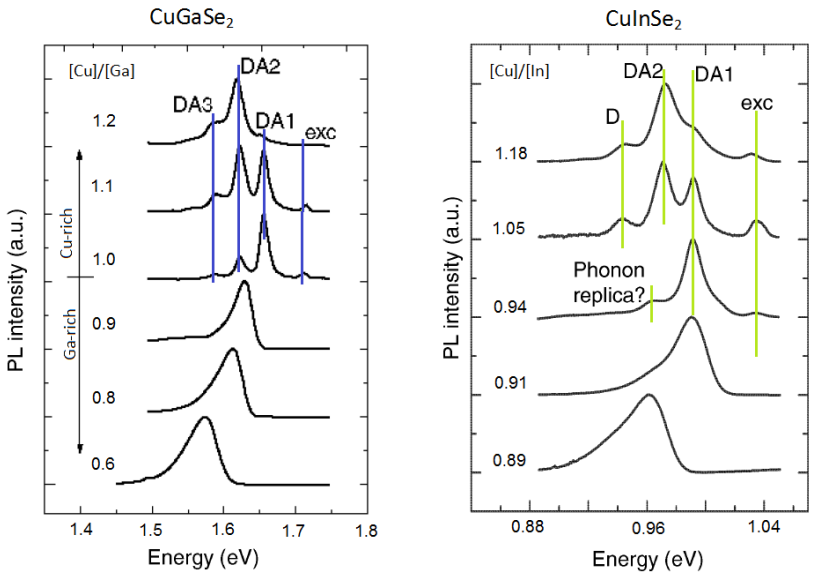

Figure 5.6: PL spectra of $CuGaSe_2$ and $CuInse_2$ as a function of composition [16].

For the analysis of the PL peaks in the presence of potential fluctuations two cases are distinguished in literature: (a) absence of merging of the donor states with the conduction band and (b) donor states are shallow and merge with the conduction band.

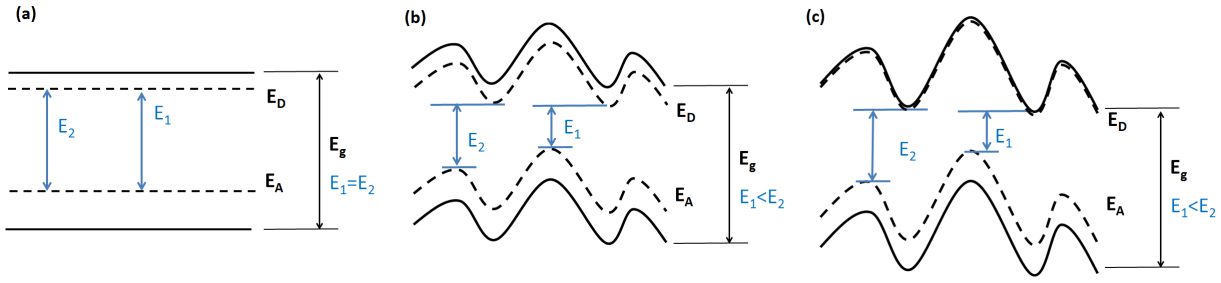

Figure 5.7: Effect of potential fluctuations on the band edges and DAP emission
(a) non-compensated semiconductor,
(b) compensated semiconductor (no merging),
(c) intermediate or strongly compensated semiconductor (donor levels merge with E_c) [180].

(a) No merging with E_c: quasi-DAP theory

In the theory of reference [180] the effect of potential fluctuations is explained for DAP recombinations. In this case the donor states do not merge with the conduction band (figure 5.7(b)). DAP transitions always involve tunnel processes, since the donors and acceptors are not located at the same site. In a weakly compensated semiconductor, this tunnel contribution does not affect the energy of the emission (besides the Coulomb term) because the bands are flat. In the case of bent bands, the tunneling between spatially separated donors and acceptors can considerably reduce the energy of the transition. A broad range of energies is available for these DAP transitions, leading to a broadening of the emission energy spectrum. Broadening of the PL bands can also stem from intentional (band gap grading) and unintentional (lateral changes in stoichiometry) inhomogeneities [5]. As the average emitted photon energy is lower than that in the uncompensated case, a red-shift relative to the uncompensated case can be noticed. The DAP emission will be labelled as 'quasi'-DAP recombination, after reference [180]. The recombination energy $E_{q\text{-}DAP}$ can be estimated with

$$\begin{aligned} E_{q-DAP} &= E_{DAP} - 2\gamma \\ E_{q-DAP} &= E_g - (E_A + E_D) - 2\gamma \end{aligned} \tag{5.11}$$

The emission is broadened and red-shifted by on average 2γ, which hinders the determination of defect activation energies involved in the PL processes [19, 150]. As γ increases with increasing impurity concentration (equation 5.10), the red-shift will be larger. $E_{q\text{-}DAP}$ is sensitive to changes in the excitation power as the rate of excitation determines the free carrier concentration and hence changes γ (equation 5.10) [84].

•*q-DAP: P_{exci} dependence*
An important feature of transitions under the influence of fluctuating potentials is a large blue-shift with increasing excitation intensity. This is due to two reasons: at low excitation power, the photo excited carriers are preferably in the potential valleys, electrons in potential minima and holes in potential maxima, and the spectrum is maximally red-shifted. As the excitation power increases, the probability to populate defects outside the minima and maxima of the band edges increases. Furthermore the amplitude of the fluctuating potentials [6, 84, 234] decreases as the increase of free carriers (increase of p) neutralizes defects states (decrease of N_t) and the screening of the remaining charged defects. An increase in excitation intensity gives as a result a flattening of the fluctuating potentials and thus a blue-shift in the energy position of luminescence maximum. This flattening of the fluctuating potentials leads to a decrease of the peak width, and finally at high very excitation powers the unperturbed spectrum can be obtained. Following reference [180] a large shift in energy per decade (equation 5.6) of excitation power in comparison with the flat band case can be measured. The higher the compensation, the higher the value of B. For Cu-poor CIGS material large B values in the range of 7-19 meV/decade have been found [75, 84, 120, 132, 234].

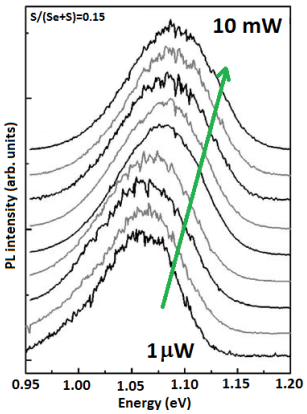

Figure 5.8: Typical experimental result of excitation power dependent PL measurements on Cu-poor CIGS thin-film (λ_{exci} = 514 nm, T = 4.5 K). With decreasing P_{exci} the spectra shift towards lower energy [84].

•*q-DAP: T dependence*
If the temperature is increased, the emission peak in strongly compensated semiconductors is found to red-shift at low temperatures. At low temperature there is a lack of complete thermalization of the carriers trapped in different potential wells, which leads to an incomplete filling of the deepest wells due to their smaller capture probability [5, 180]. As temperature increases, carriers become mobile and thermalize into the deepest wells. The situation relaxes with the establishment of a single quasi-Fermi level. The emission energy will shift to lower energy as temperature increases. For CZTS red-shifts of $1.5{\cdot}10^{-4}$ eV/K [21] and $4.7{\cdot}10^{-4}$

eV/K [176] are found in literature. For CIGS larger red-shifts are found; between $8.0{\cdot}10^{-4}$-$1.3{\cdot}10^{-3}$ eV/K [16, 84, 233, 235].
The analysis of the PL intensity dependence as a function of temperature can be ambiguous because of the thermal redistribution processes in the potential fluctuations [5] and because of the different proposed fitting models (equations 5.4, 5.7, 5.8, 5.9). In reference [21] the small activation of 4 meV energy obtained via a fitting of equation 5.8 is interpreted as related to the release of electrons from shallow potential wells.

(b) Merging with E_c: BI, TI theory
In the case of a compensated heavily doped semiconductor for which $N_d a_e^3 > 1$, $N_a a_h^3 < 1$ (heavy doping condition satisfied by the donors) (with a_e and a_h the Bohr radius of donor and acceptor state respectively [236]) there are no bound states associated with isolated donors, but well-defined isolated states associated with acceptors (figure 5.7(c)) [181, 236]. Fairly deep states in the band tail resemble impurity rather than band states, as they are strongly localized. Localized states in the conduction band tail are due to a point-like cluster of large number of donors [181, 236]. The shallow donor levels may easily overlap with the conduction band while the acceptor levels follow the fluctuations of the valence band [233]. As can be seen in figure 5.9 the conduction and valence band (E_c and E_v) are shifted below and above their positions in an uncompensated material (E_c^0 and E_v^0), this because of the large number of charged defects. The level above which electrons/holes are free (E_c and E_v) are shifted by γ_e towards lower energy and γ_h towards higher energy. Because the larger effective mass of holes, γ_h is smaller.

In a heavily doped p-type semiconductor the main types of transitions [236] are listed underneath. The transitions are indicated in figure 5.9.

- Band-Band (BB): recombination of free electrons with free holes
- Band-Tail (BT): recombination of free electrons with holes localized at deep tail levels
- Band-Impurity (BI): recombination of free electrons with holes localized at acceptors levels (represents free-to-bound recombination)
- Tail-Impurity (TI): electrons trapped at deep states in the conduction band tail recombine with holes localized at acceptors levels (represents DAP recombination)
- Tail-Tail (TT): electrons trapped at deep states in the conduction band tail recombine with holes localized at acceptors in deep states of the valence band tail (not main transition type, only for very strongly compensated heavily doped semiconductor)

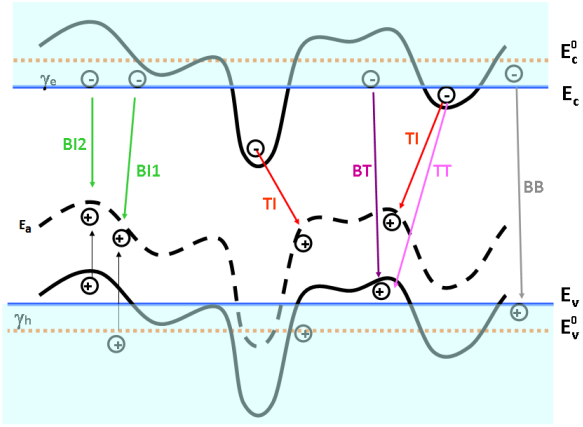

Figure 5.9: Recombination transitions in strongly compensated heavily doped semiconductor. $E_{c,v}^0$ are the edges of the band gap of an undoped semiconductor. $E_{c,v}$ are the levels above/under which electrons/holes are free (adapted from reference [236]).

Interband recombination (BB, BT, TT) governs the luminescence spectrum at higher energy compared to the transitions related to impurity levels (BI, TI). Characteristics of the band edge and impurity related luminescence are given underneath.

Edge luminescence: BB, BT and TT transitions
At low temperatures, due to the potential fluctuations, the holes are mostly captured by deep band states within the band gap and BT transition is dominant. The energy of the peak maximum decreases (red-shift) with increasing temperature, because of the thermal release of holes from shallower wells [236,237]. As temperature increases further the BB band transitions become dominant. With increasing temperature a red- to blue-shift appears. At intermediate temperatures two maxima due to BT and BB transitions may appear in the luminescence spectrum figure 5.10 [236].

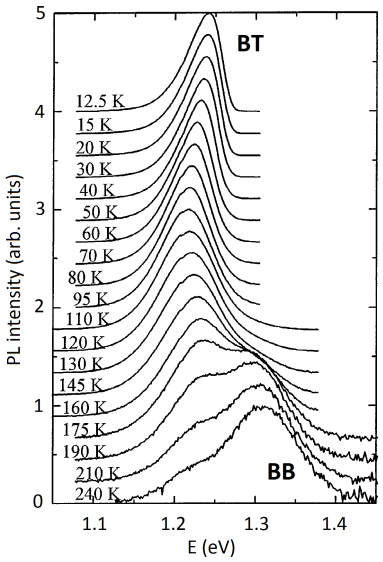

Figure 5.10: Normalized PL spectra of CIGS measured at different temperatures. The BB recombination becomes visible around 140 K [237].

Impurity related transitions: BI and TI transitions
As indicated in references [84,181,233] the recombination radiation emitted from a p-type compensated semiconductor at low temperatures is governed by BI and TI transitions.

- Tail-impurity: At low temperatures, the electrons are distributed in localized tail states in quasi equilibrium. At low temperature the maximum of the emission lies near the energy $h\nu = E_g\text{-}E_A\text{-}\gamma_e$ (with E_A acceptor energy) [236]. In case of low excitation power and temperature increase, the emission peak maximum decreases due to thermal liberation of electrons from the shallower donor wells [84, 236]. Electrons thermally released from the shallower donor wells can move to deeper wells.

- Band-impurity: Two kinds of BI recombinations are distinguished depending on the position of the acceptor in the semiconductor (figure 5.9) [84]. If the acceptor is in a region where holes are not free (potential valley for holes) a low energy BI2 recombination occurs, it can be assumed that the hole is first captured by a localized tail state and then non-radiatively by an acceptor state. If the acceptor is in a region where holes are free, it gives rise to the so-called BI1 recombination. As temperature increases, a change from BI2 to BI1 recombination (blue-shift) occurs because the hole has sufficient thermal energy to become free. At low temperatures and low excitation rates the maximum of the BI luminescence is given by $h\nu = E_g\text{-}E_A$ [236]. As BI recombination dominates at higher temperatures, a red to blue-shift can be understood as a TI to BI transition [84].

Overview transitions in compensated material
A general overview of the peak shifts with increasing temperature in the case of compensated heavily doped semiconductor is presented in table 5.3.

Table 5.3: PL peak shifts in compensated material

Increasing T	q-DAP	TI	BI	BT	BB
Shift	red	red	blue	red	blue

5.2.2 Penetration depth of excitation light

As the light absorption in a semiconductor depends on energy (equations 5.1 and 5.2), the penetration depth of the incident light depends on the excitation wavelength. As CIGS and CZTS have a high absorption coefficient ($\alpha \approx 10^5$/cm for CIGS (figure 2.18) and $\alpha \approx 10^4$/cm for CZTS (figure 2.26) in the wavelength range 300-700 nm), photons with energy above the band gap are absorbed very close to the surface while photons with lower energy (but still larger than E_g) penetrate deeper into the absorber layer [36]. Different excitation energies can thus probe different regions of the sample and can thus be used to distinguish near surface and rather deeper bulk contributions [186]. The choice of excitation light can thus have an effect on the PL measurements in terms of dominant peak if there is an inhomogeneous distribution of defects. Due to the high absorption coefficient, only a fraction of the absorber layer close to the buffer is investigated in PL [131, 228, 238]. A SCAPS simulation of the 1/e penetration depth for a CIGS layer (assumed homogeneous) of 2 µm (E_g = 1.2 eV), CdS layer of 50 nm and ZnO layer of 300 nm is presented in figure 5.11. The incident light power is 100 mW/cm^2. The absorption coefficient for the material $CuIn_{1-x}Ga_xSe_2$ in the SCAPS programme is interpolated internally between the defined extremum compositions (x = 0, x = 1) and is around 10^5 cm^{-1} [239]. The simulation shows that the 1/e penetration depth in the absorber changes from 70 to 120 nm in the 400-650 nm wavelength range. The penetration depth will further be dependent on the specific Ga grading in the absorber.

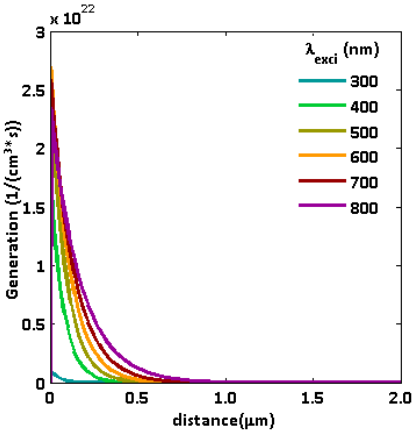

Figure 5.11: SCAPS simulation of penetration depth.

According to reference [79] the 1/e penetration depth, for composition ratios of y = 1 and x = 0.18-0.20, is 200, 55 and 25 nm for excitation wavelengths of respectively 700, 500 and 300 nm. According to reference [78], in which smaller absorption coefficients are found, the 1/e penetration depth (in case y = 1, x = 0.38 or in case of y = 0.91, x = 0.4) for excitation wavelengths of 700, 500 and 300 nm is estimated to be around 333, 111 and < 50 nm, respectively. In this work, most PL measurements are performed at an excitation wavelength of 500 nm. The penetration depth region is, according to references [78, 79], estimated between 55-120 nm.

Generated electron-hole pairs will recombine with a characteristic lifetime. During this time the carriers can drift and/or diffuse. Due to this transport, the recombination may occur in a place different from the one of excitation [238].
- Depending on the GGI ratio; different minority *diffusion* lengths ranging from 0.2 to 1.5 µm at room temperature are reported [4, 6, 47, 240, 241] (for GGI ratio around 0.3 the diffusion length is around 0.5 µm). The diffusion length of the minority carriers can be written as $L_{diff} = \sqrt{D\tau_e} = \sqrt{\frac{kT}{e}\mu_e\tau_e}$ [238]. The temperature dependence is difficult to calculate as the temperature dependence of the electron mobility values are still to be explored [6,241]. Reported hole mobility values for polycrystalline films are in the range of 0.1-170 $cm^2/(V{\cdot}s)$ [4,6,241] depending on the sample (for example GGI ratio or substrate temperature during growth [4]). The mobility tends to increase during the lowering of the temperature, after a certain temperature it decreases again. The temperature were the maximum mobility is reached, is dependent on the sample [4]. From the literature reports at room temperature it is difficult to deduce the effect of the diffusion length on PL measurements at 10 K, however the region wherein recombination takes place could be larger than the region determined by light generation.
- Besides diffusion, excited carriers can also be subjected to *drift* as a consequence of the electric field induced by the Ga grading. A drift of excited carriers toward the minimum of the band gap was seen at low temperatures in cathodeluminescence measurements reported in reference [242]. The electron drift length was calculated to be about 250-500 nm.

5.2.3 Band gap determination for interpretation of PL spectra

5.2.3.1 Issues regarding EQE analysis

Temperature dependence of E_g: In order to estimate the spectral shift between the PL emission peaks and band gap of the material, information about the band gap of the absorber at the temperatures of the PL measurements is necessary. One could think to use the band gap which can be extracted from EQE measurements. However as pointed out in section 5.1.2, the extraction of this band gap is not unambiguous. Moreover, even if 'the correct' band gap could be determined from EQE measurements, this is still the value at room temperature. This room temperature value will be too low, as the band gap increases with temperature. The temperature dependence of the band gap can in general be described by the empirical formula (Varshni model [71])

$$E_g(T) = E_g(0) - \frac{\alpha T^2}{T + \beta}$$

where $E_g(0)$ is the band gap at a temperature of 0 K, α and β are constants. The variation of the band gap in semiconductors is usually explained by electron-phonon interaction and the thermal expansion of the crystal lattice [70]. The shift of the band gap with temperature makes the interpretation of emission shifts as a function of temperature difficult. This band gap shift can compensate emission energy blue-shifts or enhance red-shifts with increasing temperature.

Effect Ga grading: It is important to notice that the band gap calculated from EQE, is the band gap at the position of the Ga dip and hence the minimal band gap. As the excitation light in PL measurements is already absorbed in the first part of the absorber layer (before the Ga dip), it is not correct to relate the calculated EQE band gap with the emission energy in the PL spectra of CIGS samples. Information about the band gap of the specific region of absorption is necessary to interpret PL results.

5.2.3.2 PL excitation

To determine the band gap at the temperature at which the PL measurements are performed, one could use PL excitation (PLE) measurements. In a PLE measurement, the excitation wavelength

is varied and the emission wavelength is kept constant. This is different from a PL emission measurement where a certain excitation wavelength is chosen and the emission intensity of the sample is measured over a certain wavelength range.
When the energy of excitation in a PLE measurement is larger than the band gap energy of the absorber, electron-hole pairs can be formed which can recombine radiatively through the impurity levels. The increase of the emission luminescence at the long wavelength side in a PLE measurement, is thus related to the absorption spectrum. Therefore in a PLE spectrum an increase of the emission intensity is visible as the excitation wavelength decreases. The problems related to the fitting model (linear or square root fit) still remain (section 5.1.2).
In the presence of potential fluctuations the cut-off of the excitation spectrum is related to the absorption spectrum but not identical to it because the efficiency of the emission is also involved as demonstrated in references [233, 243]. With different emission energies the PLE probes different depths of the potential fluctuations: at low/high emission energy, the carriers are in deep/shallow potentials wells such that the PLE onset is lower/higher. As the onset and slope of the PLE signal depend strongly on the luminescence emission energy chosen in the PLE experiment, no exact value of the band gap can be determined as shown in figure 5.12.

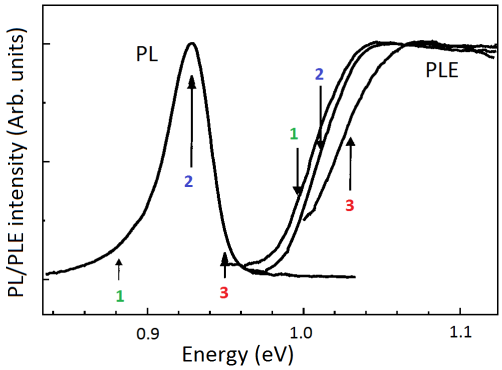

Figure 5.12: PL and PLE spectra of In-rich CuIn(Ga)Se_2. PLE spectra are performed at different detection energies of the PL spectrum [233].

5.2.4 Set-up

PL measurements are performed in collaboration with Lumilab, research group of the department of Solid State Sciences at Ghent University. The basic equipment set-up for low temperature PL measurements includes an excitation source, a cryostat containing the sample and a detection system as indicated in figure 5.13.

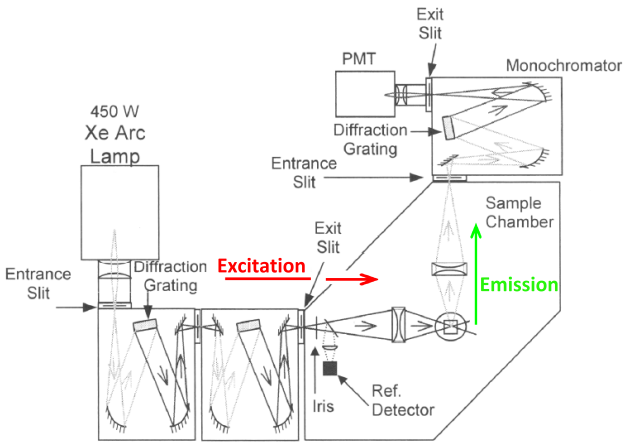

Figure 5.13: PL set-up.

PL measurements were performed with a fluorescence spectrometer (FS920, Edinburgh Instruments). The above band gap excitation source was a Xe arc lamp with double excitation monochromator or argon laser. The advantage of using a Xe arc lamp instead of a laser (which can deliver higher excitation power), is the possibility to vary the excitation wavelength. In order to eliminate higher order diffraction signals from the excitation light, the emission was filtered with a high-pass filter (600, 850 or 1000 nm cutt-off energy depending on the measurement). The excitation light makes an angle of about 45° with the sample surface. The spot size is around 0.5 cm^2. The excitation power (P_{0exci}), measured in front of the lens located before the cryostat, was in the order of 100 mW/m^2. Gray filters were placed in front of the cryostat window in order to decrease the excitation power. Grey filters were put in front of the sample to vary the excitation intensity. As low temperatures are necessary to obtain defect information from PL measurements, a He contact gas cryostat is used to cool the sample to a temperature of 10 K. Emission light was detected with a liquid nitrogen cooled germanium detector.
PLE measurements are performed in collaboration with Luminescent Lanthanide Lab, research group of the Department of Inorganic and Physical chemistry at Ghent University. In PLE measurements a super continuum white light laser (Fianium, 20 MHz 100 ps pulses in a range tunable between 400 and 2000 nm) was used as a 'quasi steady-state' source for excitation. After monochromation the emission signals were detected with single photon counting equipment (Hamamatsu R5509-72 PMT NIR-detector). A closed cycle cryostat was used in this set-up.

6 Experimental results of optical defect characterization

Contents

6.1 CZTS: Effect of anneal and buffer layer thickness

6.1.1 Motivation

During the short, high temperature annealing step, the precursor film is allowed to recrystallize to form a large-grained CZTS absorber layer [39]. An investigation of this important step in the device fabrication is done by a comparison of two different annealing methods. Furthermore in general, a deeper insight in the defect structure and fundamental material properties of CZTS is necessary to achieve higher solar cell efficiencies for this material. Most CZTS PL studies show a broad peak around 1.3 eV [21, 24, 176–178]. Two broad PL bands were detected

in reference [179]. The large line width of the PL spectra indicates that the material is strongly compensated. Another indication of the presence of potential fluctuations is the PL peak shift to higher energies with increasing excitation power [5,16,84,180,181]. As a result of the compensation, the determination of defect activation energies involved in the PL processes is hindered as indicated in section 5.2.1.2.

Below the results of the investigations concerning the defect structure of CZTS thin-film solar cells by means of PL measurements are described. Additional information about the separation of the band edge and PL emission was provided by PLE measurements. Three reactively sputtered CZTS thin-film solar cells are investigated which differ in absorber layer (different sputter targets and annealing step) or buffer layer thickness. Device performances of the cells are compared as well as their morphology and composition.

6.1.2 Preparation and performance

Cell preparation The CZTS thin-film solar cell structure is presented in figure 6.1. Substrates were prepared by direct current sputtering of Mo (350 nm) onto cleaned soda-lime glass slides. CZTS precursor films were deposited on the Mo layer by reactive pulsed dc magnetron co-sputtering of Cu, Sn and Zn in an H_2S atmosphere. The thickness of the absorber layer is around 2 µm. The CdS buffer layer (50 nm) is deposited by CBD. The window layer of ZnO (90 nm)/ZnO:Al (350 nm) was deposited by RF-sputtering, the contact grid Ni/Al/Ni (3 µm) by evaporation. The previous description applies for all cells; sputter targets, annealing step and buffer layer thickness are different and will be described below.

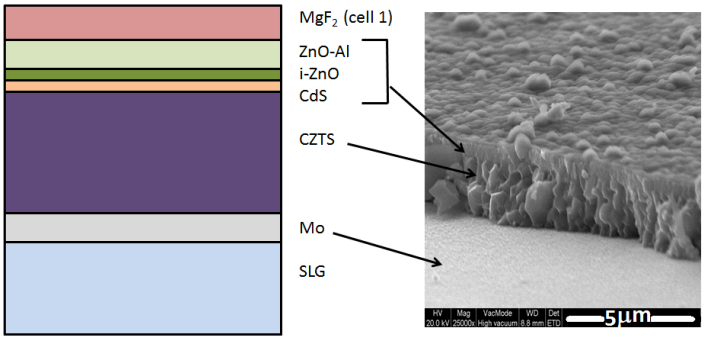

Figure 6.1: Left: cell structure, right: SEM image of cell1.

Cell1 is deposited by co-sputtering using metallic Cu:Sn (2:1) alloy and pure Zn targets in an atmosphere of H_2S. The precursors were annealed, face-down on glass, in a tube furnace under a static argon atmosphere without added sulfur for 3 minutes at 550°C (for more details see reference [244]). This cell has an additional MgF_2 anti-reflection coating (105 nm).

Cell2 and cell3 have the absorber layer in common with each other but differ in buffer layer thickness. The absorber layers are reactively sputtered in H_2S atmosphere using Zn and Cu:Sn (65:35) alloy targets. The samples are subsequently annealed in a sulfur atmosphere (graphite box) for 10 min (for more details see reference [245]). For cell2 the CBD was performed once. For sample cell3 the CBD was performed twice, which leads approximately to a double thickness. In experiments with repeated CdS depositions on glass, it has been seen to produce around double the thickness as determined by measuring the Cd intensity in XRF. The differences between all cells are summarized in table 6.1.

Table 6.1: Difference between investigated cells.

		Anneal		
	AR MgF_2	time (min)	S atmosphere	CdS thickness (nm)
cell1	yes	3	no	50
cell2	no	10	yes	50
cell3	no	10	yes	100

Solar cell device parameters Cell performance characteristics can be found in table 6.2. The I-V curves of cell2 and cell3, measured just after the production of the cells, are visible in figure 6.2.

Table 6.2: Cell performance characteristics of CZTS solar cells (numbers provided by Uppsala University).

sample	$\eta(\%)$	V_{oc} (mV)	J_{sc} (mA/cm^2)	FF (%)
cell1	3.50	528	16.6	43.4
cell2	6.05	657	14.8	62.3
cell3	5.62	652	14.5	59.3

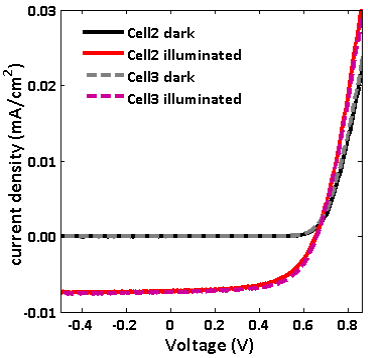

Figure 6.2: Illuminated and dark I-V curves of cell2 and cell3 (Uppsala university).

6.1.3 Spectral response

EQE measurements were performed without background illumination at room temperature in collaboration with ELIS (department of Electronics and Information Systems at Ghent University). Because some scratches were made on the samples, EQE measurements were performed on a limited surface. Therefore the intensity could be hindered by some shadowing. For a comparison the normalized spectra are shown in figure 6.3. The EQE spectra give information about the difference in absorption at the long wavelength side and about the effect of the buffer thickness at the short wavelength side.

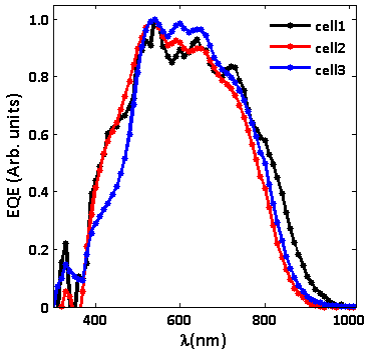

Figure 6.3: Normalized EQE of CZTS solar cells.

Long wavelength side: band gap determination
In the case of an ideal solar cell, the quantum efficiency would be a step function that is unity for all wavelengths below the wavelength corresponding to the absorber band gap and zero above. In reality, the cut-off will not be abrupt because of band tails in compensated material (see section 5.1.1). The non-abrupt cutt-off is visible in figure 6.3. A linear extrapolation of the squared EQE yields a rough estimate of the band gap at room temperature. As the absorber layer is the same for cell2 and cell3, the band gaps are, within experimental error, identical; $E_g = 1.49 \pm 0.03$ eV for cell2 and $E_g = 1.46 \pm 0.03$ eV for cell3. The values are close to the band gap expected for of CZTS (≈ 1.5 eV) [150]. The onset of absorption for cell1 lies at longer wavelengths. This difference can be caused by different annealing process and related composition differences as shown in references [177, 246]. The latter cannot be confirmed by EDX measurements as no clear difference in elemental composition is measured. The band gap of cell1 is estimated as $E_g = 1.41 \pm 0.07$ eV.

Short wavelength side: effect of buffer layer thickness
As a result of a doubled thickness of the buffer layer in cell3, the EQE in the short wavelength region (400-500 nm) is lower compared to cell2, because more light is absorbed in the thicker buffer layer. This optical loss at short wavelengths for cell3 results in a lower efficiency (5.62%) compared to cell2 (6.05%). From around 500 nm the EQE curves of the two cells cross. This means from excitation wavelengths of 500 nm there will be good absorption (EQE 81%) in the absorber layer.

6.1.4 Morphology

By SEM images an idea of the absorber quality and morphology can be obtained (figure 6.4). For cell1 the MgF_2 layer is visible above the ZnO window layer. In none of the cells the CdS buffer layer is distinguishable. The morphology of the cells is quite similar, small grains are present.

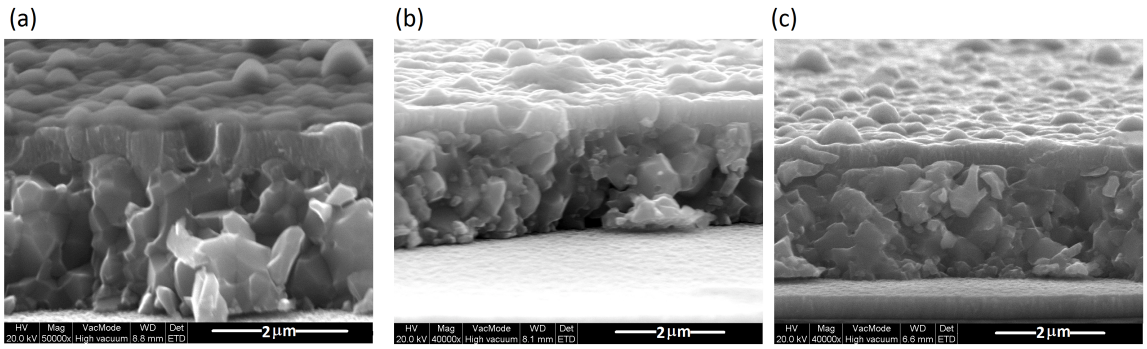

Figure 6.4: SEM images of the investigated cells (a) cell1, (b) cell2, (c) cell3.

6.1.5 Composition

XRF

The metal composition of the non-annealed sample (precursor film) is measured with X-ray fluorescence spectroscopy (XRF), calibrated with Rutherford backscattering. Numbers were provided by Uppsala University. The results of the measurements performed at samples from the same run ('sister piece') are presented in table 6.3 and show that all precursor films have a slightly Zn-rich composition.

Table 6.3: XRF measurements on CZTS precursor films (numbers provided by Uppsala University).

	Atomic percent			Ratios	
Sister piece of	Cu	Zn	Sn	Cu/(Sn+Zn)	Zn/Sn
cell1	0.46	0.28	0.26	0.84	1.1
cell2 and cell3	0.47	0.29	0.24	0.89	1.2

For cell1 no composition information after annealing is available, cell2 and cell3 are measured with EDX after annealing. By comparing the EDX measurement with the XRF measurement on the precursor sample, a shift between EDX and XRF is calculated. The EDX measurement performed after annealing, was calibrated by this value. Measuring with EDX (acceleration voltage 20 kV) from the top on the annealed samples, calibrated against XRF, shows that a small amount of Sn is lost, giving a stoichiometric Cu/Sn ratio, while the Zn-excess is not changed (Cu/(Sn+Zn) = 0.91 and Zn/Sn = 1.2).
Sulfur composition after annealing of glass/Mo/CZTS samples is difficult to measure because the sulfur and molybdenum peaks in the EDX spectrum are not easily distinguished as an overlap exists between the sulfur K lines and the molybdenum L lines at about 2.3 keV. Therefore the acceleration voltage was reduced below 12 kV in order to reduce the penetration depth whereby Mo is not detected. By reducing the acceleration voltage the Zn peak is not visible any more. A reference sample without Mo, which consists of CZTS deposited on Si, is made in the same run. A comparison of S/Sn on the Si/CZTS reference sample and glass/Mo/CZTS is possible and is performed for cell2 and cell3. The overall S content is around 50% in these samples. In conclusion, EDX/XRF measurements show that the samples are Zn-rich.

EDX - Difference in S composition between cell1 and cell2

EDX line scan measurements (performed in collaboration with Lumilab, research group of the department of Solid State Sciences at Ghent University) of S_K, Cu_K, Zn_K, Mo_L, Sn_L and Mg_K lines are performed on a cross section of cell1 and cell2 (figure 6.5). To separate the Cu and Zn signals (their L lines at lower energy are very close), the acceleration voltage must be high (15 kV), which implies lower spatial resolution.

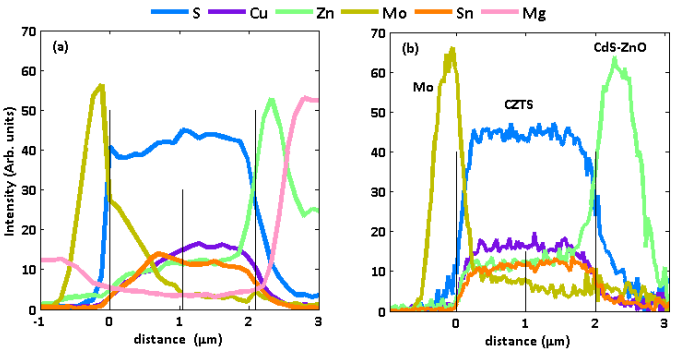

Figure 6.5: EDX line scan measurements of (a) cell1, (b) cell2. Black lines indicate begin, middle and end of the absorber layer.

Because of a high number of different elements in the solar cell, the specific geometry of the sample (signals from Mo and ZnO layer near absorber could overlap with S and Zn signals coming from the absorber layer) and overlapping peaks, it should be stated that the concentration results are only semi-quantitative and will only be used to investigate if there is a large influence of the different annealing step in H_2S between cell1 and cell2. No absolute values concerning the composition will be used from these measurements. Spectrum corrections have been applied in order to obtain semi-quantitative concentration values. This includes subtraction of the background and calculation of the number of counts for each element by measuring the areas of the X-ray peaks of each element. When peaks are overlapping, peak deconvolution is applied. The number of counts is subsequently converted into elemental concentrations by comparison with a standard and taking into account a sensitivity factor. As overlapping Mo and S signals hinder a correct measurement at the back of the absorber layer, ratios between different elements are calculated in the first half of the cell (surface region).
Although the annealing for both cells was different, the S/(Cu+Zn+Sn) ratio is approximately the same for both cells as visible in table 6.4. From the EDX cross sections it could be concluded that the difference in annealing does not lead to a clear composition difference between the cells.

Table 6.4: Composition ratios between cell1 and cell2 determined from EDX.

sample	Cu/(Zn+Sn)	Zn/Sn	S/(Cu+Zn+Sn)
cell1	0.68	1.07	1.11
cell2	0.65	1.10	1.09

6.1.6 Photoluminescence

6.1.6.1 PL emission

Position dependence and fitting procedure
The PL spectra of the CZTS cells consist in most cases of a very broad peak without any substructure which makes the interpretation rather difficult. However differences in shape between the spectra exist as result of differences in relative intensity of individual peaks, which can be related to spatial variations within the cells. The variations in peak intensities in the spectra can also be obtained by changing the sample position with respect to the excitation spot. By slightly rotating the sample or shifting it in the vertical position, another spot on the sample is illuminated or the horizontal penetration depth can be altered as illustrated in figure 6.6 (the possible effect of interference will be discussed in section 6.6). The variations in individual peak intensities are an important aid to verify if a correct fitting is reached.

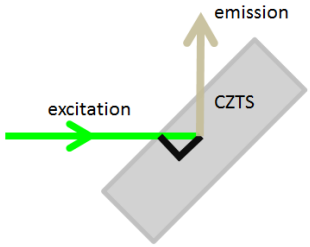

Figure 6.6: Position of sample relative to excitation and emission light.

The PL spectra (of CZTS as wells as of CIGS) can be decomposed in multiple, broad Gaussian components ($a \cdot \exp(-((x-b)/c)^2)$, with a the amplitude parameter, b the peak position and c the peak width parameter) [17]. In the fitting procedure, a shift of maximum 3 meV for each component between different cells, was allowed as the emission peaks can shift relative to each other because of a change in temperature, excitation power and defect density for DAP recombinations. If the donor or acceptor density decreases, the average separation increases, which reduces the Coulomb term and lowers the emission energy [18]. The fitting is applied on normalized spectra in which the background is subtracted, the intensity and peak width of each component is kept variable. The fitting is first performed on the spectra which reveal most substructure. In order to check if the fitting is correct, the fitting is, keeping the energy positions fixed, applied to other spectra measured at different positions/excitation angles. As excitation wavelength dependent measurements in some cases reveal a decrease or increase of some components, the accuracy of the fitting is further checked on the excitation wavelength dependent spectra. In the last step, temperature dependent spectra are fitted. At higher temperature these spectra reveal, in some cases, more clearly the contribution of individual peaks. In the fitting of the temperature dependent spectra a certain decrease of the PL peak energy as temperature increases (band gap decrease and/or red-shift as a result of potential fluctuations) is taken into account. In the fitting of PL spectra of different cells/samples, the whole series of peaks is shifted to higher or lower energy. The fitting error on the energy position of each Gaussian component is estimated in the order of 5 meV.
For cell2 and cell3 it is rather straightforward that same defects would appear because the absorber layer is made in the same run. As the composition of cell1 is not very different (see section 6.1.5), the assumption that same transitions could appear, is investigated. As the PL spectra of cell1 lie at lower energy, the energy positions of the fitting for cell2(3) are shifted towards lower energy. The intensity and the broadness of the peaks could vary. It is found that the spectra of cell1 could be fitted with the same energy separation between the peaks as for cell2(3).

Position dependence cell3

A description of the cell which showed the clearest individual contributions will be given first. Figure 6.7(a) shows spectra of measurements of cell3 performed at different positions and at different openings of the excitation monochromator slits. In the low intensity spectrum two main peaks can easily be distinguished. The distinction between the two peaks disappears as the PL intensity increases. The spectra can be fitted with the same three Gaussian peaks (figure 6.7(b)).

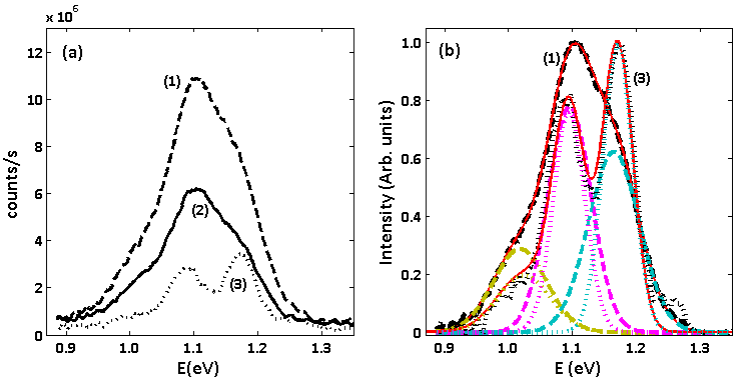

Figure 6.7: (a) PL spectra of cell3 at different positions (λ_{exci} = 500 nm, T = 10 K), b) normalized and fitted spectra of position (1) and (3).

Position dependence cell2

In figure 6.8 the spectra of cell2 (measured with different set-up and hence different positions) are shown. Only a small dependence on the sample position can be noticed. Both spectra can be fitted with the same three Gaussian peaks as applied for cell3.

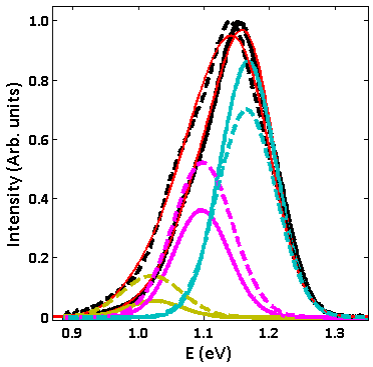

Figure 6.8: Spectra of cell2 at different positions (λ_{exci} = 550 nm, T = 10 K).

Position dependence cell1

Figure 6.9 shows the emission spectra of cell1 which are recorded with a Xe arc lamp lamp and an argon laser for excitation. The spectra look very different as sample position is changed. Again three Gaussian peaks suffice to fit the spectra. Peak 1 is more pronounced for position 1, peak 2 is more pronounced for position 2. It is this position dependence that made it possible to distinguish the contributions.

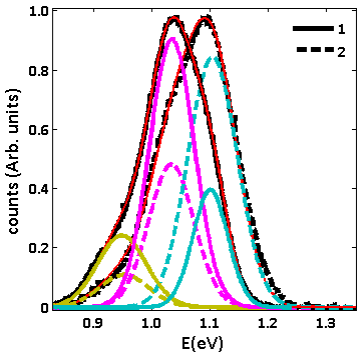

Figure 6.9: PL spectra at 5 K for cell1 measured with different excitation source. Position 1: laser (λ_{exci} = 514 nm) Position 2: lamp (λ_{exci} = 550 nm).

Comparison PL spectra of different cells

The spectra of all cells at low temperature are compared in figure 6.10. The spectrum of cell1 is shifted over around 60 meV towards lower emission energy compared to the spectra of cell2 and cell3. This is in accordance with the lower band gap energy extracted from EQE measurements for cell1. Cell2 and cell 3 have the same absorber layer therefore the emission appears in the same energy region (figure 6.10(b)). In none of the spectra phonon replicas or any structure in the exciton region can be seen. Each spectrum shows broad emission bands which are an indication of fluctuating potentials in Cu-poor/Zn-rich material [150]. The maximum of the emission (around 1.04 eV for cell1 and 1.15 eV for cell2(3)) appears for all cells at significantly lower energy compared to literature (normally around 1.3 eV). Another remarkable difference compared to literature is the appearance of three contributions in the spectra instead of one broad peak.

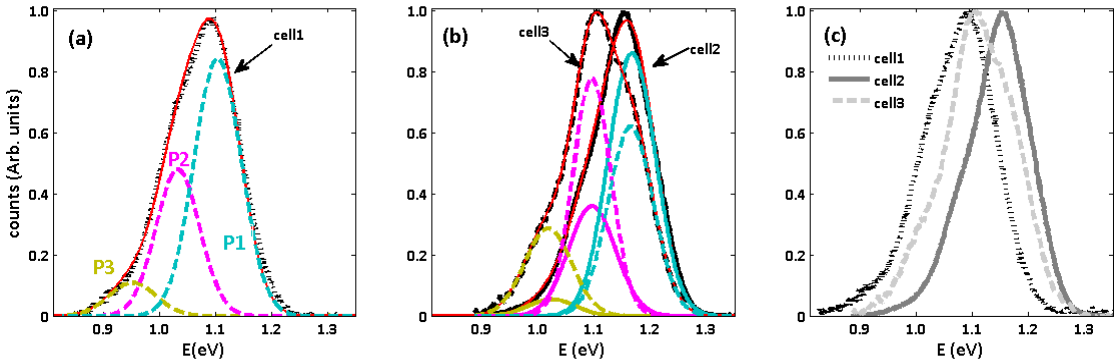

Figure 6.10: Normalized and fitted PL spectra of
(a) cell1 (λ_{exci} = 514 nm, T = 5 K, position 1),
(b) cell2 (λ_{exci} = 550 nm, T = 10 K) and cell3 (λ_{exci} = 500 nm, T = 10 K),
(c) Comparison PL spectra cell1-3.

All spectra can be fitted with 3 Gaussian peaks, labelled from high to low energy as P1, P2 and P3. From the fitting it is clear that the differences in shape of the spectra are a result of differences in relative intensity of individual peaks. The energy separations between the peak maxima is similar for the three cells as presented in table 6.5.

Table 6.5: Peak positions and difference.

	E_{max} (eV)			ΔE_{max} (eV)	
	P3	P2	P1	P1-P2	P1-P3
cell1	0.952	1.033	1.104	0.071	0.152
cell2	1.022	1.096	1.167	0.071	0.145
cell3	1.019	1.095	1.165	0.070	0.146

Excitation wavelength dependence of PL spectra

Excitation wavelength dependent measurements of cell2 and cell3 (figure 6.11) at constant low temperature reveal, in accordance with the EQE results, the effect of absorption by the buffer layer. Lower intensities for excitation wavelengths smaller than 500 nm are noticed for cell3 compared to cell2 and are an evidence of a thicker buffer layer of cell3. The ratios of the intensity maxima for excitation at 450 nm and 500 nm (absorption in buffer/transmission through buffer) are 0.43 for cell2 and 0.31 for cell3.

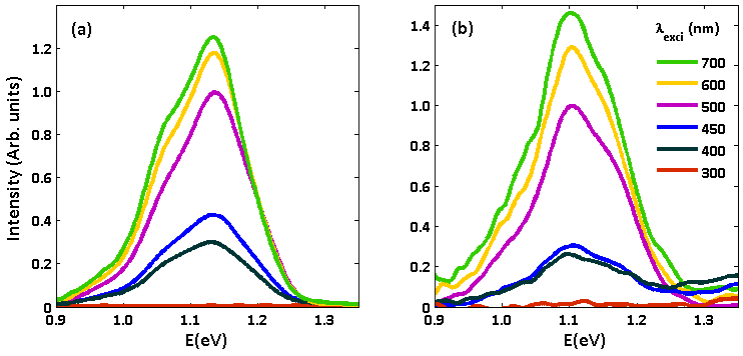

Figure 6.11: Excitation wavelength dependent spectra normalized to the maximum of the spectrum at λ_{exci} = 500 nm (T = 10 K) (a) cell2, (b) cell3.

Excitation power dependence of PL spectra

In excitation power dependent PL measurements on cell2 (figure 6.12(a)) gray filters were placed in front of the cryostat window in order to decrease the excitation power. The excitation power measured in front of the lens located in front of the cryostat ($P0_{exci}$), was in the order of 290 mW/m^2.

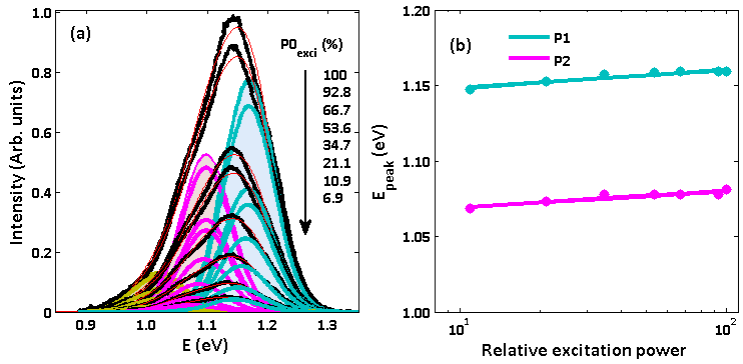

Figure 6.12: (a) emission spectra of cell2 at different excitation powers (λ_{exci} = 500 nm, T = 5 K), (b) emission peak energy of P1 and P2 as a function of excitation power.

The measurements exhibit a large blue-shift with increasing excitation power. The emission peak energy for peaks with highest intensities (P1 and P2) as a function of excitation power is shown in figure 6.12(b). A linear fit according to $E_{peak} = C + B \cdot \log(P_{exci})$ (equation 5.6) gives as a result for B 11 ± 2 meV/decade of excitation intensity for P1 and 12 ± 2 meV/decade for P2. These rather large values are an indication of the presence of potential fluctuations in the material [21, 176].

Temperature dependence of PL spectra

The emission spectra as a function of temperature for cell1 and cell2 are shown in figure 6.13. All temperature dependent PL spectra can be fitted with 3 Gaussian peaks. As the temperature for the detection of PL emission is limited to 70 K, no fitting of the temperature dependence of the peak intensity is made. Moreover as indicated in section 5.2.1.2, the interpretation of the fitting results is not straightforward because of different proposed fitting models and the effect of potential fluctuations.

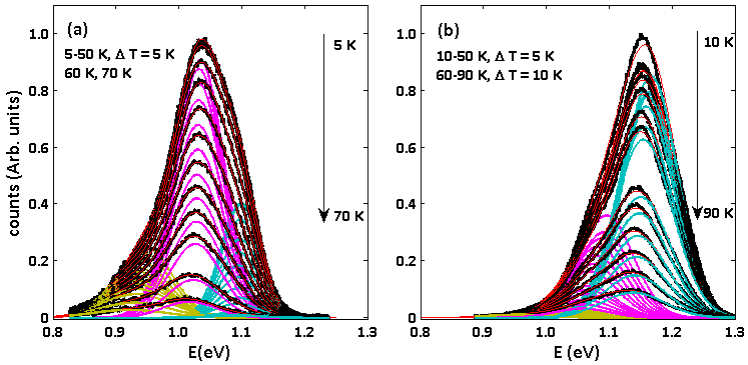

Figure 6.13: Temperature dependent measurement at λ_{exci} = 550 nm (a) cell1, (b) cell2

The red-shift with increasing temperature can be related to the decrease of the band gap with increasing temperature but it may also be a result of potential fluctuations in the material (see section 5.2.1.2). In material without potential fluctuations a blue-shift (or no shift) should appear with increasing temperature for DAP (free to bound) recombinations [16]. Reference [180] states that the emission energy of a q-DAP transition shifts to lower energy as the temperature increases. For a tail-defect and band-tail transition a red-shift is expected for the emission energy. A blue-shift with increasing temperature is expected for a band-defect transition [84, 236, 247]. In the investigated temperature region no change from a red-shift to a blue- shift, which could indicate a transition from tail-defect to band-defect recombination or from band-tail to band-band recombination [84, 233, 247], is visible. Moreover for the latter transitions, the low energy signal is quenched in favour of the high energy signal [233, 237]. This is not clearly seen in the spectra of figure 6.13. The appearance of only a red-shift, the absence of red to blue-shift and absence of the strong quenching of the low energy signal favours the explanation of the emission peaks by q-DAP transitions. More information could be obtained if the PL signal could also be detected at higher temperatures.

6.1.6.2 PL excitation

Importance of PLE measurement

In order to estimate the spectral shift between the PL emission peaks and band gap of the material, it is important to compare both values at the same temperature and preferably also for the same absorber. As the PL peak maximum for the investigated cells is found at much lower energies (around 1.04 or 1.15 eV) compared to the peak around 1.3 eV which is normally measured, the energy separation between the band gap determined in literature (1.52-1.64 eV at 10 K [19, 20]) would be very large. Relying on literature results is thus very likely to lead to incorrect interpretations, therefore PLE measurements on the investigated cells were performed. These PLE measurements have moreover the advantage that the same CZTS area as for the PL measurements is investigated.

Temperature dependence PL-PLE

In figure 6.14 the temperature dependence of PL and PLE spectra for cell2 is shown. The excitation wavelength for the PL measurements was 550 nm, the emission wavelength for the PLE measurements was 1070 nm which equals the wavelength of the maximum intensity in the PL spectra of cell2. It is visible that the long wavelength side of the PLE spectra is structureless: a free exciton band is not resolved, which confirms the presence of potential fluctuations in the material. The increase of the excitation spectrum intensity at the long wavelength side is not identical to the optical absorption spectrum because the efficiency of the emission in case of potential fluctuations is also involved, as demonstrated in section 5.2.3. Therefore no absolute value of the band gap can be determined, only an estimate can be given.

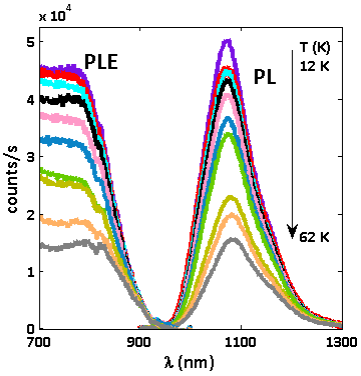

Figure 6.14: Temperature dependence of PL and PLE for cell2, the arrow indicates temperature decrease from 12 to 62 K.

The linear extrapolation of squared PLE (labelled as $E_{g,PLE}$) at 12 K is 1.42 ± 0.04 eV. This value is smaller than the band gap values at low temperature found in literature (1.52-1.64 eV at 10 K [19, 20]) and is smaller than the band gap value at room temperature determined form EQE values. The appearance of the PL emission at an energy lower than expected (around 1.2-1.3 eV at low temperature (5-20 K) [21–24]), is hence in accordance with the smaller band gap value found by PLE measurements. This result shows that PLE measurements can give valuable additional information. For a complete understanding a study of the temperature dependence of the band gap might be performed. Low emission energy might further be related with the low excitation power which is used in the measurements performed here, in comparison with literature, where laser excitation is most often used. The separations between $E_{g,PLE}$ and the emission peak energies at 12 K are given in table 6.6. The differences are large (250-400 meV), indicating that rather deep defects are involved in the q-DAP transitions. In CIGS the shift between the PLE onset and PL maximum is smaller than 200 meV [75, 233, 235, 243, 247].

Table 6.6: Peak positions of cell2 and energy separation with $E_{g,PLE}$ = 1.42 eV at T = 12 K.

	P1	P2	P3
E_{max} (eV)	1.167	1.096	1.022
$E_{g,PLE}$ - E_{max} (eV)	0.251	0.322	0.396

The temperature dependence of the peak energy for P1 and P2 (peaks with highest intensity) of cell1 and cell2 in relation with the temperature dependence of $E_{g,PLE}$ for cell2 are displayed in figure 6.15. In the investigated temperature region for cell2 (12-110 K) a red-shift of about 48 meV ($4.8 \cdot 10^{-4}$ eV/K) is seen for the emission peak energies. Similar decrease for cell1 can be noticed. The red-shift is rather small and in accordance with references [21, 176].

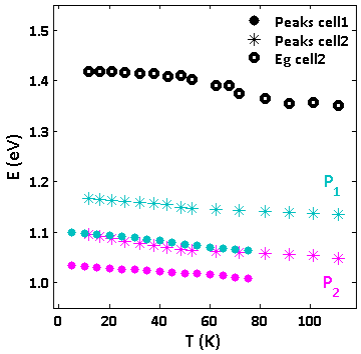

Figure 6.15: Comparison of temperature dependence of P1 and P2 of cell1 and cell2 and $E_{g,PLE}$ of cell2.

A clear decrease of the linear extrapolations of squared PLE as a function of temperature can be noticed on figure 6.15. The maxima of the PL peaks roughly follow this band gap shift. The red-shift of the PL spectrum expected for q-DAP recombination compared to the band gap decrease with increasing temperature seems rather small. This might be related to the deep energetic position of the defects. This is in accordance with reference [179] which shows that the temperature dependence of two peak maxima in the spectra follow more or less the temperature dependence of the band gap as calculated in reference [20]. In that study the two PL bands showed a strong blue-shift with increasing excitation power (15 meV/decade) and were explained by band-defect transitions involving the same deep acceptor (280 meV) but in different CZTS phases with a different band gap.

6.1.7 Defect interpretation

Despite annealing differences between the cells, all spectra could be fitted with three Gaussian contributions for which the energy separation was kept constant. All spectra exhibit a large blue-shift with increasing excitation power which is typical for recombination in highly compensated semiconductors where potential fluctuations are present. Because of the relatively large spectral shift of the emission peaks from the band gap energy determined via PLE measurement, q-DAP pair recombination seems the most probable PL recombination mechanism.

Two explanations for the occurrence of three PL peaks are evident: 1) q-DAP recombination between different defect pairs and 2) q-DAP recombination of one dominant defect pair in different phases of the polycrystalline absorber. As explained below, the experiments do not clearly favour one of these models, a combination of both may also be possible.

1) q-DAP recombinations between different defects

For the first explanation information about possible defects in CZTS is necessary. So far, in comparison with CIGS, considerably less experimental and computational efforts have been spent in determining formation energies and defect level positions in CZTS. Generally, from section 2.3.2.6, experimentally determined thermal activation energies are lower than compared to theoretical first principles calculations. The latter do however not completely agree on the nature of the dominant defects and the level positions they introduce in the CZTS band gap. The large defect activation energies predicted by theoretical calculations (see table 2.8 in section 2.3.2.6) seem confirmed by the large shift between the band gap determined from PLE and the emission maxima in CZTS measured in this study. At this moment, it seems not obvious to link the results for the observed three PL peaks to these theoretical predictions. The exact determination of the correct defect activation energies is hindered by: the dependence of the

peak position on excitation power, the unknown value of γ in the relation of q-DAP emission energy $E_{h\nu} = E_g\text{-}(E_A+E_D)\text{-}2\gamma$ (equation 5.11), the dependence on detection energy in PLE measurements (see section 5.2.3.2). Further experimental and computational studies are necessary to provide clarity into the origin of the donors and acceptors involved in the PL processes.

2) Same q-DAP recombination mechanism in different phases in the absorber layer
The differences in peak energy between P2 and P1, and P3 and P1 (see Table 6.5) might be related to the difference in band gap energy between the kesterite and disordered phase (0.04 eV [167]), and kesterite and stannite phase (0.12 eV [151]-0.15 eV [248]), respectively. If the peaks in the PL spectrum are assigned to a q-DAP transitions between the same, or very similar types of defects in three coexisting CZTS phases, one could consider that P3, P2 and P1 arise from stannite, the disordered phase and kesterite, respectively. An inhomogeneous distribution of these three CZTS phases may then explain the dependence of the PL spectrum on the excitation spot position on the sample.
Although the kesterite, disordered and stannite phases are quite likely to be formed in the CZTS absorber, other phases should also be considered as the complex phase diagram of Cu, Zn, Sn and S predicts the formation of secondary phases during the absorber growth. In order to provide an explanation for the PL peaks, their PLE onset (band gap) must be around 1.3 eV. Possible candidates, that moreover are likely to be formed, are tetragonal Cu_2SnS_3 and SnS (see section 2.3.2.4). The latter phase is normally found at the back contact of the cell. Whether or not this region can be excited during PL measurement depends on the CZTS absorption coefficient. Figure 6.16 present the normalized intensity versus penetration depth in the CZTS absorber following $I = I_0 \cdot \exp(-\alpha d)$ with $\alpha = 10^4$ cm^{-1} or $\alpha = 10^5$ cm^{-1}. Excitation light could reach the SnS phase at the back contact if the absorption coefficient is 10^4 cm^{-1}. As shown in section 2.3.2 theoretical studies point towards higher absorption coefficient than experimental studies. More information about the exact phase composition of the absorber would be helpful for the interpretation of the photoluminescence data. Unfortunately, experimentally it is not straightforward to assess phase information due to overlapping peaks in X-ray diffraction and Raman spectra [39].

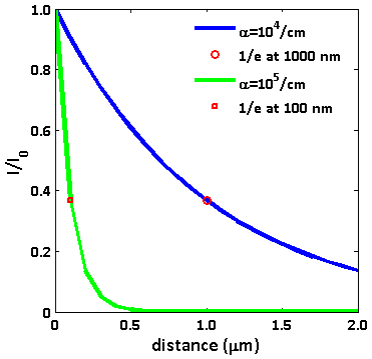

Figure 6.16: Comparison of light absorption profiles (λ_{exci} = 500 nm) at different absorption coefficients.

6.1.8 Summary

Photoluminescence spectroscopy has been performed to reveal the defect structure in Cu-poor, Zn-rich CZTS thin-film solar cells, grown by reactive sputtering. Despite different procedures in the annealing and sputtering processes for cell1 and cell2(3), three broad peaks could be revealed in all spectra. On the contrary, the energy range for emission seems to be dependent on the deposition process of the CZTS absorber. The effect of potential fluctuations is clearly seen on the PL spectra by a broadening of the peaks and a strong blue-shift as excitation power

increases. All spectra were fit, at different temperatures and excitation powers, with three Gaussian contributions. Via PLE measurements the energetic distance between the PL emission and band gap energy was estimated for cell2. As this distance is large, the involvement of carrier trapping by deep-level defects is very likely. A complete explanation of the contributions in the PL spectra requires more information about basic defect properties in CZTS and about the phase composition of the absorbers in these samples. The fact that the relative peak contributions exhibit considerable spatial differences strongly indicates that inhomogeneity in phase composition and/or defect distribution is important for these cells.

6.2 CIGS: Effect of substrate temperature and influence of an Sb layer

6.2.1 Motivation

In section 4.2 the results of electronic defect spectroscopy (by admittance spectroscopy) on CIGS solar cells deposited at reduced substrate temperature with a thin Sb layer (7, 12 nm) between the CIGS absorber layer and the metal back contact (series1) are reported. So far, admittance spectra could not reveal a direct effect of Sb on the defect structure. The defect activation energy of the dominant shallow acceptor was found around 30 meV. In this section the possible effect of an Sb layer on the defect structure is explored via optical spectroscopy (by means of PL) on two series of cells which provide additional information on the effect of growth temperature and the effect of Sb layer thickness.

• *Effect of Sb layer and influence of process temperature*
First a series of cells (labelled as series2) is investigated which provide information about substrate temperature and the effect of an Sb layer. As substrate temperature can have an effect on interdiffusion of the elements, three different growth temperatures on samples with and without an additional Sb layer with constant thickness underneath the CIGS absorber layer are compared. Based on the PL results, a defect identification is proposed.

• *Effect of Sb layer with varying thickness*
Thereafter the results of a series of cells made at same low growth temperature but varying thickness of Sb layer (series1) are discussed. Similarities between PL results of the different series are pointed out.

So far in literature, no pronounced effect of Sb doping on the defect structure was found by PL. In reference [249] no additional PL peak appears for a molecular beam deposited $CuInSe_2$ thin-film prepared with an additional Sb source. The same applies for reference [144] in which a $CuInS_2$ single crystals doped with Sb were investigated.

6.2.2 Effect of Sb layer and influence of process temperature

6.2.2.1 Preparation and performance

Cell preparation In table 6.7 the synthesis conditions of the cells taken up in this study are summarized, along with the results of solar cell performance measurements. Cells with Sb layer are referred to as Sb doped (SbD) and reference cells, without Sb layer, are labelled as non-doped (ND). For Sb doped cells, an Sb layer of 10 nm was evaporated on top of a Mo coated soda-lime glass substrate prior to CIGS three stage co-evaporation. In order to prevent immediate evaporation of the Sb layer at the start of the first stage, the substrate temperature was initially kept low (200°C, see table 6.7) and gradually increased until the end of the first stage. To investigate the effect of substrate temperature, three maximum substrate temperatures were used which were below or around the 'standard' substrate temperature (600°C). The maximum substrate temperature was 380°C for the low temperature process cell (LT), 400°C for the higher temperature process cell (HT) and 460°C for the cell processed at highest temperature (HHT). For the latter cell, only a non-doped version was available. During the second and third stages the temperature was constant. As low growth temperatures and the Sb layer can have an effect on the Na in-diffusion from the soda lime glass, an additional NaF PDT treatment was performed on the cells to minimize the difference of Na diffusion at different substrate temperatures. CdS buffer, ZnO window layer and Ni-Al grid were deposited after NaF PDT. Cells do not have

anti-reflection coating. A detailed description of the preparation can be found in reference [145].

Solar cell device parameters Table 6.7 shows a slight decrease of the cell efficiency upon Sb-doping. This is opposite to the results of series1 cells with variable Sb layer thickness (see table 4.2). The best cells are clearly those grown at the highest substrate temperature.

Table 6.7: Substrate temperatures and device performance of serie2 samples (numbers provided by Empa).

	T substrate (°C)						
Cell	1st stage	2nd/3rd stage	ND/SbD	V_{oc} (mV)	J_{sc} (mA/cm^2)	FF (%)	η(%)
HHT	200	460	ND	716	31.6	74.1	16.8
	400						
HT	200	420	ND	681	31.5	72.4	15.5
	400		SbD	648	30.0	73.2	14.3
LT	200	380	ND	662	32.7	69.7	15.1
	380		SbD	639	32.9	63.2	13.3

6.2.2.2 Spectral response

EQE measurements were carried out at room temperature in the 365 nm-1190 nm wavelength range, as described in [145]. The results are shown in figure 6.17. To estimate the band gap (E_g) the long wavelength flank of the spectra was fitted to the relation for a direct band gap semiconductor ($\alpha^2 \propto$ (E-E_g)). This cut-off wavelength at room temperature yields an underestimate for E_g at the temperature of the PL measurements (around 10 K). The E_g values for LT and HT cells are similar (around 1.12-1.13 eV); for the HHT cell it is markedly higher (around 1.16 eV). The error on the estimated band gaps is around 50 meV. There is, however, no clear distinction between the band gaps of SbD and ND cells. The latter is in agreement with reference [139], but in disagreement with references [146, 220].

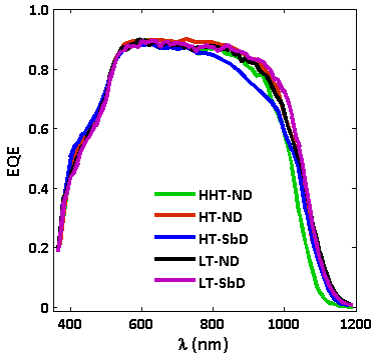

Figure 6.17: EQE spectra of devices of series2 (performed by Empa).

6.2.2.3 Morphology

SEM cross section images, shown in figure 6.18, were taken to investigate differences in film morphology, more specific in grain size of the absorbers between cells. In agreement with reference [144], the SEM cross sections of the investigated cells reveal no clear differences in grain size between SbD and ND cells. On the other hand, an increase in grain size is observed when increasing the substrate temperature, in accordance with previous studies [140,143]. CIGS thin-films grown at high substrate temperature have also been reported to exhibit a higher density [250], which may affect the interdiffusion between absorber and buffer layer, as will be discussed further on.

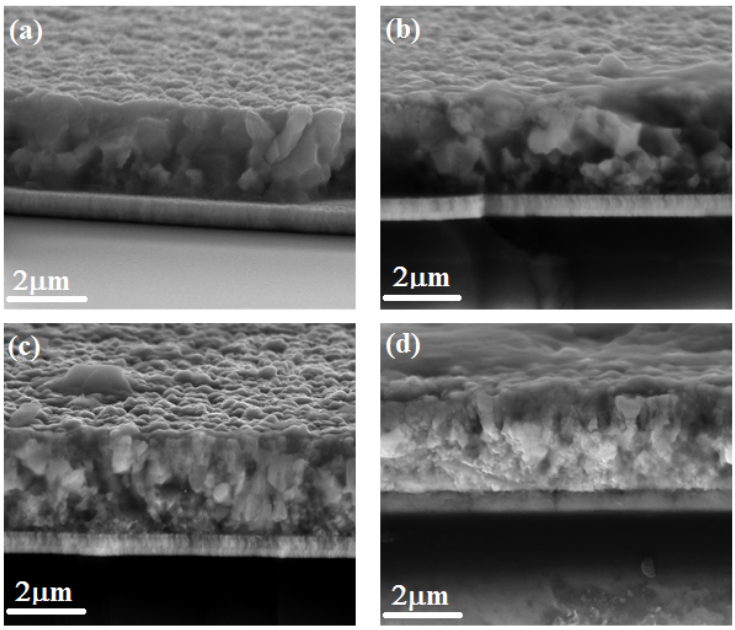

Figure 6.18: SEM cross section images of (a) HHT-ND, (b) HT-ND, (c) LT-ND, (d) LT-SbD.

6.2.2.4 Composition

According to reference [145] the average CGI ratio is 0.79 and the average GGI ratio is 0.38 as determined by XRF measurements. Cells have thus a Cu-poor composition. As both substrate temperature [125] and Sb doping [145] may have an effect on the interdiffusion of the elements during the three stage evaporation, EDX line scan on cross section and TOFMS measurements have been performed to obtain composition depth profiles.

1) TOFMS

Artefacts of the grid

TOFMS measurements are performed in collaboration with Horiba Scientific (France). Figure 6.19 shows depth profile signals normalized to the Zn signal as this signal is expected to be the same for each sample. Because of the sputtering of the grid, there is a 'delay' in the signals which is clearly seen in the Zn, Cd and S signal. These signals appear again after the disappearance of the Al and Ni signal. Because of this artefact the Cu, In, Ga and Se signals have not completely vanished when the Mo signal is already present. This artefact is not an issue for further interpretation of the composition depth profiles.

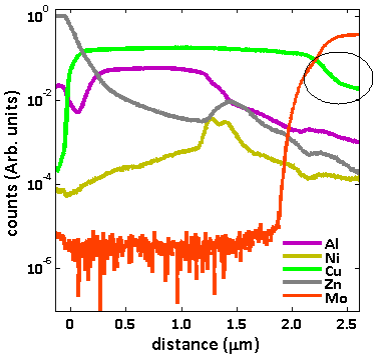

Figure 6.19: TOFMS measurements of sample LT-SbD. The on-zero Cu signal at the back of the cell is an effect of the Ni/Al grid on top of the cell.

Cu-In-Ga-Se profiles

Figure 6.20 shows the Cu-In-Ga-Se profiles (normalized to Zn signal) of Sb doped cells made at high (HT) and low substrate temperature (LT).

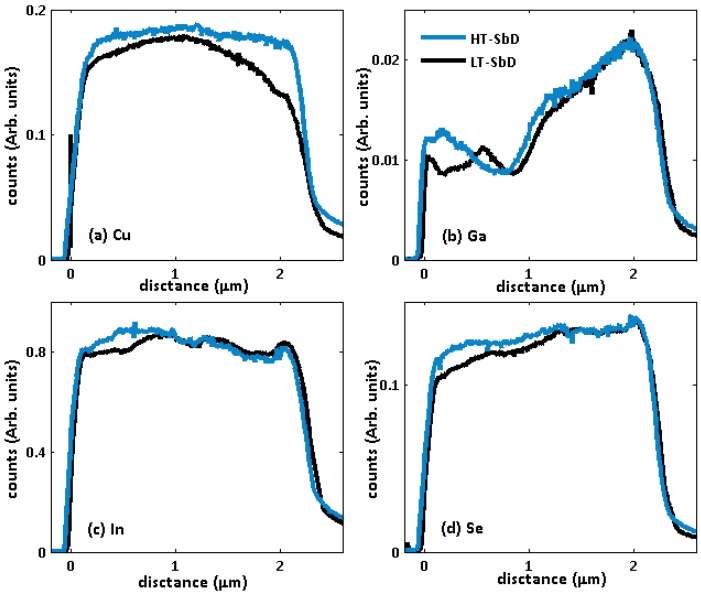

Figure 6.20: Comparison of Cu-In-Ga-Se TOFMS profiles of samples LT-SbD and HT-SbD. (a) Cu, (b) Ga, (c) In and (d) Se.

Cu profile A comparison between the Cu profiles reveals that the low substrate temperature is not sufficient to have a good inter-diffusion of Cu elements (figure 6.20(a)). The Cu signal decreases towards the back and the front contact. The Cu distribution of sample HT-SbD shows a flatter Cu distribution. This result is in accordance with reference [125] in which CIGS absorbers were made by three stage co-evaporation at different substrate temperatures to investigate the influence of Na. It was shown that the thermal energy of 370°C (very close to LT temperature of 380°C) is not sufficient to homogenize the Cu concentration gradients in CIGS absorber. Besides substrate temperature, the Cu distribution further depends on the deposition rates and Na content which can hinder In, Ga and Cu diffusion especially at low substrate temperature.

Ga-In profile A double graded Ga profile, with higher Ga content to the front and back of the film is visible in figure 6.20(b). The highest In amount is located near the position of the Ga dip (figure 6.20(c)). For LT-SbD cell, it seems that the location of the Ga dip is located more towards the back contact and the amount of Ga at the front contact is lower than for the HT-SbD cell. These findings are in accordance with reference [145] in which TOF-SIMS measurements were performed on samples LT-ND, LT-SbD and HHT (figure 6.21). This figure reveals that sample HHT has the highest GGI ratio at the absorber surface and at the Ga dip. The higher band gap, determined via EQE, can be understood from this.
As the location and depth of this dip have been found to be crucial for device performance [73], the different Ga profiles as a result of different substrate temperature and Sb layer can, besides the different grain sizes, also play an important role in the device performance.

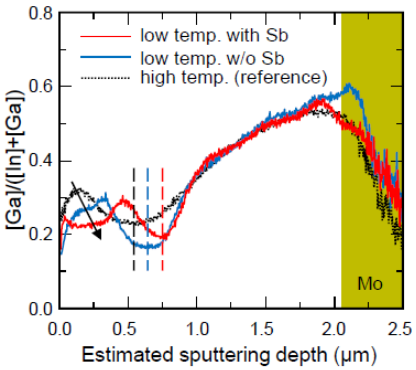

Figure 6.21: GGI depth profiles in CIGS layers of LT-SbD (red), LT-ND (blue) and HHT-ND (black) [145].

Se profile Figure 6.20(d) shows that the amount of Se decreases towards the front of the absorber. The amount of Se is higher for HT-SbD.

Sb profiles

As shown in section 4.2.4 TOFMS measurements are able to detect the very thin (10 nm) Sb layer and Sb diffusion profile. Although the Sb layer is only 10 nm and the substrate temperatures were quite low, antimony diffusion towards the front contact is visible in all Sb doped cells (HT and LT) (figure 6.22). There is a higher Sb diffusion in the HT cell compared to LT cell. Although the Sb seems to diffuse towards the front of the layer, no increase in grain size was seen in SEM pictures of Sb-doped cells (figure 6.18) compared to non-doped cells. The absence of grain size increase for cells having an Sb layer is opposite to the result found for series1 (see section 4.2.3).

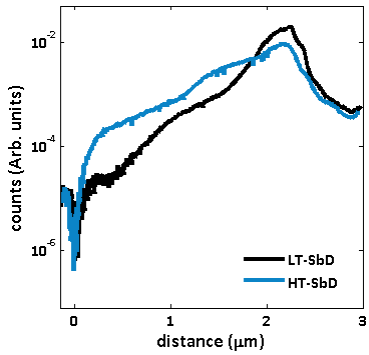

Figure 6.22: Sb diffusion in Sb doped cells.

Na profiles

As Na diffusion from the soda lime glass can be lowered by the low substrate temperature and hindered by the Sb layer on top of the Mo contact (as demonstrated in reference [141]), a Na post deposition was performed to ensure Na in the cells. Figure 6.23 shows that substrate temperature has indeed a large influence on the Na diffusion profile; Na diffusion from the soda lime glass in the HT cell is larger than in the LT cells. The higher Na concentration in the HT cell, in combination with the higher substrate temperature, could explain the larger grain size of the absorber material which was seen in SEM pictures (figure 6.18). As the presence of Na can alter the diffusion of elements during growth [124], a different Na profile could lead to a different Ga depth profile as shown in figure 6.20(b). For the LT cell, the Na increase from 0.6 µm towards the front contact could be related to the Na coming from the Na PDT step.

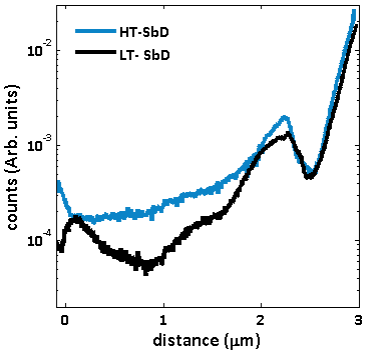

Figure 6.23: Na diffusion in Sb doped cells made at different substrate temperature.

Cd profile

Figure 6.24 shows that the cell made at low substrate temperature has a high diffusion of Cd into the absorber layer. This was also found in EDX measurements (see section 6.2.2.4).

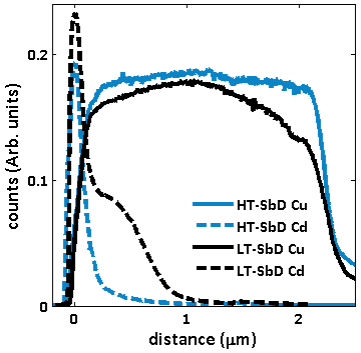

Figure 6.24: SIMS Cd diffusion profiles in relation with Cu profiles.

2) EDX

The characteristic X-rays of Cu_K, Se_L, Cd_L, In_L and Ga_L were monitored by EDX at an acceleration voltage of 15 kV in collaboration with Lumilab (research group of the department of Solid State Sciences at Ghent University). The resolution of the EDX scan is rather low, because of the large interacting volume and a partial overlap of peak energies of certain monitored elements. The latter makes the interpretation of the data difficult. Nonetheless the results of EDX line scans of cell cross-sections are in accordance with TOFMS composition measurements, discussed in the previous section and with composition data in reference [145].

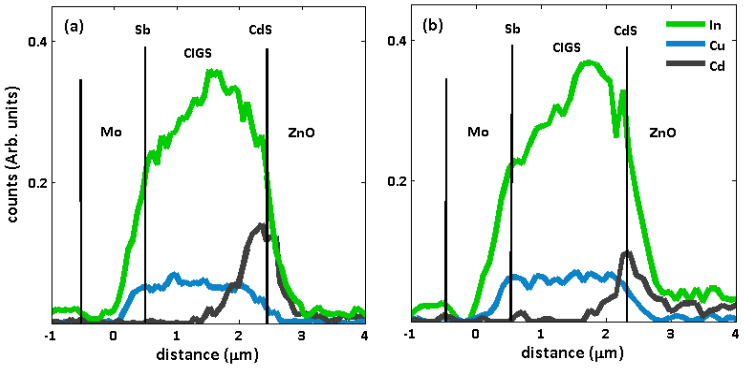

Figure 6.25: EDX line scan of cross section of In, Cu, Cd and Ga profile (normalized on Se signal) (a) LT-ND, (b) HT-ND.

The EDX measurements (figure 6.25) are indicative of a larger in-diffusion of Cd into the CIGS absorber for the LT cells compared to the HT cells. In literature, CIGS films grown at low substrate temperature have been reported to have a more Cu-poor surface [125], where Cu vacancies can be occupied by Cd. A higher in-diffusion in the LT cells may also result from a lower film density obtained at low substrate temperature [250].

6.2.2.5 Photoluminescence

PL measurements are performed in order to investigate if Sb doping and/or variation in substrate temperature have an effect on the defect structure. Excitation wavelength, excitation power and temperature dependence of the PL spectra will be discussed.

Excitation wavelength dependence

As we are primarily interested in defects in the absorber layer, we detected the PL of the samples in the near infra-red range ($E \leq E_g$ (CIGS) $\approx$ 1.15 eV). PL emission scans are shown in figure 6.26, in which a marked influence of the excitation wavelength in the 300-650 nm range is observed. The PL results do not yield direct evidence for Sb incorporation in the absorber as no additional peak(s) appear in the spectra of samples with Sb layer.

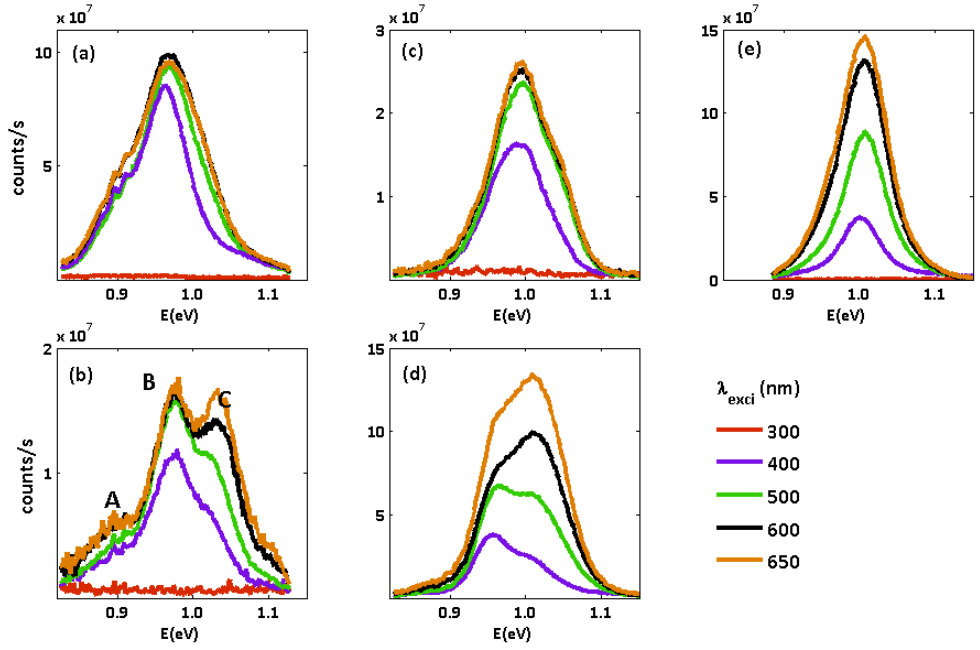

Figure 6.26: PL emission as a function of excitation wavelength (T = 5 K). (a) LT-ND, (b) LT-SbD, (c) HT-ND, (d) HT-SbD, (e) HHT-ND. Peak A, B, C are indicated in (b).

300 nm light does not excite PL from the absorber, as it is completely absorbed by the window layer (E_g (ZnO:Al) $\propto$ 3.5 eV (354 nm)). Light in the λ = 400-500 nm range is in part absorbed by the thin CdS buffer layer, but also penetrates in the absorber, as it is obvious from the PL intensity. In this range the PL intensity exhibits an increase that can be readily explained by an incomplete absorption in the buffer layer. In the 500-650 nm excitation range, all light should be absorbed only in the CIGS layer. Nonetheless, (slight) changes in the PL spectral shape and intensity are noted, in particular in the range of the highest energy peak for the SbD samples (figure 6.26(b, d)). This may be an indication of gradients in the defect distribution near the CdS/CIGS interface, related to the penetration depth of the excitation light in the absorber. Simulations, performed by the numerical simulation programme SCAPS [251], show that the 1/e penetration depth in the absorber changes from 70 to 120 nm in the 400-650 nm wavelength range if a homogeneous CIGS layer is assumed. The penetration depth may be further influ-

enced by the specific Ga grading in the absorber.

In spite of the differences in shape among the different samples, all PL spectra can be decomposed in three broad Gaussian components, labelled as A, B, C (figure 6.26(b) and figure 6.27). In view of the large band widths and overlap, the fitting error on these positions is estimated in the order of 5 meV. The energy of the peak maximum (10 K) and difference in energy of the peak maximum can be found in table 6.8.

Table 6.8: PL peak positions and distances between them for series2.

	Peak energy (eV)			Peak difference (eV)	
Cell	A	B	C	B-A	C-B
LT-ND	0.897	0.967	1.036	0.070	0.069
LT-Sb	0.910	0.976	1.037	0.066	0.061
HT-ND	0.920	0.985	1.042	0.065	0.057
HT-Sb	0.885	0.955	1.019	0.070	0.064
HHT	0.942	1.005	1.063	0.062	0.058
				Average (eV)	
				0.066	0.061

The PL spectra of the HHT cell (figure 6.26(e)) are shifted towards higher energy. This is related to the higher GGI profile for sample HHT as shown in figure 6.21. The energy separation between the peak positions of peaks C and B and between B and A is similar for all cells. This suggests that same defects are involved in the different cells. The peak at highest energy (peak C) is most pronounced for the SbD cells (figure 6.27(a)). The second peak (B) is clearly visible for all samples and is the dominant peak in the ND cells. The lowest energy peak (A) is most clearly distinguished for the LT cells (figure 6.27(b)).

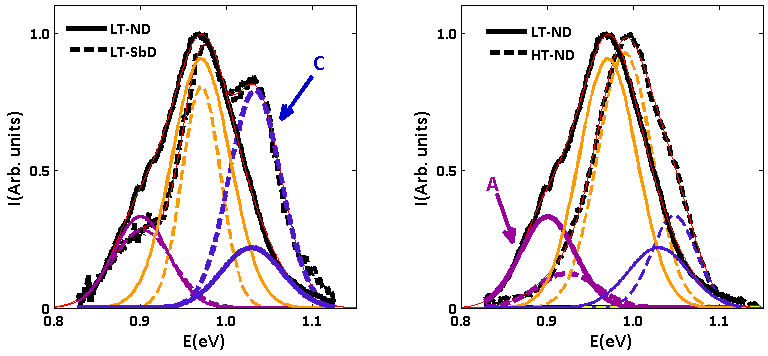

(a) LT-ND and LT-SbD cells (b) LT-ND and HT-ND cells

Figure 6.27: Comparison of normalized PL spectra (λ_{exci} = 600 nm, T = 5 K).

An overview of the fittings of all cells is presented in figure 6.80(c). The energy of the peak maximum of peak C is set to zero here.

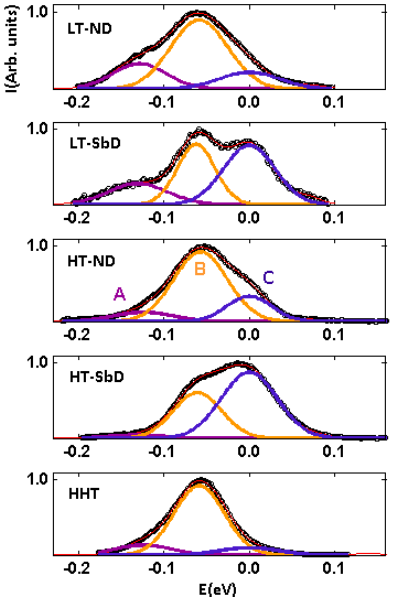

Figure 6.28: Comparison of normalized PL spectra (λ_{exci} = 600 nm, T = 5 K).

All peaks are quite broad and the spectra do not exhibit phonon replicas nor exciton transitions. This is a clear signature of highly compensated CIGS material [236]. As concluded from the compositional study, the CIGS absorber is Cu-poor. Hence it is expected to exhibit a high concentration of copper vacancies and to be highly compensated [84, 252]. Peaks in the PL spectra of a highly compensated semiconductor are usually assigned to quasi-DAP recombination [84] (see section 5.2.1.2). The tunneling of carriers between spatially separated donors and acceptors, at different local potential, can considerably reduce the transition energy. Hence, potential fluctuations hamper an accurate determination of the donor and acceptor binding energies. As a result of potential fluctuations distinctive excitation power and temperature dependencies of the PL spectra are expected [16, 84, 180]. In the following these are examined.

Excitation power dependence

Excitation power dependent PL measurements at low temperature have been performed. The excitation power (P_{0exci}), measured in front of the lens located before the cryostat, was in the order of 100 mW/m^2 (λ_{exci} = 500 nm). Gray filters were placed in front of the cryostat window in order to decrease the excitation power. Figure 6.29 shows the fitted spectra of sample HHT measured at different excitation powers. The blue-shift with increasing excitation power is indicated.

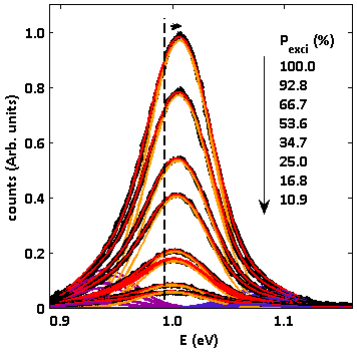

Figure 6.29: Excitation power dependent PL measurement of HHT non doped cells (λ_{exci} = 550 nm, T = 8 K).

In figure 6.30 the excitation power dependence of the PL peak position is shown for the samples for which the peak position is corresponding with peak B. A fitting, assuming a linear relation between the peak position ($\sim$ peak B) and the logarithm of excitation power (equation 5.6), yields shifts of 8.5, 17.0, 11.4 and 11.1 meV/decade for HHT-ND, HT-ND, LT-ND and LT-SbD cells, respectively. This large blue-shift (B $>$ 5 meV/decade) is a second indication of potential fluctuations in PL measurements as explained in section 5.2.1.2.

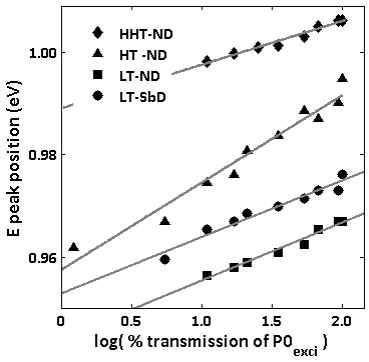

Figure 6.30: Emission peak energy as a function of excitation power.

Temperature dependence

PL spectra as a function of temperature reveal a pronounced red-shift of the spectra upon increasing temperature (figure 6.31). For all cells, the PL intensity also decreases as temperature increases. In view of the presence of three overlapping peaks in all spectra, the temperature dependence of intensity is rather complicated and differs for different cells. The difference in temperature dependence can be due to different excitation powers in the measurements.

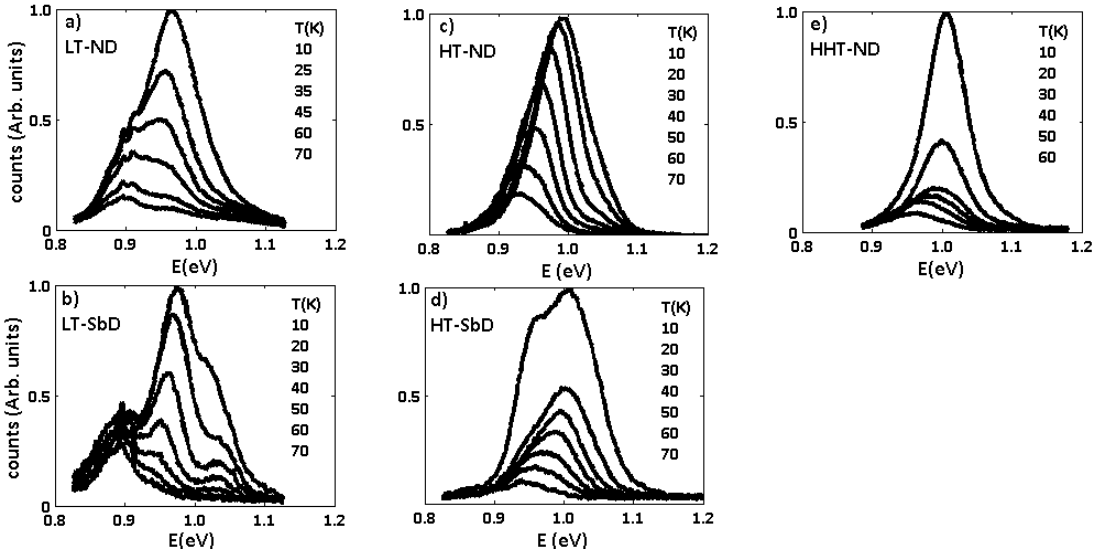

Figure 6.31: Temperature dependent PL spectra for (a) LT-ND, (b) LT-SbD, (c) HT-ND, (d) HT-SbD, (e) HHT-ND (λ_{exci} = 500 nm).

Over the complete measured temperature range, a decomposition in three Gaussian peaks allows a good reproduction of the spectra. In figure 6.32 the temperature dependence of the peak positions for the spectra at an excitation wavelength of 500 nm for the HT-ND and HT-SbD cell is shown. For the B peak of the HT-ND cell a red-shift of 0.9 meV/K was observed and for the B peak of the HT-SbD cell 0.8 meV/K. For CIGS red-shifts ranging from 0.15 meV/K to 1.30 meV/K [16, 75, 84, 233, 235] have been found. As the band gap decrease with increasing temperature is reported to be very small (0.11 meV/K) [85,86] or even absent below 100 K [84], the red-shift of the PL emission peaks cannot be explained only by a decrease of the band gap as

the temperature increases. The large red-shift is yet another indication of potential fluctuations in compensated material as explained in section 5.2.1.2. In the measured temperature range no transition of red-to-blue shift is noticed, which could point to BT to BB recombination or TI to BI recombination (see section 5.2.1.2).

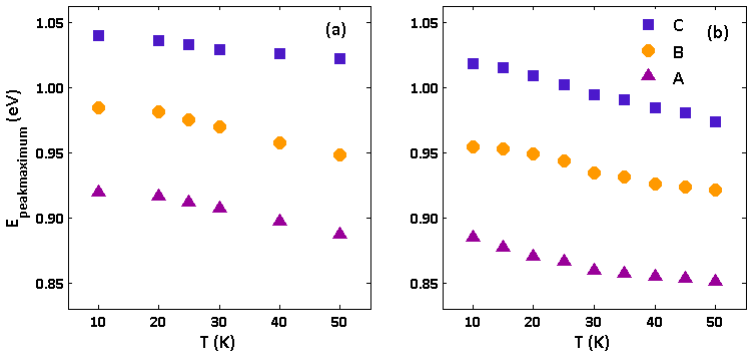

Figure 6.32: Temperature dependence of the three peak positions for (a) HT-ND and (b) HT-SbD (λ_{exci} = 500 nm).

6.2.2.6 Defect interpretation

As mentioned before, the PL signals originate from the CIGS layer close to the interface with the buffer, relatively far from the back contact and the Sb layer. The PL experiments reveal a marked influence of both the substrate temperature during the absorber growth and of Sb doping on the defect distribution in CIGS near the buffer/absorber interface. Moreover, the spectral width, the excitation power and temperature dependence of the PL spectra are compatible with q-DAP recombination in a semiconductor which is strongly compensated. In this case information about the discrete defect states is smeared out by lowering of the DAP transition energy by 2γ and by broadening of the spectra. Therefore no direct information about the defect binding energies E_D+E_A can be obtained. In addition, reported defect identifications in CIGS, based on binding energies for donors and acceptors, are often conflicting.
In the following, an identification based on literature results is proposed based on the distances between the PL peaks, as given in table 6.8, and on the stoichiometry of the samples as evidenced by composition depth profiling results. Other interpretations may, however, still be possible.

Since the material is Cu-poor, it can be assumed that the acceptor of the DAP is the copper vacancy (V_{Cu}). Based further on the stoichiometry of the samples and theoretical predictions of the formation energy of defects found in reference [91], V_{Se} and In_{Cu} are expected to be the most abundant intrinsic donors in CIGS, compensating the V_{Cu} acceptors.
Other theoretical calculations do not agree with reference [91]. References [114,118] suggest that trap levels can only be contributed by Se-related defects, and that cation vacancy and cation antisite defects cannot form defect levels in the CIGS band gap. Moreover the activation energy of the deep donor V_{Se} is calculated at 0.85 eV referred to the conduction band minimum. These calculations cannot be united with three PL contributions and the energy of the PL peaks. Also theoretical calculations of reference [116] cannot be brought in agreement with the PL results, as defect activation energies of the most likely defects are quite high. These large activation energies do not allow to form donor-acceptor pair recombinations which could explain the energy whereupon PL peaks are detected. The latter recent calculation results have, so far, not been used in reports to explain experimental results.

In reference [253] PL experiments (as a function of temperature and excitation power) on co-evaporated $CuInSe_2$ thin-films with varying Cu/In ratio were performed. The emission spectrum of Cu-poor material showed two broad emission peaks which were assigned to V_{Cu}-V_{Se} and V_{Cu}-

In_{Cu} DAP recombination. The same identification was proposed in references [235, 253–255]. Adopting also this identification for peak C and peak B, the PL results indicate that In_{Cu} (associated with peak B) is the dominant donor defect in most of the cells, especially in the ND samples, at least in the region close (100-200 nm) to the buffer/absorber interface. The results further indicate that Sb-doping leads to a higher concentration in the V_{Se} donor defect (associated with peak C), which in addition appears to exhibit a positive gradient towards the absorber bulk as shown by excitation wavelength dependent measurements. This effect of Sb doping could be related to a hindered diffusion of Na in the absorber layer due to the Sb layer. In reference [141] it is reported that Na diffusion from the soda lime glass is hindered by the presence of an Sb layer on top of the Mo contact. As the presence of Na in the CIGS film and/or surface may impede Se loss [108,125,126], a lower Na concentration in Sb doped cells might thus lead to a higher Se loss and hence a higher V_{Se} concentration.

Finally, the PL measurements reveal an increased contribution of peak A in LT cells. In references [98, 256] it has been shown by that chemical bath deposition of CdS on CIGS may lead to changes in the PL spectrum, introducing a low energy peak. The associated deep electronic level, at E_c-210 meV [256] was assigned to the Cd_{Cu} donor, formed by the substitution of Cu by Cd in the Cu-poor material (see section 2.3.1.3 doping model of inversion layer). In accordance with these PL studies, the low energy peak A may be identified as Cd_{Cu}-V_{Cu} DAP recombination.

6.2.2.7 Summary

The influence of a thin Sb layer evaporated on the Mo back contact in CIGS cells processed by multistage evaporation at reduced substrate temperatures was investigated. Device performance values showed a small decrease in the cell efficiency upon Sb-doping and an increase upon increasing substrate temperature. EQE and SEM measurements showed a clear effect of substrate temperature, but no obvious effect of the Sb layer. Element depth profiles by TOFMS and EDX cross section measurements showed the influence of the substrate temperature on the composition. The diffusion of Sb into the CIGS layer is demonstrated via TOFMS measurements. In low temperature cells an enhanced Cd diffusion into the CIGS layer could be measured by both techniques. The PL spectra do indicate effects of both substrate temperature and Sb doping on the defect composition in the CIGS absorber. For all the cells, the PL spectra exhibit three broadened Gaussian peaks, which red-shift with increasing temperature and blue-shift with increasing excitation power. These are features of potential fluctuations in Cu-poor highly compensated CIGS. For low temperature cells a PL peak at low energy, attributed to q-DAP recombination between V_{Cu} and Cd diffusion related donors, is more pronounced. PL peak P2 is related to a In_{Cu}-V_{Cu} q-DAP transition. Sb doped cells have a more pronounced peak at high energy. The PL results indicate a positive concentration gradient in the associated donor defect, probably V_{Se}, towards the absorber bulk.
The suggestions for the defect assignments proposed in this section are not definitive. In the subsequent sections investigations are performed to obtain further experimental support.

6.2.3 Effect of Sb layer with varying thickness

6.2.3.1

The deposition process of the cells of series1 (Sb0, Sb7 and Sb12) as well as their performance parameters are discussed in section 4.2. TOFMS measurements on Sb0 and Sb12 did not reveal large depth profile differences.

6.2.3.2 Spectral response

EQE measurements show an increase in carrier collection on the long wavelength side for cells with a Sb layer (figure 6.33). This provides an explanation for the increase in J_{sc} for these cells (table 4.2) and could be related to larger grain size (see section 4.2.3). No obvious shift of the onset of absorption is observed for cells with and without Sb layer. This is in accordance with reference [139]. References [220] and [146] on the other hand demonstrate a band gap decrease of $CuInS_2$ with increasing Sb doping. A linear extrapolation of squared EQE ($\alpha^2 \propto (E\text{-}E_g)$) gives an estimate of the minimal band gap at room temperature, which is around 1.14 ± 0.07 eV for all cells.

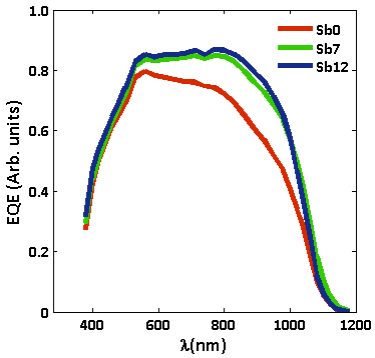

Figure 6.33: EQE of the investigated samples (performed by Empa).

6.2.3.3 Photoluminescence

Comparison between PL spectra at low temperature

Figure 6.34 shows that the emission peaks of the spectra measured at low temperature are broad without any narrow lines in the near-band gap excitonic region. These features are an indication of potential fluctuations in a highly compensated semiconductor (see section 5.2.1.2). The low temperature spectra of all cells could be fitted with three Gaussian peaks when allowing for a margin of 3 meV to take into account possible peak shifts as a result of a difference in excitation power. Figure 6.34(a) shows a comparison at low temperature of Sb0 and Sb7, while figure 6.34(c) presents a comparison between Sb0 and Sb12. The peak differences (C-B = 0.061 eV and C-A = 0.069 eV) are the same as for in the PL spectra of series2 samples (section 6.2.2).
The samples with antimony layer at the back do not give any additional PL features (e.g. additional peaks) compared to the cell without Sb layer, even-though Sb was found at the top of the layer in TOFMS measurements (see section 4.2.4). This result is in accordance with references [144, 249] in which no additional PL peak was found for Sb doped samples.

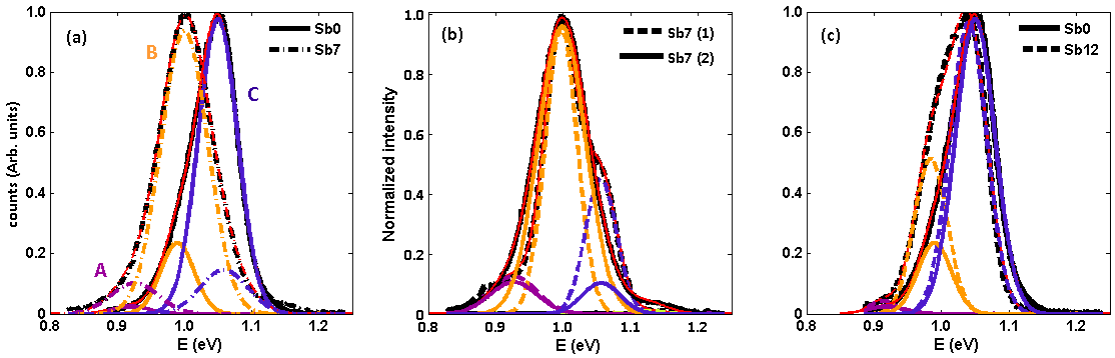

Figure 6.34: Fits of (a) Sb0 (Sb7) at λ_{exci} = 550 nm (520 nm) and T = 5 K, (b) Sb7 at two different positions: position 1 (2) at λ_{exci} = 520 nm (550 nm) and T = 10 K, (c) Sb0 and Sb12 at λ_{exci} = 550 nm and T = 5 K.

An overview wherein the spectra are shifted, such that energy of the peak maximum of peak C is set to zero eV, is presented in figure 6.80(a).

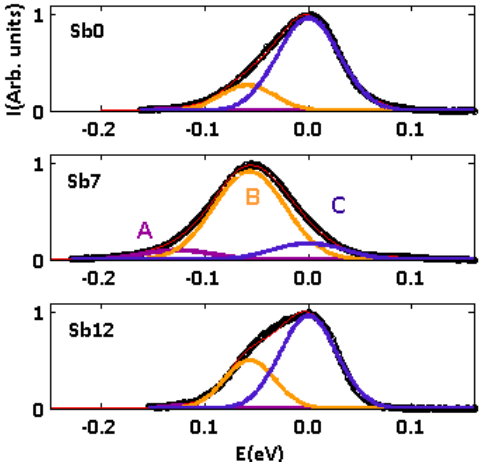

Figure 6.35: Fits of Sb0, Sb12 at λ_{exci}= 550 nm and Sb7 λ_{exci}= 520 nm (T = 5 K).

It is remarkable that the spectrum of Sb7 appears at lower emission energy (figure 6.34(a)), compared to the spectra of Sb0 and Sb12. From the fitting of the spectra, it seems that the energy shift of the emission spectra between Sb0 and Sb7 is not related to a shift in band gap energy but to a difference in the dominant PL emission peak. The dominant peak is shifted from peak C for Sb0 to peak B for Sb7. A possible explanation for the dominance of another peak, could be a large inhomogeneity in the Sb7 absorber. In order to test this, the PL measurement was repeated with another excitation spot location. The position dependent measurements (figure 6.34(b)) of sample Sb7 show that there is only a small change in the relative intensities of individual peaks upon excitation spot. This small change can be explained by small inhomogeneities in the sample. It appears from the position dependent measurements that the spectra of Sb7 are reproducible. A difference in the spectra due to large inhomogeneity in the film can thus be excluded.
Another possibility to explain the different spectra, is by a different composition for sample Sb7 compared to Sb0 or Sb12. XRF measurements, performed in collaboration with the research group CoCooN (research group of department of Solid State Sciences at Ghent University), showed no difference in the global composition of the CIGS absorber layers. As PL is a surface sensitive technique, it might be that there is only a composition difference at the surface of the absorber layer, which is not detected by XRF measurements as this technique measures the

average composition of the whole absorber layer. To gain insight in the CIGS surface composition XPS measurements have been performed. These reveal a larger Se and In content in the Sb7 sample compared to Sb0 sample. The Cu content in Sb7 sample is lower. The difference in PL spectra might be due to the difference in surface composition.

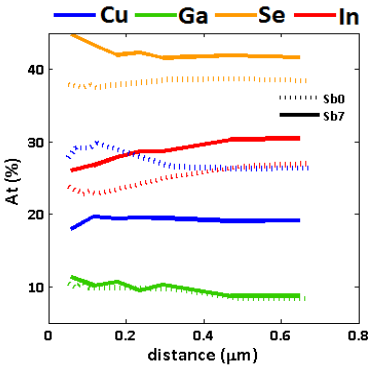

Figure 6.36: Elemental composition of the surface of Sb0 and Sb7 measured by XPS.

The PL spectra of Sb0 and Sb12 (figure 6.34(c)) are more similar, the intensity of peak B is higher for sample Sb12. No significant dependence of the spectra upon excitation spot position was found for these samples.

Temperature dependent measurements

PL spectra of all cells as a function of temperature are presented in figure 6.37. Temperature dependent measurements for Sb0 and Sb12 (figures 6.37(a) and (c)) clearly reveal the presence of more than one broad contribution in the spectra.

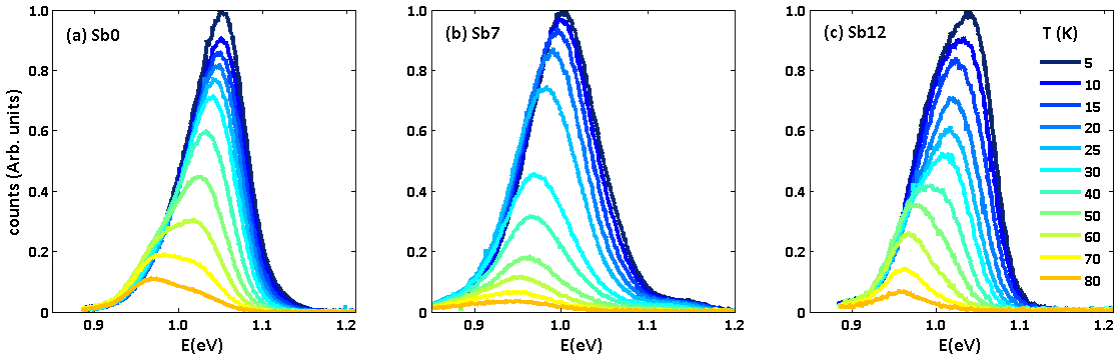

Figure 6.37: Temperature dependent PL measurements. (a) Sb0 λ_{exci} = 550 nm, (b) Sb7 λ_{exci} = 520 nm, (c) Sb12 λ_{exci} = 550 nm.

In figure 6.38 a comparison of the spectra of Sb0 at 5 K and 60 K is shown. At higher temperature peak B becomes more pronounced as a result of a more rapid decrease of the dominating recombination (peak C) at low temperature.

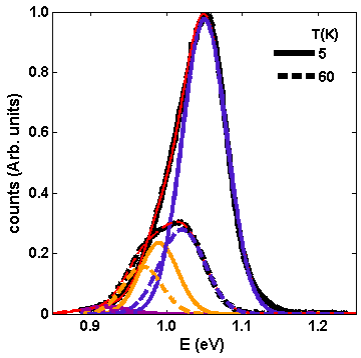

Figure 6.38: Fit on the temperature dependent spectra of Sb0 (5 and 60 K).

Figure 6.37 shows that the spectra shift towards lower energy (red-shift) as temperature increases. The systematic red-shift can be explained by q-DAP recombination in the presence of potential fluctuations in highly compensated material [16, 180, 181, 234]. The temperature dependence of peak C of sample Sb0 shows a shift of 0.47 meV/K in the temperature range of 5-80 K.

Excitation power dependence

Excitation power dependent measurements are performed on sample Sb7. A linear fit according to $E_{peak} = C + B \cdot \log(P_{exci})$ (equation 5.6) is calculated for the individual contributions of the excitation power dependent spectra (figure 6.39). The B shift is 8.0 ± 2.0 meV/decade for peak C, 7.0 ± 0.5 meV/decade for peak B and 10 ± 3 meV/decade for peak A. The calculation error is smallest when the peak maximum is clearly visible (for peak B). The presence of potential fluctuations in the material is indicated by the large B value (B > 5 meV/decade) [5].

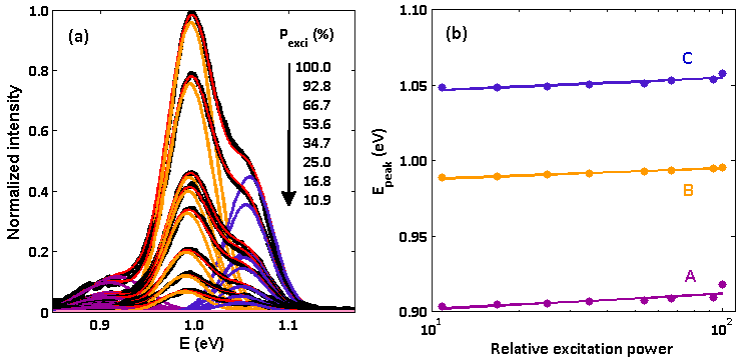

Figure 6.39: Excitation power dependent measurements
(a) fit at spectra of Sb7 (λ_{exci} = 550 nm, T = 10 K),
(b) peak maximum as a function of excitation power.

Comparison of series of cells with Sb layer

Figure 6.40 shows a comparison of cells from series1 (Sb0) and series2 (HT-ND). In both series the same PL contributions occur, with different intensities. The grain size, which is remarkably larger for samples in series1 (figure 4.20) compared to series2 (figure 6.18), has no effect on the dominant PL peaks. The intensity of peak A is very small for samples in series1. The red-shift of the PL peaks as temperature increases and the blue-shift with increasing excitation power are lower for series1 compared to series2.

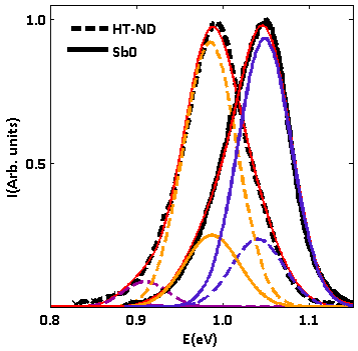

Figure 6.40: Fits of Sb0 (λ_{exci} = 550 nm) and HT-ND (λ_{exci} = 550 nm) (T = 5 K).

6.2.3.4 Defect interpretation

Direct information about the energetic position of the involved defects can, also for these samples, not be simply extracted since potential fluctuations are present. Based on the Cu-poor stoichiometry of the samples (CGI = 0.86), it can be assumed that the acceptor in the recombination process is the dominant shallow V_{Cu} acceptor which is revealed by admittance spectroscopy in section 4.2.
No large difference of the dominant defects, and hence PL peaks, is expected between series1 and series2. This is confirmed by the appearance of same contributions in the PL spectra as revealed in figure 6.40. Therefore, we assume that the same dominant defects are present in series1 as in series2. In the previous section (section 6.2.2) a q-DAP recombination of V_{Cu}-V_{Se} for PL peak C and V_{Cu}-In_{Cu} for PL peak B was suggested, in accordance with experiments in references [235, 253, 254] and the DFT calculations of reference [91]. The assignment of peak B to an In_{Cu} related defect transition (made in section 6.2.2.6) has found more experimental support in the experiments performed on series1. It seems the In content, detected by XPS measurements, at the surface region in sample Sb7 is larger than this of sample Sb0. The larger intensity of peak B for sample Sb7 could be understood. No further experimental support was found for the assignment of peak A and C.

6.2.3.5 Summary

CIGS solar cells made at low substrate temperature with or without an additional Sb layer (7 or 12 nm) are subjected to optical spectroscopy by means of PL. The influence of potential fluctuations, as a result of Cu-poor material, was noticed by the broad PL peaks which show a large blue shift as the excitation power increases. The same fitting with three Gaussian peaks, as used for spectra of samples in series2, could also be applied on the spectra of samples in series1. Similar to spectra of series2, no additional emission peaks were found for samples with Sb layer. The PL measurements on cells of series1 confirm the measurements of series2. The dominant emission peak for samples Sb0 and Sb12 is peak C, while it is peak B at lower energy for sample Sb7. The spectra are reproducible for changes in the excitation spot position, which exclude large inhomogeneity in the CIGS absorber layer. No large composition difference between the samples could be measured by XRF, while XPS measurements revealed a small composition difference at the surface of the samples.
In conclusion, optical nor electric measurements could reveal a direct effect of the presence of the Sb layer in the solar cells, neither in series1 nor in series2.

6.3 CIGS: Effect of Se evaporation rate, thinning of absorber and post annealing

The first part of this section reports about the effect of different Se evaporation rates during CIGS growth on the efficiency and defect structure. Thereafter the results concerning PL measurements on thinned absorber layers, which provide defect information throughout the absorber layer, is given. In the last part the effect of different post annealing methods, which intended to alter the defect structure and hence PL spectra, is discussed.

6.3.1 Effect of different Se evaporation rate

6.3.1.1 Motivation

Studying the influence of the selenium flux on the growth and performance of CIGS thin-films is important for at least two reasons [257]. First, solar cells based on CIGS are on the edge of large-scale production. Questions related to device quality versus process speed or minimal use of materials have gained more importance. A precise control and knowledge of the elemental composition in the vapour flux is hence necessary. The second reason is that the Se flux (as well as the Na supply) is reported to have an influence on the texture [25, 27, 257–259], may control the V_{Se} defect or V_{Se}+V_{Cu} complex defect formation [25, 258–260] and therefore may play an important role in the solar cell performance [25,257,259]. In reference [25] it was found that preferred orientation became <220> (which is believed to produce a lower density of non-radiative recombination centers [26]) for the film with higher Se flux while it tended to be <112> with lower Se flux. Usually Cu(In,Ga)Se_2 absorbers are in the three stage co-evaporation process prepared under high Se excess in order to obtain high conversion efficiency [27, 28]. However reference [27] reports that at high Se evaporation rate, performance was deteriorated as a result of a development of pores. A precise control of the Se flux is thus necessary and optimum in Se flux should be found for a good cell performance.

6.3.1.2 Preparation and performance

Cell preparation In this section samples with different evaporation rate of Se during the CIGS deposition are investigated. The series is labelled as series3. After the low temperature CIGS deposition process (450-500°C), samples had NaF PDT. The highest Se source temperature was used in sample 'SeH'. Samples 'SeL1' and 'SeL2' were produced at reduced Se evaporation rate. In the latter case the vapour pressure of Se is still quite high, especially because a low temperature deposition process is used wherein the re-evaporation rate of Se is reduced compared to a high temperature deposition process. CdS buffer, ZnO window layer and Ni-Al grid were deposited after NaF PDT. The cells do not have anti-reflection coating.

Solar cell device parameters The best cell characteristics can be found in table 6.9. Cells with low Se evaporation rate (SeL1-2) appear to obtain the highest efficiency. This observation is different from the trend of higher efficiency for higher Se evaporation rate [27, 28].

Table 6.9: Sample characteristics of series3 (numbers provided by Empa).

Sample	Evaporation rate Se	Device performance					
		V_{oc} (mV)	J_{sc} (mA/cm^2)	FF (%)	η (%)	R_s (Ωcm^2)	R_p (Ωcm^2)
SeH	high	675	29.5	75.1	14.9	0.9	2855
SeL1	low	700	31.0	74.7	16.2	0.9	3720
SeL2	low	710	30.6	74.3	16.1	0.9	2484

6.3.1.3 Spectral response

The low short-circuit current of sample SeH (table 6.9) can be related to the bad collection of charge carriers generated by long wavelength photons as shown by EQE measurements in figure 6.41. An increase of EQE at the long wavelength side for samples with reduced Se evaporation rate (SeL1-2) is visible. The absorption edge at the long wavelength side is similar for all cells. A linear extrapolation of the squared EQE gives an estimate of the (minimum) band gap of the absorber at room temperature. The band gap for all cells is around 1.16 ± 0.09 eV. Due to a small number of data points, the error is rather large. Reference [25] shows an increase of the band gap energy for a lower Se content. This effect can of course also depend on other (specific) growth parameters, a comparison is therefore difficult.

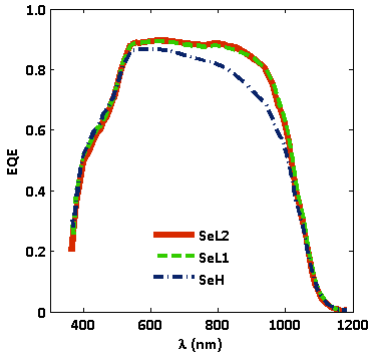

Figure 6.41: EQE of samples with different Se evaporation rate (provided by Empa).

6.3.1.4 Morphology

As a small grain size can result in higher recombination rate and hence smaller efficiency, it is useful to take a look at SEM pictures. From the SEM pictures of samples for which the buffer and window layer is etched away, it seems that grain size for the sample with reduced evaporation rate (SeL2 figures 6.42(c, d)) is larger than for the sample with higher Se evaporation rate (SeH figures 6.42(a, b)). This is opposite to the results of reference [25] in which smaller grain sizes are found with decreasing Se flux. As the variation in Se flux could be different, it is perhaps difficult to compare different results.

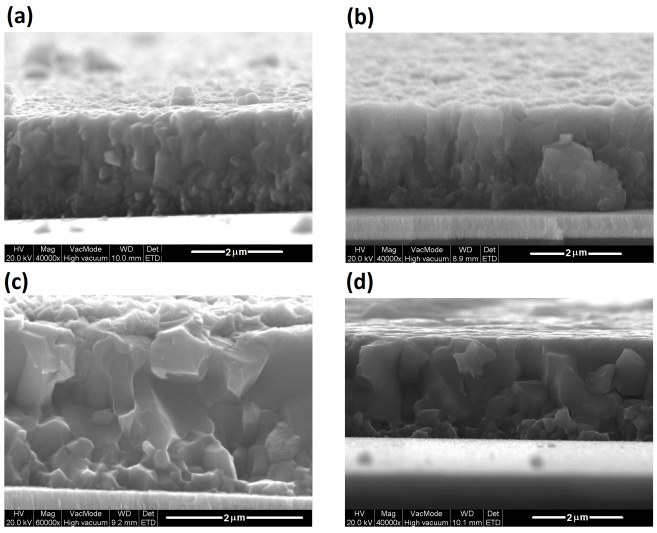

Figure 6.42: SEM images of absorber layers of (a, b) SeH, (c, d) SeL2.

6.3.1.5 Composition

XRF composition values can be found in table 6.10. No large differences can be noticed in the composition despite a difference in Se evaporation rate and difference in efficiency values. The lack of large composition changes due to an altered Se evaporation rate is in accordance with reference [27] but in disagreement with reference [258]. The CGI-ratios show that the samples have a Cu-poor composition. As the GGI-ratio is generally around 0.3-0.4 [73], the average GGI ratios of the investigated samples are rather large.

Table 6.10: XRF values and composition ratios of series3 (numbers provided by Empa).

	Composition, at %				Elemental ratio	
Sample	Cu	In	Ga	Se	CGI	GGI
SeH	21.4	15.5	11.1	52.0	0.80	0.42
SeL1	21.9	15.4	10.8	51.9	0.83	0.41
SeL2	21.6	15.2	11.2	52.0	0.82	0.42

6.3.1.6 Photoluminescence

Low temperature PL

Figure 6.43 shows PL measurements at low temperature (10 K) for all samples. Up to four quite broad peaks are visible in the spectra in contrast to the single broad peak that is expected for Cu-poor CIGS [16]. All spectra can be very well fitted using four Gaussian peaks (A-D) indicated in figure 6.43.

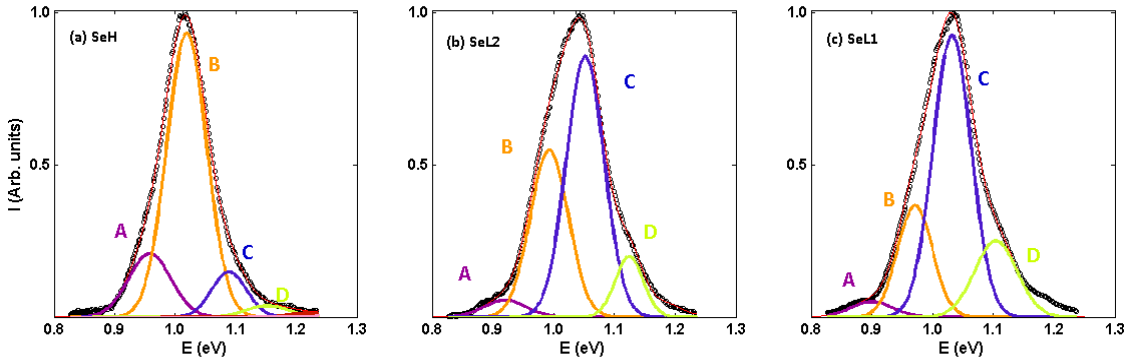

Figure 6.43: Fit of PL spectra (T = 10 K, λ_{exci} = 500 nm) of cells made at different Se evaporation rate.

Figure 6.44 shows PL measurements of SeH and SeL2 at the same excitation power and angle between excitation light and sample. Peak B in the spectra of sample SeH lies slightly closer to peak B of the spectra of SeL2.

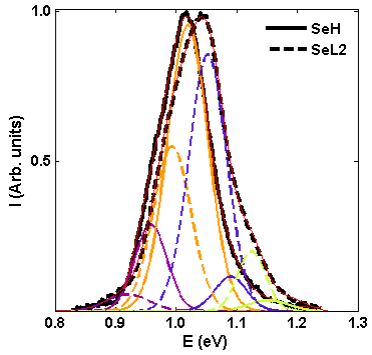

Figure 6.44: PL spectra of SeH and SeL2 under the same measurement conditions (T = 10 K, λ_{exci} = 500 nm).

The dominant PL emission of sample SeH is related to a deeper defect transition (peak B). Emission of samples SeL2 and SeL1 is dominated by peak C which appears at higher energy and is therefore related to shallower defect transitions. The differences in dominance of the emission peaks can be ascribed to the effect of different Se evaporation rate. In section 6.2.2.6 it was suggested that peak C is related to a DAP recombination involving the V_{Se} donor defect. As samples SeL2 and SeL1 have low Se evaporation rate, which results, according to references [25, 258–260], in a higher V_{Se} defect concentration, the relation of peak C to a V_{Se} defect could be reasonable.
The lower EQE at the long wavelength side for sample SeH might be related to the dominance of deeper defect transitions. Defects located deeper in the band gap enhance the higher recombination rate [6]. As in samples SeL1-2 a more shallow defect transition is dominant, the recombination rate could be lower for these samples. A similar reasoning was reported in reference [255]. As many other parameters (such as grain size, resistance, grading) are determinative for the final device performance, this specific PL peak dominance cannot be regarded as a strict indication for high efficiency.

Temperature dependent PL measurements
Temperature dependent PL measurements give a further indication for the fitting and assignments of the peaks. Further an unusual temperature dependence and small red-shift of the spectra with increasing temperature is found.

• ***Indication for fitting:*** Another argument to relate the dominant peak of sample SeH to peak B is found in temperature dependent spectra. Figure 6.45 shows spectra of samples SeH and SeL2 for which buffer and window layer are etched away in HCl. Samples are labelled as '-HCl'. Figures 6.45(a) and (b) show the temperature dependent spectra (normalized to the maximum of the spectrum of 10 K) of both samples. Figure 6.45(c) and (d) represent all spectra, normalized to their maximum.

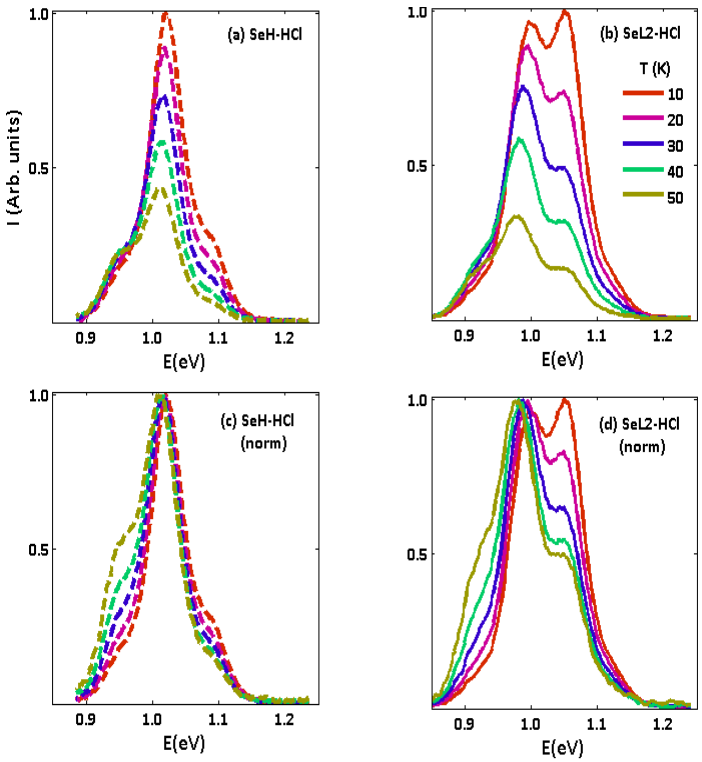

Figure 6.45: Temperature dependent PL spectra of SeH-HCl (a, c) (λ_{exci} = 550 nm) and SeL2-HCl (b, d) (λ_{exci} = 600 nm). Figures(a, b) are normalized at the maximum of the spectrum at 10 K, each spectrum in figures(c, d) is normalized to its maximum.

Figures 6.45 (b, d) show that due to a rapid decrease of peak C in the spectra of sample SeL2-HCl, peak B becomes the dominant peak at higher temperatures. In the spectra of sample SeH-HCl, peak B is also the dominant peak at higher temperatures. From figure 6.45(c, d) it seems that the intensity evolution of peak B in sample SeH-HCl and SeL2-HCl are similar. Furthermore from figures 6.45(c, d) it seems that relative intensity of the peak at lowest energy (between 0.90-0.94 eV), increases as the temperature increases. Because of the similar temperature evolution, the peak at lowest energy is for both samples assigned to peak A. The subsequent peak should than for both samples be peak B.

• ***Unusual temperature dependence of intensity:*** Temperature dependent luminescence analysis can be used to identify the type of transition by the shift of the peaks or to determine the defect level energies (see section 5.2). Normally, a decrease in the intensity is expected for defect related luminescence transitions.
For PL measurements of this series, an unexpected temperature evolution of the PL intensity is found. The greatest deviation, presented in figure 6.46, was seen in spectra of sample SeL1. Upon increasing temperature, the PL intensity of peak B, at lower emission energy, increases instead of the expected decrease.

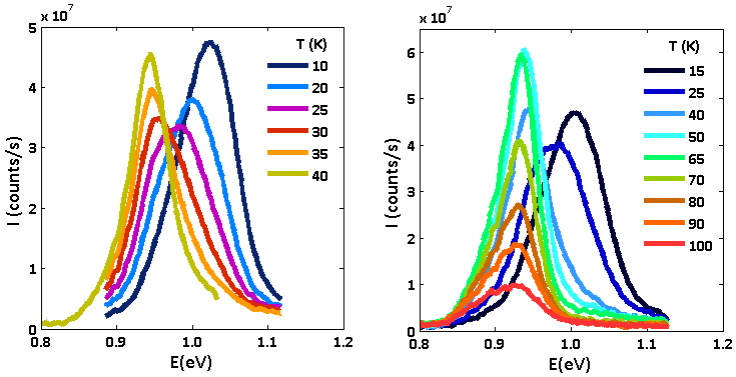

Figure 6.46: PL spectra of SeL1 as a function of temperature at λ_{exci} (a) 550 nm, (b) 650 nm.

Figure 6.47 shows PL measurements as a function of temperature between 10 and 50 K for the different cells. The very large intensity increase of peak B is not observed for all cells. The intensities of peaks A and B seem to decrease very slowly or even increase as temperature increases. Figure 6.47 shows further that the intensity evolution is not identical between the different samples and not even for different measurements on the same sample as shown in figures 6.47(c) and (d). As the excitation spot as well as the excitation power can be altered between different measurements, a variation of the spectra can be related to spatial inhomogeneities between different samples and in the samples.
The determination of an activation energy via the analysis of the PL intensity as a function of temperature (equation 5.4) is not unambiguous for these samples due to the demonstrated unusual temperature dependence of the PL spectra. Moreover it is shown below (by the small red-shift of the spectra with increasing temperature and by excitation power dependent measurements) that there is a slight influence of potential fluctuations. In this case determining activation energies is further hindered as thermal redistribution processes in the potential wells can take place (section 5.2.1.2).

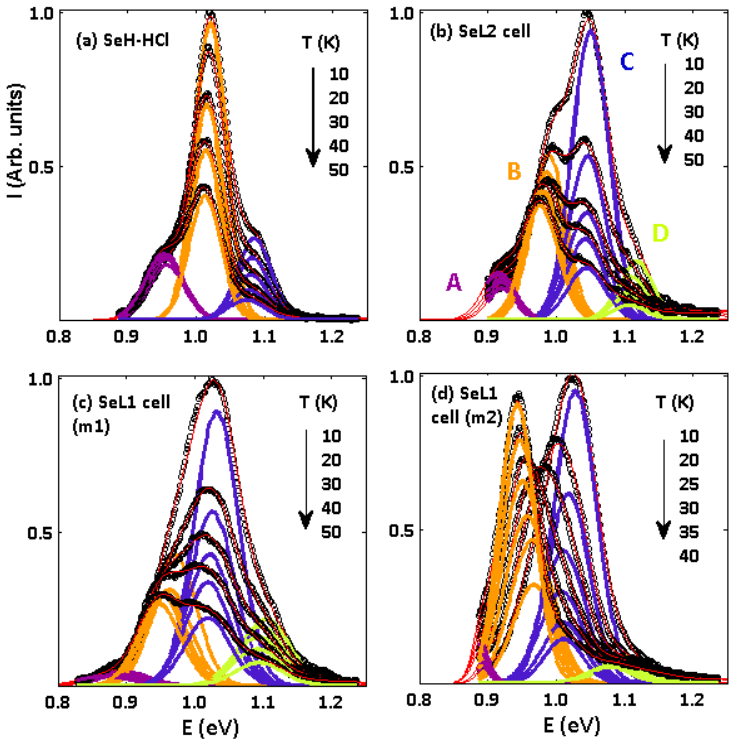

Figure 6.47: Fit of temperature dependent PL spectra (λ_{exci} = 550 nm) for samples (a) SeH-HCl, (b) SeL2, (c) SeL1 (measurement 1), (d) SeL1 (measurement 2).

The observation of an increase in intensity of a PL peak with increasing temperature is very unusual. Reports on such observations are very scare. In reference [186] a similar strange PL temperature behaviour was noticed for a Cu-rich, Se deficient $CuInSe_2$ thin-film grown by vacuum evaporation. Two deep PL emissions peaks around 0.86 eV and 0.82 eV were detected (figure 6.48(a, b)). The temperature dependence of the emission at 0.86 eV showed anomalous temperature behaviour; the PL intensity increased with temperature up to about 60 K, and thereafter the intensity decreased. At 110 K the PL intensity was completely quenched. The temperature dependence of the emission around 0.82 eV showed a normal decrease in PL intensity with increase in temperature.

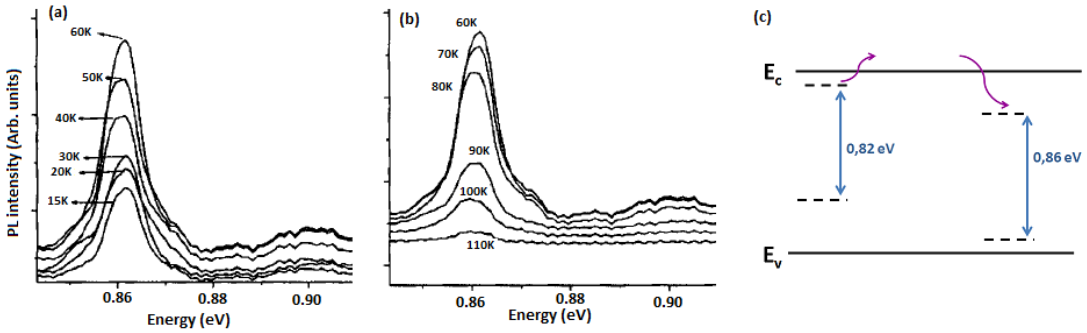

Figure 6.48: Temperature dependence of PL intensity of peak 0.86 eV. (a) Variation from 15 to 60 K. (b) Variation from 60 to 130 K [186]. (c) Band diagram which may explain an increase in PL intensity with increase in temperature. The electrons thermally emitted by the shallowest donor level are recaptured by the deeper donor level.

It is proposed in reference [186] that electrons (figure 6.48(c)), are thermally released from a shallow donor level to the conduction band and subsequently are trapped by a deeper donor. As more and more electrons are trapped by this deeper level, naturally an increase in the PL intensity of the associated band occurs. The PL band of the first donor level will decrease as temperature increases. Once the thermal excitation energy of the second defect level is exceeded, the emission intensity of this level will also decrease. This mechanism of passing electrons to deeper donors could be suggested as an explanation for the increase of the PL intensity as temperature increases. Alternatively there might exist thermally activated direct transfer of charge carriers from a defect to a deeper defect. Such process will depend on the local concentration of defects, which may provide an explanation for the variation of intensity decrease/increase between the samples.

• ***Temperature dependence of PL emission peak:*** For the most intense peaks (B and C), the peak shifts towards lower emission energy as temperature increases. This red-shift can be a result of a decreasing band gap energy with increasing temperature or can be related to transitions in the presence of potential fluctuations. The red-shift is $1.5{\cdot}10^{-4}$ eV/K for the highest intensity peak of SeL2 cell (peak C) and $2.3{\cdot}10^{-4}$ eV/K for peak B of sample SeH-HCl (buffer and window layer removed). For Cu-poor CIGS normally larger red-shift are found; between $8.0{\cdot}10^{-4}$ - $1.3{\cdot}10^{-3}$ eV/K [16, 84, 233, 235]. The smaller red-shift for the investigated samples could be regarded as an indication that the material is less compensated.

Excitation power dependent PL measurements

If potential fluctuations have a significant influence on the PL spectra, a large blue-shift with increasing temperature should appear in excitation power dependent measurements. Figure 6.49 represents the PL spectra as a function of excitation power of samples SeH-HCl and SeL2-cell at low temperature. The figure shows that the peak energy increases as the excitation power increases. A fitting of $E_{peak} = C + B{\cdot}\log(P_{exci})$ (equation 5.6) is performed to investigate the influence of potential fluctuations. The value of B equal to 5 meV/decade is on the edge of the distinction between compensation/no compensation in the material, this means a shift considerably larger than 5 meV/decade would present a clear indication of potential fluctuations in the material [5].

The B value for the most intense peak of sample SeH-HCl is 3.6 ± 0.5 meV/decade. The B value for peak C of sample SeL2-cell is 8.0 ± 0.5 meV/decade. One can see that dependent on the sample, B values are below/above the 5 meV/decade threshold which indicates a rather small influence of potential fluctuations in these samples.

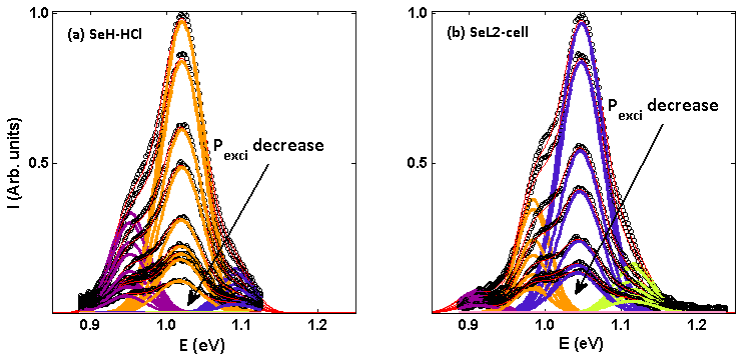

Figure 6.49: Fit excitation power dependent scans at 10 K for samples (a) SeH-HCl (λ_{exci} = 500 nm) (b) SeL2-cell (λ_{exci} = 550 nm).

6.3.1.7 Summary

No large difference in composition between cells, deposited at reduced substrate temperature, with relatively high or low Se evaporation rate could be found via XRF. Despite similar composition, samples with reduced Se evaporation rate (SeL1-2) appear to have higher EQE values at the long wavelength side and hence higher efficiency (in disagreement with the expectations). A possible explanation might be the larger grain size, shown by SEM, for SeL samples compared to SeH samples. However as indicated in reference [82] there is no simple dependence of efficiency on the grain size. PL spectra show up to 4 emission peaks. Temperature and excitation power dependent PL measurements do not show a large effect of potential fluctuations. The dominant PL emission of sample SeH is related to deeper defect levels (peak B), while for samples SeL1-2 the dominant PL emission is related to shallower defect levels (peak C). The dominance of the deeper defect transition for sample SeH could result in an enhanced recombination rate and hence lower efficiency. A more thorough understanding of the observed increase of efficiency with decrease in Se evaporation rate could be obtained via additional studies concerning texture and the effect on the inversion layer. By decreasing the Se evaporation rate the net carrier concentration can decrease as a result of the creation of V_{Se} donor defects. A decreased carrier concentration can increase the inversion of the surface whereby the tunnelling probability and hence (near) interface recombination reduces [28].

6.3.2 In-depth defect information by thinning of absorber layers

6.3.2.1 Motivation

In PL studies only a small region at the absorber surface is investigated. This is due to the large absorption coefficient of CIGS which leads to a small penetration depth [36, 131]. As shown in section 5.2.2, the 1/e penetration depth for excitation wavelengths of 700 and 300 nm is 200-300 nm and 25-50 nm respectively. For all excitation wavelengths only the surface region ($\leq$ 300 nm) is thus probed. It must be noticed that due to carrier diffusion and drift, the region wherein recombination takes place could be larger than the region determined by light generation. Depth information of the defect structure in the absorber can be obtained by a variation of the excitation wavelength as longer excitation wavelengths penetrate slightly deeper in the absorber layer. Due to the increase of penetration depth with increasing excitation wavelength, a larger region can be probed with an increase of PL intensity as a consequence.

In order to investigate if there is a difference between low or high evaporation rate on the defect structure, surface information obtained by PL may perhaps not be representative for the possible effect on the whole absorber layer. This is a first reason to perform PL measurements as a function of absorber thickness. Furthermore as the samples have a non-uniform depth profile (especially In and Ga element profiles), this as well can have an influence on the defects throughout the absorber layer. Depending on the in-depth position and hence the local composition, more insight in the identification of the defect structure could be gained. To investigate the effect of adjusted Se evaporation rate on the whole absorber layer and the PL dependence on composition throughout the absorber, PL measurements are performed on absorber layers thinned by Br etching with variable etching times.

PL measurements on thinned CIGS samples by Br etching are reported in reference [261] and reveal that as the thickness of the absorber layer decreases, the PL emission shifts towards higher energy because of an increasing GGI ratio towards the back contact. Reference [242] shows a cathodeluminescence emission peak at higher energy if the sample is excited at the back of the CIGS layer. Different peaks are assigned to regions of varying GGI. Reference [228] shows that with variation of the total GGI ratio in different samples, the luminescence peak energy continuously shifts towards higher energy through the addition of Ga.

6.3.2.2 Sample preparation

Samples SeH and SeL2 are etched in HCl to remove window and buffer layer (sample labelled as '-HCl'). Afterwards the samples are etched for different times in a Br-methanol solution to thin the absorber layer (table 6.11). The samples etched for 5 and 12 minutes are referred to as '-Br1' respectively '-Br2'. The thinning of the layers was confirmed by talystep and SEM measurements.

Table 6.11: Etching procedures to obtain a variation in thickness of absorber layer.

Etch	No	HCl	HCl+5 min Br	HCl+12 min Br
Label	-cell	-HCl	-Br1	-Br2

6.3.2.3 Morphology

The thinning of the absorber layer can be deduced from SEM images presented in figure 6.50. As samples SeL2 and SeH are etched simultaneously, the thickness of the layers after Br etch should be similar. This is confirmed in the SEM images. The thickness for samples -HCl, -Br1 and -Br2 are respectively 2.40, 1.58 and 0.72 µm.

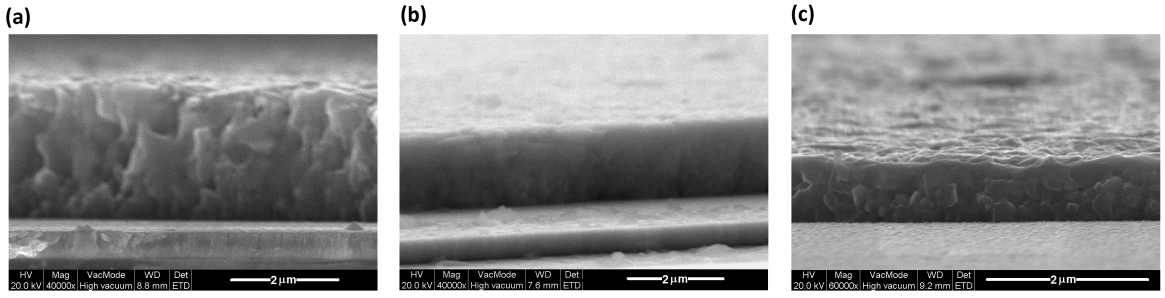

(a) SeH (a) -HCl, (b) -Br1, (c) -Br2.

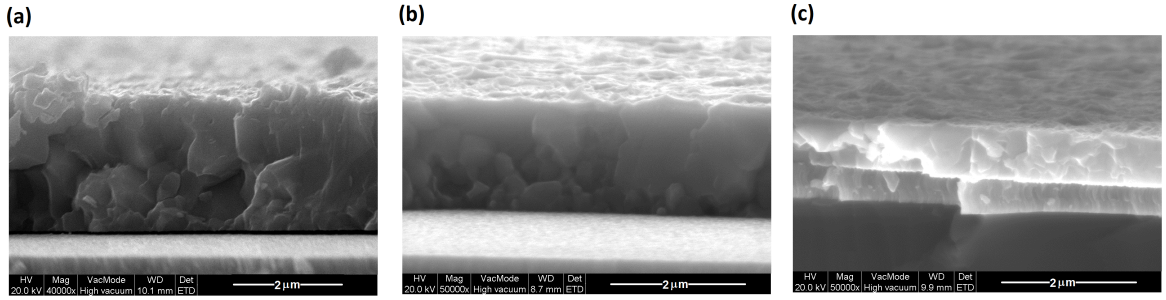

(b) SeL2 (a) -HCl, (b) -Br1, (c) -Br2.

Figure 6.50: SEM images of HCl and Br etched samples.

6.3.2.4 Composition

SIMS profiles are necessary to determine the composition at the surface of the thinned absorber layers. In addition, the SIMS profiles provide information about a possible change in the Se concentration which is reported as a result of the Br etch [212–214]. This can of course also influence the PL spectra.
SIMS measurements have been performed by Empa on samples SeH-HCl and SeH-Br2. Reference [27] states that there is no difference in elemental composition as Se pressure is altered. However as the experimental conditions are different, the composition of sample SeL2 could be different. The Cu, In, Ga and Se profiles are shown in figure 6.51 where 0 corresponds to the front surface of the sample, after removal of the front contact and buffer layer. The front surface positions of sample SeH-Br1 and SeH-Br2 are indicated. An increased Se profile at the surface for SeH-HCl (figure 6.51(a)) as well as for SeH-Br2 (figure 6.51(b)) is noticed. The effect of the Br etch on the Se profile cannot be unambiguously derived from the SIMS measurements. The Cu, In and Ga profile are not altered by the Br etching. No direct effects of the Br etch is therefore expected in PL measurements.

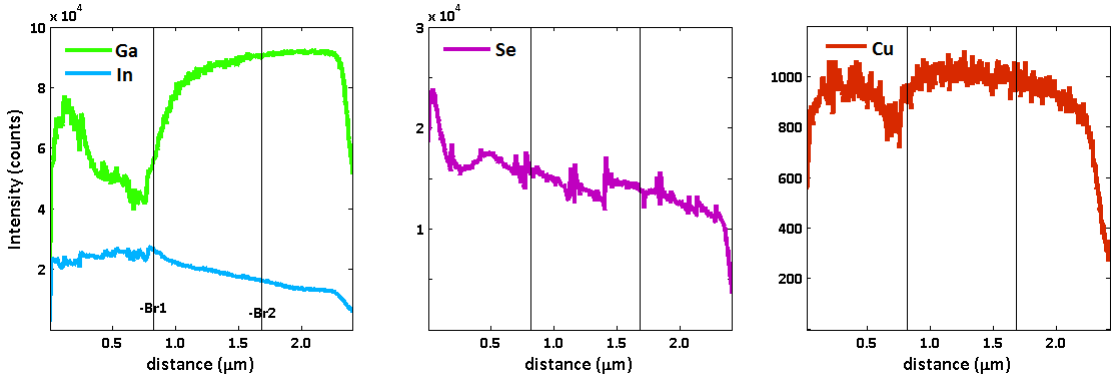

(a) SeH-HCl

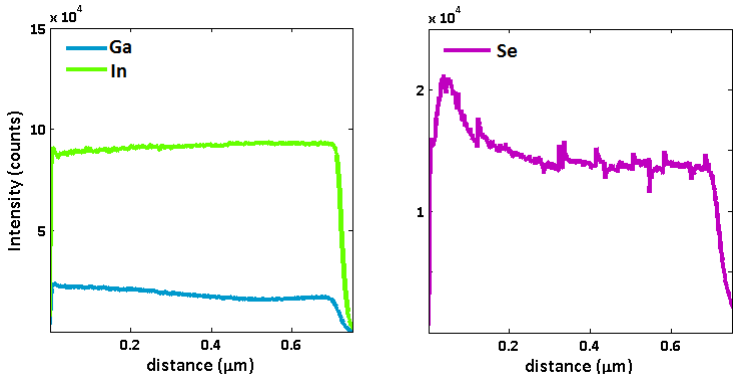

(b) SeH-Br2

Figure 6.51: SIMS depth profile (performed by Empa) of (a) complete (b) and thinned absorber layer.

At the position of the Ga dip, the In concentration is increased and the Cu concentration is slightly decreased. The In concentration decreases strongly towards the back of the solar cell. As the band gap throughout the absorber is dependent on Ga/In composition, the PL emission can shift towards lower (in the Ga dip) and higher (at the back) emission energy. An attempt is made to calculate the GGI ratio throughout the absorber layer starting from the Ga and In SIMS profiles and calibrated XRF values which give an average of the In and Ga compositions throughout the layer (table 6.10). The average of the SIMS depth profiles is set equal to the XRF value which leads to the GGI profile illustrated in figure 6.52. The GGI ratio at the surface after the HCl etch is around 0.30, after the first Br etch is around 0.28 and after the second Br etch is around 0.49. The same was done for CGI profile.

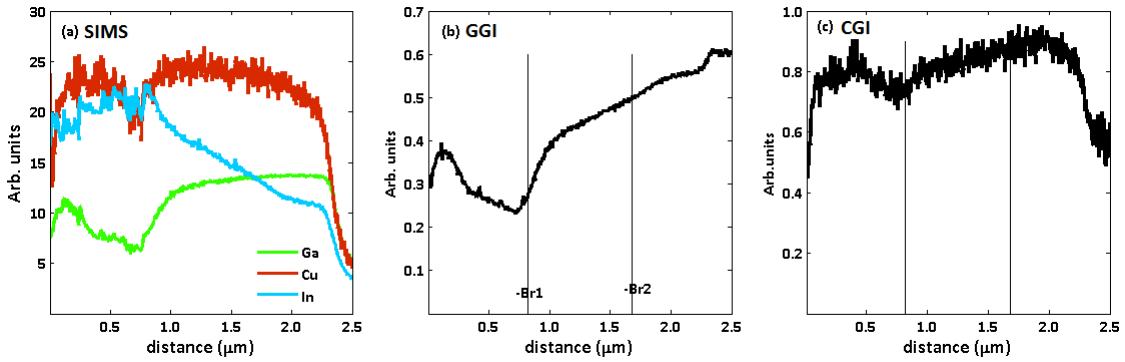

Figure 6.52: Estimation of GGI (b) and CGI (c) profiles from SIMS (a) and XRF measurements of sample SeH.

Band gap variation by GGI ratio
In the following an estimate of the maximal band gap energy shift between the different surface compositions of the samples -HCl, -Br1 and -Br2 is made. This shift will determine which of the emission peaks will be regarded as the dominant. The maximal shift will be deduced from the band gap energy dependence of the GGI ratio. It must be noted that a reduction of the Cu concentration can also lead to an increase of the band gap. As the Cu concentration in the investigated sample is quite constant (figure 6.51(a)), such an effect on the band gap can be excluded.
A change in the GGI ratio induces a slightly non-linear band gap change following equation 2.10 described in section 2.3.1.3. On the basis of equation 2.10 a change of about 0.1 of the ratio x results a band gap energy difference of 60 meV. This calculation is in agreement with references [73, 83] wherein the band gaps at the surface and at the Ga dip are experimentally determined by IVT and EQE analysis. As determined from figure 6.52 the GGI ratio at the surface of samples -HCl and -Br1 is more or less similar. The GGI ratio increases from the surface of sample -Br1 to the surface of sample -Br2 with 0.2. This increase could lead to a band gap energy shift up to 120 meV.

6.3.2.5 Photoluminescence

PL measurements at low temperature of the different thinned absorber layers are compared in order to obtain in-depth information of the defect structure. Additional in-depth information is provided by excitation wavelength dependent measurements at low temperature in which the excitation wavelength is altered from 300 to 700 nm. First the results of sample SeH are discussed, thereafter the results of sample SeL2.

Sample SeH
1) Comparison of low temperature spectra on SeH with different thickness
• ***After HCl etch*** Figures 6.53(a) and (b) show two PL measurements (m1 and m2) at 10 K on sample SeH-HCl. Depending on the excitation spot, differences in the intensities of contributions can be noticed which are related to local variations in the layer. However large changes in the PL spectra are not visible.

• ***After first Br etch*** The emission energy of SeH-Br1 is shifted 23 meV towards lower energy compared to the spectra of SeH-HCl. Despite different composition (especially Ga and In composition), the spectra of SeH-Br1 look very similar to SeH-HCl. No change in the dominant peak occurs. At high emission energy peak D appears on the spectra of SeH-Br1.

• ***After second Br etch*** The PL spectra of SeH-Br2 appear at higher energy. The energy shift of the PL spectra of SeH-HCl and SeH-Br2 is 112 meV. The spectrum of SeH-Br2 is similar to this of SeH-HCl. It seems that the higher Ga content towards the back side of the absorber has, besides the shift towards higher emission energy, no influence on the relative intensities of PL peaks in the spectra.

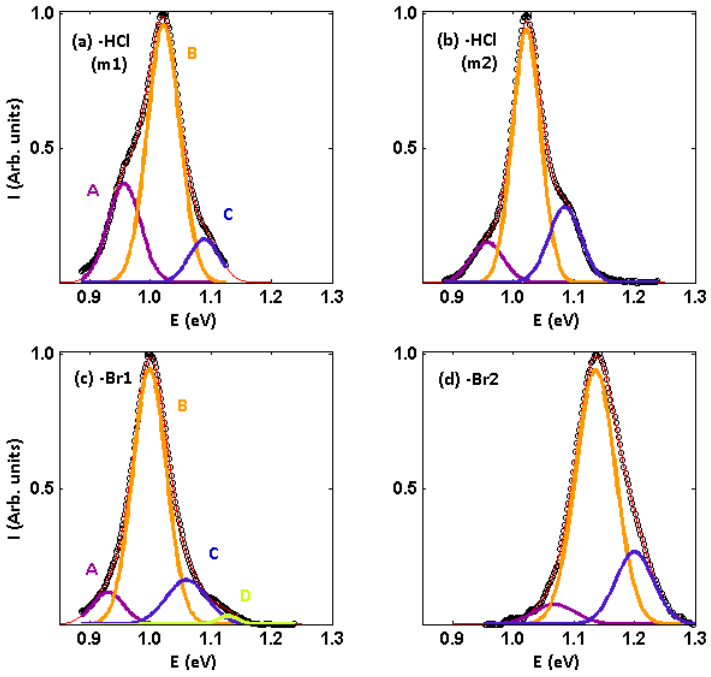

Figure 6.53: PL on SeH absorber layer with varying thickness (T = 10 K, λ_{exci} = 500 nm).

In section 6.2 the PL peak at low energy for CIGS solar cells produced at reduced substrate temperature was related the deep electronic level (E_c-210 meV [256]) of the Cd_{Cu} donor in accordance with references [98, 256]. This assignment was supported by EDX and TOFMS measurements which showed a higher Cd diffusion in cells with increased emission at lowest energy. The PL spectra of the thinned absorber layers do not support this assignment as peak A does not disappear in the PL spectra of thinned absorber layers in which no in-diffused Cd is expected any more. Another deep level defect transition should be responsible for the PL emission of peak A. It could be noted that the theoretical calculations of reference [262] point toward a lower activation energy for this Cd_{Cu} defect. Since no PL peak disappears in the spectra of a thinned absorber layer, the contribution of a Cd_{Cu} defect related transition could be regarded as very unlikely.

2) Excitation wavelength dependence of samples SeH with varying thickness

No shift in the dominant PL peak with increasing excitation wavelength is visible for samples SeH with varying thickness. Peak B is dominant throughout the whole absorber layer. A possible explanation is that due to the high Se evaporation rate, peak C which could be related to V_{Se}, is suppressed throughout the whole absorber layer. The intensity of all PL peaks increases as excitation wavelength increases. For sample SeH-Br1, peak D increases as excitation wavelength increases. This peak could be related with band-impurity transmission since the energy of PL emission is high. The transition could be related to shallow acceptor V_{Cu} defect. The appearance of peak D might be related with the small dip in the concentration of the Cu profile at position -Br1, visible in SIMS profiles (figure 6.51). However more evidence for the assignment of this peak is necessary.

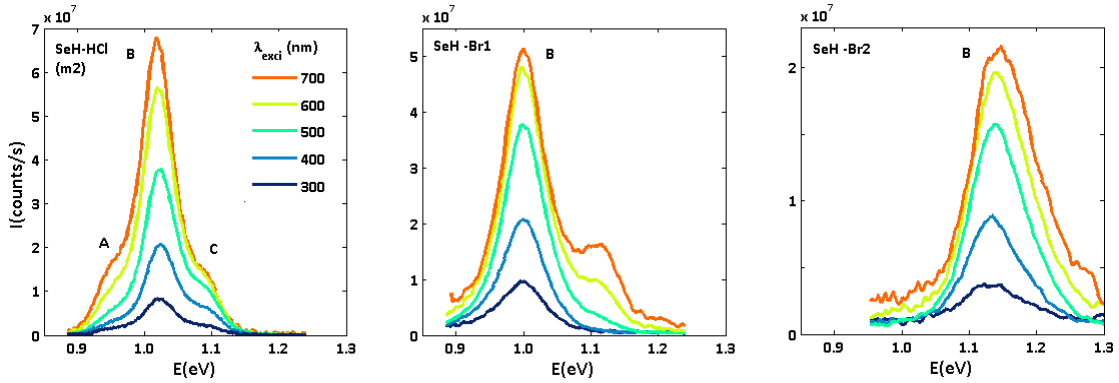

(a) PL spectra as function of λ_{exci} for sample SeH with varying thickness.

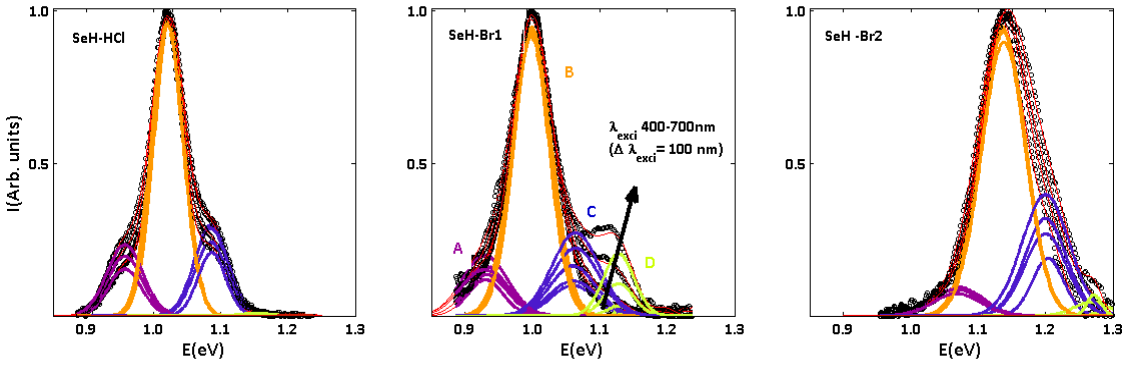

(b) Normalised and fitted spectra as function of λ_{exci}.

Figure 6.54: Excitation wavelength dependent measurements on SeH-HCl, -Br1, -Br2 (T = 10 K).

Sample SeL2

1) Comparison of low temperature spectra on SeL2 with varying thickness

• ***Comparison of cell and HCl etched sample*** Figures 6.55(a) and (b) represent measurements on the complete cell and on the HCl etched sample. No change in the peak dominance is visible between the spectra. From this it can be assumed that the window and buffer layer do not largely influence the PL measurements.

• ***After first Br etch*** The emission energy of sample SeL2-Br1 is shifted 37 meV towards higher energy compared to the emission of SeL2-HCl. The small shift towards higher energy is not expected. If the absorber thickness of SeL-Br1 is related to the SIMS profile of sample SeH, a shift towards lower energy should occur, like it was the case for sample SeH-Br1. Unfortunately no SIMS profile of SeL2 is available which could provide the exact GGI ratio of the surface of SeL2-Br1. Due to an altered Se evaporation the profiles could be altered. From figure 6.55(c) it appears that peak B is dominant in sample SeL2-Br1. Since the In concentration at this position is higher than for samples SeL2-HCl and SeL2-Br2, peak B could be assigned to a In_{Cu} defect related transition. This possibility will be further discussed underneath via excitation wavelength dependent measurements on samples SeL2-HCl and Sel2-Br1.

• ***After second Br etch*** The PL spectrum of sample SeL2-Br2 is shifted 120 meV towards higher energy compared to PL spectrum sample SeL2-HCl. Peak C is dominant as is the case for SeL2-HCl. This can be related to a decrease of the In concentration towards the back.

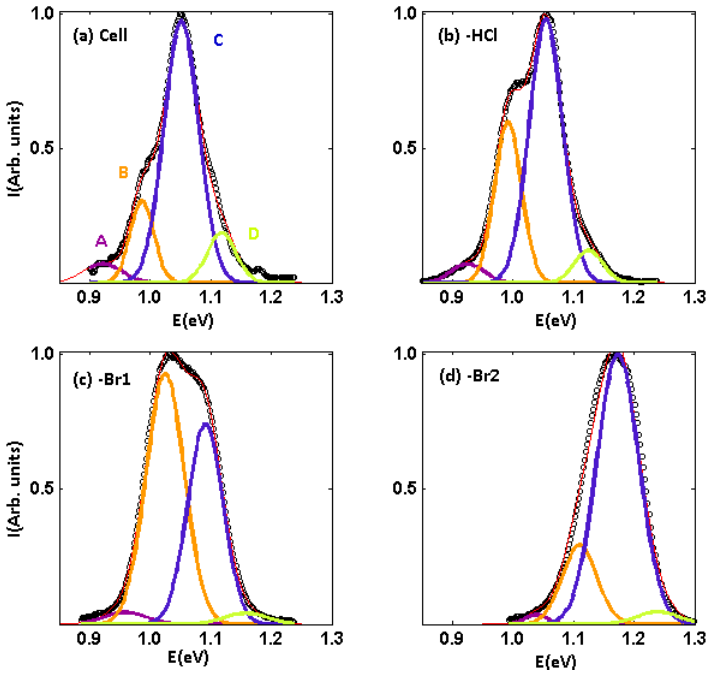

Figure 6.55: PL on thinned samples of SeL2 (T = 10 K, λ_{exci} = 500 nm).

2) Excitation wavelength dependence of samples Sel2 with varying thickness
Figure 6.56 shows that peak B becomes dominant as excitation wavelength increases in the PL spectra of sample SeL2-HCl. In the spectra of sample SeL2-Br1, peak B is dominant for small excitation wavelengths but not for large excitation wavelengths. For sample SeL2-Br2 no change in the dominant peak appears, in fact the PL is completely dominated by peak C in this case. From the excitation wavelength dependent measurements and the results in figure 6.55 it can be suggested that peak B becomes dominant in the sample region where the In concentration is high. The In concentration will be the largest at the surface of sample -Br1 because there is a higher In concentration at the position of the Ga dip. This finding is thus not in contradiction with the suggestion (made in section 6.2.2.6) to relate peak B with an In related defect e. g. In_{Cu}. The shift in the dominant peak of samples SeL2 with varying thickness was not visible for samples SeH with varying thickness. For sample SeH, peak B is dominant throughout the whole layer probably due to a reduced intensity of peak C. A small intensity increase of peak D with increasing excitation wavelengths, which was also noticed in sample SeH-Br1, is visible.

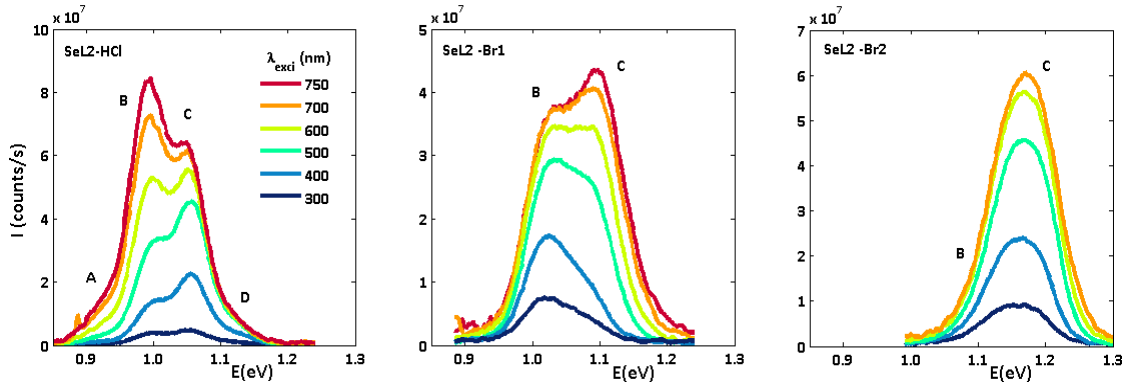

(a) PL spectra as function of λ_{exci} for sample SeL2 with varying thickness.

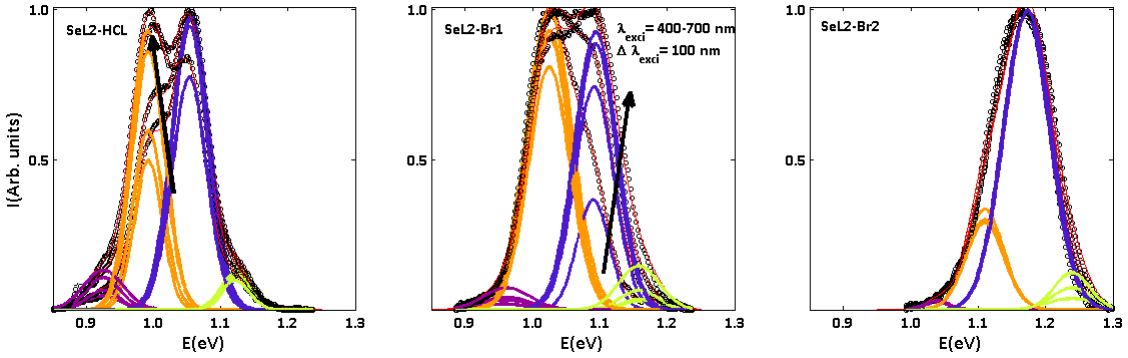

(b) Normalised and fitted spectra as function of λ_{exci}.

Figure 6.56: Measurements as function of λ_{exci} on SeL2-HCl, -Br1, -Br2 (T = 10 K).

6.3.2.6 Summary

The PL spectra on thinned CIGS absorber layers confirm a dependence of the PL emission energy on the GGI ratio as reported in references [228, 238, 242, 261]. The energy shift of the emission peak is related to the GGI ratio change of the different surface compositions. PL spectra reveal no change in the dominant peak for samples SeH with varying absorber thickness. A different situation occurs in the PL spectra for sample SeL2; peak B is dominant at a position around the Ga dip (sample -Br1), peak C is dominant at the front and back of the absorber (samples -HCl and -Br2). The relative increase of peak B in the PL spectra could be related to an increase of In around the Ga dip. This could be regarded as an experimental support for the suggestion that peak B is related to an In_{Cu} defect related transition. Since no PL peaks disappears on the PL spectra of thinned absorber layers, these experiments contradict the suggestion that peak A would be related to a Cd_{Cu} defect.
These investigations reveal that the region in which PL emission occurs, is limited to the absorber surface. On the PL spectra of a complete absorber there is no emission visible in the energy range at which emission at the back of the absorber layer occurs. Basically the same number of PL contributions, with same energy separations appear regardless of the thickness of the absorber layer. In reference [242] it is suggested that the peak at lowest energy in cathodoluminescence spectra from the front side, arises from the minimum band gap region and the peak at higher energy arises from the surface region with higher GGI ratio. This suggestion can not be unified with the findings presented in this report. With thinning of the absorber layer, no peak (related to surface region) disappears. Furthermore as the energy separation between the peaks in reference [242] is dependent on the GGI profiles, different energy separations between the peaks would be found for different GGI profiles. This is not the case for the investigated samples in this thesis. From presented results concerning thinning experiments there is no evidence that PL contributions arise from different regions, with different band gap energies, in the absorber.

6.3.3 Effect of different post annealing methods

6.3.3.1 Motivation

From the PL spectra of samples with high (SeH) and low (SeL1-2) Se evaporation rate, it seems that there is a shift in the dominant PL peak. The dominant peak (peak C) for samples produced at low evaporation rate, we previously (section 6.2.2.6) assigned to a V_{Se}-V_{Cu} DAP defect transition. Although such assignment seems confirmed by the dominance of this defect for samples with low Se evaporation rate, an attempt is made in this section to get further experimental support for relating peak C to V_{Se} defect. To do so, three different post annealing treatments on HCl etched samples (which provides bare CIGS absorber layers) are performed. The first treatment is a post selenisation which is intended to lower the concentration of V_{Se} defects as demonstrated in references [4, 263]. The second consists of an air anneal which is reported lower the V_{Se} defect concentration indirectly [132, 264]. Last, a vacuum anneal is intended to increase the V_{Se} defect concentration, following references [265–267].

6.3.3.2 Sample preparation

All post treatments are performed on HCl etched samples for which the buffer and window layer are removed. The post selenisation (labelled as -PSe) (in collaboration with CoCooN, research group of the department of Solid State Sciences at Ghent University) is performed at 400°C during 2h. The air annealing (labelled as -PAir) is performed 400°C following reference [132]. The time of temperature increase and anneal was 2 hours. The vacuum anneal (labelled as -PVac) (in collaboration with Lumilab, research group of the department of Solid State Sciences at Ghent University) is performed at 400°C during 1.5h, the increase of temperature took 1.5h. An overview of the post treatment methods and the sample labels is given in table 6.12.

Table 6.12: Post annealing treatments on HCl etched samples.

Post treatment	No	Selenisation	Air anneal	Vacuum anneal
Label	-HCl	-PSe	-PAir	-PVac

6.3.3.3 Photoluminescence

An overview of the different post treatments effects on the PL spectra of SeH and SeL2 is presented in figures 6.57 and 6.58 respectively. Figures 6.57(a) and (b) (which represent spectra of two measurements (m1-m2) on sample SeH-HCl) and figures 6.58(a) and (b) (which represent PL spectra of sample SeL2 on a complete cell and sample -HCl) show that the spectra reveal small intensity variations for the different peaks. These variations can mainly be ascribed to composition inhomogeneities in the absorber layer. This makes the interpretation of the effect of some post treatments more difficult. A clear assignment of an effect of post treatment on PL spectra should therefore be based on large peak intensity variations or a shift in the dominant peak.

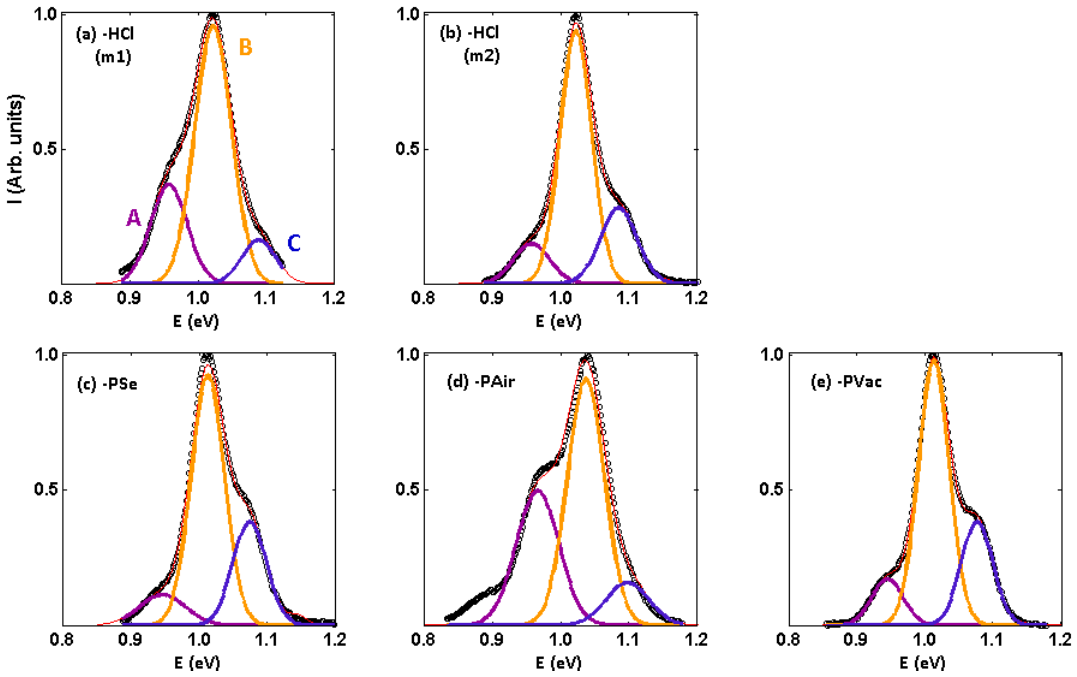

Figure 6.57: PL on sample SeH with different post treatments (T = 10 K, λ_{exci} = 500 nm).

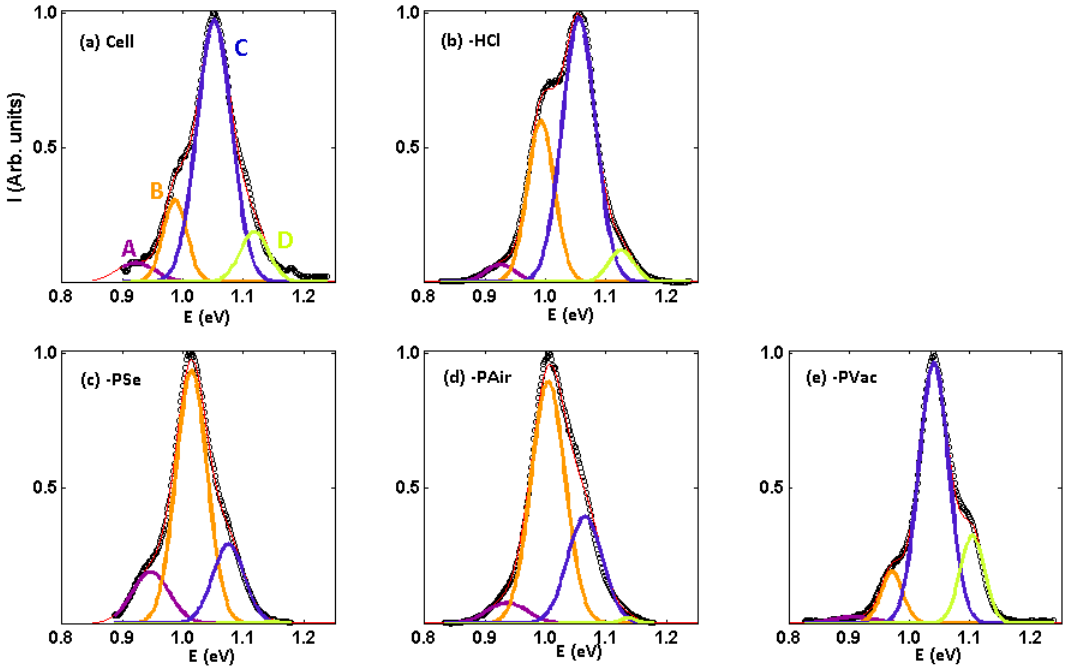

Figure 6.58: PL on sample SeL2 with different post treatments (T = 10 K, λ_{exci} = 500 nm).

For each post treatment a literature overview will be given first. Afterwards the effect of the post treatment on the PL spectra will be discussed and related with the defect structure.

Effect of post selenisation

Literature overview post selenisation: In reference [4] it is shown that melt-grown $CuInSe_2$ crystals annealed under excess Se result in a p-type crystal. Crystals annealed under low Se pressure exhibits n-type conductivity. The n-type crystals can be converted to p-type crystals by annealing in Se atmosphere because under high Se pressure the V_{Se} donors are suppressed. The PL spectrum of the crystal with low Se pressure has a dominant V_{Se}-V_{Cu} defect transition

which disappears when the crystal is annealed under high Se pressure.
References [4, 263] investigated the effect of annealing in different atmospheres on $CuGaSe_2$ crystal. The high energy peak disappears in the PL spectra of the crystals after annealing under O_2 and Se atmosphere, suggesting that the Se vacancy defects are compensated by either oxygen or Se. The high energy PL peak remains when annealing in H_2 atmosphere. The peak at lower energy, which is ascribed to a defect pair ($2V_{Cu}+ Ga_{Cu}$), was not altered by the annealing.

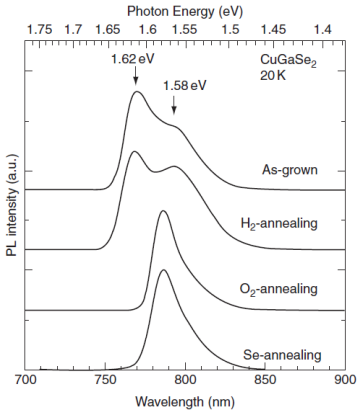

Figure 6.59: PL spectra of as-grown, H_2, O_2 and Se annealed $CuGaSe_2$ single crystals [4].

Results post selenisation:
⋆ SeH: No large change due to post selenisation can be noticed on the spectra in figure 6.60(a).
⋆ SeL2: In contrast to sample SeH, a large effect on sample SeL2 is visible (figure 6.60(b)). For sample SeL2 peak C, which is dominant in sample SeL2-HCl, disappears after post selenisation. It could be argued, that as sample SeL2 is made at reduced Se evaporation rate, a large concentration of V_{Se} could be present in sample SeL2-HCl. Due to the post selenisation, the V_{Se} donor defects could be outweighed whereby the intensity of the peak related to this defect is lowered. A reduction of the compensation could result in a small blue-shift of the spectra. The lowering of peak C in the spectrum of the sample SeL2-PSe, could be regarded as an evidence that peak C is related to a defect transition in which V_{Se} takes part. Figures 6.60(c, d) show that the temperature dependence of the spectra after post selenisation are similar for both samples and to the temperature dependent spectra of sample SeH-HCl in figure 6.45(a).

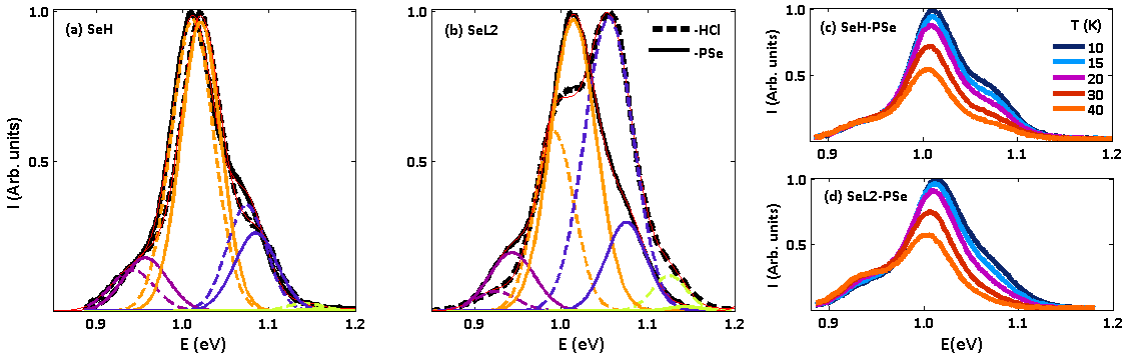

Figure 6.60: Effect of post selenisation (λ_{exci} = 500 nm, T = 10 K) on spectra of samples (a) SeH and (b) SeL2. Figures c and d show the temperature dependence of the spectra.

Effect of air anneal

Literature overview air anneal: Reference [132] shows optical measurements performed on air/oxygen post growth annealed CIGS thin-films (figure 6.61). The broad unstructured PL spectrum of a Cu-poor film changes to a structured Cu-rich PL spectrum after annealing at 400°C. It seems that the effect of potential fluctuations on the spectra as disappeared. It is concluded that air annealing, due to the reaction with oxygen, has reduced the donor density and high compensation. A possible explanation for the passivation or reduction of the donor density is a change of V_{Se} donor in an O_{Se} acceptor. This defect is postulated to be electrically inactive (neutral) because oxygen and selenium have the same valence state (2-). Annealing performed in inert Ar gas and N_2 was performed to ensure the change in the PL spectra is due to chemical changes and not related to a temperature effect. Except for a shift of the spectra, no change was found after Ar and N_2 annealing. Reference [132] states that temperatures of 400°C are necessary to induces the Cu-poor to Cu-rich shift in the spectrum.

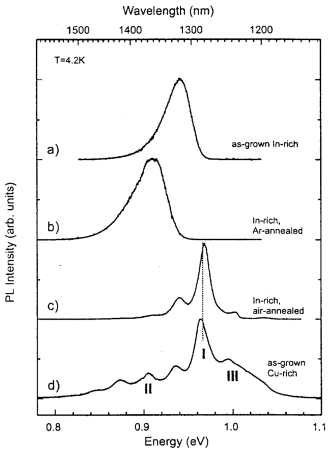

Figure 6.61: PL spectra for different annealing. Peak 1 and 2 are DAP recombinations followed by phonon replicas. Peak 3 is assigned to a Ga rich phase [132].

In reference [264] In-rich $CuInSe_2$ and $Cu(In,Ga)Se_2$ co-evaporated films were annealed in air at 400°C. A slight blue-shift of the spectrum and increase of full width at half maximum was noticed after air annealing. The blue-shift of the luminescence was interpreted as a reduction of the compensation. It was suggested that the chemical reaction V_{Se}+O which results in O_{Se}, is responsible for the passivation of donor states. The change in compensation was confirmed by decrease of the band-tail character of the absorption edge, revealed by PL excitation experiments. After annealing of a $CuInSe_2$ layer, the broad PL spectrum changed to a structured spectrum. For a CIGS layer no transformation to a structured PL spectrum occurred, only a blue-shift was noticed (figure 6.62).

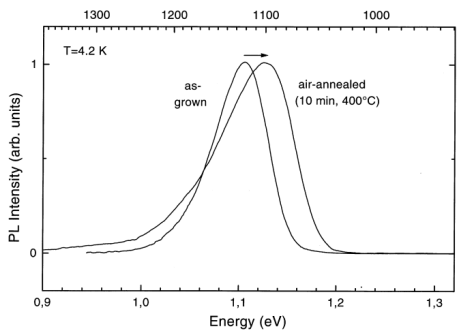

Figure 6.62: PL spectrum of a CIGS layer before and after annealing in air. A broadening of the peak and small blue-shift is visible [264].

Results air anneal:
⋆ SeH: The spectrum after annealing looks very similar to the spectrum before annealing. As the intensity of peak C was relatively small in the spectrum before annealing, the effect of the air anneal on the sample is not clearly visible. In accordance with reference [264] a small blue shift of the spectrum after annealing can be noticed. The relative intensity of the peak at the lowest energy (peak A) has increased. This low energy peak is thus not a result of an O_{Se} defect as it is present in the PL spectra of etched as well as of complete cells. Based on the existing information it is not straightforward to assign the defects present in the PL transition of peak A. An additional contribution appears below 0.9 eV (indicated in figure 6.63 with (*)).
⋆ SeL2: Air annealing leads to a relative decrease of peak C as presented in figure 6.63(b). This could be explained by the mechanism in which V_{Se} donor is passivated by the formation of O_{Se} defect. As no additional peak appears, no peak can be related to this O_{Se} defect which could be formed by the annealing. A small blue-shift is also visible.

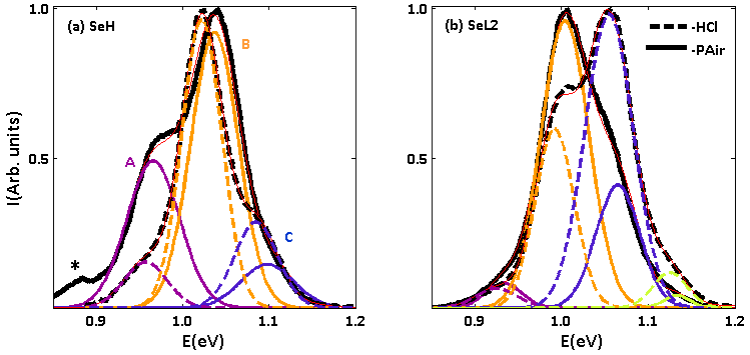

Figure 6.63: Effect of air anneal (λ_{exci} = 500 nm, T = 10 K) on spectra of samples (a) SeH and (b) SeL2.

Effect of vacuum anneal
Literature vacuum anneal: Reference [265] has reported that a directly sputtered CIGS thin-film annealed under vacuum exhibits a loss of Se. Annealing under Se containing atmosphere revealed an increase in Se with a enhanced crystallinity as a result. In reference [266] the PL peak for a vacuum annealed Cu-rich $CuInSe_2$ sample, grown by molecular beam epitaxy on GaAs, was broader, had a higher intensity and was red-shifted. Due to the reduction in hole concentration and the decrease of Se molar fraction, a formation of V_{Se} donors was proposed. A reduction in carrier concentration upon vacuum annealing was also reported in reference [267]. The PL emission peak related to V_{Se} was found to increase for $CuGaSe_2$ single crystals annealed in vacuum.

Results vacuum anneal:
⋆ SeH: A very small increase of peak C is visible in the spectra of the sample SeH after vacuum annealing. However the variation is not larger than the variation between measurements on different spots of the same sample. A small red-shift is seen.
⋆ SeL2: A relative increase of peak C and small red-shift is visible after vacuum annealing of sample SeL2. This results in a relative decrease of the intensities of peaks A, B and D.

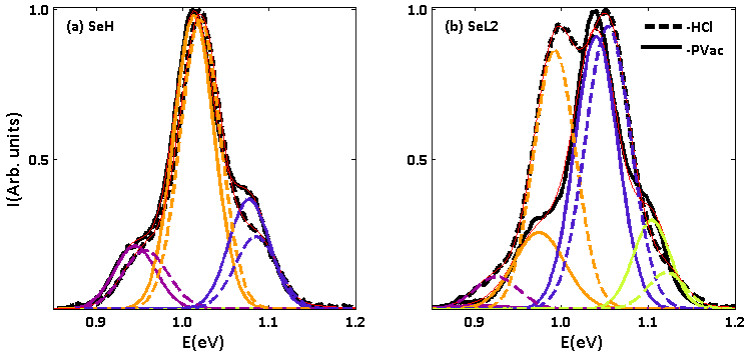

Figure 6.64: Effect of vacuum anneal (λ_{exci} = 600 nm, T = 10 K) for samples (a) SeH and (b) SeL2.

6.3.3.4 Summary

Generally, the post treatments, which intended to alter the V_{Se} defect concentration, did not have a large effect on sample SeH but did clearly have an effect on sample SeL2. The treatments only changed the intensities of peak C. It seems the effect of the post treatments is dependent on the production parameters during co-evaporation process of the CIGS absorbers and hence dependent on the initial defect structure. The large intensity changes of peak C in the PL spectra of post treated samples of SeL2, seems to support the assignment of peak C to a transition in which V_{Se} is involved. From the experiments it could be suggested that the PL peaks, other than peak C, are not related to a V_{Se} defect transition.

6.4 CIGS: Effect of K and/or Na and influence of incorporation method

6.4.1 Motivation

The use of PI substrates needs distinct incorporation of the alkaline metals (Na and K) and low growth temperatures. The low substrate temperature [73], the presence of Na [123, 124] as well as the presence of K [136] can have an influence on the diffusion of the elements during growth. As a result a change in the defect formation can occur. Reference [75] indicates that the Na incorporation method has a large influence on the PL properties and hence on the efficiency. In this study we investigate by PL the effect of various Na and K introduction methods (during third stage of CIGS deposition and/or PDT) on the defect structure of CIGS layers deposited at low growth temperature on PI foil.

6.4.2 Preparation and performance

Cell preparation The CIGS absorber is grown at low substrate temperature ($< 500°C$) on a Mo coated PI foil. Na and K are introduced during third stage of the co-evaporation and/or by PDT deposition (see table 6.13). A reference alkali free sample, without any Na or K is made (labelled as Wto). KF and NaF PDT deposition was performed at a temperature of 350°C directly after the finishing growth of the CIGS layers in the presence of Se. The CdS buffer layer was deposited by CBD which in standard conditions leads to a thickness of 50-60 nm. For sample NaK_{PDT} the buffer layer thickness was thinner (around 30 nm) by changing the dipping duration. On top of the CdS buffer layer i-ZnO/ZnO:Al, MgF_2 layers and Ni/Al grid were deposited.

Table 6.13: Investigated samples with variation of Na and K incorporation.

sample	3^{rd} stage	PDT
Wto	/	/
Na_{th}	Na	/
$K_{th}Na_{PDT}$	K	Na
Na_{PDT}	/	Na
NaK_{PDT}	/	Na+K

As it is expected that the junction properties for sample NaK_{PDT} are altered, an HCl etched was performed such that PL measurements could also be performed directly on the bare absorber layer. The sample will be labelled as NaK_{PDT}-HCl. To investigate if a KF PDT treatment leads to a surface effect or has an effect in the bulk of the absorber layer, a Br etch was also performed for 8 minutes on NaK_{PDT} sample. This sample is labelled as NaK_{PDT}-Br.

Solar cell device parameters Table 6.14 presents the performance parameters of the investigated cells. The efficiency for the sample without K or Na in the absorber layer is very low. Poor adherence to the Mo contact was noticed for this sample. The performance characteristics confirm that by addition of Na and/or K, efficiency can be strongly enhanced. The highest efficiency (around 18.18 %) is obtained for sample NaK_{PDT}.

Table 6.14: Performance parameters of series4 (numbers provided by Empa).

Sample	V_{oc} (mV)	J_{sc} (mA/cm^2)	FF	η(%)	R_s (Ωcm^2)	R_p (Ωcm^2)
Wto	549	30.2	59.3	9.8	1.1	14610
Na_{th}	684	32.7	74.8	16.7	0.4	4700
$K_{th}Na_{PDT}$	704	30.9	69.3	15.1	0.9	5024
Na_{PDT}	686	33.4	77.8	17.8	0.7	9508
NaK_{PDT}	685	34.7	76.4	18.2	1.0	11296

6.4.3 Spectral response

EQE measurement on $K_{th}Na_{PDT}$ is performed on a similar sample and is shown to illustrate the lower EQE at the long wavelength side and small shift of the absorption edge towards longer wavelengths which points towards a slightly smaller band gap for this sample. EQE measurements of Na_{PDT}, Na_{th} and NaK_{PDT} show that no large changes appear around the absorption region. A band gap of about 1.13-1.14 $\pm$ 0.07 eV is calculated via a linear extrapolation of the squared EQE which yields an estimate of the minimum band gap at room temperature. The higher efficiency of sample NaK_{PDT} is at least in part related to an increase in EQE for short wavelengths due to the smaller thickness of the buffer layer for this sample. The samples which had Na (Na_{th}) or K ($K_{th}Na_{PDT}$) addition during the third stage show a decreased EQE at long wavelengths.

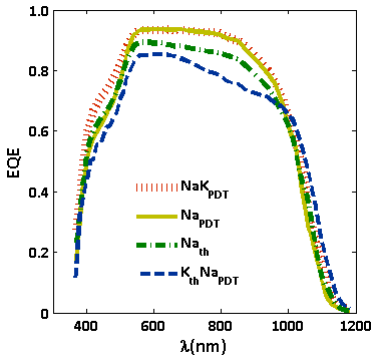

Figure 6.65: EQE spectra of series4 (performed by Empa).

6.4.4 Morphology

SEM pictures of Na_{PDT} and Na_{th} reveal very large grains (figure 6.66). The thickness of the absorber layer is around 2.2-2.3 µm.

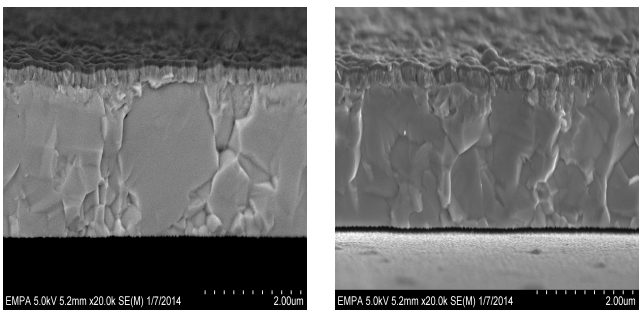

(a) Na_{th} (b) Na_{PDT}

Figure 6.66: SEM micrographs (provided by Empa) of cross sections of samples Na_{PDT} and Na_{th}.

A planar SEM picture of NaK_{PDT}-Br is shown in figure 6.67. Rounded structures on the surface and on the cross section are visible. These may be related to the Br etch. No Cd traces were found in planar EDX measurements for this sample. The thickness of the Br etched sample is around 2.0 µm; only a small fraction (around 300 nm) of the absorber layer is etched away.

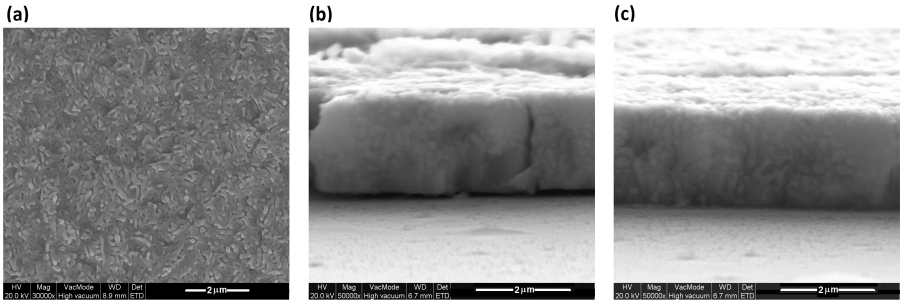

Figure 6.67: SEM pictures of $NaK_{PDT}Br$ (a) planar, (b-c) cross section.

6.4.5 Composition

Average CGI and GGI ratios of the CIGS absorber films, determined by XRF, are in the range of 0.78-0.82 and 0.33-0.38. The samples are thus quite stronly Cu-poor. As in PL only the first region of the absorber is investigated, it is useful to have composition depth profiles which provide more detailed information on the surface composition of the samples. Element depth profiles were measured by SIMS and provided by Empa. In order to compare SIMS depth profiles of different samples (figure 6.68), the signals were normalized to the Zn signal of the ZnO layer, since this layer is expected to be the same for each sample.
For samples which were modified with K or Na during the third stage ($K_{th}Na_{PDT}$ and sample Na_{th}), the Ga profile is strongly changed at the front of the samples (figure 6.68(a)): the Ga concentration is lower for these samples compared to the others. In literature it is reported that Na [124, 136] and K [136] can impede Ga and In interdiffusion. Reference [126] showed that Na from SLG can impede CIGS phase formation at low substrate temperature. Furthermore the samples with K or Na treatment during third stage show a Cu depleted area at the front of the sample (figure 6.68(c)). The Cu signal for samples which only had PDT treatment also exhibits a decrease near the surface, but less abrupt. A Cu depletion was also observed at the surface of the CIGS layer for alkali-containing substrates (enamel and glass) in reference [136].

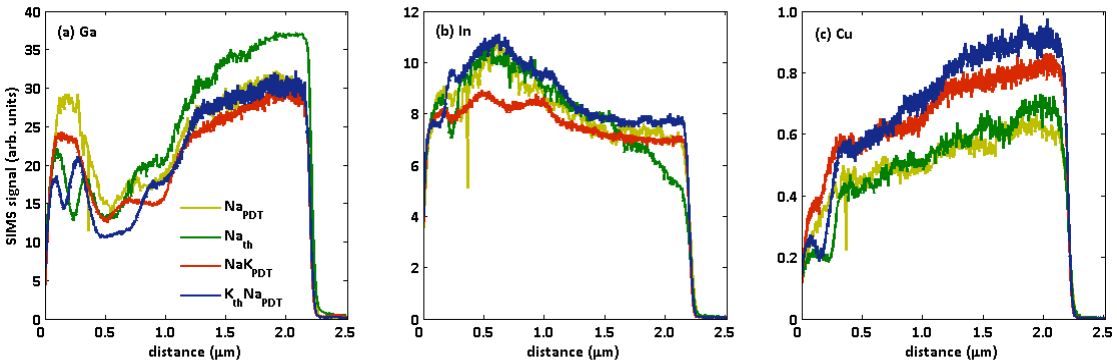

Figure 6.68: SIMS spectra (a) Ga, (b) In, (c) Cu (performed by Empa).

Figure 6.69 presents the Na, K and Ga profiles. There is a small contamination of Na and K in all samples. It is remarkable that the Na concentration for cell with NaF PDT followed by KF PDT (NaK_{PDT}) is lower compared to the sample with only NaF PDT (Na_{PDT}). This result is in accordance with references [29, 134] in which a removal of Na, in samples which had a KF PDT treatment after NaF PDT treatment, was seen.

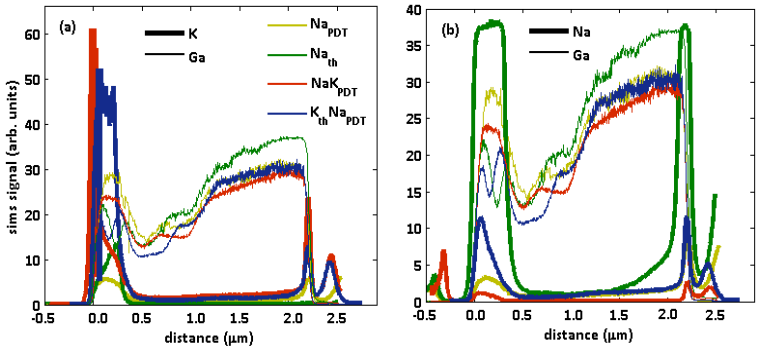

Figure 6.69: SIMS spectra (a) Ga and K, (b) Ga and Na (performed by Empa).

6.4.6 Photoluminescence

6.4.6.1 PL emission

Number of peaks

Figure 6.70 shows PL spectra at $\lambda_{exci} = 550$ nm and low temperature for the different samples. Up to five peaks with rather small peak width can clearly be distinguished, despite the Cu-poor composition. One exception are the spectra of sample NaK_{PDT} for which only four peaks are visible. All peaks lie in the energy range 0.8 and 1.3 eV. The appearance of the same 5 peaks in samples with or without Na or K implies that there are no additional peaks related to Na or K introduction. It should be noted that sample $K_{th}Na_{PDT}$ shows even an additional peak at high energy. The appearance of five distinct peaks is surprising as normally the PL spectra of Cu-poor material show a single, broad emission band. The detailed structure of the spectra points towards a strongly reduced effect of potential fluctuations. Another indication for the virtual absence of potential fluctuations is that the energy of the highest emission peak is quite high compared to the minimal band gap estimated at room temperature via EQE (1.13 eV section 6.4.3). Although a larger band gap at the absorber surface and small increase of the band gap with decreasing temperature is expected (33 meV between 5 and 300 K according to reference [85]), a large red-shift of the spectra due to potential fluctuations is not expected.

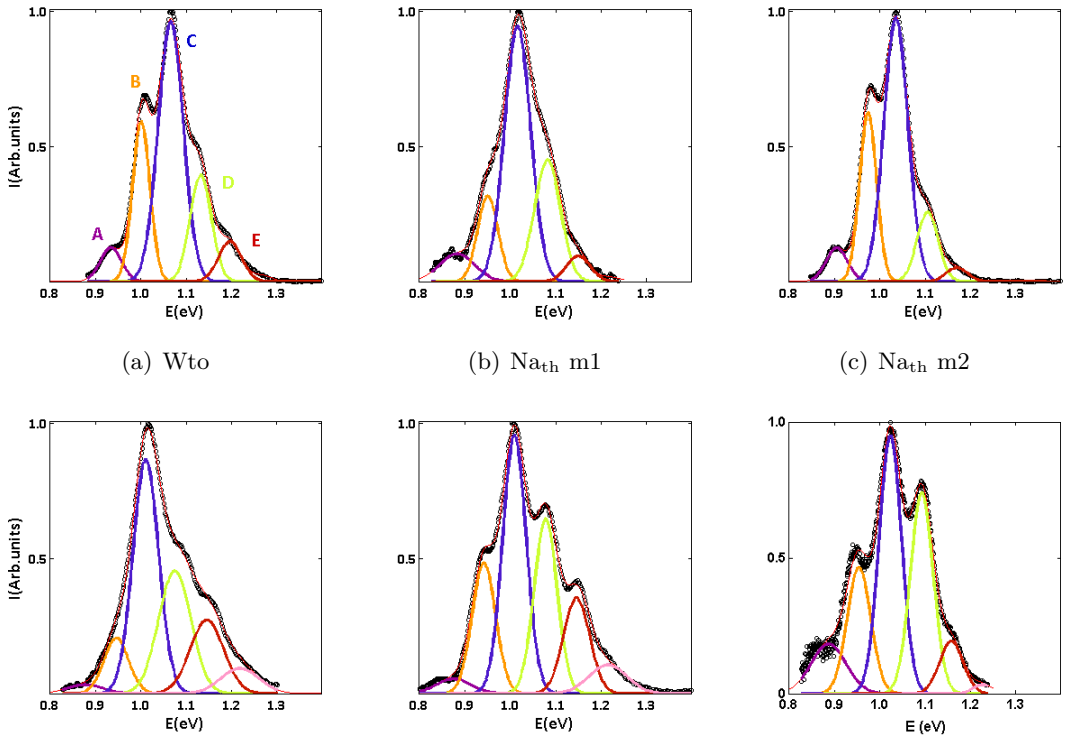

(a) Wto (b) Na_{th} m1 (c) Na_{th} m2

(d) $K_{th}Na_{PDT}$ m1 (e) $K_{th}Na_{PDT}$ m2 (f) $K_{th}Na_{PDT}$ m3 (λ_{exci}=600 nm)

(g) Na_{PDT} (h) NaK_{PDT}

Figure 6.70: PL spectra at λ_{exci} = 550 nm (T = 10 K). (m1, m2, m3: three different measurement positions.

In literature only few reports [17, 268] show PL spectra with multiple distinguishable peaks. In these reports samples were co-evaporated and had a slightly Cu-poor composition. In reference [17] five distinct PL transitions are shown. Multiple Gaussian fits showed that the deepest level lies 406 meV from the band edge while the shallowest emission was very close to the band edge. The emission peaks were very regularly spaced (around 91 meV) for the four lowest energy peaks. As the cell had relatively high performance, it was suggested that the presence of deep levels contributing to radiative recombination did not necessarily preclude the material from reaching a high efficiency. Reference [268] reported four PL emission peaks for which the energy separation between the peaks was around 60-70 meV. The near band edge luminescence, around 1.25 eV, was assigned to exciton recombination. The other observed PL emission peaks were ascribed to donor-acceptor pair transitions. No suggestion for the origin of the defects was given.

Since five PL peaks are measured in our study and since the energy spacing between the peaks is quite regular (between 65-75 meV), an effort was made to vary the measurement conditions in order to exclude possible instrumental sources which could create such regular pattern. First,

specific measurement errors due to the set-up can be excluded, as the PL spectra measured with another measurement set-up (in collaboration with Luminescent Lanthanide Lab) were identical. Second, it is tempting to relate the structure of the spectra with an interference effect. However since a rotation of the sample with respect to the light source and detector did not change the energy separation between two maxima, no clear evidence of a large effect of interference could be given. Another argument is that spectra of a sample for which CdS was removed by HCl etching and of a sample with reduced CIGS thickness (by Br etching) did not show a difference in the energy spacing of peak maxima (see further figure 6.74). Furthermore the unusual temperature (see further section 6.4.6.1) behaviour of the intensity of the PL peaks with increasing temperature can also not be explained by interference. Based on these arguments the effect of interference is not taken into account in the discussion of the PL spectra in this section. A more comprehensive discussion concerning a possible effect of interference can be found in section 6.6.
Finally, the transmission of the emission filter which was used to exclude second order diffraction in PL measurements was tested. As the transmission of the filter is constant in the wavelength region of the PL spectra (900-1500 nm), as shown in figure 6.71, an error due to the filter can also be excluded.

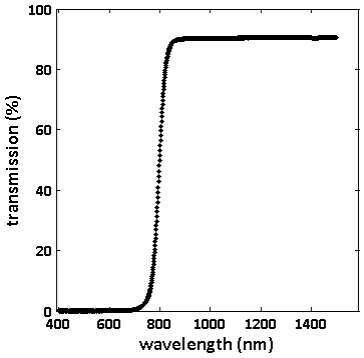

Figure 6.71: Transmission of 780 nm filter.

Another explanation for spectra with more or less equal separation between the peaks can be the occurrence of phonon replicas of defect related transitions. However different arguments can be given against such interpretation: the intensity ratios between the peaks are not the same for different measurements on a sample and are not the same for the different samples. Furthermore the intensity ratios between the peaks also change differently for different samples with excitation wavelength and temperature. This should not be the case for phonon replicas. Indeed, their relative intensities are determined by a Poisson distribution [10]. Another argument against phonon replicas is found in the LO-phonon energy, which is reported around 30 meV [4, 5, 16]. This is considerably smaller than the separation between the peaks in the PL spectra. It can be concluded that the PL peaks are not related to instrumental errors, nor to phonon replicas or interference effects in the sample.

Dominant PL peaks at low temperature
A Gaussian fitting with five peaks, labelled from low to high energy as A to E, is performed on the low temperature spectra of the cells in figure 6.70. In the fitting the energy separations between the peaks used in the fitting of the other series was maintained. A small energy shift of the whole series was allowed in order to account for a possible small difference in band gap between the cells. In the samples Wto, $K_{th}Na_{PDT}$, Na_{PDT} and Na_{th} peak C is the dominant peak. No shift in the dominance of the peaks can be noticed due to Na addition (via PDT or during third stage) (figure 6.70). Only in sample NaK_{PDT}, peak B is dominant. This may also

be interpreted as a decrease in intensity of peak C.
Figure 6.72 presents an overview. In figure 6.72(b) the spectra are shifted such that the maximum of peak C is positioned at zero eV. In the comparison of figure 6.72(a) it is visible that the spectra of sample $K_{th}Na_{PDT}$ and lie at lower emission energy and that the spectra of Na_{PDT} lie at higher emission energy. Taking into account that the penetration depth of the excitation light is limited to the surface region, this difference in emission energy can be explained by a difference in Ga concentration at the surface as shown in SIMS profiles (figure 6.68(a)). The lowest and highest Ga concentration (and hence band gap) at the front of the absorber for samples are found for samples $K_{th}Na_{PDT}$ and Na_{PDT} respectively.

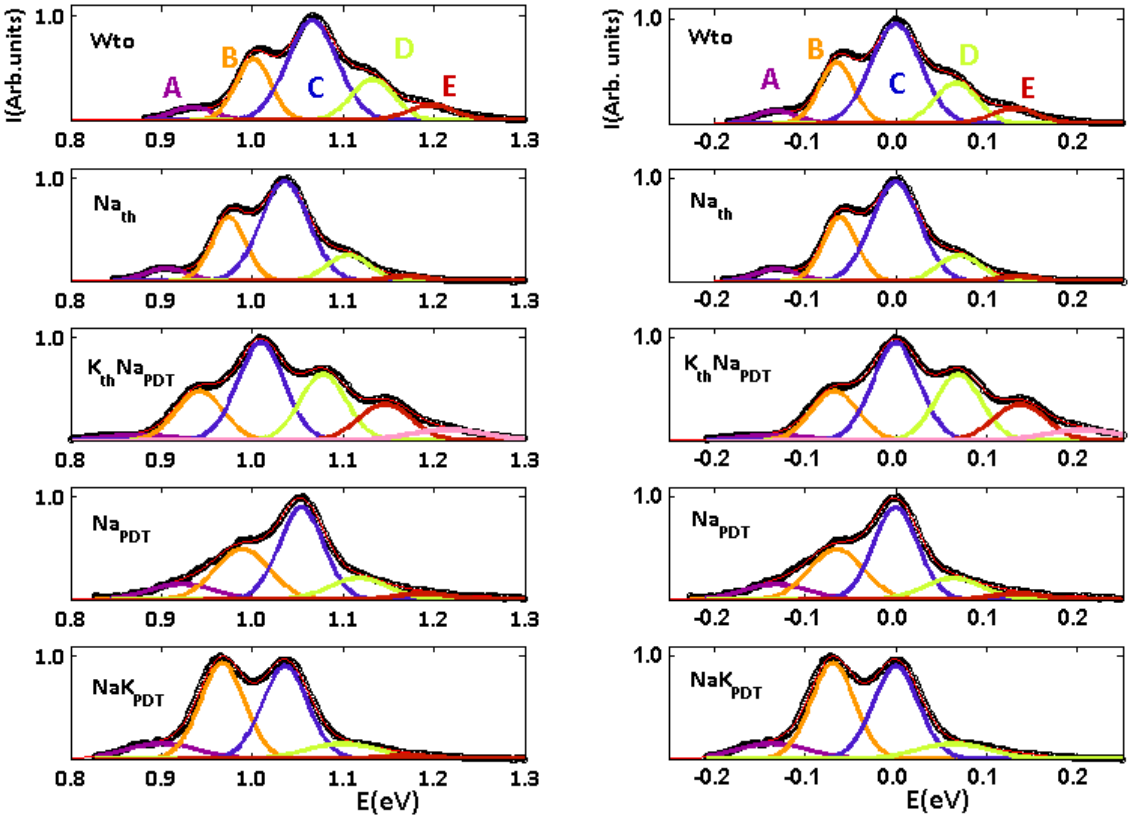

(a) Spectra (T = 10 K, λ_{exci} = 550 nm). (b) Shifted spectra (T = 10 K, λ_{exci} = 550 nm).

Figure 6.72: PL spectra of series4.

Excitation wavelength dependent measurements
In excitation wavelength dependent measurements (figure 6.73), the penetration depth increases as the excitation wavelength increases. The PL excitation wavelength dependence will mainly be discussed for the peaks with highest intensities (B and C). For none of the samples there is a change in the dominant peak as the excitation wavelength increases. Peak C is dominant at the surface and deeper in the absorber layer for samples Na_{PDT}, Na_{th} and $K_{th}Na_{PDT}$ (figures 6.73(a), 6.73(b), 6.73(c)). PL measurements on NaK_{PDT} cells (at two different positions labelled as m1 and m2) as well as on an HCl etched NaK_{PDT} sample (figure 6.73(d), 6.73(e), 6.73(f)) show that peak B is dominant for each wavelength. No significant difference appears between PL spectra on complete cell and HCl etched sample. On figure 6.73(d) the relative increase of peak B is smaller than the increase of peak C, as the excitation wavelength increases. This seems to indicate that the defects related with peak C are relative to those for peak B, less present at the surface but more deeper in the absorber. In all samples the increase of peak D and E is limited or decreases for long excitation wavelengths. These emission peaks could thus be related to the surface.

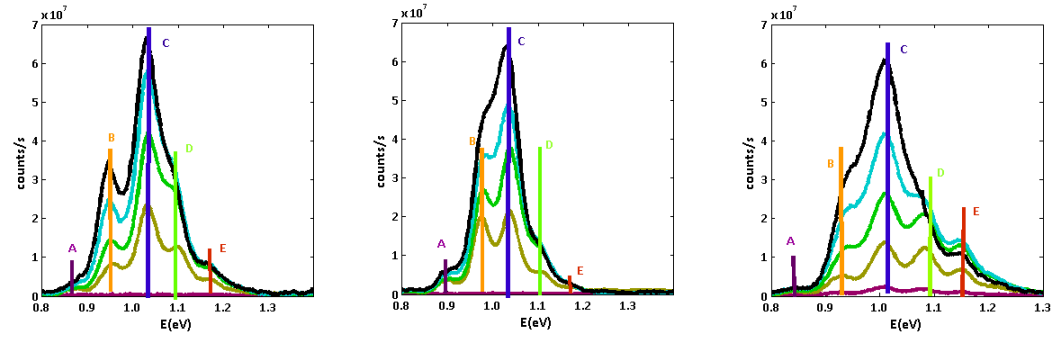

(a) Na_{PDT} (b) Na_{th} (c) $K_{th}Na_{PDT}$

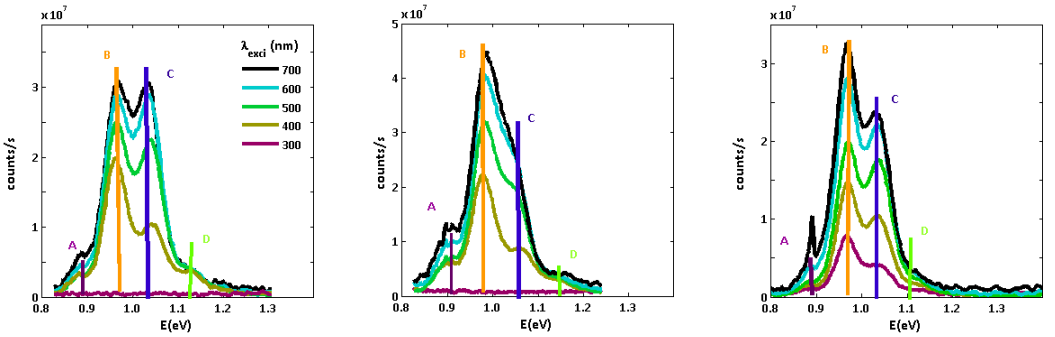

(d) NaK_{PDT} Cell m1 (e) NaK_{PDT} Cell m2 (f) NaK_{PDT}-HCl

Figure 6.73: PL spectra as a function of λ_{exci} (T = 10 K).

Thinning absorber layer: limitation of KF PDT effect to the surface

In the previous it was demonstrated that peak B is dominant only in the PL spectra of the sample which had KF PDT treatment. Furthermore it was shown by excitation wavelength dependent measurements, that the effect of the KF PDT treatment is rather limited to the surface of the absorber layer. This can further be demonstrated by a PL measurement on a Br etched NaK_{PDT} sample.

As shown by SEM measurements, only a small part (around 300 nm) of the CIGS surface is etched away by the Br etch on sample NaK_{PDT}. Due to this small etch, no large shift of the PL emission energy is expected. Figure 6.74 shows that the Br etch results in a different spectrum compared to the spectrum of the HCl etched sample. The HCl etched sample has peak B as the dominant peak, the Br etched sample has peak C as the dominant peak. The results on the Br etched sample confirm that the dominance of peak B (related to deeper defect transitions) is rather limited to the near surface.

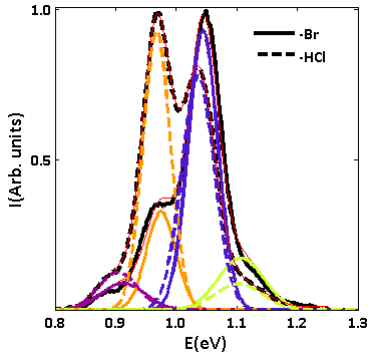

Figure 6.74: PL spectra of HCl and Br etched NaK_{PDT} (λ_{exci} = 550 nm, T = 10 K).

In accordance with the results in section 6.3.2.5, the measurement on the Br etched sample could not give evidence for a Cd_{Cu} defect related PL peak in the spectra. This result does not support the suggestion for the identification of peak A in section 6.2.2.6. In the spectra of Br thinned sample (NaK_{PDT}-Br) no peak disappears, which would otherwise be the case if the PL peak would be related to an defect only present at the front of the absorber. In reference [269] the Cd_{Cu} defect is regarded as a possible candidate to be beneficial for the junction properties. As a Cd_{Cu} related defect transition was not measured by PL, the performed PL experiments can not confirm nor contradict the suggestion.

Excitation power dependent measurements

The spectra reveal a small blue shift with increasing excitation power. From the fitting of $E_{peak} = C + B \cdot \log(P_{exci})$ (equation 5.6) it appears that the blue shift is not very large (around 3-6 meV/decade for B) and lies within the range expected for DAP recombination in non-compensated material (B ≈ 1-5 meV/decade) [16]. From this, it can be deduced that there is no large influence of potential fluctuations in the material.

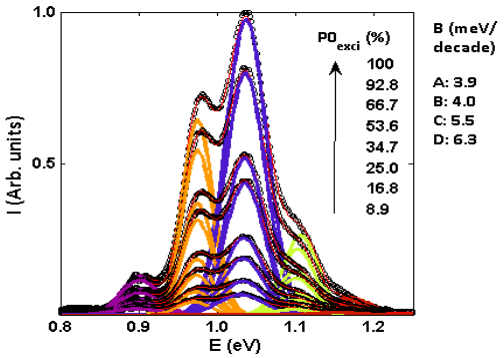

Figure 6.75: Excitation power dependent measurement of Na_{th} (λ_{exci} = 550 nm and T = 10 K) .

Temperature dependent measurements

In figure 6.76 peaks A-C show a very small red-shift as temperature increases ($2 \cdot 10^{-4}$ eV/K for peak B, $8 \cdot 10^{-5}$ eV/K for peak C). As the shift is very small, there cannot be a large effect of potential fluctuations in the material. Temperature dependent measurements confirm the absence or at least a very small effect of potential fluctuations in the material. Peak D shows a small blue-shift with increasing temperature, which rather points towards a free to bound recombination in non-compensated material [16]. As the intensities of peak A, D and E are rather small, the error on the fitting could be quite high and it is difficult to make firm statements about their shifts.

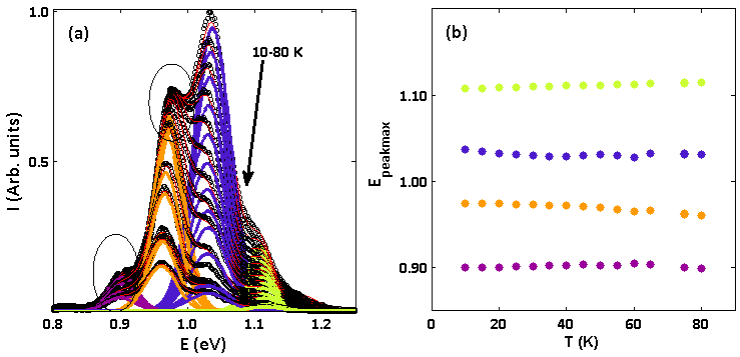

Figure 6.76: (a) Temperature dependent measurement of Na_{th} (λ_{exci} = 550 nm and T = 10 K), (b) energy of peak maximum as a function of temperature.

Figures 6.77(a, b) show temperature dependent spectra of Na_{th} and NaK_{PDT}-HCl. The intensity of peaks A and B decreases very slowly (or increases slowly) compared to the intensity decrease of peaks C and D. This intensity evolution as a function of temperature is in accordance with the evolution for samples of series3 (section 6.3).

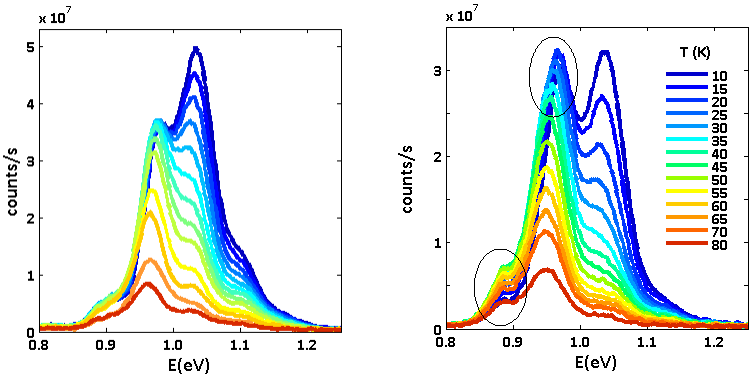

(a) Na_{th} λ_{exci} = 550nm (b) NaK_{PDT}-HCl λ_{exci} = 550 nm

Figure 6.77: Temperature dependent measurements show an unusual evolution of PL intensity.

6.4.6.2 PL excitation

In order to gain more reliable information (low temperature, same excitation region in absorber as for PL, same excitation spot on the sample) about the band gap, PLE measurements were performed, using a continuum laser as excitation source. Due to the laser excitation, large spikes in the wavelength region 1000-1100 nm appear in the spectra, which have been removed. Due to these spikes, the precise determination of the band gap at low temperature is hindered. Nevertheless the PLE measurements give an idea about the separation between PL and the edge of absorption. The PLE spectrum is set to 1 at an excitation wavelength of 950 nm.
Figure 6.78 presents the PLE spectra at emission wavelength of 1260 nm and PL spectra of sample NaK_{PDT} and Na_{th}. The PLE spectra as well as the PL emission peak at 1200 nm coincide for both samples. The PLE spectrum shows a small overlap with the PL spectrum. This can be due to the presence of potential fluctuations as shown in reference [243]. This reference showed that in the presence of potential fluctuations, the slope of the absorption edge can be altered if the emission wavelength of PLE measurement is changed. This was not observed in the PLE measurements we performed. As pointed out by excitation power and temperature dependent measurements (section 6.4.6.1), there is only very limited influence of potential fluctuations on the PL spectra expected. The overlap between PLE and PL spectra could point towards of a secondary phase in the absorber as the energy of PL emission is higher than the energy of PL onset. Unfortunately PLE spectra do not provide enough detailed information in the wavelength region of interest.

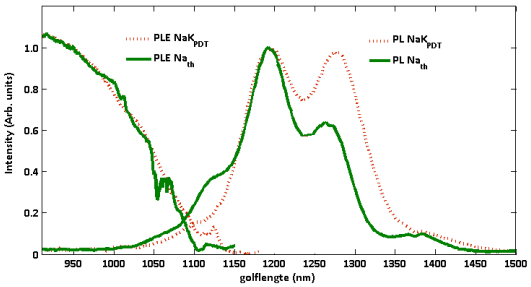

Figure 6.78: PLE and PL spectra (T = 10 K) of sample Na_{th} and NaK_{PDT}.
λ_{exci} for PL is 500 nm, λ_{emmi} for PLE is 1260 nm.

6.4.7 Defect interpretation

From the PL measurements on series4 it is not straightforward to obtain more evidence for suggested defect identifications of the PL peaks made in section 6.2.2.6. The peak at low emission energy (peak A) is present in all samples and can be tentatively related to deep defect transitions. No large change between the intensity of the peak is noticed for the different samples (figure 6.70). Since experiments on thinned absorber layers still exhibited a clear peak A component, it is not very likely that peak A should be assigned to a Cd_{Cu} defect related transition as suggested in section 6.2.2.6. Peak A should be related to another deep defect related transition. More investigations are necessary to find the origin of this peak.
In section 6.2.2.6 the dominant PL peaks (peaks B and C) were suggested to be related with a recombination of In_{Cu}-V_{Cu} for peak B and defect transition of V_{Se}-V_{Cu} for peak C based on references [235, 253, 254]. The decrease in intensity of peak C relative to peak B in sample NaK_{PDT} can be due to an effect of K on the V_{Se} defect (compensation of these donors) or to the fact that two PDT treatments are performed in the presence of Se on this sample. As discussed in previous section (section 6.3), Se post annealing can reduce the intensity of peak C.
The emission peak D appears very close to the band gap energy of the absorber as presented by PLE measurements (figure 6.78). Therefore a free to bound transition to the shallow defect V_{Cu} could be suggested, taking into account the small calculated activation energy (30 meV) and low formation energy [91]. The limited increase of peak D for larger excitation wavelengths could be related to the increase of Cu content after the first 400 nm of the absorber layer (figure 6.68).
Emission peaks E and F (the latter is only found in sample $K_{th}Na_{PDT}$) are, compared to the other samples, only quite intense for sample $K_{th}Na_{PDT}$. As the spectra can only be compared relative to each other, the origin of the increase of the high energy peaks could also be an intensity decrease of the low energy peaks in this sample. The energy of emission peaks E and F lie around/above the PLE absorption edge. An exciton related peak can however probably be excluded, as exciton related peaks are reported to be sharp and their intensity would decrease quickly as temperature increases. Exciton peaks have only been reported for in Cu-rich absorber material [228, 234]. The full width at half maximum is for a Cu-rich $CuGaSe_2$ single crystal reported to be as small as 2-3 meV [16]. It could be suspected that the high energy emission peaks are due to a different phase with a higher band gap energy (Cu-poor phase, Na or K related phase [121]). The low Cu concentration at the absorber surface, measured in SIMS, could be an indication for this. Excitation wavelength dependent measurements show that the contributions of these high energy peaks are limited to the surface. More investigations should be performed to elucidate the origin of these high energy PL peaks more conclusively.

6.4.8 Summary

The influence of Na and K added during third stage of deposition and/or by PDT in thin-film CIGS solar cells was investigated. The effect of alkaline element incorporation as well as an effect of the incorporation method was shown in EQE and SIMS measurements. Highest efficiency was obtained for a sample which had NaF PDT followed by KF PDT. In reference [11] it was suggested that due to KF PDT the junction properties have been improved. The improvement was, according to this reference, related to a Cd_{Cu} defect. In all PL spectra up to five emission peaks between 0.8 and 1.3 eV were observed. The energy separation between the peak energies was the same as for the other series. Since no additional proof of a large effect of interference could be given based on the rotation of the sample, the PL peaks were explained as defect transitions. However since five peaks appear an additional study based on reflectance measurements was performed. A more thorough discussion concerning the effect of interference is given in section 6.6.
PL measurements as a function of temperature and excitation power do not exhibit large peak shifts which indicates that the effect of potential fluctuations in the absorbers is rather small

despite the Cu-poor composition. The incorporation of Na or K does not give rise to additional PL peaks but leads for the sample with KF PDT to a change in the relative intensities of certain existing peaks. PL measurements for this sample indicate a relatively higher concentration of deeper donor defects (peak B), or a lower concentration of shallower donors (peak C) near the interface. For all other samples peak C was found to be the dominant peak. PL peaks close to or even above the CIGS band gap might be related to the presence of a secondary phase with higher band gap. By thinning the absorber layer, the existence of a Cd_{Cu} related defect could not be supported nor contradicted. PL measurements performed on series4 could not provide further additional experimental support nor contradictions concerning the suggested defect identifications (section 6.2.2.6). Supplementary measurements providing phase information would be useful for further interpretation of the PL spectra. In conclusion PL measurements revealed that the defect composition at the surface of a sample with KF PDT treatment is different from that of samples which had no KF PDT treatment. This is in agreement with the suggested altered junction properties due to KF PDT [11].

6.5 CIGS: PL overview

Overview of device performance

An overview of the device performances of all investigated CIGS thin-film solar cells is given in table 6.15. Generally the efficiency from series1 to series4 increases. The increase in efficiency cannot be ascribed to a V_{oc} or J_{sc} increase alone, but to the combined effect of both parameters. Higher R_p values are generally seen for series with highest efficiency.

Table 6.15: Overview of device performances of different CIGS series (numbers provided by Empa).

Sample	V_{oc} (mV)	J_{sc} (mA/cm^2)	FF (%)	η (%)	R_s (Ωcm^2)	R_p (Ωcm^2)
Device performance serie1.						
Sb0	641	28.8	65.7	12.1	0.8	704
Sb7	637	31.2	68.4	13.6	0.9	900
Sb12	646	31.8	65.9	13.5	0.9	712
Device performance series2.						
LT-ND	662	32.7	69.7	15.1		
LT-SbD	639	32.9	63.2	13.3		
HT-ND	681	31.5	72.4	15.5		
HT-SbD	648	30.0	73.2	14.3		
HHT	716	31.6	74.1	16.8		
Device performance series3.						
SeH	675	29.5	75.1	14.9	0.9	2855
SeL1	700	31.0	74.7	16.2	0.9	3720
SeL2	710	30.6	74.3	16.1	0.9	2484
Device performance series4.						
Wto	549	30.2	59.3	9.8	1.1	14610
Na_{th}	684	32.7	74.8	16.7	0.4	4700
$K_{th}Na_{PDT}$	704	30.9	69.3	15.1	0.9	5024
Na_{PDT}	686	33.4	77.8	17.8	0.7	9508
NaK_{PDT}	685	34.7	76.4	18.2	1.0	11296

Overview of PL spectra of different series

An overview of PL measurements at low temperature is presented in figures 6.79 and 6.80. The spectra of the last mentioned figure are shifted such that emission energy of peak C coincides with zero eV.

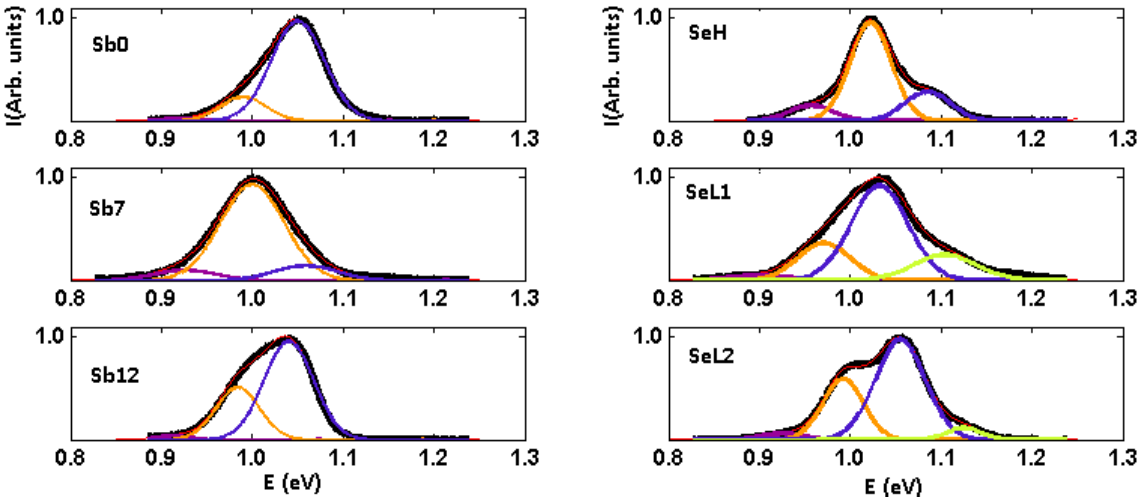

(a) Series1

(b) Series3

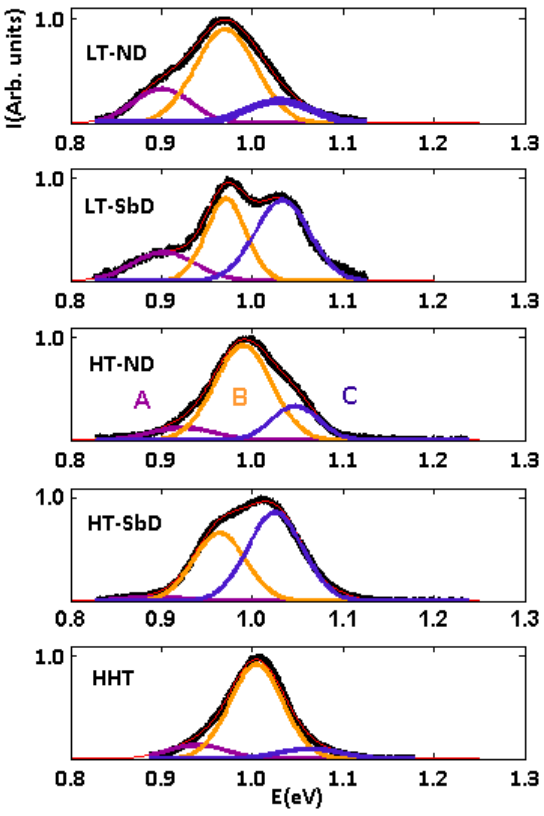

(c) Series2

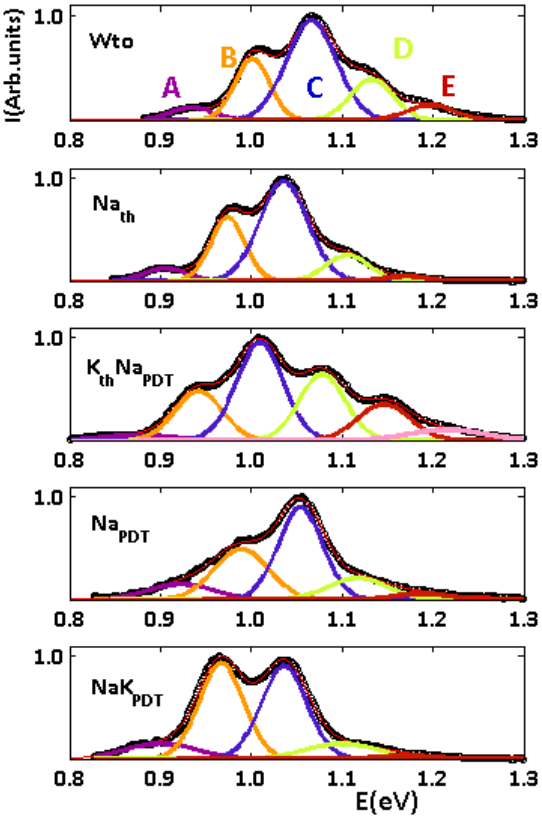

(d) Series4

Figure 6.79: PL spectra of
(a) Series1: T = 5 K, λ_{exci} = 550 nm,
(b) Series3: T = 10 K, λ_{exci} = 500 nm,
(c) Series2: T = 5 K, λ_{exci} = 600 nm,
(d) Series4: T = 10 K, λ_{exci} = 550 nm.

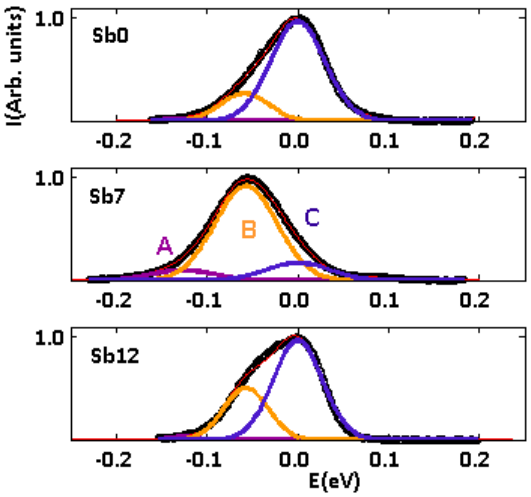

(a) Series1

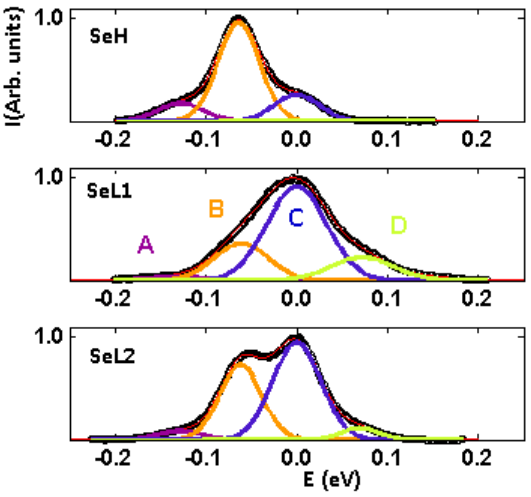

(b) Series3

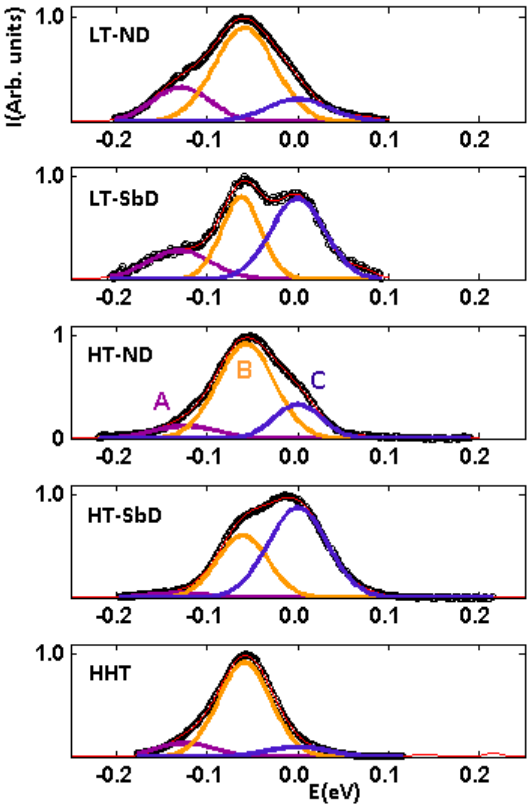

(c) Series2

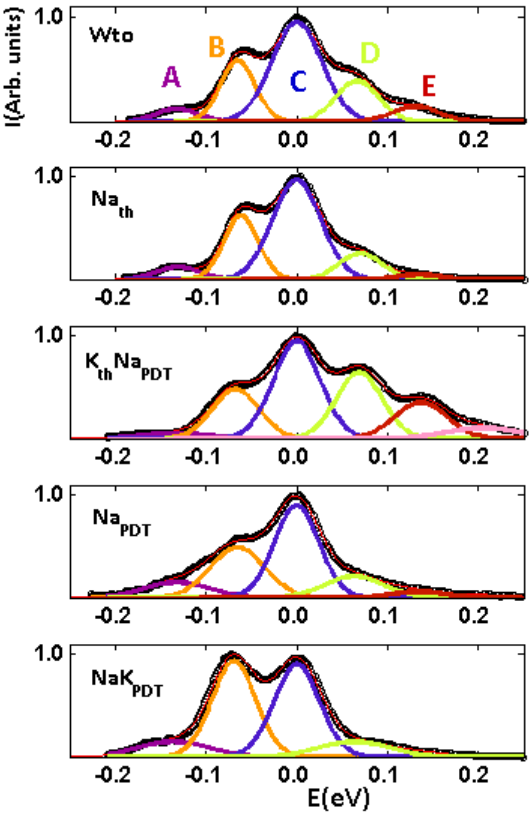

(d) Series4

Figure 6.80: PL spectra of
(a) Series1: T = 5 K, λ_{exci} = 550 nm,
(b) Series3: T = 10 K, λ_{exci} = 550 nm,
(c) Series2: T = 5 K, λ_{exci} = 600 nm,
(d) Series4: T = 10 K, λ_{exci} = 550 nm.

Despite the broad PL peaks, a consistent decomposition for all spectra was possible. All spectra of all cells can be fitted with the same energy separation (with allowed margin of ± 3 eV) between the peaks. The energy separation between subsequent peaks is between 65-75 meV. Furthermore, in all PL spectra peak B or peak C is the dominant PL peak. In the first PL studies (series1-2), it was suggested that peak B and peak C were related to In_{Cu}-V_{Cu} and V_{Se}-V_{Cu}

q-DAP transitions respectively. The suggestions were made based on the Cu-poor composition of the samples, formation and activation energies calculated in reference [91] and a comparison with literature reports [235,253,254] especially reference [253] which showed similar temperature dependence and separation between the peaks. Further experimental evidence for the relation between PL peak B with a In_{Cu} transition was found in XPS measurements which enabled to explain the dominance of PL peak B for Sb7 and PL peak C for Sb0. At the surface of sample Sb7 an enhanced In concentration was found which is in agreement with an enhanced intensity of PL peak B for this sample. PL measurements performed on the subsequent series (3-4) aimed to find more experimental verifications for the suggested explanation of the PL spectra.
An additional indication for the relation of peak B with In_{Cu} was found in PL measurements on thinned absorber layers of sample SeL2 from series3. At the front of the absorber layer peak C was dominant, at the position around the Ga dip and hence increased In concentration, peak B became dominant. The dominance of the peaks changed in agreement with the composition variation throughout the absorber layer. In the search for additional indications concerning the V_{Se} defect related transition, post annealing experiments which intended to alter the intensity of this transition, were performed on series3. As the post annealing did not have an effect on peak B but did clearly alter the PL intensity of peak C, we could assign peak C to V_{Se} defect related transition with more experimental evidence.

The results of an attempt to find correlations between the PL characteristics and efficiency values on the one hand and absorber parameters on the other hand are described below.

Investigation of correlation between efficiency and PL characteristics
Number of peaks: It is quite remarkable that with increasing performance of the cells, PL peaks can be more easily resolved and the number of PL contributions increases. As more PL transitions, generally point towards more recombinations paths and/or more defects present in the material, a large number of PL transitions is expected to result in low efficiency. From the results presented in figure 6.79 it appears this is not the case for the investigated samples. Same result was found in reference [17] which suggests that the appearance of more radiative transition peaks could point towards less non-radiative recombination paths. On the other hand the statement that more PL peaks result in better efficiency, could not be easily applied as sample 'Wto' from series4 has multiple PL peaks but low efficiency. For this sample the poor adhesion could play a role in the low obtained efficiency despite a possible good quality of the absorber layer. It could be concluded that with the optimization of the low temperature deposition process, higher efficiencies could be obtained despite the appearance of an increased number of PL peaks in the spectra.

Peak width: The full width at half maximums (FWHM) of the PL peaks are quite large. The appearance of broad peaks is in agreement with the expectation that the material is compensated as a result of the Cu-poor composition. Cu-poor material results in broader peaks as indicated in reference [120]. This reference reports for epitaxial layers of $CuGaSe_2$, FWHM values of 45-60 meV for Cu-poor material (Cu/Ga ratios between 0.9-0.6) and FWHM values between 20-35 meV for Cu-rich material (Cu/Ga ratios between 1.1-1.0). It appears that from series1 to series4 the FWHM of the peaks decreases while in general efficiency of the cells increases. The FWHM of the dominant peak for cells of different series is 71 meV, 61 meV, 58 meV and 50 meV for series1 to series4 respectively. For series4, which shows the narrowest peaks, the effect of potential fluctuations and hence a large degree of compensation could not unambiguously be demonstrated by excitation power and temperature dependent PL measurements. The peak width is not just inversely proportional with the efficiency as the efficiency for sample 'Wto' is low despite small peak width.

Peak dominance: Although defects in the absorber layer will have an influence on the device performance, no simple correlation between PL peak dominance and efficiency could be found. For example, best efficiency for series2 was obtained for sample HHT for which peak B was dominant. In series3 best efficiency was obtained for cell SeL1 for which peak C was dominant. As cell efficiency is determined by a range of parameters, different parameters between the cells could mask the effect of defects on efficiency. The relation between PL peak dominance and efficiency is furthermore complicated by the absence of absolute PL intensity information. The observed changes in intensity of the PL peaks are relative to each other.

It appears that a correlation between PL characteristics and efficiency values is not easily found as PL examines only the defects in the absorber layer whereas the efficiency provides information about the whole cell. Effects of absorber parameters on the PL spectra are investigated below.

Investigation of correlation between absorber parameters and PL characteristics

Composition: An overview of the composition ratios is given in table 6.16. The CGI and GGI ratios of serie1-3 are quite similar. The variation of the ratios is larger in series4 than between the different series. The PL variations (number of peaks, peak width) between the different series cannot be simply explained by a difference in CGI and GGI ratios. Rather surprisingly the peak width is not even related in a straightforward way with the CGI ratio.

Table 6.16: Overview CGI and GGI ratios (numbers provided by Empa).

Samples	CGI	GGI
Series1	0.86	0.38
Series2	0.80	0.38
Series3	0.81	0.41
Series4	0.78-0.82	0.33-0.38

Grain size: A larger grain size generally resulted in larger efficiency (series1-3). However large grain size is not a sufficient condition to obtain the best efficiency for all investigated cells. Sample Sb7 (figure 4.20 b) as well as sample Na_{PDT} (figure 6.66(b)) both have large grain size, but the PL spectra (number and width of peaks) and obtained efficiency are far from similar for both cells. It can be concluded that no straightforward correlation between the PL spectra, efficiency and grain size could be found.

Growth temperature: Series1-3 and 4 had similar substrate temperature during CIGS deposition (450-500°C). The cells of series2 are deposited (except for HHT) at lower maximum substrate temperature (380-420°C). As the deposition temperatures between the different series are overlapping, different substrate temperatures can also not explain the differences in the PL spectra as well as evolution in efficiency.

6.6 CIGS: Effect of interference on PL spectra

As a result of reflection at the back of the absorber layer, emission light in a PL measurement can be reflected which causes interference with emission light at the surface. The condition for constructive interference at a thin layer (figure 6.81) can be calculated via the optical path difference of the reflected light (equation 6.1). Constructive interference will occur if the optical path difference equals an integer multiple (N) of the wavelength of the light (λ) and is dependent on refractive index (n) of the layer, thickness of the layer (d) and angle of incidence of the incoming light (and thus on the refraction angle θ_r) [270].

$$2 \cdot d \cdot n \cdot cos(\theta_r) = N \cdot \lambda \tag{6.1}$$

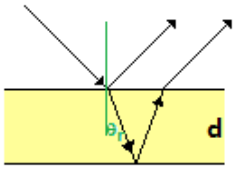

Figure 6.81: Interference at a thin layer.

The condition for constructive interference in PL at a thin layer can be calculated in a similar way as for reflection. In the sections below, the question whether the structure observed in the PL spectra of CIGS and CZTS thin-film solar cells is caused by interference, is investigated in more detail. In the first section below, the expected effect upon changing the detection angle is shown by a reflectance simulation. Thereafter comparisons between PL and reflectance spectra are discussed.

6.6.1 CIGS

6.6.1.1 Detection angle dependence of interference pattern

PL measurements in the set-up described in section 5.2.4 are performed at a detection angle of 45°. As the interference pattern is dependent on the optical path length of the light, it can be altered by changing the angle of detection of the light. A change in the peak separations between the peaks as well as a total energy shift of the pattern is expected when the angle is varied.
Using the simulation programme 'OpenFilters' a calculation is performed to estimate the difference in peak separations of the fringes and total energy shift for different detection angles. In the simulation of a CIGS absorber, the effect of the GGI grading is not taken into account. A CIGS absorber layer of 2.7 μm with refractive index of 3 is assumed in accordance with to references [271, 272]. In reference [271] refractive index values are reported depending on the GGI ratio of the CIGS layer. For an GGI ratio of 0.31 an n value around 3 is tabulated for the energy region of interest (figure 6.82). Similar n and k values are reported in reference [272]. In reference [69] an overview of reported n and k values can be found. According to this reference refractive index values are ranging from 2.7 to 3.1 at a wavelength of 1000 nm.

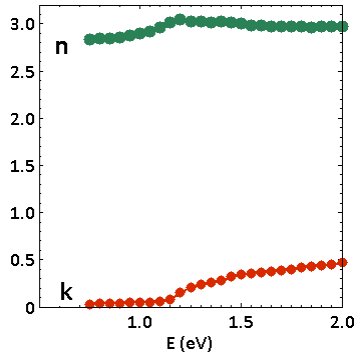

Figure 6.82: n and k values reported for x = 0.31 in the energy region 0.75 - 2.0 eV according to reference [271].

Figure 6.83 shows the result of the simulation for different detection angles. From this figure we can conclude that:

- The energy separation between the interference peaks is not altered significantly when varying the detection angle between 30° and 60°. The peaks are separated by an energy of around 0.079 eV as indicated in table 6.17.
- A small angle variation of 10° (e.g. 40°-50°) already results in a global shift of 0.010 eV, an angle variation of 20° (e.g. 40°-60°) would result in a shift of 0.020 eV.

When varying the detection angle in PL measurement by rotating the sample holder, one would expect, from these simulations, to see a global shift of the peak positions in the spectrum upon turning the sample in the case interference dominates the spectrum. On the other hand, hardly any effect on the energy separation between the PL peaks is expected.

Figure 6.83: Simulated interference patterns for different detection angles.

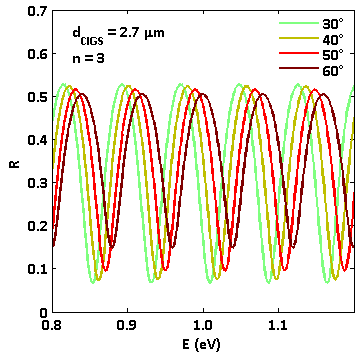

Table 6.17: Energy separation of calculated interference pattern ('Open Filters') for a CIGS layer thickness of 2.7 µm.

Angle	E_{peak1}	E_{peak2}	ΔE_{peak}
0°	0.957	1.033	0.076
30°	0.970	1.048	0.078
40°	0.980	1.059	0.079
45°	0.984	1.063	0.079
50°	0.990	1.069	0.079
60°	0.999	1.079	0.080

Figure 6.84(a) shows two PL spectra at 10 K of Sb7 for which the angle of detection was altered. A rotation of the sample only results in a small intensity variation, no shift of the spectrum towards smaller or larger energies is visible. This is shown more clearly in the normalized spectra (figure 6.84(b)). A shift of 10 meV as predicted for a change of 10° of the detection angle should already be clearly visible.

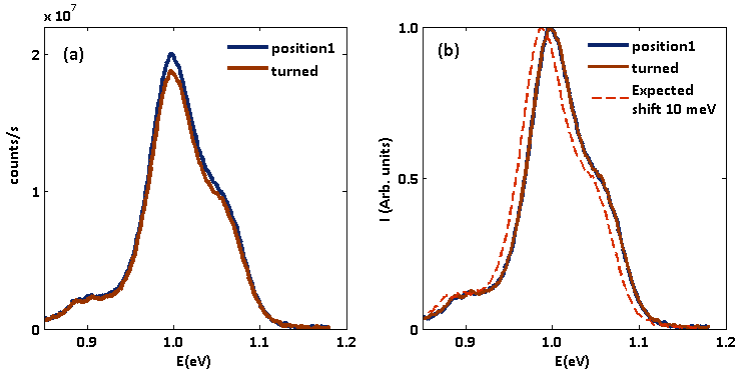

Figure 6.84: (a) PL spectra of Sb7 at 10 K detected at different angle, (b) Normalized spectra and expected shift (dotted line).

The rotation test was further performed on other samples of different series. As shown in figure 6.85, no overall shift of the PL spectrum was visible upon turning the samples.

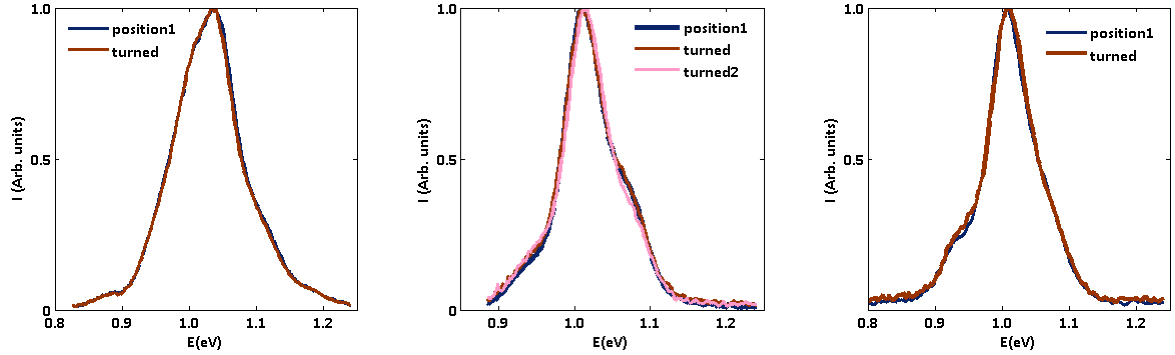

(a) SeL1-cell (b) SeH-PSe (c) SeL2-PSe

Figure 6.85: Normalized PL spectra for angle dependence test for different samples (T = 10 K).

As shown in figures 6.84 and 6.85 the separation of the peaks is not altered upon turning the sample with respect to the detector. Furthermore the expected shift of 10 meV between angle of 40° and 50° (small variation around optimum detection angle 45°) is not visible. From the angle dependence test, no indication was found that the PL spectra would be largely influenced by the detection angle and hence by interference.
It should moreover be noted that the difference between the PL spectra was larger when different excitation spots were probed (vertical displacement of sample sometimes in combination with turning of the sample) as shown in figure 6.86.

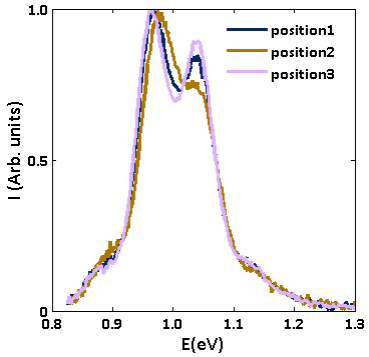

Figure 6.86: Normalized PL spectra of NaK_{PDT} at 10 K for different positions.

6.6.1.2 Comparison of reflectance and PL spectra

Differences between reflectance and PL measurements

As changing the detection angle did not reveal indications for the effect of interference on the PL spectra, reflectance (R) measurements at room temperature were performed in order to measure the energy separation between the interference fringes. Reflectance measurements were performed under a small incidence angle ($\approx 0°$) with a FTIR set-up (BUKER Hyperion 2000 Infrared microscope).

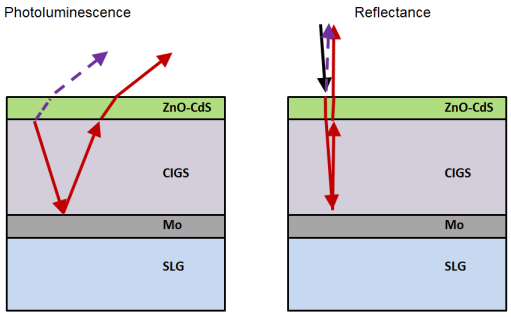

Figure 6.87: Expected light path in PL and R measurement.

A scheme of the expected light path in PL and R measurements is shown in figure 6.87. For the PL measurement PL light is assumed to originate form the front part of the absorber layer. For a good comparison between R and PL measurements, differences between the two measurements are listed below:

1) *Phase shift*
In PL, light emitted directly to the detector (dotted purple arrow) does not have a phase shift, while in R measurements direct reflected light (dotted purple arrow) has a phase shift. Because of a phase difference of 180°, minima of the reflectance spectrum should coincide with maxima of the PL spectra.

2) *Detection angle difference*
PL measurements are performed under ± 45° while R measurements are performed under ± 0°. As shown in table 6.17 the energy separation (calculated via 'Open Filters') between the interference fringes does not change significantly for the two angles (3 meV). The difference in incidence R angle and PL detection angle induces as global shift over 0.030 eV of the minima and maxima in the spectra. In a comparison of PL and reflectance spectra one should take this energy shift into account. For this reason, later on in this section we will mostly compare energy

separations between peaks in PL and R spectra, and not the absolute positions. R spectra will be shifted for this.

3) *Effect of buffer and window layer*
In reflectance measurements buffer and window layer have an effect on the interference pattern. This is not the case for PL measurements (figure 6.87). In figure 6.88 a comparison of R spectra on complete cells and on samples without buffer and window layer (-HCl etched samples) is shown. A difference in energy spacing between the peaks and a shift of the spectra is visible. Table 6.18 shows that, as expected, the energy separation in R spectra of a complete cell is larger than for -HCl sample. These measurements indicate that the energy separation found for R spectra of a complete cell is only an underestimate for the energy spacing in PL spectra.

Figure 6.88: Measured reflectance spectra at 0° for sample a) SeH and b) SeL2 cell and -HCl.

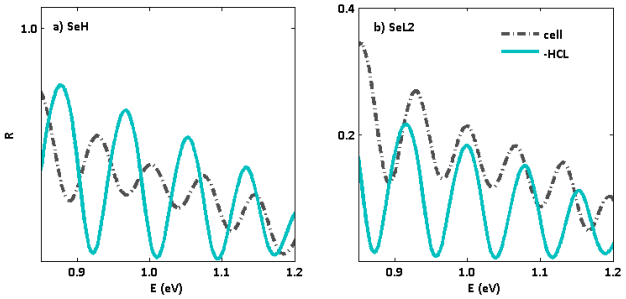

Table 6.18: Energy separations (ΔE) of R spectra with and without CdS and ZnO layer

Sample	ΔE (eV)	
	SeL2	SeH
cell	0.067	0.071
-HCl	0.081	0.086

As PL light is assumed to be generated at the front part of the absorber, no effect of removing window and buffer layer is expected and confirmed in figure 6.89 (samples of series3 and series4). The PL spectra of the complete cell ('cell') and after removal of the window and buffer layer ('-HCl') do not show a shift of the spectra relative to each other nor a difference in energy separations between the PL peaks. PL spectra of cell and -HCl samples could be fitted with the same PL peak sequence.

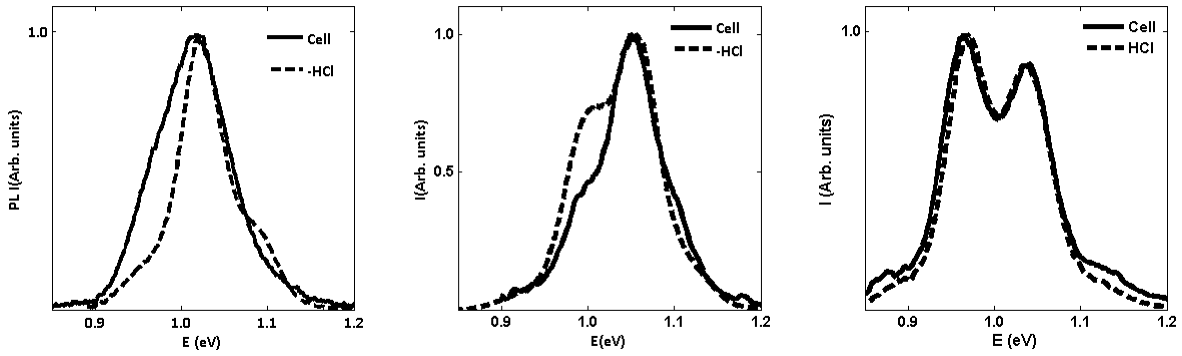

(a) SeH (b) SeL2 (c) NaK_{PDT}

Figure 6.89: PL spectra of cell and -HCl etched samples (T = 10 K).

A comparison (figure 6.90) of PL and R spectra of samples -HCl shows that the peak separations of R and PL spectra are not equal.

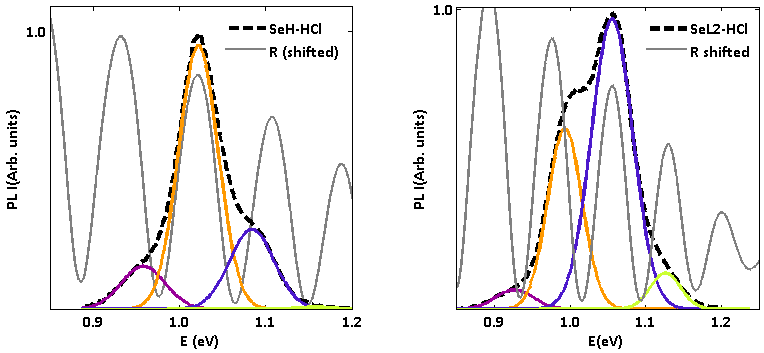

(a) SeH (b) SeL2

Figure 6.90: PL and (shifted) R spectra of cell and -HCl etched samples.

A direct comparison of PL and R spectra is further complicated by the different measurement temperatures. Reflectance measurements are performed at room temperature while PL measurements are performed in the temperature range 10 - 80 K. Furthermore the measurement spot is different between the two measurement types; inhomogeneities in film thickness, film roughness can alter reflectance measurements, inhomogeneities in composition can influence PL measurements.
Apart from differences between reflectance and PL measurement configurations and conditions, one has to take into account a possible variation of the cells themselves when comparing reflectance measurements of different series. Between the different series and cells there can be a variation in CIGS absorber layer thickness and composition. The thickness of all layers is in between 2.4 µm and 2.7 µm. This small thickness variation between the layers could result in a difference between the interference fringes as shown in figure 6.91. In the simulation the energy separation for d = 2.4 µm is calculated as 0.086 eV and for d = 2.7 µm calculated as 0.077 eV. Furthermore, the composition of the absorber layers, and in particular the GGI depth profile, is different for the different series of samples. As the GGI profile could affect the position where the recombination process measured in PL takes place, the expected influence of interference patterns on PL spectra can be different between the investigated samples.

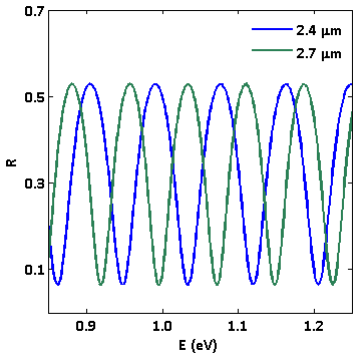

Figure 6.91: Simulated interference patterns at 0° for two CIGS layers with different thickness.

Reflectance measurements for different series
Reflectance measurements are performed on complete cells of the different series (shown in figure 6.92). The energy spacing between reflectance maxima (in the energy interval of PL emission) for the different series are tabulated in table 6.19. Small variations could be related to variations in absorber thickness and/or differences in GGI profiles. These R measurements on complete cells will, based on the above arguments, only provide an underestimate for the energy spacing in PL spectra. As indicated in the CIGS PL overview (section 6.5) all PL spectra could be fitted

using an energy peak separation of 0.060-0.075 eV. In order to explain the separtions in PL by interference effect, the energy spacings of R spectra of complete cells are thus expected to be smaller than 0.060-0.075 eV. The energy separations of R measurements are for series2-4 very similar to the PL energy separations. For series1 the energy separations in the R spectra are even larger.

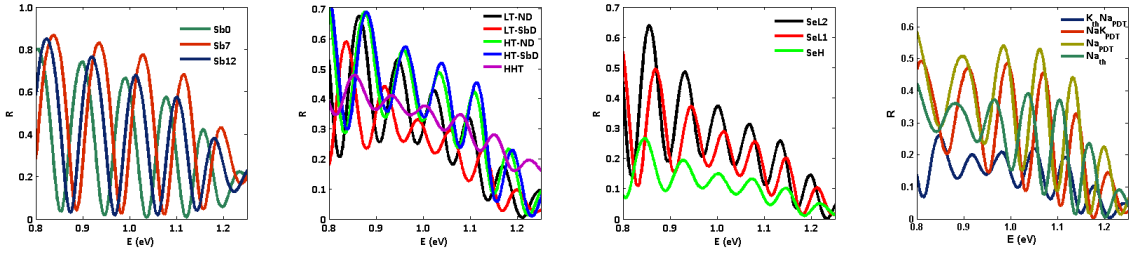

(a) Series1 (b) Series2 (c) Series3 (d) Series4

Figure 6.92: Reflectance spectra of all investigated CIGS thin-film solar cell series.

Table 6.19: Energy separations of reflectance spectra of CIGS series.

Sample	ΔE_R (eV)	Sample	ΔE_R (eV)
Sb0	0.097	SeL2-cell	0.067
Sb7	0.094	SeL1-cell	0.066
Sb12	0.093	SeH-cell	0.071
LT-ND	0.077	$K_{th}Na_{PDT}$	0.069
LT-SbD	0.069	Na_{th}	0.071
HT-ND	0.077	Na_{PDT}	0.076
HT-SbD	0.076	NaK_{PDT}	0.077
HHT	0.072		

In the following, possible variations on the intensity of individual PL contributions and the dependence of thickness of the absorber layer will be discussed. The effects observed in these spectra indicate that the structure seen in them is not solely due to interference.

Variation of intensity of particular PL contributions

- In all temperature dependent PL measurements (figures 6.31, 6.37, 6.47, 6.77) it is shown that PL peaks at lower energy remain more prominent (or even increases) as temperature increases. Because of the strong dependence of the intensity of individual PL peaks on temperature, it seems that underlying processes, resulting in changes in the PL spectra, should be present.

- PL spectra of various CIGS samples show a dependence of individual PL peaks on excitation wavelength (e.g. figures 6.26, 6.56, 6.73). Upon increasing the excitation wavelength (larger penetration depth) some peaks showed a change in the relative PL intensity.

- In section 6.3.3 it is show that by post annealing of the sample (selenization, air and vacuum anneal), the spectrum can be altered.

The features listed above are not obvious to explain by an interference effect only.

Effect of thinning of the absorber layer

As the interference pattern is dependent on the path length of the light, it will be largely altered (separation of subsequent peaks and shifting of the spectra) by changing the thickness of the absorber layer (see equation 6.1). A variation of the energy separations would give direct

evidence of the effect of interference. Thinning experiments have been performed on different samples of series3 and one sample of series4.

Series3: The thickness of both thinned samples of series3 (samples SeL2 and SeH (lower and higher Se evaporation rate respectively)) was determined by SEM measurements (table 6.20). The influence of a thinner absorber layer on the interference pattern in R spectra is clearly visible in figure 6.93. Table 6.20 presents the difference in energy spacing between the interference maxima of samples -HCl, -Br1 and -Br2. As the layer becomes thinner, the separation between the peaks becomes larger.

Figure 6.93: Measured reflectance spectra as a function of absorber thickness for both samples of series3.

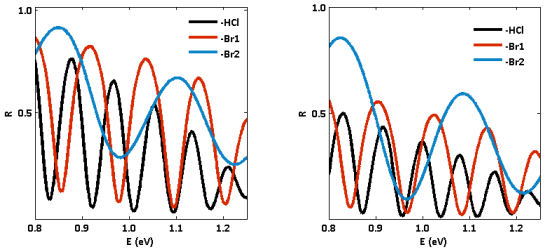

(a) SeH (b) SeL2

Table 6.20: Thickness absorber layer (d) and energy separations (ΔE) of measured interference patterns for thinned cells.

Sample	d (μm)	ΔE (eV)	
		SeL2	SeH
cell	2.40	0.067	0.071
-HCl	2.40	0.081	0.086
-Br1	1.58	0.113	0.118
-Br2	0.72	0.260	0.251

In section 6.3.2 it was shown that the PL spectra of the thinned absorber layers could be fitted with the same energy separations between the peaks as the non-etched samples. PL and R spectra of samples -Br1 and -Br2 are compared below.

-Br1

For sample SeH-Br1 an additional PL peak appears around 1.1 eV (figure 6.94(c)) with increasing excitation wavelength. The separation between this additional peak and the peak with highest intensity (around 1.0 eV) is around 0.113 eV which is quite similar to the energy separation of the reflectance spectra (0.118 eV) shown in table 6.20.

For sample SeL2-Br1 the energy separation between the peaks with highest intensity is not comparable with the energy separation of reflectance measurements (figure 6.94(d)). An energy separation of 0.113 eV as shown in table 6.20 is not in agreement with the energy spacing of PL peaks.

As noted before, the effect of the excitation wavelength on the PL spectra (clearly visible for both samples) is also not understood yet.

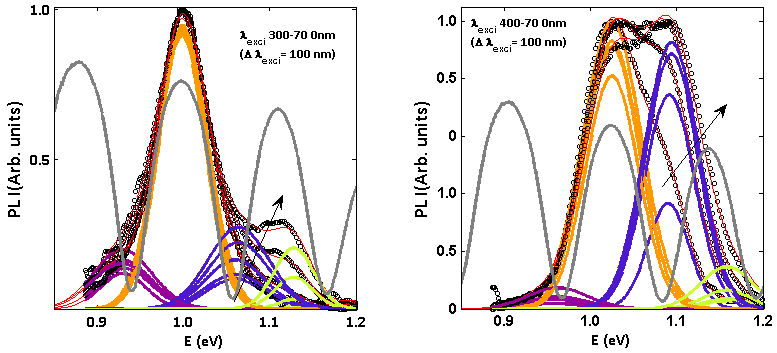

(c) SeH-Br1 (d) SeL2-Br1

Figure 6.94: Excitation wavelength dependent PL spectra and shifted R spectra of samples -Br1.

-Br2

The energy separations of the broad interference fringes in R measurements are large (figure 6.95). Therefore the PL spectra are not expected to be largely influenced by interference effects.

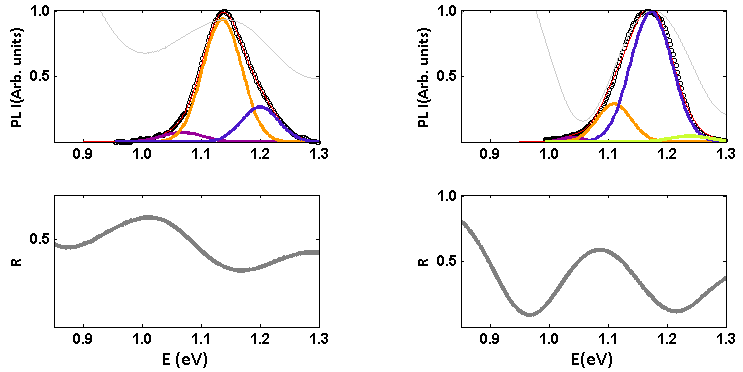

(a) SeH-Br1 (b) SeL2-Br1

Figure 6.95: Upper: PL spectra and shifted R spectra, lower: R spectra for samples -Br2.

No clearly resolved PL peaks were detected for samples SeH-Br2 and SeL2-Br2. The small wavelength (figures 6.54 and 6.56) and (small) temperature dependence (figure 6.96) of the PL spectra were regarded as an indication for different PL contributions in the spectra. PL spectra of both samples could be fitted with the same PL peak sequence as for the complete cells (figure 6.95).

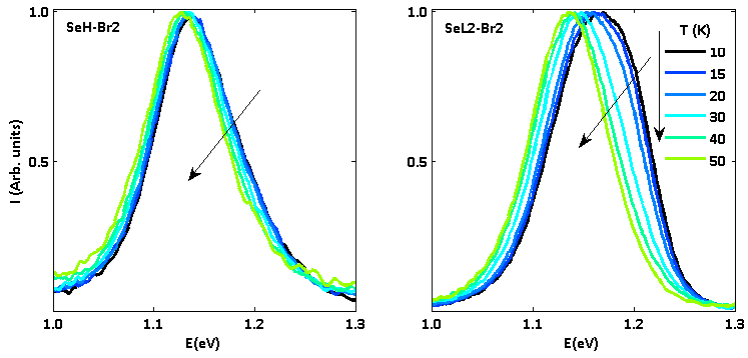

Figure 6.96: Normalized temperature dependent spectra of samples -Br2.

Series4: Sample NaK_{PDT} of series4 was etched over about 300 nm. A very small shift is visible, however the spectrum of the Br etched sample can still be fitted with same energy separations between the peaks as for the sample without etch. As shown in figure 6.91 an energy separation difference of approximately 10 meV is expected from the simulation between an absorber layer with thickness of 2.4 µm and 2.7 µm. A difference of 10 meV is not seen in the peak spacing.

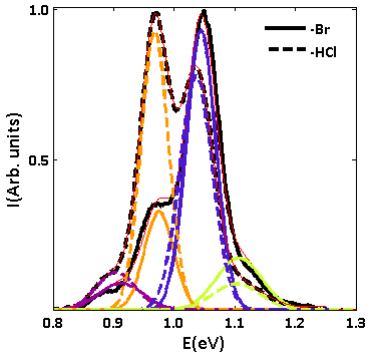

Figure 6.97: PL NaK_{PDT} (T = 10 K).

6.6.2 CZTS

6.6.2.1 Comparisons of reflectance and PL spectra

Differences between reflectance and PL measurements - Reflectance simulations
As the angle of detection is different for reflectance and PL measurements, the effect of the angle on the interference pattern will also be deduced for CZTS samples via a simulation with the programme 'OpenFilters'. For the simulation following values are used: d(CZTS absorber) = 2 µm, n = 2.734 (for E = 1 eV, T = 300 K) [39], d(CdS) = 50 nm, n = 2.3, d(ZnO) = 350 nm, n = 2 [273], d(MgF_2) = 105 nm, n = 1.44 [273]. A comparison of simulated reflectance spectra for sample cell1 at 0°, 45° and angles in between is shown in figure 6.98. Table 6.21 shows the separation between peaks. As the spacing of the peaks at larger detection angle is larger than for 0°, the spacing of the reflectance measurement at 0° can be regarded as a minimum spacing between the PL peaks.
Another difference between reflectance and PL measurements concerns the exact position of PL emission. As the absorption coefficient for CZTS (section 2.3.2) is lower than for CIGS, emission may occur deeper in the CZTS absorber layer. This effect is not taken into account in the simulation.

Figure 6.98: Simulated reflectance spectra of complete cell (cell1: MgF_2-ZnO-CdS-CZTS).

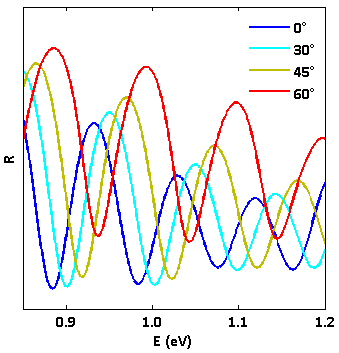

Table 6.21: Energy separation of calculated interference pattern for cell1.

Angle	E_{peak1}	E_{peak2}	ΔE_R
0°	1.029	0.932	0.097
45°	1.072	0.970	0.103
30°	1.049	0.950	0.099
60°	1.097	0.993	0.104

Reflectance measurements of different cells

Reflectance measurements on complete cells at a detection angle of 0° yield a peak spacing of 0.092-0.098 eV for the different cells. As shown via the reflectance simulation the energy spacing at 45° detection angle is expected to be slightly larger. Removing buffer, window and anti-reflection coating would even further increase the spacing as shown in figure 6.88.

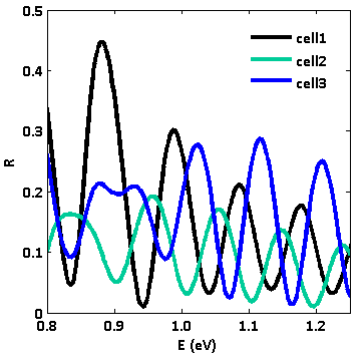

(a)

Figure 6.99: Measured reflectance spectra of all CZTS thin-film solar cells.

Comparison of spacing in PL and reflectance spectra of different cells

As shown in section 6.1.6 the PL peak separation for the CZTS thin-film solar cells in this work was indicated around 0.070-0.081 eV. This separation is markedly smaller than the separation obtained from reflectance measurements of complete cells at 0° (0.092-0.098 eV as shown in figure 6.99). The spacing at 45° and without buffer and window layer should be larger. Position dependent measurement on sample cell 3 showed clearly individual peaks for position2 (figure 6.100). The two largest peaks are separated around 0.081 eV from each other. The reflectance energy separation for cell3 is 0.092 eV (figure 6.99) for detection angle of 0°. The PL energy spacing and reflectance energy spacing are not in full accordance with each other. More experiments are necessary to evaluate the effect of interference on the PL spectra of the CZTS cells in an unambiguous way.

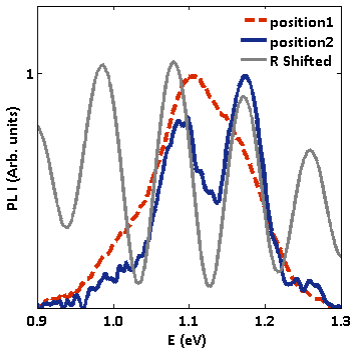

Figure 6.100: PL (45°, T = 10 K) and (shifted) reflectance measurement (0°, T = 300 K) of cell3.

6.6.3 Summary

There are definitely arguments in favour of a significant influence of interference on the PL spectra of the solar cells measured in this work:

- the appearance of five quasi equidistant PL peaks in the spectra of series4 is most remarkable as indicated already in section 6.4.6.

- for the thinned absorber layer of sample SeH-Br1 the energy separation between the peak with highest intensity and the additional peak is very similar to the separation in reflectance measurements.

Although these are strong indications not all observed phenomena can (so far) be explained by interference effects alone:

- there is an absence of an energy shift of the spectra upon changing detection angle,
- reflectance energy peak separations of complete cells are similar or larger and not, as expected, markedly smaller than PL energy peak separations,
- a clear disagreement between the energy spacing in R and PL spectra of HCl-etched samples and sample SeL2-Br1 is noted,
- the excitation wavelength and temperature dependence of the PL spectra as well as the effect of post annealing cannot be straightforwardly explained by interference alone.

Although different arguments could be given in favour of underlying defect related mechanisms as the cause for most prominent PL contributions, more experiments are definitely necessary to separate unambiguously the effect of interference from the PL emission. As the interference effect is quite complicated (e.g. multiple reflections at different interfaces, angle dependence), and PL and R measurements cannot be performed under exact the same circumstances, simulations could provide valuable information.

Summary

Contents

Conclusions

This dissertation work, aimed for the defect characterisation of two types of thin-film solar cell. The defect characterisation and defect control is important as defects in the absorber have an impact on the electrical properties of the solar cell: they may determine the conductivity type of the layer or promote recombination of photo-excited charge carriers. As recombined charge carriers cannot be collected, recombination is detrimental for device performance and must therefore be limited. Defect investigations are furthermore necessary to find out the mechanism behind the beneficial effect of incorporated impurity atoms such as Sb, Na and K. Two types of thin-film based solar cells are investigated by means of optical and/or electric spectroscopy.

The first type of thin-film solar cells under investigation included a $\mathbf{CuIn_{1-x}Ga_xSe_2}$ **(CIGS)** absorber layer. All CIGS samples as well as the EQE spectra, performance values and SIMS profiles of some samples were provided by the Laboratory of Thin Films and Photovoltaics (Empa, Zürich). For the applied electric characterisation techniques, it is shown that a barrier (most probably a non-ohmic back contact barrier [14, 200]) can introduce a capacitance transient [12]. As this hinders the study of defects with DLTS at low temperature, it has been opted to perform a more fundamental DLTS study (without relating the signals to specific defects) which explores more clearly to which extent the multi-layer structure of the thin-film solar cell influences the DLTS measurements. Therefore DLTS measurements performed on different CIGS thin-film solar cells (with different buffer layers and composition) were compared with measurements performed on the corresponding simplified metal/semiconductor/metal (M/S/M) samples. In general, very similar DLTS signals are recorded for complete cells and M/S/M structures. An effect of a possible inversion layer and oxide layer, investigated among others by additional etches, could not be demonstrated. A direct effect of influences of window and buffer layers and of the specific surface properties on the DLTS spectra can be excluded. Current-voltage measurements revealed Fermi level pinning. Understanding its origin might be an important step in the interpretation of DLTS signals at high temperature (above the N1 signal).

In this work, the results of optical spectroscopy and admittance spectroscopy (AS) are related and interpreted in terms of defects present in the material. Four series of thin-film solar cells, which aimed for low production cost (low temperature CIGS deposition process and/or low-cost substrate) ánd high efficiency were investigated. All series were made at reduced substrate temperature. Different optimisation procedures to enhance performance were applied on the

different series. Although reaching high performance with low temperature process was in the beginning of this work regarded as quite challenging, one could say the optimisation procedures were very successful; the maximum efficiency of the investigated cells has increased from the first investigated series towards the last investigated series. Nowadays a record efficiency of 20.4% [29] has been achieved with a low temperature deposition process on a flexible polymer substrate.

All photoluminescence (PL) measurements were performed in the temperature range 10-100 K in order to detect defect related transitions. Although PL spectra were rather broad, multiple components could clearly be distinguished in them. No near band edge luminescence or phonon replicas were detected. The feature of broad peaks is ascribed to the presence of potential fluctuations in highly compensated semiconductors, which was (for most cells) clearly confirmed by excitation power dependent measurements. Due to potential fluctuations, direct information about the energetic position of the involved defects could not be simply extracted.

• For the cells of **series1** an attempt was made, by Empa, to enhance grain growth as lower substrate temperatures could result in reduced grain sizes and hence in lower performance due to grain boundary recombination. To enhance grain growth, an Sb layer on top of the Mo contact was included in the cells. The thickness of the Sb layer was 0, 7 or 12 nm. SEM images revealed that, despite the low growth temperatures and limited in-diffusion of Sb (shown by TOFMS element depth profile measurements), very large grains can be obtained by including an Sb layer in the structure of the thin-film solar cell. As efficiency has increased as well, one could conclude that for this series the Sb addition had the desired effect. Admittance measurements on samples with and without additional Sb layer could not reveal a difference in defect structure between both samples. Admittance spectra exhibit a capacitance step to the geometric capacitance plateau in the low temperature region (5-60 K). Due to its independence of applied bias, this capacitance step is assigned to a dielectric freeze-out. C-T data in the low temperature region, showing that the carrier relaxation is very similar for both samples, confirm the absence of a change in the nature of the dominant acceptor upon Sb treatment. By analysing the capacitance step, the activation energy of the dominant shallow acceptor level was estimated at about 25 $\pm$ 5 meV. In view of the Cu-poor composition of the cells, we suggest that V_{Cu} is the intrinsic defect which provides the p-type conductivity of the CIGS absorber.

PL measurements on series1 revealed up to three broad peaks in the energy region 0.9-1.1 eV, labelled from low to high emission energy as A-C. For the sample with an Sb layer of 7 nm, the dominant peak was peak B, whereas for the other samples the dominant peak was peak C. The peaks are ascribed to quasi donor-acceptor pair recombinations in the presence of potential fluctuations (q-DAP). Based on the Cu-poor stoichiometry of the samples, we assumed that the acceptor in the recombination processes is the dominant shallow V_{Cu} acceptor which is revealed by AS. For the dominant PL peaks, a q-DAP recombination of V_{Cu}-V_{Se} is suggested for the PL emission at highest energy (peak C), a q-DAP recombination of V_{Cu}-In_{Cu} is suggested for peak B. The suggestions were based on the stoichiometry of the samples and theoretical predictions of the formation energy of defects found in reference [91]. The same or very similar identification was proposed in references [235, 253–255]. XPS measurements revealed a slightly larger In concentration at the surface of the sample with Sb layer of 7 nm. This was in accordance with assigning the dominant peak in the PL spectrum of this sample to In_{Cu}-V_{Cu}.

• As substrate temperature can, besides the effect on grain growth, also have an effect on the interdiffusion of the elements during growth, the combined effect of substrate temperature and Sb layer underneath the CIGS absorber is investigated in the samples of **series2**. Cells, with or without Sb layer, were made at three different reduced substrate temperatures. As opposed to the results of series1, no beneficial effect of the incorporation of an Sb layer on grain size or efficiency was seen for these samples. It appears the effect of Sb is dependent on the deposition parameters of the CIGS absorbers. The findings concerning the effect of substrate temperatures are in agreement with the expectations: with increase of substrate temperature grain size as

well as efficiency increase.
PL measurements on samples of series2 revealed again three broad emission peaks. For samples made at lowest substrate temperature, the PL peak at lowest energy is more pronounced. As element depth profile measurements (EDX and TOFMS) are indicative of a larger in-diffusion of Cd into the CIGS absorber for the cells made at the lowest substrate temperature, it was suggested that the PL peak at lowest energy could be related with a Cd_{Cu}-V_{Cu} q-DAP transition. For Sb doped cells, the PL emission at highest energy (suggested to be V_{Cu}-V_{Se} q-DAP transition) is more pronounced and increases with increasing excitation wavelength. A positive concentration gradient in the associated donor defect, probably V_{Se}, towards the absorber bulk is suggested.

• An investigation on the effect of an altered Se evaporation rate was performed on cells of **series3**. Efficiency as well as grain size are higher for cells made at lower Se evaporation rate. PL measurements reveal up to four broad peaks, labelled from low to high energy as A-D (peaks A-C correspond to the peaks observed in series1-2). The spectra of the cell made at lower Se evaporation rate show a dominant transition related to higher PL energy (peak C, V_{Se}-V_{Cu}) whereas the spectra of the cell made at higher Se evaporation rate show a pronounced PL peak related lower PL energy (peak B, In_{Cu}-V_{Cu}).
By means of Br etching, the absorber layer could be thinned, which enabled to perform PL measurements at 'different depths' in the absorber layer. Three different samples were investigated; a sample without thinning, a sample thinned to around the position of the Ga dip and a sample thinned further than the position of the Ga dip. The same PL peaks appear but at different emission energy for the different samples. For the thinnest absorber layer a shift of the emission peak towards larger energy is clearly noticed, which is in accordance with the increase of the band gap energy towards the Mo back contact. From the PL measurements on samples with varying absorber layer thickness it was shown that only the absorber surface region is probed in the PL measurement. For the sample at reduced evaporation rate, peak B became dominant in the PL spectra of an absorber thinned to the position around the Ga dip. As the In concentration is relatively higher around the Ga dip in the absorber layer, this further supports the assignment of peak B to a transition involving In_{Cu} defect. As in PL spectra of thinned absorber layers, the PL peak at lowest energy (peak A) does not disappear, the earlier made suggestion of a Cd_{Cu} related defect transition is most probably incorrect.
By performing post annealing treatments in Se atmosphere, air and vacuum, an attempt was made to change the V_{Se} defect concentration and hence force a change in the intensity of the related PL emission peak. While annealing in Se atmosphere and in air are expected to decrease the V_{Se} related defect transition, the vacuum annealing should increase the transition. The expected effects of the different annealing treatments were clearly visible on the peak C intensity in PL spectra of the sample made at reduced Se evaporation rate. The annealing experiments seem to support the relation of peak C to a transition in which V_{Se} is involved.

• Besides a low temperature CIGS deposition process, thin-film solar cells with polyimide substrates need distinct incorporation of Na and K. Different incorporation methods of Na and K and their effect on performance and defect structure were investigated in **series4**. It is shown that the enhanced performance, due to incorporation of Na and K, is largely dependent on the incorporation method. The highest efficiency was obtained for the sample in which KF post deposition treatment (PDT) was performed after NaF PDT. For this sample an improvement of the junction properties is suggested as high efficiency can be reached with a thinner CdS buffer layer [29]. Remarkably, the Na concentration at the surface of the absorber, revealed by SIMS element depth profile, was lower than in the case of NaF PDT alone. SIMS measurements revealed furthermore that the presence of Na and K has an influence on the diffusion of the elements during growth. Although high efficiencies are obtained, PL measurements revealed clearly five PL emission peaks (only four for the sample with highest efficiency) with remarkably smaller

peak width compared to all other spectra. To investigate the possible effect of interference on these (and hence on other) PL spectra an angle dependence test was performed. No shift of the spectra was visible by slightly rotating the sample holder to alter the detection angle. From this measurement we could not show a large effect of interference on the spectra. No additional PL peaks due to Na or K incorporation arise. The dominance of the PL peaks of the sample which had highest efficiency is different compared to the spectra of the other samples. It has been shown by thinning the absorber layer that the effect is limited to the surface of the absorber layer. PLE and PL spectra show a small overlap, which could suggest the influence of a second phase.

The second type of thin-film solar cells under investigation included a **Cu_2ZnSnS_4(CZTS)** absorber layer. The cells as well as performance and XRF values were provide by Ångström Solar Center (University Uppsala, Sweden). PL measurements on three different CZTS cells (different annealing or double CdS buffer layer thickness) revealed three broad bands for all CZTS samples. Relative peak contributions are strongly dependent on the excitation spot which indicates that inhomogeneity in phase composition and/or defect distribution is important for these cells. Band gap determination at low temperature, performed by means of PLE, revealed a relatively large spectral shift of the emission peaks from the band gap energy. Therefore q-DAP pair recombination seems the most probable PL mechanism. Since the CZTS absorber can include different phases, q-DAP recombination from different phases seems to be a plausible cause for the appearance of different peaks.

Perspectives

This work demonstrates that the performance of the thin-film solar cell depends on many different parameters such as the grain size, shunt resistance, substrate temperatures, presence of different impurity elements (Na, K, Sb) and their incorporation method, evaporation rates, annealing, grading profiles, etc. As a result it is not always straightforward to determine the specific role of the defects on the performance characteristics and to compare the characterization results of different samples. Moreover, it is not evident to directly determine and compare defect concentrations with the methods used.

In this work the defect characterization of CZTS and CIGS based thin-film solar cells was performed by means of optical as well as electric defect characterization techniques. The information obtained by the different techniques could not be compared or directly linked to each other. Only the activation energy of the shallowest acceptor in CIGS, determined by admittance spectroscopy, could be related to PL measurements. The absence of a comparison between PL and DLTS measurements is partly due to the non-straightforward interpretation of DLTS signals. As the DLTS signals have properties which are unusual for a defect signal, one cannot be completely sure if defect related information is obtained at all. Therefore the obtained information should be used with caution as a wrong interpretation of the DLTS signals could lead to an erroneous understanding of the fundamental properties of the absorber material. Even though the interpretation of DLTS signals is not straightforward, the signals are still intriguing. In future investigations one could try to study basic Schottky diode structures in which front and back contact metals can be varied such that the effect of different metal contacts and therewith the effect of Fermi level pinning can be further explored. Supplementary information about recombination mechanisms obtained via other electric techniques could be useful for the interpretation of DLTS signals. Temperature dependent current-voltage measurements (I-V-T), for example, could provide information about the dominant recombination path via a comparison of the activation energy of the saturation current with the band gap energy. As the series resistance can have an influence on the activation energy values, I_{sc}-V_{oc} measurements are recommended

for I-V-T analysis. In addition, as Schottky diodes structures provide a more elementary method to investigate the intrinsic properties of the absorber layer, I-V-T measurements on these structures might give more insight concerning the barrier formation at the Schottky diode interface and the dominant conduction process. This information could be of great help for the further understanding of DLTS signals of M/S/M structures and eventually also of thin-film solar cells.

Photoluminescence could provide a more reliable tool to investigate defects present in the material. However as the effect of interference could give rise to erroneous attribution of PL bands, investigations concerning the effect should definitively gain more attention. The assignment of the PL signals in terms of defects is, as for DLTS, not straightforward as proven by the very divergent results and interpretations present in literature. Part of the discrepancies could lie in the large variation of the investigated samples; measurements have been performed on single crystals or different polycrystalline thin-film layers, made with different deposition techniques and varying compositions (whether or not graded). To explain and especially to compare PL signals, element depth profile information has proven to be indispensable as it can help in interpreting global shifts of the PL spectra and differences in relative peak intensities for different cells or in different (depth) positions in the absorber. As all PL transitions are related to the band gap of the investigated semiconductor layer, it is quite strikingly that in the majority of the PL reports, information about band gap at the specific low temperature is missing. In this work it has been shown that additional PLE information is (although influenced by potential fluctuations) valuable for the interpretation of PL spectra. As PL measurements on CIGS thin-film solar cells are complicated by the grading of the band gap, a more basic study could be performed on samples without grading. Other additional helpful information for the PL study of CIGS and especially CZTS, consists of information about possible different phases in the absorber material. In this work an attempt was made to go beyond the standard measurements by seeking for in-depth defect information and post annealing. As it appeared that the PL peak in which the V_{Se} defect is involved, could be altered by annealing, the method could be used in further experiments on different samples to find evidence for this PL component in the samples. Another possible suggestion for future PL research contains a more thorough study of the effect of substrate temperature on the spectra. All PL studies in this work were performed on cells made at reduced substrate temperature. From the PL results of series2 it appeared that the PL peak at lowest energy was more pronounced for the cells made at the lowest substrate temperatures. To investigate this further and to explain the origin of this peak more clearly, a comparison of PL measurements on cells made at different substrate temperatures (ranging from above normal to below normal substrate temperature) could be suggested.

Acknowledgements

My gratitude goes to Prof. H. Vrielinck who gave me the opportunity to do this thesis for which I'm deeply grateful. Thank you for your trust, support during my work, fruitful discussions and very precise proofreading of this thesis. Thank you for offering your help whenever needed and baking delicious cakes at special occasions.
Further I thank Prof. J. Lauwaert for the continuous support and inspiring discussions. Thanks for always answering my questions, sharing knowledge and time. Without your experience and patience for contacting square mm solar cells into the DLTS set-up it would have been so much harder.

A large number of people have contributed to make the accomplishment of this thesis possible.

- I want to thank the collaborators which provided me interesting thin-film solar cells and ensured that my research kept going. Fabian Pianezzi (Empa) is acknowledged gratefully for providing excellent CIGS cells and for critical reading my articles and answering all my questions. Thanks to Prof. Ch. Platzer-Björkman and her group for the CZTS cells and interesting discussions. The visit at Ångström Solar Center gave me a better insight into thin-film solar cells.

- During my thesis I used a lot of measurement techniques and different set-ups. Without the help of a lot of experienced people it would have been much more difficult the get nice results. Concerning PL, I want to thank Prof. P. Smet and Prof. D. Poelman for the collaboration and for their comments on my work. Thanks to the Lumilab members for creating a nice atmosphere during PL measurements. Thank Jonas B. , Jonas J. , Anthony and Katrien for your time and support during my search to find a signal. I want to thank Prof. R. Van Deun for the collaboration concerning PLE measurements and Anna for her help. Thanks to Prof. Ch. Detavernier for giving me access to the admittance set-up and Wouter for measuring some important XRF results. Further I want to thank Samira Khelifi for performing EQE measurements, Olivier Janssens for SEM measurements and Nico De Roo for XPS measurements, Els Bruneel for providing me with Br solution, Davy Deduytsche for performing talystep measurements, Boris for post-selenization of some samples and Bert for putting my sample under glow discharge. I want to thank Agnes Tempez for putting a lot of effort in measuring the 10 nm thick Sb layer with TOFMS.

- My thanks goes to all people who contributed to my motivation and enthusiasm about my work. Therefore I want to thank all nice people from the conferences and summerschools. I would like to give special thanks to my office mate Klaas for the nice time. I am thankful to my parents and grandparents who encourage and support me at all time. Thanks to my friends for providing distracting entertainment. Last but not least I want to thank my friend Olivier for his tolerance, optimism and patience.

Wishing you all the best !
Lisanne van Puyvelde

List of symbols and abbreviations

Symbol	name	unit
α	Absorption coefficient	cm^{-1}
A	Area	cm^2
A^*	Richardson constant	A m^{-2} K^{-2}
a_B	Bohr radius	m
C	Capacitance	F
$c_{n,p}$	Capture constant of electrons and holes	cm^3/s
$D_{n,p}$	Diffusion coefficient for electrons and holes	cm^2/s
E	Electric field	V/cm
ΔE_c	Conduction band offset	eV
E_a	Activation energy of the saturation current density	eV
$E_{c,v}$	Conduction or valence band energy	eV
E_F	Fermi energy	eV
$E_{Fn,\ Fp}$	Quasi-Fermi level for electrons and holes	eV
E_g	Band gap energy	eV
E_{ph}	Photon energy	eV
$e_{n,p}$	Emission constant of electrons and holes	s^{-1}
ε_0	Permittivity of the vacuum	F/m
ε_r	Relative permittivity	
η	Conversion efficiency	%
FF	Fill factor	%
φ_b^p	Barrier height for holes at the interface	eV
G	Conductance	S
h	Planck constant	J s
J	Current density	mA/cm^2
J_0	Saturation current density	mA/cm^2
J_{ph}	Photo-generated current density	mA/cm^2
J_{sc}	Short-circuit current density	mA/cm^2
k_b	Boltzmann constant	eV/K
λ	Wavelength	nm
m^*	Effective mass	kg
$L_{n,p}$	Diffusion length of electrons and holes	nm
n	Free electron density	cm^{-3}
n	Ideality factor	
n_i	Intrinsic carrier density	cm^{-3}
$N_{a,d}$	Shallow acceptor or donor concentration	cm^{-3}
$N_{c,v}$	Density of states in the conduction or valance band	cm^{-3}

Symbol	Name	Unit
N_t	Defect concentration	cm^{-3}
p	Free hole density	cm^{-3}
q	Elemental charge	C
ρ	Charge density	C/cm^3
$R_{p,s}$	Parallel and series resistance	Ωcm^2
$\sigma_{c,v}$	Capture cross-section for electrons and holes	Ωcm^2
σ	Conductance	S/cm
T	Temperature	K
$\tau_{c,v}$	Lifetime of electrons and holes	ns
$\mu_{n,p}$	Mobility of electrons and holes	cm^2/Vs
$1/\tau$	Rate constant	1/s
V_{bi}	Built-in voltage of the pn-junction	V
V_{oc}	Open-circuit voltage	V
v_{th}	Thermal velocity	cm/s
W	Depletion width	μm

Abbreviation	Description
ac	Alternating current
AS	Admittance spectroscopy
CBD	Chemical bath deposition
CIGS	$CuIn_{1-x}Ga_xSe_2$
CZTS	Cu_2ZnSnS_4
dc	Direct current
DLCP	Drive level capacitance profiling
DLTS	Deep level transient spectroscopy
EDX	Energy dispersive X-ray analysis
EQE	External quantum efficiency
OVC	Ordered vacancy compound
PDT	Post deposition treatment
PL	Photoluminescence
PLE	Photoluminescence excitation
PP-TOFMS	Plasma profiling time of flight mass spectrometry
PI	Polyimide
PV	Photovoltaic
QNR	Quasi neutral region
SCR	Space charge (depletion) region
SCAPS	One-dimensional solar cell simulation software
SEM	Scanning electron microscopy
SIMS	Secondary ion mass spectroscopy
SLG	Soda-lime glass
SRH	Shockley-Read-Hall recombination
XPS	X-ray photoelectron spectroscopy
XRF	X-ray fluorescence spectroscopy
x (GGI)	Relative Ga concentration [Ga]/([Ga]+[In])
y (CGI)	Relative Cu concentration [Cu]/([Ga]+[In])

List of publications

Papers in international, peer reviewed journals

- L. Van Puyvelde, J. Lauwaert, A. Tempez, W. Devulder, S. Nishiwaki, F. Pianezzi, C. Detavernier, A. N. Tiwari, H. Vrielinck, Electronic defect study on low temperature processed Cu(In,Ga)Se_2 thin film solar cells and the influence of an Sb layer, *J. Phys. D: Appl. Phys.*, In press, 2014
- L. Van Puyvelde, J. Lauwaert, P. F. Smet, F. Pianezzi, S. Buecheler, S. Nishiwaki, A. N. Tiwari, H. Vrielinck, Deep level transient spectroscopy measurements on Mo/Cu(In,Ga)Se_2/metal structure, *Thin solid films*, In press, 2014
- L. Van Puyvelde, J. Lauwaert, P. F. Smet, S. Khelifi, T. Ericson, J. J. Scragg, D. Poelman, R. Van Deun, C. Platzer-Björkman, H. Vrielinck, Photoluminescence investigation of Cu_2ZnSnS_4 thin-film solar cells, *Thin solid films*, In press, 2014
- L. Van Puyvelde, J. Lauwaert, F. Pianezzi, S. Nishiwaki, P. Smet, D. Poelman, A. N. Tiwari, H. Vrielinck, Influence of an Sb doping layer in CIGS thin-film solar cells: a photoluminescence study, *J. Phys. D: Appl. Phys.*, 47 (045102), 2014
- J. Lauwaert, J. Lauwaert, L. Van Puyvelde, J. Thybaut, H. Vrielinck, Modelling of capacitance transients of thin-film solar cells: a valuable tool to gain information on perturbing layers or interfaces, *Appl. Phys. Lett.*, 104 (053502), 2014
- J. Lauwaert, L. Van Puyvelde, J. Lauwaert, J. Thybaut, S. Khelifi, M. Burgelman, F. Pianezzi, A. N. Tiwari, H. Vrielinck, Assignment of capacitance spectroscopy signals of CIGS solar cells to effects of non-ohmic contacts, *Sol. Energy Mater. Sol. Cells*, 112: 78-83, 2013

Conference contributions

- L. Van Puyvelde, F. Pianezzi, P. Reinhard, P. F. Smet, J. Lauwaert, S. Buecheler, A. N. Tiwari, H. Vrielinck, Photoluminescence defect study on potassium and sodium doped Cu(In,Ga)Se_2 thin film solar cells, *MRS Spring meeting*, 2015
- J. Lauwaert, L. Van Puyvelde, H. Vrielinck, Regression analysis of capacitance transients: a method to obtain information on the electric structure of thin-film solar cells, *Photovoltaic Solar Energy*, 29th European conference, 2014
- L. Van Puyvelde, J. Lauwaert, F. Pianezzi, A. N. Tiwari, H. Vrielinck, Deep-level transient spectroscopy (DLTS) measurements on Mo/CIGS/Metal structures, *E-MRS May Spring meeting*, 2014

- L. Van Puyvelde, J. Lauwaert, P. F. Smet, D. Poelman, R. Van Deun, T. Ericson, J. J. Scragg, C. Platzer-Björkman, S. Khelifi, H. Vrielinck, Photoluminescence and DLTS investigation of reactively sputtered Cu_2ZnSnS_4 thin film solar cells, *E-MRS May Spring meeting*, 2014

- J. Lauwaert, L. Van Puyvelde, S. Khelifi, M. Burgelman, H. Vrielinck, Effect of non-ideal contacts in capacitance spectroscopy of Cu(In,Ga)Se_2 solar cells, *MRS Spring meeting*, 2013

- L. Van Puyvelde, J. Lauwaert, P. Smet, D. Poelman, C. Detavernier, F. Pianezzi, S. Nishiwaki, A. N. Tiwari, S. Khelifi, M. Burgelman, H. Vrielinck, Combining optical and electrical studies to unravel the effect of Sb doping on CIGS solar cell, *MRS Spring meeting*, 2013

- L. Van Puyvelde, J. Lauwaert, P. Smet, D. Poelman, C. Detavernier, F. Pianezzi, S. Nishiwaki, A. N. Tiwari, S. Khelifi, M. Burgelman, H. Vrielinck, Combining optical and electrical studies to unravel the effect of Sb doping on CIGS solar cell, *Photovoltaic technical conference*, 2013

- L. Van Puyvelde, J. Lauwaert, H. Vrielinck, Optimization of thin film solar cells through defect characterization, *Energy Challenge Symposium*, 2013

- J. Lauwaert, L. Van Puyvelde, J. Vanhellemont, H. Vrielinck, Assignment of anomalous DLTS signals to additional barriers in Cu(In,Ga)Se_2 solar cells, *Defects in Semiconductors*, 27th International conference, 2013

- L. Van Puyvelde, J. Lauwaert, M. Burgelman, H. Vrielinck, Evidence of deep defects in CIGSe solar cells from DLTS trap filling study, *E-MRS Spring Meeting*, 2012

- L. Van Puyvelde, P. Matthys, P.F. Smet, J. Lauwaert, H. Vrielinck, Back to basics: study of defects in single crystal $CuInS_2$ solar cell absorber material, *Crystallography*, 7th Belgian symposium, 2012

Appendix

Contents

A.1 The pn-junction

A.1.1 Depletion width

In a pn-diode a region of fixed space charge near the junction, in which almost no free charges are present, is the depletion region. In figure A.101 the depletion width W = x_n + x_p. x_n (x_p) denotes the width of the space charge region on the n-side (p-side) of the junction. The voltage drop (built-in potential V_{bi}) over the depletion region caused by the electric field, implies a drop in the energy levels of the conduction and the valence band which is labelled as band-bending [3]. In equilibrium p(x) and n(x) are given by [274]

$$\begin{aligned} p(x) &= N_v\, exp\Big(-\frac{E_F - E_v(x)}{kT}\Big) \\ &= N_v\, exp\Big(-\frac{E_F - E_{vp}}{kT}\Big)\, exp\Big(-\frac{e\psi(x)}{kT}\Big) \\ &= p_{p0}\, exp\Big(-\frac{e\psi(x)}{kT}\Big) \end{aligned}$$

$$\begin{aligned} n(x) &= N_c\, exp\Big(-\frac{E_c(x) - E_F}{kT}\Big) \\ &= N_c\, exp\Big(-\frac{E_{cn} - E_F(x)}{kT}\Big)\, exp\Big(-\frac{e\psi(x) - V_{bi}}{kT}\Big) \\ &= n_{n0}\, exp\Big(-\frac{e\psi(x) - V_{bi}}{kT}\Big) \end{aligned}$$

With

$$\begin{aligned} E_v(x) &= E_{vp} - e\psi(x) \\ E_c(x) &= E_{cn} - e\psi(x) + V_{bi} \end{aligned}$$

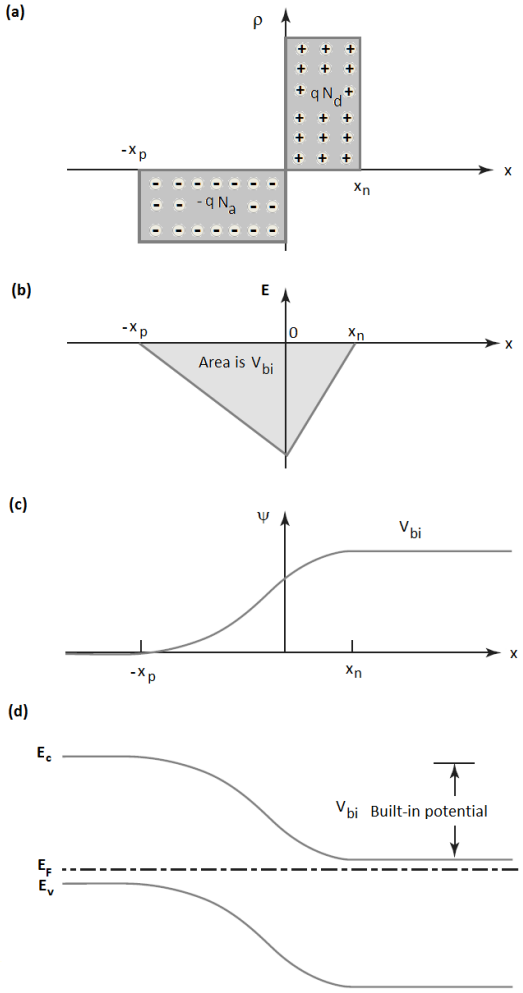

Figure A.101: pn-junction in thermal equilibrium (a) charge density, (b) field distribution, (c) potential variation, (d) energy band diagram [3].

Hereby n_{n0} and p_{p0} represent respectively the electron concentration in the n-area and the hole concentration in the p-area sufficiently far from the junction (quasi neutral region). N_c and N_v are the conduction band and valence band effective densities of state (equation 3.14).

The electric field E(x) and the potential ψ(x) can be calculated with the Poisson equation (with $\varepsilon = \varepsilon_0 \cdot \varepsilon_r$) [3, 274].

$$\frac{\partial E(x)}{\partial x} = -\frac{\partial^2 \psi(x)}{\partial x^2} = \frac{\rho(x)}{\epsilon}$$

For simplicity, it is assumed that the dopants are fully ionized in the depletion region (depletion approximation). The potential can be written as [274]

$$\psi = \begin{cases} 0 & x < -x_p \\ \frac{eN_a}{2\epsilon}(x + x_p)^2 & -x_p < x < 0 \\ -\frac{eN_d}{2\epsilon}(x - x_n)^2 + V_{bi} & 0 < x < x_n \\ V_{bi} & x_n < x \end{cases}$$

The depletion width W (x_n+x_p) can be calculated via the charge neutrality condition ($x_p N_a = x_n N_d$) and the continuity of the potential in x = 0 [3, 274, 275].

$$W = \sqrt{\frac{2\epsilon}{e}\left(\frac{1}{N_a} + \frac{1}{N_d}\right) V_{bi}} \tag{A.2}$$

Due to the charge neutrality equation, if $N_d >> N_a$ in case of n^+p-junction, the width of the space charge region on the p-side region is much larger than that on the n-side.

A.1.2 Under bias

If an external voltage is applied, the Fermi level is no longer constant [3, 61, 274, 275]. The concentrations of electrons and holes are determined by the positions of the quasi Fermi levels. If the n-type region is at ground potential, all voltages are referred to the quasi Fermi level E_{Fn} [274]. A positive applied voltage V_a lowers the Fermi level in the p-type area by an amount eV_a lower than E_{Fn} (figure A.102 b). The internal potential barrier decreases and the width of the depletion region decreases. In formula A.2 V_{bi} is replaced by V_{bi}-V_a.

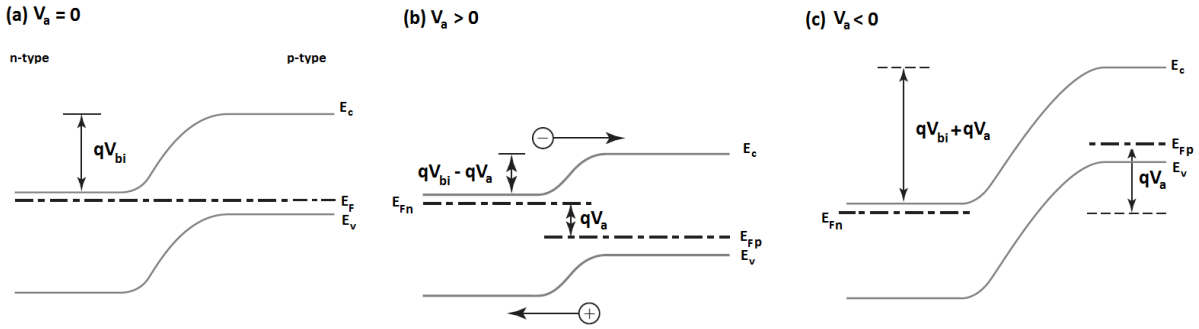

Figure A.102: Energy band diagram and quasi Fermi levels of pn-junction (a) no bias, (b) forward bias, (c) reverse bias [274].

For $V_a > 0$ the diffusion current gets the upper hand [275]. Minority carrier holes diffuse in the quasi neutral n-type region over a distance L_p [275], minority carrier electrons diffuse in the quasi neutral p-type region over a distance L_n (minority carrier injection). The diffusion of minority carriers into the quasi neutral region causes the so-called recombination current [47, 275], since the injected minority carriers recombine with the majority carriers in these regions.
For $V_a < 0$ the total voltage across the depletion width is increased (figure A.102 c). The depletion width enlarges [274,275]. The diffusion currents for both type of carriers decrease: minority carriers are extracted over a diffusion length distance. The drift currents are mostly limited by the number of minority carriers available for drift. The drift current does not change significantly when an external bias is applied [274]. The minority injection ($V_a > 0$) and extraction $V_a < 0$ are depicted in figure A.103.

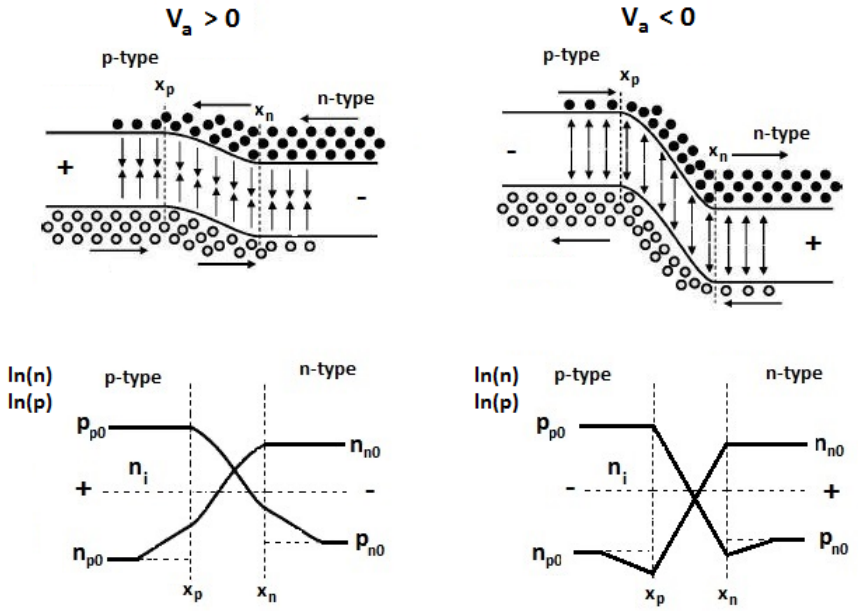

Figure A.103: Upper: charge carrier transport in a biased pn-junction, Lower: charge carrier density (adapted from reference [275]).

The current voltage characteristic for the ideal case can be deduced if following assumptions are made [3, 55, 274]:
(1) there is an abrupt depletion layer (W << L_n, L_p), (2) the Boltzmann approximation for n and p are valid, (3) the total current is small in comparison with drift and diffusion current, (4) the injected minority carrier densities are small compared with the majority-carrier densities, (5) there is no external source of carrier generation and no recombination of charge carriers occurs within the space charge region. As a result electron and hole currents are constant through the depletion layer.

The minority carrier density at the edge of the depletion region (quasi neutral region) can be calculated. The continuity equation for holes with low injection and no electric field in the neutral region reduces to (R recombination rate, G generation rate) [3, 274]

$$\frac{\partial p}{\partial t} = G_p - R_p - \frac{1}{q}\frac{\partial J_p}{\partial x} = G_p - \frac{p - p_0}{\tau_p} - p\mu_p\frac{\partial E}{\partial x} - \mu_p E\frac{\partial^2 p}{\partial x} + D_p\frac{\partial^2 p}{\partial x^2} = G_p - \frac{p - p_0}{\tau_p} + D_p\frac{\partial^2 p}{\partial x^2}$$

In steady state and in the dark (G = 0) the equation simplifies to

$$0 = -\frac{p - p_0}{\tau_p} + D_p\frac{\partial^2 p}{\partial x^2}$$

The hole density at the edge of the depletion region (x = x_n) is (L_p= $\sqrt{D_p\tau_p}$ diffusion length of minority carriers, τ_p hole lifetime, D_p hole diffusion coefficient) [3, 274]

$$p_n(x) - p_{n0} = p_{n0}\left[exp\left(\frac{qV}{kT}\right) - 1\right] exp\left(-\frac{x - x_n}{L_p}\right)$$

For low injection and low field, the minority carrier current is a diffusion current. The diffusion current for holes is [3, 274]

$$J_p(x_n) = -qD_p\frac{\partial p_n}{\partial x}\Big|_{x_n} = \frac{qD_p p_{n0}}{L_p}\left[exp\left(\frac{qV}{kT}\right) - 1\right]$$

The continuity equation in the depletion region is equal to $\frac{1}{q}\frac{\partial J_n}{\partial x} = -\frac{1}{q}\frac{\partial J_p}{\partial x} = R - G$. The magnitude of the change in current across the depletion region is
$\partial J_n = |\partial J_p| = q\int_{x_n}^{-x_p}(R-G)dx \approx 0$ which is negligible. Hence the diffusion currents (J_p and J_n) are constant across the depletion region. The total current can be written as the sum of the diffusion currents of electrons and holes at a certain place. The final results for the current density is [2, 3, 47, 274, 275]

$$\begin{aligned} J &= J_n(-x_p) + J_p(-x_p) = J_n(-x_p) + J_n(x_n) \\ J &= \left(\frac{qD_p p_{n0}}{L_p} + \frac{qD_n n_{p0}}{L_n}\right)\left(exp\left(\frac{qV}{kT}\right) - 1\right) \\ J &= J_0\left(exp\left(\frac{qV}{kT}\right) - 1\right) \end{aligned} \tag{A.3}$$

Equation A.3 is the Schockley equation with J_0 the saturation current density and V the applied voltage. J_0 is the superposition of the generation current from the n-type and p-type semiconductor. $n_{p0} = n_i^2/N_a$ is the equilibrium electron concentration in the p-region (n_i^2 intrinsic concentration). $p_{n0} = n_i^2/N_d$ is the equilibrium hole concentration in the n-type region. As n_i^2 equals $N_c N_v exp(-E_g/kT)$, the saturation current can be written as [2, 47, 274]

$$\begin{aligned} J_0 &= \frac{qD_p p_{n0}}{L_p} + \frac{qD_n n_{p0}}{L_n} \\ &= q\, n_i^2\left(\frac{D_n}{N_a L_n} + \frac{D_p}{N_d L_p}\right) \\ &\sim exp\left(\frac{-E_g}{kT}\right) \end{aligned}$$

The saturation current density is determined by the band gap. If the band gap increases, the saturation current decreases. In this expression for the saturation current, the recombination in the depletion region is neglected, only the recombination in the quasi neutral part has been taken in to account. In section 2.1.3.2 more general expressions which take into account recombination in different regions can be found. As L equals $\sqrt{D\tau}$, the saturation current density depends on the carrier lifetime. For a single sided p^+n- junction ($p_{n0} >> n_{p0}$) the saturation current density can be written as [3]

$$\begin{aligned} J_0 &= \frac{qD_p p_{n0}}{L_p} \\ &= q\,\frac{n_i^2}{N_d}\sqrt{\frac{D_p}{\tau_p}} \\ &= q\,\frac{N_c N_v exp(-E_g/kT)}{N_d}\sqrt{\frac{D_p}{\tau_p}} \end{aligned} \tag{A.4}$$

A.1.3 Under illumination

A pn-junction can transform the energy contained in an incident photon current of light into an external electric energy. On the basis of the working principle of the solar cells lies the photovaltaic effect. Photons incident on a semiconductor are absorbed if they have an energy larger than the band gap of the semiconductor. The absorbed photons can generate electron-hole pairs (electrons are excited from the valence band to the conduction band; a mobile electron and hole are generated) [47].

In the depletion layer of the pn-junction, generated minority carriers are separated from the majority carriers by drift under the influence of the present electric field. The increase in the concentration of minority carriers leads to the flow of minority carriers across the depletion region into the quasi-neutral regions. Electrons flow from the p-type into the n-type region and holes from the n-type into the p-type. The photo-generated minority carriers behave like the much smaller population of thermally generated minority carriers in the cell under dark conditions [47]. After charge separation, the electrons finds themselves in an n-type material, in which there are very few holes to recombine with. Electrons can be collected by the front electrode. Holes exit the device through the back contact electrode. Minority carriers created in the quasi neutral regions have to reach the depletion region by diffusion. Carriers generated in the depletion region and in the regions up to the minority carrier diffusion length from the depletion region contribute to the photo-generated current [2].

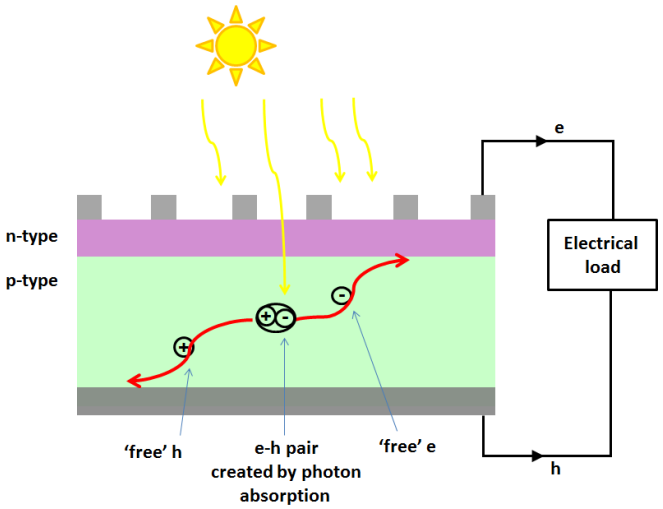

Figure A.104: The incident light is absorbed in the p-type absorber layer. Electron-hole pairs are generated and separated (adatpted from [47]).

For the calculation of the J-V curve under illumination, the photo-generation rate G is assumed to be uniform (this situation appears when the device is illuminated with long-wavelength light which is weakly absorbed). In case of moderate illumination, the concentration of majority carriers does not change significantly while the concentration of minority carriers strongly increases (figure A.105).

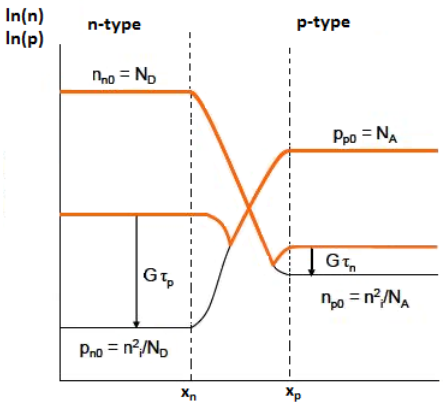

Figure A.105: Concentration profile of mobile charge carriers in an illuminated pn-junction [2].

The steady-state situation for minority carriers for the n-type side, when G is not zero can be

written as [2]

$$\frac{\partial^2 p}{\partial x^2} = -\frac{p - p_0}{L_p^2} - \frac{G}{D_p}$$

The solution for the concentration profile of holes in the quasi neutral region of the n-type semiconductor is described as [2]

$$p_n(x) - p_{n0} = G\tau_p + p_{n0}\left[\left(exp\left(\frac{qV}{kT}\right) - 1\right) - G\tau_p\right] exp\left(-\frac{x - x_n}{L_p}\right)$$

The corresponding current density is at the depletion edge (for p-type x = x_n)

$$J_p(x_n) = -qD_p \frac{\partial p_n}{\partial x}\Big|_{x_n} = \frac{qD_p p_{n0}}{L_p}\left[exp\left(\frac{qV}{kT}\right) - 1\right] - qGL_p$$

The contribution of photo-generated charge carriers to the current in the depletion region has to be taken into account. The effect of recombination in the depletion region is again neglected (R = 0). The contribution of optical generation from the depletion region to the current density is given by [2]

$$\partial J_n = |\partial J_p| = q\int_{x_n}^{-x_p} (R - G)dx = qGW$$

Because the total current density in the steady state is constant across the junction, the total current density can be determined as the sum of the electron and hole current densities at the edges of the depletion region [2, 47]

$$\begin{aligned} J &= J_n(-x_p) + J_p(-x_p) = J_n(-x_p) + J_n(x_n) \\ J &= \left(\frac{qD_p p_{n0}}{L_p} + \frac{qD_n n_{p0}}{L_n}\right)\left[exp\left(\frac{qV}{kT}\right) - 1\right] - qG(L_n + L_p + W) \\ J &= J_0\left[exp\left(\frac{qV}{kT}\right) - 1\right] - J_{ph} \\ \text{with } J_{ph} &= qG(L_n + L_p + W) \text{ the photo-current} \end{aligned} \tag{A.5}$$

From equation A.5 it is clear that carriers which contribute to the photo-generated current are generated in the depletion region and in the regions up to the minority carrier diffusion length from the depletion region [2]. Any minority carrier generated within a diffusion length of the depletion edge, can diffuse to the junction and be swept away. Minority electrons (holes) generated well beyond a length L_n (L_p) recombine with holes (electrons). Under illumination the dark current density of a pn-junction (equation A.3) is shifted downwards by the photo-generated current density J_{ph}. The flow of photo-generated carriers causes the photo-generation current. By convention this photo-current is negative since, if we forward-bias the diode, electrons move from front (n-type) to back (p-type) within the device. This current direction is opposite to the direction of the photo-current.

A.2 Schottky contact

A.2.1 Band alignment

When a metal is brought into contact with a semiconductor, a certain amount of band bending occurs. In this way the difference between the Fermi energies of the metal and that of the semiconductor is compensated. A flow from electrons in the material with higher Fermi energy

to the other material occurs. The charge redistribution gives rise to a local built-in electric field. Because the metal has a much higher charge density, the band bending (and depletion) is primarily present in the semiconductor. The amount of band bending and direction of electron transfer is dependent on: the semiconductor type, the work function of the metal (ϕ_M), the work function of the semiconductor (ϕ_{SC}) and also the electron affinity (χ_S) of the semiconductor [61,210]. Figure A.106 represents the alignment of the Fermi levels at equilibrium depending on the type of semiconductor and values of ϕ_M and ϕ_{MS}.

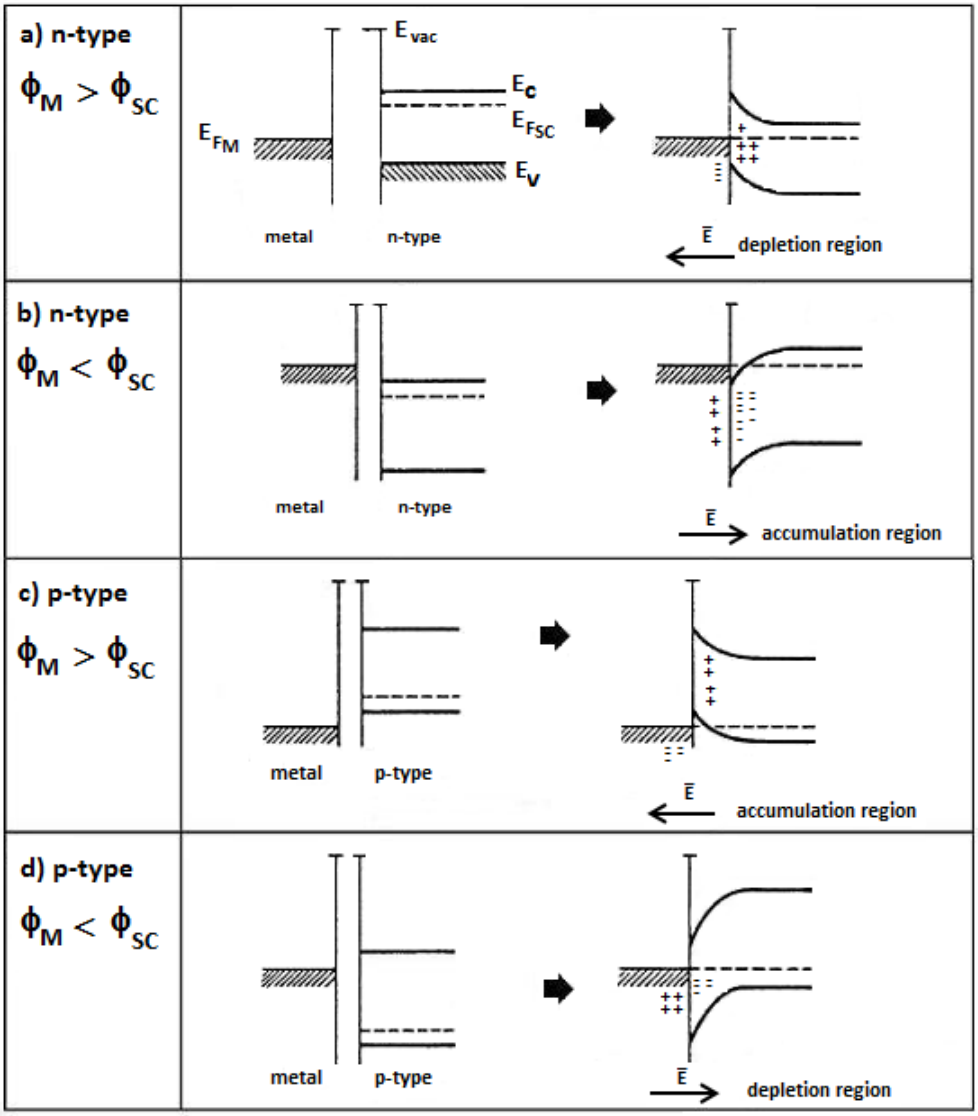

Figure A.106: Band diagram before and after metal semiconductor contact depending on type of semiconductor and work functions [210].

Depending on the semiconductor type and work function, a rectifying contact or Ohmic contact is formed [55].
If $\phi_M > \phi_{SC}$, the energy bands of the semiconductor actually shift downward with respect to those of the metal. Electrons are extracted form the semiconductor into the metal.

- In the case of an n-type semiconductor (figure A.106(a)) (electrons are the majority carriers) a depletion region is formed. The depletion region appears near the junction and a diode-like behaviour, similar to a pn-junction when an external bias is applied, is obtained. A Schottky contact is formed.

- If the semiconductor is p-type (figure A.106(c)), the electrons which are extracted from the semiconductor, are taken from the p-type dopants which then become ionized. This process thus creates more holes or majority charge carriers. In this case, there is no depletion region, but majority carriers are accumulated near the junction area and the diode-like behaviour is not observed. Majority carriers are free to flow in either direction under the influence of an external bias. In this case an Ohmic contact is formed.

On the other hand, if $\phi_M < \phi_{SC}$, the energy bands in the semiconductor shift upward with respect to those of the metal and the electrons are transferred from the metal into the semiconductor.

- For a n-type semiconductor (figure A.106(b)) electrons coming from the metal accumulate near the junction. An accumulation layer is formed and an Ohmic behaviour is observed.
- For a p-type semiconductor (figure A.106(d)) the junction is a Schottky contact because the p-type dopants are occupied with electrons. A depletion region and hence a Schottky contact is formed.

In the case of a rectifying contact, the existence of the depletion region includes that there is a potential barrier across the junction which can be shifted by an amount equal to -eV when an external voltage V is applied between the metal and the semiconductor [3].
It is important to note that for a Schottky contact the majority carriers are responsible for the current transport [55]

reverse: majority carriers from the metal overcome the barrier (low temperature dependence)

forward: injection from the semiconductor into the metal

In a pn-junction the minority carriers give rise to the current [2]

reverse: minority carriers diffuse into the depletion region (extraction, temperature dependent)

forward: minority injection from n- and p-sides

Bibliography

[1] NREL. Best research PV cell efficiencies. Technical report, NREL, 2014.

[2] M. Zeeman. *Syllabus Solar cells*. Delft University of Technology.

[3] S. M. Sze. *Physics of semiconductor devices*. Wiley-Interscience, 1969.

[4] S. R. Kodigala. *Thin films and nanostructures $Cu(In_{1-x}Ga_x)Se_2$ based thin film solar cells*. Academic Press, 2010.

[5] D. Abou-Ras, T. Kirchartz, and U. Rau. *Advanced characterization techniques for thin film solar cells*. Wiley, 2011.

[6] R. Scheer and H. W. Schock. *Chalcogenide photovoltaics: physics, technologies, and thin film devices*. Wiley, 2011.

[7] P. Blood and J. W. Orton. *The electrical characterization of semiconductors: majority carriers and electron states*. Academic Press, 1992.

[8] C. H. Henry and D. V. Lang. Nonradiative capture and recombination by multiphonon emission in GaAs and GaP. *Phys. Rev. B*, 15:989–1016, 1977.

[9] J. Riediger. *Impact of gallium on the defect landscape of sulfur-based chalcopyrite solar cells*. PhD thesis, University Oldenburg, 2013.

[10] J. Van Gheluwe. *Karakterisering van CdTe/CdS en $CuInS_2$ op Cu-tape dunnefilm zonnecellen met behulp van fotoluminescentiespectroscopie en deep level transient spectroscopy*. PhD thesis, Ghent University, 2007.

[11] F. H. Pianezzi. *Electronic transport and doping mechanisms in $Cu(In,Ga)Se_2$ thin film solar cells*. PhD thesis, University Zürich, 2014.

[12] K. Decock. *Defect related phenomena in chalcopyrite based solar cells*. PhD thesis, University Gent, 2012.

[13] V. Mertens. *Capacitance spectroscopy on copper indium diselenide based solar cells*. PhD thesis, University Oldenburg, 2005.

[14] J. Lauwaert, S. Khelifi, K. Decock, M. Burgelman, and H. Vrielinck. Signature of a back contact barrier in DLTS spectra. *J. Appl. Phys.*, 109(063721), 2011.

[15] T. Eisenbarth, T. Unold, R. Caballero, C. A. Kaufmann, and H. W. Schock. Interpretation of admittance, capacitance-voltage, and current-voltage signatures in $Cu(In,Ga)Se_2$ thin film solar cells. *J. Appl. Phys.*, 107(034509), 2010.

[16] S. Siebentritt and U. Rau. *Wide-gap chalcopyrites*. Springer, 2006.

[17] D. N. Hebert, J. A. Soares, and A. A. Rockett. Photoluminescence and photoluminescence excitation spectroscopy of $Cu(In,Ga)Se_2$ thin films. *Mater. Res. Soc. Symp. Proc.*, 1165:93–100, 2010.

[18] R. E. Hollingsworth and J. R. Sites. Annealing temperature effects on $CuInSe_2$/CdS solar cells. *Solar Cells*, 16:457–477, 1986.

[19] K. Hönes, E. Zscherper, J. Scragg, and S. Siebentritt. Shallow defects in Cu_2ZnSnS_4. *Physica B*, 404:4949–4952, 2009.

[20] P. K. Sarswat and M. L. Free. A study of energy band gap versus temperature for Cu_2ZnSnS_4 thin films. *Physica B*, 407:108–111, 2012.

[21] J. P. Leitão, N. M. Santos, P. A. Fernandes, P. M. P. Salomé, A. F. da Cunha, J. C. González, G. M. Ribeiro, and F. M. Matinaga. Photoluminescence and electrical study of fluctuating potentials in Cu_2ZnSnS_4-based thin films. *Phys. Rev. B*, 84(024120), 2011.

[22] M. J. Romero, H. Du, G. Teeter, Y. Yan, and M. M. Al-Jassim. Comparative study of the luminescence and intrinsic point defects in the kesterite Cu_2ZnSnS_4 and chalcopyrite $Cu(In,Ga)Se_2$ thin films used in photovoltaic applications. *Phys. Rev. B*, 84(165324), 2011.

[23] J. P. Leitão, N. M. Santos, P. A. Fernandes, P. M. P. Salomé, and A. F. da Cunha. Study of optical and structural properties of Cu_2ZnSnS_4 thin films. *Thin solid films*, 519:7390–7393, 2011.

[24] Y. Miyamoto, K. Tanaka, L. Oonuki, N. Moritake, and H. Uchiki. Optical properties of Cu_2ZnSnS_4 thin films prepared by sol-gel and sulfurization method. *Jpn. J. Appl. Phys.*, 47:596–597, 2013.

[25] M. M. Islam, T. Sakurai, S. Ishizuka, A. Yamada, H. Shibata, K. Sakurai, K. Matsubara, S. Niki, and K. Akimoto. Effect of Se/(Ga+In) ratio on MBE grown Cu(In,Ga)Se_2 thin film solar cell. *J. Cryst. Growth*, 311:2212–2214, 2009.

[26] Q. Cao, O. Gunawan, M. Copel, K. B. Reuter, S. J. Chey, V. R. Deline, and D. B. Mitzi. Defects in Cu(In,Ga)Se_2 chalcopyrite semiconductors: a comparative study of material properties, defect states and photovoltaic performance. *Adv. Energy Mater.*, 1:845–853, 2011.

[27] K. H. Kim, K. H. Yoon, J. H. Yun, and B. T. Ahn. Effects of Se flux on the microstructure of Cu(In,Ga)Se_2 thin film deposited by a three-stage co-evaporation process. *Electrochem. Solid-State Lett.*, 9:382–385, 2006.

[28] V. Deprédurand, T. Bertram, D. Regesch, B. Henx, and S. Siebentritt. The influence of Se pressure on the electronic proper ties of $CuInSe_2$ grown under Cu-excess. *Appl. Phys. Lett.*, 105(172104), 2014.

[29] A. Chirilă, P. Reinhard, F. Pianezzi, P. Patrick Bloesch, A. R. Uhl, C. Fella, L. Kranz, D. Keller, C. Gretener, H. Hagendorfer, D. Jaeger, R. Erni, S. Nishiwaki, S. Büecheler, and A. N. Tiwari. Potassium-induced surface modification of Cu(In,Ga)Se_2 thin films for high-efficiency solar cells. *Nature Mater.*, 12:1107–1111, 2013.

[30] P. Jackson, D. Hariskos, R. Wuerz, O. Kiowski, A. Bauer, T. M. Friedlmeier, and M. Powalla. Properties of Cu(In,Ga)Se_2 solar cells with new record efficiencies up to 21.7%. *Phys. Status Solidi RRL*, pages 1–4, 2014.

[31] M. A. Green, K. Emery, Y. Hishikawa, W. Warta, and E. D. Dunlop. Solar cell efficiency tables (version 44). *Prog. Photovolt: Res. Appl.*, 22:701–710, 2014.

[32] N. Amaroli and V. Balzani. *Energy for a sustainable world.* Wiley-VCH, 2011.

[33] D. J. C. MacKay. *Sustainable energy-without the hot air.* UIT Cambridge, 2009.

[34] C. Ngô and J. B. Natowitz. *Our energy future- resources, alternatives and the environment.* Wiley and sons, 2009.

[35] J. Poortmans and V. Arkhipov. *Thin film solar cells fabrication, characterization and applications.* Wiley and sons, 2006.

[36] W. N. Shafarman and L. Stolt. *Handbook of photovoltaic science and engineering.* Wiley, 2003.

[37] J. Nelson. *The physics of solar cells.* Imperial College Press, 2003.

[38] European Photovoltaic Industry Association. Global market outlook for photovoltaics 2014-2018. Technical report, 2014.

[39] K. Ito. *Copper zinc tin sulfide-based thin-film solar cells.* Wiley, 2014.

[40] G. Conibeer and A. Willoughby. *Solar cell materials, developing technologies.* Wiley, 2014.

[41] J. A. AbyShame. *Investigation of Cu-In-Ga-Se thin film growth dynamics for high efficiency solar cells.* PhD thesis, Colorado school of Mines, 2003.

[42] Avancis. Avancis achieves new certification record for thin-film module NREL certified efficiency of CIS module with 16.6%. *http://www.avancis.de/en/press/press-releases*, 2014.

[43] M. Jiang and X. Yan. *Solar cells - research and application perspectives, Chapter 5.* Intech, 2013.

[44] C. Wadia, A. P. Alivisatos, and D. M. Kammen. Materials availability expands the opportunity for large-scale photovoltaics deployment. *Environ. Sci. Technol.*, 43:2072–2077, 2009.

[45] T. Kato, H. Hiroi, N. Sakai, S. Muraoka, and H. Sugimoto. Characterization of front and back interfaces on Cu_2ZnSnS_4 thin-film solar cells. *Proc. 27th European Photovoltaic Solar Energy Conference and Exhibition, Frankfurt, Germany*, pages 2236–2239, 2012.

[46] P. Reinhard, A. Chirilă, P. Blösch, F. Pianezzi, S. Nishiwaki, S. Büecheler, and A. N. Tiwari. Review of progress toward 20% efficiency flexible CIGS solar cells and manufacturing issues of solar modules. *J. Photovolt.*, 3:572–580, 2013.

[47] M. D. Archer and R. Hill. *Clean electricity from photovoltaics.* Imperial College Press, 2001.

[48] M. Nichterwitz. *Charge carrier transport in Cu(In,Ga)Se_2 thin-film solar-cells studied by electron beam induced current and temperature and illumination dependent current voltage analyses.* PhD thesis, University Berlin, 2012.

[49] S. F. Büecheler. *Investigation of compound semiconductors as buffer-layer in thin film solar cells.* PhD thesis, University Zürich, 2010.

[50] M. Marinkovic. *Contact resistance effects in thin film solar cells and thin film transistors.* PhD thesis, University Bremen, 2013.

[51] H. Flammersberger. *Experimental study of Cu_2ZnSnS_4 thin films for solar cells.* PhD thesis, University Uppsala, 2010.

[52] D. K. Schroder. *Semiconductor material and device characterization.* Wiley, 2006.

[53] C. Platzer-Björkman. *Band alignment between ZnO-based and Cu(In,Ga)Se_2 thin films for high efficiency solar cells.* PhD thesis, University Uppsala, 2006.

[54] P. Pistor. *Formation and electronic properties of In_2S_3/Cu(In,Ga)Se_2 junctions and related thin film solar cells.* PhD thesis, University Berlin, 2009.

[55] M. Razeghi. *Fundamentals of solid state engineering.* Springer, 2006.

[56] U. Malm, J. Malmström, C. Platzer-Björkman, and L. Stolt. Determination of dominant recombination paths in Cu(In,Ga)Se_2 thin-film solar cells with ALD-ZnO buffer layers. *Thin Solid Films*, 480:208–212, 2005.

[57] B. Morel, D. Mencaraglia, J. P. Connolly, A. Darga, V. Gorge, and Z. Djebbour. Investigation of recombination processes in CIGS based solar cells with submicrometer absorber layers. *Conf. Proc. EUPVSEC, Valencia, Spain*, pages 3432–3435, 2010.

[58] H. Bayhan and A. Sertap Kavasuğlu. Tunnelling enhanced recombination in polycrystalline CdS/CdTe and CdS/Cu(In,Ga)Se_2 heterojunction solar cells. *Solid-State Electron.*, 49:991–996, 2005.

[59] H. Bayhan and M. Bayhan. An analysis of the effect of illumination to the reverse and forward bias current transport mechanisms in an efficient n-ZnO/n-CdS/p-Cu(In,Ga)Se_2 solar cell. *Solar energy*, 87:168–175, 2013.

[60] U. Rau, A. Jasenek, H. W. Schock, F. Engelhardt, and Th. Meyer. Electronic loss mechanisms in chalcopyrite based heterojunction solar cells. *Thin Solid Films*, 361:298–302, 2000.

[61] S. S. Li. *Semiconductor physical electronics.* Springer, 2006.

[62] S. Khelifi. *Characterization and modelling with Scaps of the performance of solar cells.* PhD thesis, University Gent, 2010.

[63] K. Klenk. Characterisation and modelling of chalcopyrite solar cells. *Thin Solid Films*, 387:135–140, 2001.

[64] M. C. Turcu. *Defect energies, band alignments, and charge carrier recombination in polycrystalline Cu(In,Ga)$(Se,S)_2$ alloys.* PhD thesis, Technical University Dresden, 2004.

[65] D. Rudmann. *Effects of sodium on growth and properties of Cu(In,Ga)Se_2 thin films and solar cells.* PhD thesis, Swiss federal institute of technology Zürich, 2004.

[66] S. Siebentritt. Why are kesterite solar cells not 20% efficient? *Thin Solid Films*, 535:1–4, 2013.

[67] M. A. Contreras, M. J. Romero, B. To, F. Hasoon, R. Noufi, S. Ward, and K. Ramanathan. Optimization of CBD CdS process in high-efficiency Cu(In,Ga)Se_2-based solar cells. *Thin Solid Films*, 403:204–211, 2002.

[68] L. M. Peter. Towards sustainable photovoltaics: the search for new materials. *Phil. Trans. R. Soc. A*, 369:1840–1856, 2011.

[69] J. Malmström. *On the generation and recombination of Cu(In,Ga)Se_2 thin-film solar cells.* PhD thesis, University Uppsala, 2005.

[70] A. Seyhan. *Photoluminescence spectroscopy of CdS and GaSe.* PhD thesis, Middle East technical university, 2003.

[71] M. Grundmann. *The physics of semiconductors; an introduction including devices and nanophysics.* Springer, 2006.

[72] H. W. Schock and U. Rau. The role of structural properties and defects for the performance of Cu-chalcopyrite-based thin-film solar cells. *Physica B*, 308:1081–1085, 2001.

[73] A. Chirilă, S. Büecheler, F. Pianezzi, and A. N. Tiwari. Highly efficient Cu(In,Ga)Se_2 solar cells grown on flexible polymer films. *Nat. Mater.*, 10:857–861, 2011.

[74] J. J. Scragg, J. T. Wätjen, M. Edoff, T. Ericson, T. Kubart, and C. Platzer-Björkman. A detrimental reaction at the molybdenum back contact in $Cu_2ZnSn(S,Se)_4$ thin-film solar cells. *J. Am. Chem. Soc.*, 134:19330–19333, 2012.

[75] H. Zachmann, S. Puttnins, M. V. Yakushev, F. Luckert, R. W. Martin, A. V. Karotki, V. F. Gremenok, and A. V. Mudryi. Fabrication and characterisation of Cu(In,Ga)Se_2 solar cells on polyimide. *Thin Solid Films*, 519:7264–7267, 2011.

[76] U. Malm. *Modelling and degradation characteristics of thin-film CIGS solar cells.* PhD thesis, University Uppsala, 2008.

[77] U. Rau. Role of defects and defect metastabilities for the performance and stability of Cu(In,Ga)Se_2 based solar cells. *Jpn. J. Appl. Phys.*, 39:389–394, 2000.

[78] S. Minoura, K. Kodera, T. Maekawa, K. Miyazaki, S. Niki, and H. Fujiwara. Dielectric function of Cu(In,Ga)Se_2-based polycrystalline materials. *J. Appl. Phys.*, 113(063505), 2013.

[79] S. Han, A. M. Hermann, F. S. Hasoon, A. Al-Thani, and D. H. Levi. Effect of Cu deficiency on the optical properties and electronic structure of $CuInSe_2$ and $CuIn_{0.8}Ga_{0.2}Se_2$ determined by spectroscopic ellipsometry. *Appl. Phys. Lett.*, 85:576–578, 2004.

[80] M. Turcu and U. Rau. Fermi level pinning at CdS/Cu(In,Ga)(S,Se)$_2$ interfaces: effect of chalcopyrite alloy composition. *J. Phys. Chem. Solids*, 64:1591–1595, 2003.

[81] J. Bekaert, R. Saniz, B. Partoens, and D. Lamoen. Native point defects in $CuIn_{1-x}Ga_xSe_2$: hybrid density functional calculations predict the origin of p- and n-type conductivity. *Phys. Chem. Chem. Phys.*, 16:22299–22308, 2014.

[82] M. Powalla, P. Jackson, W. Witte, D. Hariskos, S. Paetel, C. Tschamber, and W. Wischmann. High-efficiency Cu(In,Ga)Se_2 cells and modules. *Sol. Energy Mater. Sol. Cells*, 119:51–58, 2013.

[83] S. Seyrling, A. Chirilă, D. Güttler, F. Pianezzi, P. Rossbach, and A. N. Tiwari. Modification of the three-stage evaporation process for $CuIn_{1-x}Ga_xSe_2$ absorber deposition. *Thin Solid Films*, 519:7232–7236, 2011.

[84] S. A. Schumacher and J. R. Botha. Photoluminescence study of potential fluctuations in thin layers of $Cu(In_{0.75}Ga_{0.25})(S_ySe_{1-y})_2$. *J. Appl. Phys.*, 99(063508), 2006.

[85] K. Yoshino, T. Shimizu, A. Fukuyama, K. Maeda, P. J. Fons, A. Yamada, S. Niki, and T. Ikari. Temperature dependence of photoacoustic spectra in $CuInSe_2$ thin films grown by molecular beam epitaxy. *Sol. Energy Mater. Sol. Cells*, 50:127–132, 1998.

[86] S. Chichibu, T. Mizutani, K. Murakami, T. Shioda, T. Kurafuji, H. Nakanishi, S. Niki, P. J. Fons, and A. Yamada. Band gap energies of bulk, thin-film, and epitaxial layers of $CuInSe_2$ and $CuGaSe_2$. *J. Appl. Phys.*, 83:3678–3689, 1998.

[87] N. H. Quang. *The role of the heterointerfaces in the Cu(In,Ga)Se_2 thin film solar cell with chemical bath deposited buffer layers.* PhD thesis, University Stuttgart, 2004.

[88] U. Rau, D. Braunger, R. Herberholz, and H. W. Schock. Oxygenation and air-annealing effects on the electronic properties of Cu(In,Ga)Se_2 films and devices. *J. Appl. Phys.*, 86(1):497–505, 1999.

[89] D. Schmid, M. Ruckh, F. Grunwald, and H. W. Schock. Chalcopyrite/defect chalcopyrite heterojunctions on the basis of $CuInSe_2$. *J. Appl. Phys.*, 73:2902–2909, 1993.

[90] D. Schmid, M. Ruckh, F. Grunwald, and H. W. Schock. Chalcopyrite/defect chalcopyrite heterojunctions on the basis of $CuInSe_2$. *J. Appl. Phys.*, 73:2902–2909, 1993.

[91] S. B. Zhang, S. Wei, and A. Zunger. Defect physics of the $CuInSe_2$ chalcopyrite semiconductor. *Phys. Rev. B*, 57:9642–9657, 1998.

[92] D. Cahen and R. Noufi. Surface passivation of polycrystalline, chalcogenide based photovoltaic cells. *Solar Cells*, 30:53–59, 1991.

[93] R. Herberholz, U. Rau, H. W. Schock, T. Haalboom, T. Gödecke, F. Ernst, C. Beilharz, K. W. Benz, and D. Cahen. Phase segregation, Cu migration and junction formation in Cu(In,Ga)Se_2. *Eur. Phys. J.*, 6:131–139, 1999.

[94] C. S. Jiang, F. S. Hasoon, H. R. Moutinho, H. A. Al-Thani, M. J. Romero, and M. M. Al-Jassim. Direct evidence of a buried homojunction in Cu(In,Ga)Se_2 solar cells. *Appl. Phys. Lett.*, 82:127–129, 2003.

[95] A. Rockett, D. Liao, J. T. Heath, J. D. Cohen, Y. M. Strzhemechny, L. J. Brillson, K. Ramananthan, and W. N. Shafarman. Near-surface defect distributions in Cu(In,Ga)Se_2. *Thin solid films*, 431:301–306, 2003.

[96] T. Nakada and A. Kunioka. Direct evidence of Cd diffusion into Cu(In,Ga)Se_2 thin films during chemical-bath deposition process of CdS films. *Appl. Phys. Lett.*, 74:2444–2446, 1999.

[97] O. Cojocaru-Mirédin, O. Choi, R. Wuerz, and D. Raabe. Exploring the p-n junction region in Cu(In,Ga)Se_2 thin-film solar cells at the nanometer-scale. *Appl. Phys. Lett.*, 101(181603), 2012.

[98] K. Ramanathan, R. Noufi, J. Granata, J. Webb, and J. Keane. Prospects for in situ junction formation in $CuInSe_2$ based solar cells. *Sol. Energy Mater. Sol. Cells*, 55:15–22, 1998.

[99] M. Turcu, O. Pakma, and U. Rau. Interdependence of absorber composition and recombination mechanism in Cu(In,Ga)S_2 heterojunction solar cells. *Appl. Phys. Lett.*, 80:2598–2600, 2002.

[100] V. Nadenau, U. Rau, A. Jasenek, and H. W. Schock. Electronic properties of $CuGaSe_2$-based heterojunction solar cells. part I. transport analysis. *J. Appl. Phys.*, 87:584–593, 2000.

[101] U. Rau. Tunneling-enhanced recombination in Cu(In,Ga)Se_2 heterojunction solar cells. *Appl. Phys. Lett.*, 74:111–113, 1999.

[102] S. Siebentritt, L. Gütay, D. Regesch, Y. Aida, and V. Deprédurand. Why do we make Cu(In,Ga)Se_2 solar cells non-stoichiometric? *Sol. Energy Mater. Sol. Cells*, 119:18–25, 2013.

[103] D. F. Marrón. *Structural and electronic characterisation of thin film solar cells based on CVD grown $CuGaSe_2$*. PhD thesis, University Berlin, 2003.

[104] S. Merdes, R. Sáez-Araoz, A. Ennaoui, J. Klaer, M. Ch. Lux-Steiner, and R. Klenk. Recombination mechanisms in highly efficient thin film Zn(S,O)/Cu(n,Ga)S_2 based solar cells. *Appl. Phys. Lett.*, 95(213502), 2009.

[105] I. Hengel, A. Neisser, R. Klenk, and M. Ch. Lux-Steiner. Current transport in $CuInS_2$:Ga/Cds/ZnO -solar cells. *Thin solid films*, 361:458–462, 2000.

[106] H. Bayhan. Study of CdS/Cu(In,Ga)Se_2 interface by using n values extracted analytically from experimental data. *Solar energy*, 83:372–376, 2009.

[107] M. Rusu, W. Eisele, R. Würz, A. Ennaoui, M. Ch. Lux-Steiner, T. P. Niesen, and F. Karg. Current transport in ZnO/ZnS/Cu(In,Ga)(S,Se)$_2$ solar cell. *J. Phys. Chem. Solids*, 64:2037–2040, 2003.

[108] D. Rudmann, A. F. da Cunha, M. Kaelin, F. Kurdesau, H. Zogg, A. N. Tiwari, and G. Bilger. Efficiency enhancement of $CuInGaSe_2$ solar cells due to post-deposition Na incorporation. *Appl. Phys. Lett.*, 84:1129–1131, 2004.

[109] S. H. Wei, S. B. Zhang, and A. Zunger. Effects of Ga addition to $CuInSe_2$ on its electronic, structural, and defect properties. *Appl. Phys. Lett.*, 72:3199–3201, 1998.

[110] M. Igalson, A. Urbaniak, and M. Edoff. Reinterpretation of defect levels derived from capacitance spectroscopy of CIGSe solar cells. *Thin Solid Films*, 517(2153), 2009.

[111] S. Lany and A. Zunger. Light- and bias-induced metastabilities in Cu(n,Ga)Se_2 based solar cells caused by the (V_{Se}-V_{Cu}) vacancy complex. *J. Appl. Phys.*, 100(113725), 2006.

[112] S. Lany and A. Zunger. Intrinsic DX centers in ternary chalcopyrite semiconductors. *Phys. Rev. Lett.*, 100(016401), 2008.

[113] M. Igalson, P. Zabierowski, D. Przado, A. Urbaniak, M. Edoff, and W. N. Shafarman. Understanding defect-related issues limiting efficiency of CIGS solar cells. *Sol. Energy Mater. Sol. Cells*, 93:1290–1295, 2009.

[114] L. E. Oikkonen, M. G. Ganchenkova, A. P. Seitsonen, and R. M. Nieminen. Redirecting focus in $CuInSe_2$ research towards selenium-related defects. *Phys. Rev. B*, 86(165115), 2012.

[115] L. Oikkonen. *Atomic-scale defects in solar cell material $CuInSe_2$ from hybridfunctional calculations*. PhD thesis, Aalto University, Helsinki, 2013.

[116] J. Pohl and K. Albe. Intrinsic point defects in $CuInSe_2$ and $CuGaSe_2$ as seen via screened-exchange hybrid density functional theory. *Phys. Rev. B*, 87(245203), 2013.

[117] J. Pohl. *Structure and properties of defects in photovoltaic absorber materials: atomic scale computer simulations of Si and Cu(In,Ga)Se_2*. PhD thesis, Technical University Darmstadt, 2013.

[118] L. E. Oikkonen, M. G. Ganchenkova, A. P. Seitsonen, and R. M. Nieminen. Vacancies in $CuInSe_2$: new insights from hybrid-functional calculations. *J. Phys.: Condens. Matter*, 23(422202), 2011.

[119] S. M. Wasim. Transport properties of $CuInSe_2$. *Solar Cells*, 16:289–316, 1986.

[120] A. Bauknecht, S. Siebentritt, A. Gerhard, W. Harneit, S. Brehme, J. Albert, S. Rushworth, and M. Ch. Lux-Steiner. Defects in $CuGaSe_2$ thin films grown by MOCVD. *Thin Solid Films*, 361:2000, 426-431.

[121] A. Laemmle, R. Wuerz, and M. Powalla. Efficiency enhancement of Cu(In,Ga)Se_2 thin-film solar cells by a post-deposition treatment with potassium fluoride. *Phys. Status Solidi*, 7:631–634, 2013.

[122] A. Laemmle, R. Wuerz, T. Schwarz, O. Cojocaru-Mirédin, P. Choi, and M. Powalla. Investigation of the diffusion behavior of sodium in Cu(In,Ga)Se_2 layers. *J. Appl. Phys.*, 115(154501), 2014.

[123] Rockett. A. The effect of Na in polycrystalline and epitaxial single-crystal $CuIn_{1-x}Ga_xSe_2$. *Thin Solid Films*, 480:2–7, 2005.

[124] S. Ishizuka, A. Yamada, M. M. Islam, H. Shibata, P. Fons, T. Sakurai, K. Akimoto, and S. Niki. Na-induced variations in the structural, optical, and electrical properties of Cu(In, Ga)Se_2 thin films. *J. Appl. Phys.*, 106(034908), 2009.

[125] D. Rudmann, D. Brémaud, A. F. da Cunha, G. Bilger, A. Strohm, M. Kaelin, H. Zogg, and A. N. Tiwari. Sodium incorporation strategies for CIGS growth at different temperatures. *Thin Solid Films*, 480:55–60, 2005.

[126] D. Rudmann, D. Brémaud, A. Zogg, and A. N. Tiwari. Na incorporation into $CuInGaSe_2$ for high-efficiency flexible solar cells on polymer foils. *J. Appl. Phys.*, 97(084903), 2005.

[127] P. Reinhard, F. Pianezzi, B. Bissig, A. Chirilă, P. Blösch, S. Nishiwaki, S. Büecheler, and A. N. Tiwari. Cu(In,Ga)Se_2 thin-film solar cells and modules-A boost in efficiency due to potassium. *J. Photovolt.*, 2014.

[128] P. Choi, O. Cojocaru-Mirédin, R. Wuerz, and D. Raabe. Comparative atom probe study of Cu(In,Ga)Se_2 thin-film solar cells deposited on sodalime glass and mild steel substrates. *J. Appl. Phys.*, 110(124513), 2011.

[129] S. Wei, S. B. Zhang, and A. Zunger. Effects of Na on the electrical and structural properties of $CuInSe_2$. *J. Appl. Phys.*, 85:7214–7218, 1999.

[130] L. Kronik, D. Cahen, and H. W. Schock. Effects of sodium on polycrystalline $Cu(In,Ga)Se_2$ and its solar cell performance. *Adv. Mater.*, 10:31–36, 1998.

[131] R. Bacewicz, P. Zuk, and R. Trykozko. Photoluminescence study of $ZnO/CdS/Cu(In,Ga)Se_2$ solar cells. *Opto Electron. Rev.*, 11:277–280, 2003.

[132] I. Dirnstorfer, D. M. Hofmann, D. Meister, B. K. Meyer, W. Riedl, and F. Karg. Postgrowth thermal treatment of $CuIn(Ga)Se_2$: Characterization of doping levels of In-rich thin films. *J. Appl. Phys.*, 85:1423–1428, 1999.

[133] D. Abou-Ras, S. S. Schmidt, R. Caballero, T. Unold, H. W. Schock, C. T. Koch, B. Schaffer, M. Schaffer, P. Choi, and O. Cojocaru-Mirédin. Confined and chemically flexible grain boundaries in polycrystalline compound semiconductors. *Adv. Energy Mater.*, 2:992–998, 2012.

[134] L. M. Mansfield, R. Noufi, C. P. Muzzillo, C. DeHart, K. Bowers, B. To, J. W. Pankow, R. C. Reedy, and K. Ramanathan. Enhanced performance in $Cu(In,Ga)Se_2$ solar cells fabricated by the two-step selenization process with a potassium fluoride post deposition treatment. *J. Photovolt.*, 4:1650–1654, 2014.

[135] P. Pistor, D. Greiner, C. A. Kaufmann, S. Brunken, M. Gorgoi, A. Steigert, W. Calvet, I. Lauermann, R. Klenk, T. Unold, and M. C. Lux-Steiner. Experimental indication for band gap widening of chalcopyrite solar cell absorbers after potassium fluoride treatment. *Appl. Phys. Lett.*, 105(063901), 2014.

[136] R. Wuerz, A. Eicke, F. Kessler, S. Paetel, S. Efimenko, and C. Schlegel. CIGS thin-film solar cells and modules on enamelled steel substrates. *Sol. Energy Mater. Sol. Cells*, 100:132–137, 2012.

[137] M. A. Contreras, B. Egaas, P. Dippo, J. Webb, J. Granata, K. Ramanathan, S. Asher, A. Swartzlander, and R. Noufi. On the role of Na and modifications to $Cu(In,Ga)Se_2$ absorber materials using thin-MF (M = Na, K, Cs) precursor layers. *26th IEEE Photovoltaic Specialists Conference, California*, pages 359–362, 1997.

[138] H. Xiao and W. A. Goddard. Predicted roles of defects on band offsets and energetics at CIGS ($Cu(In,Ga)Se_2/CdS$) solar cell interfaces and implications for improving performance. *J. Chem. Phys.*, 141(094701), 2014.

[139] M. Yuan, D. B. Mitzi, W. Liu, A. J. Kellock, S. J. Chey, and V. R. Deline. Optimization of CIGS-based PV device through antimony doping. *Chem. Mater.*, 22:285–287, 2009.

[140] M. Yuan, D. B. Mitzi, O. Gunawan, A. J. Kellock, S. J. Chey, and V. R. Deline. Antimony assisted low temperature processing of $CuIn_{1-x}Ga_xSe_{2-y}S_y$ solar cells. *Thin Solid Films*, 519:852–856, 2010.

[141] T. Nakada, Y. Honishi, Yatsushiron Y., and H. Nakakoba. Impacts on Sb and Bi incorporations on CIGS thin films and solar cells. *37th IEEE Photovoltaic Specialists Conference*, pages 3527–3531, 2011.

[142] B. Tseng, G. Chang, and G. Gu. Surfactant modified growth of $CuInSe_2$ thin films. *Appl. Surf. Sci.*, 92:227–231, 1996.

[143] S. Zhang, L. Wu, R. Yue, Z. Yan, H. Zhan, and Y. Xiang. Effects of Sb-doping on the grain growth of $Cu(In,Ga)Se_2$ thin films fabricated by means of single-target sputtering. *Thin solid films*, 527:137–140, 2013.

[144] M. Ben Rabeh, N. Chaglabou, and M. Kanzari. Effect of antimony incorporation on structural properties of $CuInS_2$ crystals. *Nucl. Instr. Meth. Phys. Res. B*, 268:273–276, 2010.

[145] S. Nishiwaki, F. Pianezzi, C. M. Fella, L. Kranz, S. Büecheler, and A. N. Tiwari. Reduction of CIGS deposition temperature by addition of an Sb precursor. *Conf. Proc. EUPVSEC, Frankfurt, Germany*, 2012.

[146] M. Ben Rabeh, N. Chaglabou, and M. Kanzari. Structural, optical and electrical properties of annealed Sb-doped $CuInS_2$ thin films grown by thermal evaporation method. *Chalcogenide Lett.*, 6:83–89, 2009.

[147] H. Komaki, K. Yoshino, Y. Akaki, M. Yoneta, and T. Ikari. Characterization of Sb-doped $CuInS_2$ crystals. *Phys. Stat. Sol. C*, 0:759–762, 2003.

[148] S. M. Schleussner, T. Törndahl, M. Linnarsson, U. Zimmermann, T. Wätjen, and M. Edoff. Development of gallium gradients in three - stage $Cu(In,Ga)Se_2$ co-evaporation processes. *Prog. Photovolt: Res. Appl.*, 20:284–293, 2012.

[149] L. C. Rasmussen. *Evaluation of Cu_2ZnSnS_4 absorber films sputtered from a single, quaternary target.* PhD thesis, University Uppsala, 2013.

[150] S. Siebentritt and S. Schorr. Kesterites-a challenging material for solar cell. *Prog. Photovoltaics*, 20:512–519, 2012.

[151] J. J. Scragg. *Copper zinc tin sulfide thin films for photovoltaics.* Springer Berlin Heidelberg, 2011.

[152] J. J. Scragg, L. Choubrac, A. Lafond, T. Ericson, and C. Platzer-Björkman. A low-temperature order-disorder transition in Cu_2ZnSnS_4 thin films. *Appl. Phys. Lett.*, 104(041911), 2014.

[153] S. Schorr. The crystal structure of kesterite type compounds: a neutron and X-ray diffraction study. *Sol. Energy Mater. Sol. Cells*, 95:1482–1488, 2011.

[154] S. Chen, J. Yang, X. G. Gong, A. Walsh, and Wei. S. Intrinsic point defects and complexes in the quaternary kesterite semiconductor Cu_2ZnSnS_4. *Phys. Rev. B*, 81(245204), 2010.

[155] A. Nagoya and R. Asahi. Defect formation and phase stability of Cu_2ZnSnS_4 photovoltaic material. *Phys. Rev. B*, 81(113202), 2010.

[156] C. Persson. Electronic and optical properties of Cu_2ZnSnS_4 and $Cu_2ZnSnSe_4$. *J. Appl. Phys.*, 107(053710), 2010.

[157] M. I. Amal and K. H. Kim. Crystallization of kesterite Cu_2ZnSnS_4 prepared by the sulfurization of sputtered Cu-Zn-Sn precursors. *Thin solid films*, 534:144–148, 2013.

[158] R. B. V. Chalapathy, G. Sun Jung, and B. Tae Ahn. Fabrication of Cu_2ZnSnS_4films by sulfurization of Cu/ZnSn/Cu precursor layers in sulfur atmosphere for solar cells. *Sol. Energy Mater. Sol. Cells*, 95:3216–3221, 2011.

[159] S. Ahn, S. Jung, J. Gwak, A. Cho, K. Shin, K. Yoon, D. Park, H. Cheong, and J. Ho Yun. Determination of band gap energy (E_g) of $Cu_2ZnSnSe_4$ thin films: On the discrepancies of reported band gap values. *Appl. Phys. Lett.*, 97(021905), 2010.

[160] P. A. Fernandes, P. M. P. Salomé, and A. F. da Cunha. Study of ternary Cu_2SnS_3 and Cu_3SnS_4 thin films prepared by sulfurizing stacked metal precursors. *J. Phys. D: Appl. Phys.*, 43(215403), 2010.

[161] P. A. Fernandes, M. P. Salomé, and A. F. da Cunha. Cu_xSnS_{x+1} (x = 2, 3) thin films grown by sulfurization of metallic precursors deposited by dc magnetron sputtering. *Phys. Status Solidi C*, 7:901–904, 2010.

[162] C. Platzer-Björkman, J. Scragg, H. Flammersberger, T. Kubart, and M. Edoff. Influence of precursor sulfur content on film formation and compositional changes in Cu_2ZnSnS_4 films and solar cells. *Sol. Energy Mater. Sol. Cells*, 98:110–117, 2012.

[163] C. Cifuentes, M. Botero, E. Romero, C. Calder, and G. Gordillo. Optical and structural studies on SnS films grown by co-evaporation. *Braz. J. Phys.*, 36:1046–1049, 2006.

[164] T. H. Sajeesh, N. Poornima, C. Sudha Kartha, and K. P. Vijayakumar. Unveiling the defect levels in SnS thin films for photovoltaic applications using photoluminescence technique. *Phys. Status Solidi A*, 207:193–139, 2010.

[165] E. Guneri, F. Gode, C. Ulutas, F. Kirmizigul, C. Altindemir, and C. Gumus. Properities of p-type SnS thin films prepared by chemical bath depostion. *Chalcogenide Lett.*, 7:685–694, 2010.

[166] R. S. Sundaram, M. Engel, A. Lombardo, R. Krupke, A. C. Ferrari, Ph. Avouris, and M. Steiner. Electroluminescence in single layer MoS_2. *Nano Lett.*, 13:1416–1421, 2013.

[167] S. Chen, X. G. Gong, A. Walsh, and S. Wei. Crystal and electronic band structure of Cu_2ZnSnS_4 (X = S and Se) photovoltaic absorbers: first-principles insights. *Appl. Phys. Lett.*, 94(041903), 2009.

[168] O. Gunawan, T. Gokmen, C. W. Warren, J. D. Cohen, T. K. Todorov, D. A. R. Barkhouse, S. Bag, J. Tang, B. Shin, and D. B. Mitzi. Electronic properties of the $Cu_2ZnSn(Se,S)_4$ absorber layer in solar cells as revealed by admittance spectroscopy and related methods. *Appl. Phys. Lett.*, 100(253905), 2012.

[169] A. Nagaoka, K. Yoshino, H. Taniguchi, T. Taniyama, and H. Miyake. Preparation of Cu_2ZnSnS_4 single crystals from Sn solutions. *J. Cryst. Growth*, 341:38–41, 2012.

[170] J. M Raulot, C. Domain, and J. F. Guillemoles. Ab initio investigation of potential indium and gallium free chalcopyrite compounds for photovoltaic application. *J. Phys. Chem. Solids*, 66:2019–2023, 2005.

[171] D. Han, Y. Y. Sun, J. Bang, Y. Y. Zhang, H. Sun, X. Li, and S. B. Zhang. Deep electron traps and origin of p-type conductivity in the earth-abundant solar-cell material Cu_2ZnSnS_4. *Phys. Rev. B*, 87(155206), 2013.

[172] K. R. Choudhury, Y. Cao, J. V. Caspar, W. E. Farneth, Q. J. Guo, A. S. Lonkin, L. K. Johnson, M. J. Lu, I. Malajovich, D. Radu, H. D. Rosenfeld, and W. Wu. Characterization and understanding of performance losses in a highly efficient solution-processed CZTSSe thin-film solar cell. *38th IEEE Photovoltaic Specialists Conference (IEEE, New York, 2012)*, pages 1471–1474, 2012.

[173] E. Kask, M. Grossberg, R. Josepson, P. Salu, K. Timmo, and J. Krustok. Defect studies in $Cu_2ZnSnSe_4$ and $Cu_2ZnSn(Se_{0.75}S_{0.25})_4$ by admittance and photoluminescence spectroscopy. *Mater. Sci. Semicond. Process.*, 16:992–996, 2013.

[174] P. A. Fernandes, A. F. Sartori, P. M. P. Salomé, J. Malaquias, A. F. da Cunha, M. P. F. Graca, and J. C. Gonzalez. Admittance spectroscopy of Cu_2ZnSnS_4 based thin film solar cells. *Appl. Phys. Lett.*, 100(233504), 2012.

[175] T. P. Weiss, A. Redinger, J. Luckas, M. Mousel, and S. Siebentritt. Admittance spectroscopy in kesterite solar cells: Defect signal or circuit response. *Appl. Phys. Lett.*, 102(202105), 2013.

[176] K. Tanaka, Y. Miyamoto, H. Uchiki, K. Nakazawa, and H. Araki. Donor-acceptor pair recombination luminescence from Cu_2ZnSnS_4 bulk single crystals. *Phys. Stat. Sol.*, 203:2891–2896, 2006.

[177] H. Yoo, J. Kim, and L. Zhang. Sulfurization temperature effects on the growth of Cu_2ZnSnS_4 thin film. *Curr. Appl Phys.*, 12:1052–1057, 2012.

[178] M. A. M. Khan, S. Kumar, M. Alhoshan, and A. S. Al Dwayyan. Spray pyrolysed Cu_2ZnSnS_4 absorbing layer: A potential candidate for photovoltaic applications. *Opt. Laser Technol.*, 49:196–201, 2013.

[179] M. Grossberg, J. Krustok, J. Raudoja, and T. Raadik. The role of structural properties on deep defect states in Cu_2ZnSnS_4 studied by photoluminescence spectroscopy. *Appl. Phys. Lett.*, 101(102102), 2012.

[180] P.W. Yu. Excitation-dependent emission in Mg-, Be-, Cd-, and Zn-implanted GaAs. *J. Appl. Phys*, 48:5043–51, 1977.

[181] V. V. Osipov, T. I. Soboleva, and M. G. Foigel. Impurity radiative recombination in heavily doped semiconductors. *Sov. Phys. Semicond.*, 11:752–758, 1977.

[182] K. Oishi, G. Saito, K. Ebina, M. Nagahashi, K. Jimbo, W. Shwe Maw, H. Katagiri, M. Yamazaki, H. Araki, and A. Takeuchi. Growth of Cu_2ZnSnS_4 thin films on Si (100) substrates by multisource evaporation. *Thin Solid Films*, 517:1449–1452, 2008.

[183] C. Kapteyn. *Carrier emission and electronic properties of self-organized semiconductor quantum dots.* PhD thesis, University Berlin, 2001.

[184] V. T. R. Kuoppa. *Electrical characterization of nitrogen containing III-V semiconductors.* PhD thesis, University Helsinki, 2007.

[185] A. F. Halverson. *The role of sulfur alloying in defects and transitions in copper indium gallium diselenide disulfide thin films.* PhD thesis, University Oregon, 2007.

[186] R. Jayakrishan. *Defect analysis of semiconductor thin films for photovoltaic applications using photo-luminescence and photoconductivity.* PhD thesis, Cohin university of science and technology, 2008.

[187] P. Bräunlich, L. A. De Werd, J. Fillard, J. Gasiot, H. Glaefede, P. Kelly, D. V. Lang, and J. Vanderschueren. *Thermally stimulated relaxation in solids.* Springer, 1979.

[188] P. K. Divekar. *Fourier deep level transient spectroscopy and its application to gold in silicon.* PhD thesis, State University Oregon, 2002.

[189] T. Walter, R. Herberholz, C. Müller, and H. W. Schock. Determination of defect distributions from admittance measurements and application to $Cu(In,Ga)Se_2$ based heterojunctions. *J. Appl. Phys.*, 80:4411–4420, 1996.

[190] R. Herberholz, M. Igalson, and H. W. Schock. Distinction between bulk and interface states in $CuInSe_2$/CdS/ZnO by space charge spectroscopy. *J. Appl. Phys.*, 83(1):318–325, 1998.

[191] J. W. Lee, J. D. Cohen, and W. N. Shafarman. The determination of carrier mobilities in CIGS photovoltaic devices using high-frequency admittance measurements. *Thin Solid Films*, 480:336–340, 2005.

[192] J. V. Li, X. Li, D. S. Albin, and D. H. Levi. A method to measure resistivity, mobility, and absorber thickness in thin-film solar cells with application to CdTe devices. *Sol. Energy Mater. Sol. Cells*, 94:2073–2077, 2010.

[193] K. Decock, S. Khelifi, S. Büecheler, F. Pianezzi, A. N. Tiwari, and M. Burgelman. Defect distributions in thin film solar cells deduced from admittance measurements under different bias voltages. *J. Appl. Phys.*, 110(063722), 2011.

[194] J. V. Li, R. S. Crandall, I. L. Repins, A. M. Nardes, and D. H. Levi. Applications of admittance spectroscopy in photovoltaic devices beyond majority-carrier trapping defects. *37th IEEE Photovoltaic Specialists Conference, Seattle, Washington, 2011*, 2011.

[195] U. Rau, M. Schmidt, A. Jasenek, G. Hanna, and H. W. Schock. Electrical characterization of $Cu(In,Ga)Se_2$ thin film solar cells and the role of defects for the device performance. *Sol. Energy Mater. Sol. Cells*, 67:137–143, 2001.

[196] J. Lauwaert, L. Van Puyvelde, J. Lauwaert, J. W. Thybaut, S. Khelifi, M. Burgelman, F. Pianzzi, A. N. Tiwari, and H. Vrielinck. Assignment of capacitance spectroscopy signals of CIGS solar cells to effects of non-ohmic contacts. *Sol. Energy Mater. Sol. Cells*, 112:78–83, 2013.

[197] J. T. Heath, J. D. Cohen, and W. N. Shafarman. Bulk and metastable defects in $CuIn_{1-x}Ga_xSe_2$ thin films using drive-level capacitance profiling. *J. Appl. Phys.*, 95:1000–1010, 2004.

[198] M. Igalson and M. Edoff. Compensating donors in $Cu(In,Ga)Se_2$ absorbers of solar cells. *Thin Solid Films*, 480:480–481, 2005.

[199] U. Reisloehner, H. Metzner, and C. Ronning. Hopping conduction observed in thermal admittance spectroscopy. *Phys. Rev. Lett.*, 104(226403), 2010.

[200] J. Lauwaert, L. Callens, S. Kheliffi, K. Decock, A. Chirilă, F. Pianezzi, S. Büecheler, A. N. Tiwari, and H. Vrielinck. About RC-like contacts in deep level transient spectroscopy and $Cu(In,Ga)Se_2$ solar cells. *Prog. Photovolt: Res. Appl.*, 20(5):588–594, 2012.

[201] D. Pearman. *Electrical characterisation and modelling of schottky barrier metal source/drain MOSFETs.* PhD thesis, University Warwick, 2007.

[202] W. Mtangi. *Electrical characterisation of ZnO and metal ZnO contacts.* PhD thesis, University Pretoria, 2009.

[203] D. R. Lide. *CRC Handbook of chemistry and physics*. CRC Press, 2005.

[204] M. Sugiyama, R. Nakai, H. Nakanishi, and S. F. Chichibu. Fermi-level pinning at the metal p-type $CuGaS_2$ interfaces. *J. Appl. Phys.*, 92:7317–7319, 2002.

[205] R. T. Tung. Recent advances in Schottky barrier concepts. *Mater. Sci. Eng. R*, 35:1–138, 2001.

[206] I. M. Dharmadasa, N. B. Chaure, A. P. Samantilleke, and A. Hassan. Multi Fermi level pinning at metal/Cu(In,Ga)(Se,S)$_2$ interfaces. *Sol. Energy Mater. Sol. Cells*, 92:923–928, 2008.

[207] B. L. Sharma. *Metal-semiconductor Schottky barrier junctions and their applications*. Plenum Press, 1984.

[208] J. H. Werner and H. H. Güttler. Barrier inhomogeneities at Schottky contacts. *J. Appl. Phys.*, 69:1522–1533, 1991.

[209] W. Leroy. *A fundamental study of advanced metal/semiconductor contacts*. PhD thesis, University Gent, 2007.

[210] H. Lüth. *Solid surfaces, interfaces and thin films*. Springer, 2010.

[211] A. Chirilă, D. Guettler, D. Bremaud, S. Büecheler, R. Verma, S. Seyrling, S. Nishiwaki, S. Haenni, G. Bilger, and A. N. Tiwari. CIGS solar cells grown by a three-stage process with different evaporation rates. *Proc. 34th IEEE Photovoltaic Specialists Conference, Philadelphia, USA, June 2007*, pages 812–816, 2009.

[212] B. Canava, J. F. Guillemoles, J. Vigneron, D. Lincot, and A. Etcheberry. Selenium chemistry modifications of Cu(In,Ga)Se_2 surfaces after bromine etch. High resolution XPS studies of buried interface with chemically deposited CdS. *Electrochem. Soc.*, 2003:31–40, 2006.

[213] M. Bouttemy, P. Tran-Van, I. Gerard, T. Hildebrandt, A. Causier, J. L. Pelouard, and G. Dagher. Thinning of CIGS solar cells: part I: chemical processing in acidic bromine solutions. *Thin Solid Films*, 591:7207–7211, 2001.

[214] B. Canava, J. F. Guillemoles, J. Vigneron, D. Lincot, and A. Etcheberry. Chemical elaboration of well defined Cu(In,Ga)Se_2 surfaces after aqueous oxidation etching. *J. Phys. Chem. Solids*, 64:1791–1796, 2003.

[215] A. Kylnes. The chemical bath deposited CdS/Cu(In,Ga)Se_2 interface as revealed by X-Ray photoelectron spectroscopy. *J. Electrochem. Soc.*, 146:1816–1823, 1999.

[216] M. Nouiri, Z Ben Ayadi, K. Khirouni, S. Alaya, K. Djessas, and S. Yapi. Effect of substrate temperature and source grain size on the structural and electrical properties of CSVT grown Cu($In_{1-x}Ga_x$)Se_2 thin films. *Mater. Sci. Eng., C*, 27:1002–1006, 2007.

[217] A. Ashok Kumar, V. Janardhanam, V. Rajagopal Reddy, and P. Narasimha Redd. Evaluation of Schottky barrier parameters of Pd/Pt Schottky contacts on n-InP (100) in wide temperature range. *Superlattices Microstruct.*, 45:22–32, 2009.

[218] M. Gloeckler. *Device physics of Cu(In,Ga)Se_2 thin-film solar cells*. PhD thesis, Colorado State University, 2005.

[219] T. Sakurai, N. Ishida, S. Ishizuka, K. Matsubara, K. Sakurai, A. Yamada, G. K. Paul, K. Akimoto, and S. Niki. Investigation of relation between Ga concentration and defect levels of Al/Cu(In,Ga)Se_2 Schottky junctions using admittance spectroscopy. *Thin Solid Films*, 515:6208–6211, 2007.

[220] Y. Akaki, H. Komaki, H. Yokoyama, K. Yoshino, K. Maeda, and T. Ikari. Structural and optical characterization of Sb-doped $CuInS_2$ thin films grown by vacuum evaporation method. *J. Phys. Chem. Solids*, 64:1863–1867, 2003.

[221] A. Tempez, S. Legendre, and P. Chapon. Depth profile analysis by plasma profiling time of flight mass spectrometry. *Nucl. Instr. Meth. B*, 332:351–354, 2014.

[222] R. Aninat, G. Zoppi, A. Tempez, P. Chapon, N. S. Beattie, R. Miles, and I. Forbes. Crystallographic properties and elemental migration in two-stage prepared Cu($In_{1-x}Al_x$)Se_2 thin films for photovoltaic applications. *J. Alloys Compd.*, 566:180–186, 2013.

[223] G. Kartopu, A. Tempez, A. J. Clayton, V. Barrioz, S. J. C. Irvine, C. Olivero, P. Chapon, S. Legendre, and J. Cooper. Chemical analysis of $Cd_{1-x}Zn_xS$/CdTe solar cells by plasma profiling TOFMS. *Mater. Res. Innovations*, 18:82–85, 2014.

[224] J. Lähnemann. *Spectrally resolved current losses in Cu(In,Ga)Se_2 thin-film solar sells*. PhD thesis, University Nantes, 2008.

[225] E. S. Toberer, A. C. Tamboli, M. Steiner, and S. Kurtz. Analysis of solar cell quality using voltage metrics. *Proc. IEEE Photovoltaic Specialists Conference, Austin, Texas, June 2012*, pages 1327–1331, 2012.

[226] G. Zoppi, I. Forbes, R. W. Miles, P. J. Dale, J. J. Scragg, and L. M. Peter. $Cu_2ZnSnSe_4$ thin film solar cells produced by selenisation of magnetron sputtered precursors. *Prog. Photovolt: Res. Appl.*, 17:315–319, 2009.

[227] Mt. Wagner, I. Dirnstorfer, D. M. Hofmann, M. D. Lampert, F. Karg, and B. K. Meyer. Characterization of CuIn(Ga)Se_2 thin films - Cu-rich layers. *Phys. Status Solidi A*, 131:131–142, 1998.

[228] N. Rega, S. Siebentritt, J. Albert, S. Nishiwaki, A. Zajogin, M. Ch. Lux-Steiner, R. Kniese, and M. J. Romero. Excitonic luminescence of Cu(In,Ga)Se_2. *Thin Solid Films*, 480:286–290, 2005.

[229] J. Krustok, H. Collana, and K. Hjelt. Does the low-temperature Arrhenius plot of the photoluminescence intensity in CdTe point towards an erroneous activation energy? *J. Appl. Phys.*, 81:1442–1445, 1997.

[230] M. Grossberg, J. Krustok, K. Timmo, and M. Altosaar. Radiative recombination in $Cu_2ZnSnSe_4$ monograins studied by photoluminescence spectroscopy. *Thin Solid Film*, 517:2489–2492, 2009.

[231] J. H. Werner, J. Mattheis, and U. Rau. Efficiency limitations of polycrystalline thin film solar cells: case of Cu(In,Ga)Se_2. *Thin Solid Films*, 480:399–409, 2005.

[232] S. Siebentritt. What limits the efficiency of chalcopyrite solar cells? *Sol. Energy Mater. Sol. Cells*, 95:1471–1476, 2011.

[233] I. Dirnstorfer, M. Wagner, D. M. Hofmann, M. Lampert, F. Karg, and B. Meyer. Characterization of CuIn(Ga)Se_2 thin films; In-rich layers. *Phys. Status Solidi*, 168:163–175, 1998.

[234] A. Bauknecht, S. Siebentritt, J. Albert, and M. Ch. Lux-Steiner. Radiative recombination via intrinsic defects in $Cu_xGa_ySe_2$. *J. Appl. Phys.*, 89:4391–4400, 2001.

[235] H. Zachmann, S. Heinker, A. Braun, A. V. Mudryi, V. F. Gremenok, A. V. Ivaniukovich, and M .V. Yakushev. Characterisation of Cu(In,Ga)Se_2-based thin film solar cells on polyimide. *Thin Solid Films*, 517:2209–2212, 2009.

[236] A. P. Levanyuk and V. V. Osipov. Edge luminescence of direct-gap semiconductors. *Sov. Phys. Usp.*, 24:187–215, 1981.

[237] J. Krustok, H. Collan, M. Yakushev, and K. Hjelt. The role of spatial potential fluctuations in the shape of the PL bands of multinary semiconductor compounds. *Phys. Scr.*, 79:179–182, 1999.

[238] J. Haarstrich. *Interface modification by ion implantation and optical characterization of high-efficiency Cu(In,Ga)Se_2 solar cells.* PhD thesis, Jena University, 2011.

[239] M. Burgelman and J. Marlein. Analysis of graded band gap solar cells with SCAPS. *Proceedings of the 23rd European Photovoltaic Solar Energy Conference, Spain, 2008*, pages 2151–2155, 2008.

[240] G. Brown, V. Faifer, A. Pudov, S. Anikeev, E. Bykov, M. Contreras, and J. Wu. Determination of the minority carrier diffusion length in compositionally graded Cu(In,Ga)Se_2 solar cells using electron beam induced current. *Appl. Phys. Lett.*, 96(022104), 2010.

[241] M. Troviano and K. Taretto. Temperature-dependent quantum efficiency analysis of graded-gap Cu(In,Ga)Se_2 solar cells. *Sol. Energy Mater. Sol. Cells*, 95:3081–3086, 2011.

[242] J. Haarstrich, H. Metzner, C. Ronning, A. Undisz, T. Rissom, C. A. Kaufmann, and H. W. Schock. Luminescence properties of Ga-graded Cu(In,Ga)Se_2 thin films. *Thin Solid Films*, 520:3657–3662, 2012.

[243] S. Siebentritt, N. Papathanasiou, and M. Lux-Steiner. Photoluminescence excitation spectroscopy of highly compensated $CuGaSe_2$. *Phys. Status Solidi B*, 242:2627–2632, 2005.

[244] J. J. Scragg, T. Ericson, X. Fontané, , V. Izquierdo-Roca, A. Pérez-Rodrígeuz, T. Kubart, M. Edoff, and C. Platzer-Björkman. Rapid annealing of reactively sputtered precursors for Cu_2ZnSnS_4 solar cells. *Prog. Photovolt: Res. Appl.*, pages 31–34, 2012.

[245] T. Ericson, J. J. Scragg, A. Hultqvist, J. T. Wätjen, P. Szaniawski, T. Törndahl, and C. Platzer-Björkman. Zn(O,S) buffer layers and thickness variations of CdS buffer for Cu_2ZnSnS_4 solar cells. *Journal of Photovoltaics*, 4:465–469, 2014.

[246] M. J. Romero, H. Du, G. Teeter, Y. Yan, and M. M. Al-Jassim. Comparative study of the influence of two distinct sulfurization ramping rates on the properties of Cu_2ZnSnS_4 thin films. *Appl. Surf. Sci.*, 258:250–254, 2012.

[247] J. Krustok, J. Raudoja, M. Yakushev, R. D. Pilkington, and H. Collan. On the shape of the close-to-band-edge photoluminescent emission spectrum in compensated $CuGaSe_2$. *Phys. Status Solidi A*, 173:483–490, 1999.

[248] A. Walsh, S. Chen, S. Wei, and X. Gong. Kesterite thin-film solar cells: advances in materials modelling of Cu_2ZnSnS_4. *Adv. Energy Mater*, 2:400–409, 2012.

[249] B. Tseng, G. Chang, and S. Lin. Influences of Sb on the growth and properties of $CuInSe_2$ thin films. *Jpn. J. Appl. Phys.*, 34:1109–1112, 1995.

[250] L. Zhang, Q. He, W. Jiang, F. Liu, C. Li, and Y. Sun. Effects of substrate temperature on the structural and electrical properties of Cu(In, Ga)Se_2 thin films. *Sol. Energy Mater. Sol. Cells*, 93:114–118, 2009.

[251] M. Burgelman, P. Nollet, and S. Degrave. Modelling polycrystalline semiconductor solar cells. *Thin Solid Films*, 361:527–532, 2000.

[252] S. Siebentritt, N. Papathanasiou, and M. C. Lux-Steiner. Potential fluctuations in compensated chalcopyrites. *Physica B*, 376:831–833, 2006.

[253] Z. Zott, K. Leo, M. Ruchk, and H. W. Schock. Photoluminescence of polycrystalline $CuInSe_2$ thin films. *Appl. Phys. Lett.*, 68:1144–1146, 1995.

[254] M. Park, S. Ahn, J. Yun, J. Gwak, A. Cho, S. Ahn, K. Shin, D. Nam, H. Cheong, and H. Yoon. Characteristics of Cu(In,Ga)Se_2 (CIGS) thin films deposited by a direct solution coating process. *J. Alloys Compd.*, 513:68–74, 2012.

[255] Y. M. Shin, C. S. Lee, D. H. Shin, Y. M. Ko, E. A. Al-Ammar, H. S. Kwon, and B. T. Ahn. Characterization of Cu(In,Ga)Se_2 solar cells grown on Na-free glass with an NaF layer on a Mo film. *J. Solid State Sci. Technol.*, 2:248–252, 2013.

[256] S. Shirakata and T. Nakada. Photoluminescence and time-resolved photoluminescence in Cu(In,Ga)Se_2 thin films and solar cells. *Phys. Status Solidi C*, 6:1059–1062, 2009.

[257] G. Hanna, J. Mattheis, V. Laptev, Y. Yamamoto, U. Rau, and H. W. Schock. Influence of the selenium flux on the growth of Cu(In,Ga)Se_2 thin films. *Thin Solid Films*, 31:431–432, 2003.

[258] T. Sakurai, M. M. Islam, H. Uehigashi, S. Ishizuka, A. Yamada, K. Matsubara, S. Niki, and K. Akimoto. Dependence of Se beam pressure on defect states in CIGS-based solar cells. *Sol. Energy Mater. Sol. Cells*, 95:227–230, 2011.

[259] D. Abou-Ras, M. A. Contreras, R. Noufi, and H. W. Schock. Impact of the Se evaporation rate on the microstructure and texture of Cu(In,Ga)Se_2 thin films for solar cells. *Thin Solid Films*, 517:2218–2221, 2009.

[260] M. M. Islam, A. Uedono, T. Sakurai, A. Yamada, S. Ishizuka, K. Matsubara, S. Niki, and K. Akimoto. Impact of Se flux on the defect formation in polycrystalline Cu(In,Ga)Se_2 thin films grown by three stage evaporation process. *J. Appl. Phys.*, 113(064907), 2013.

[261] Z. Jehl, F. Erfurth, N. Naghavi, L. Lombez, I. Gerard, M. Bouttemy, P. Tran-Van, A. Etcheberry, G. Voorwinden, B. Dimmler, W. Wischmann, M. Powalla, J. F. Guillemoles, and D. Lincot. Thinning of CIGS solar cells: part II: cell characterizations. *Thin Solid Films*, 2011:7212–7215, 519.

[262] C. Persson, Y. Zhao, S. Lany, and A. Zunger. n-type doping of $CuInSe_2$ and $CuGaSe_2$. *Phys. Rev. B*, 72(035211), 2005.

[263] G. A. Medvedkin, T. Nishi, Y. Katsumata, Miyake H., and K. Sato. Study of point defects in $CuGaSe_2$ single crystals by means of electron paramagnetic resonance and photoluminescence. *Sol. Energy Mater. Sol. Cells*, 75:135–143, 2005.

[264] I. Dirnstorfer, W. Burkhardt, W. Kriegseis, I. Österreicher, H. Alves, D. M. Hofmann, O. Ka, A. Polity, B. K. Meyer, and D. Braunger. Annealing studies on CuIn(Ga)Se_2: the influence of gallium. *Thin Solid Films*, 361:400–405, 2000.

[265] J. Liu, D. Zhuang, L. Luan, M. Cao, M. Xie, and X. Li. Preparation of Cu(In,Ga)Se_2 thin film by sputtering from Cu(In,Ga)Se_2 quaternary target. *Prog. Nat. Sci.*, 23:133–138, 2013.

[266] S. Niki, I. Kim, P. J. Fons, H. Shibata, A. Yamada, H. Oyanagi, T. Kurafuji, S. Chichibu, and H. Nakanishi. Effects of annealing on $CuInSe_2$ films grown by molecular beam epitaxy. *Sol. Energy Mater. Sol. Cells*, 49:319–326, 1997.

[267] J. H. Schön, O. Schenker, H. Riazi-Nejad, K. Friemelt, Ch. Kloc, and E. Bucher. Characterization of defect levels in doped and undoped $CuGaSe_2$ by means of photoluminescence measurements. *Phys. Status Solidi A*, 161:301–313, 1997.

[268] J. Sastré-Hernández, M. E. Calixto, M. Tufino-Veázquez, G. Contreras-Puente, A. Morales-Acevedo, G. Casados-Cruz, M. A. Hernández-Pérez, M. L. Albor-Aguilera, and R. Mendoza-Pérez. Cu(In,Ga)Se_2 thin films processed by co-evaporation and their application into solar cells. *Rev. Mex. Fis.*, 57:441–445, 2011.

[269] F. Pianezzi, P. Reinhard, A. Chirilă, S. Nishiwaki, B. Bissig, S. Büecheler, and A. N. Tiwari. Defect formation in Cu(In,Ga)Se_2 thin films due to the presence of potassium during growth by low temperature co-evaporation process. *J. Appl. Phys.*, 114(194508), 2013.

[270] M. Alonso and E. J. Finn. *Fundamentele natuurkunde: 3: Golven.* Delta Press.

[271] P. D. Paulson, R. W. Birkmire, and W. N. Shafarman. Optical characterization of $CuIn_{1-x}Ga_xSe_2$ alloy thin films by spectroscopic ellipsometry. *J. Appl. Phys.*, 94:879–888, 2003.

[272] M. I. Alonso, M. Garriga, C. A. Durante Rincón, E. Hernández, and M. León. Optical functions of chalcopyrite $CuGa_xIn_{1-x}Se_2$ alloys. *Appl. Phys. A*, 74:659–664, 2002.

[273] L. A. Kosyachenko, X. Mathew, P. D. Paulson, V. Ya. Lytvynenko, and O. L. Maslyanchuk. Optical and recombination losses in thin-film Cu(In,Ga)Se_2 solar cells. *Sol. Energy Mater. Sol. Cells*, 130:291–302, 2014.

[274] H. D. Detavernier, Vrielinck. *Syllabus Solid state and nano physics.* Ghent university.

[275] R. Baets and G. Roelkens. *Syllabus Photonics.* Ghent university, 2010.